Improving the focality of magnetic stimulation coils.

Hughes, Richard Owain

Improving The Focality Of Magnetic Stimulation Coils

Richard Owain Hughes

Submitted to the University of Wales in fulfilment of the requirements for the Degree of Doctor of Philosophy

Civil and Computational Engineering Centre
College of Engineering
Swansea University

2012

Swansea University
Prifysgol Abertawe

ProQuest LLC.
789 East Eisenhower Parkway
P.O. Box 1346
Ann Arbor, MI 48106 – 1346

Summary

Magnetic stimulation is a technique that involves exciting nervous tissue in the body by passing a rapidly changing pulse of current through a coil of wire while the coil is in close proximity to the body. The changing magnetic field around the coil results in there being an electric field around the coil which includes a small electric field within the tissue. This induced electric field causes a voltage to be generated in the nervous tissue and the nerve to be excited. Unfortunately, due to the breadth of the electric field profile around a coil, tissue that it is not intended to be stimulated is usually excited as well as the intended tissue.

This work presents a novel tri-modular computer program approach to improving the focality of the electric field around a stimulating coil by applying field modelling and the mathematical technique of optimisation to altering the coil geometry. Several new coil shapes are suggested and a new shape that is readily buildable using current methods – the Gull-Wing Coil – is proposed. It is shown that this shape can meet a required normalised nerve membrane potential requirement.

The technique of modelling coils as being made of infinitesimally thin wire is investigated and new validatory results presented.

The novel use of a **T-Φ** Finite Element Method (FEM) formulation to model magnetic stimulation coils is reported upon. Results are presented from using this formulation in both the frequency and time domains, together with results from combining the time domain models with lumped circuit element models of a stimulating machine. New results relating to the issues involved in applying the formulation to stimulating coil problems are presented. A method of running a circuit coupled time domain **T-Φ** FEM model followed by one run of a frequency domain **T-Φ** FEM model in order to obtain the resistance and inductance of a coil when used with a biphasic stimulator is suggested and demonstrated to work.

Acknowledgements

I would like to thank:

- Dr A McCowen, Professor K Morgan and Professor O Hassan for their help, supervision, suggestions and encouragement. I would particularly like to thank Dr McCowen for giving of his time in having regular supportive meetings throughout the duration of this work, for his patience in helping me deal with the issues that arose during the work and for his assistance in coping with the problems associated with my extended period of illness and absence from the work. I should also like to thank Dr McCowen for always greeting me in a friendly and positive way.

- Dr P Ledger for his assistance at the beginning of the Finite Element Method modelling undertaken during this work.

- Mr A Thomas, Mr J Starzewski, and the other staff of The Magstim Company for their time, help, support and assistance with this work. I should also like to thank the company for allowing me to use their equipment and resources, and for their gratefully received sponsorship.

- My mother and sister for their boundless love, help and support during this work and particularly during my period of illness.

This work was funded by the European Social Fund via the Welsh European Funding Office. I should like to extend my thanks for this support.

Contents

Definitions

$\mathbf{A}$	Magnetic vector potential
$\mathbf{B}$	Magnetic flux density
C	Optimisation compound function value
C_m	Nerve membrane capacitance
C_S	Stimulating machine capacitance
$\mathbf{D}$	Electric flux density
$\partial(\Omega_c+\Omega_n)$	The far outer boundary of a Finite Element model
$\mathbf{E}$	Electric field intensity
E_0	Peak electric field magnitude (at beginning of current pulse)
$\mathbf{H}$	Magnetic field intensity
i	Circuit current
i_m	Current through nerve membrane
$\mathbf{J}$	Electric current density
j	$\sqrt{-1}$
l_C	Coil inductance
L_S	Stimulator inductance
L_{tot}	Stimulator and coil circuit combined inductance
O	Optimisation objective function value
P	Optimisation penalty function value
r_C	Coil resistance
R_m	Nerve membrane resistance
R_S	Stimulator resistance
R_{tot}	Stimulator and coil circuit combined resistance
$\mathbf{T}$	Current vector potential
$\mathbf{T_e}$	Current vector potential (due to eddy-currents)
$\mathbf{T_s}$	Current vector potential (due to source)
V	Electric scalar potential
V_m	Nerve membrane potential

V_{nm} Normalised nerve membrane potential

V_0 Initial voltage across stimulator capacitor

Γ_{cn} Non-end surfaces of conductors

Γ_E The end faces of conductors

ε_r Relative permittivity

ε_0 Absolute permittivity

μ_r Relative permeability

μ_0 Absolute permeability

ρ Volume charge density

σ Conductivity

τ_m Nerve membrane time constant

Φ Magnetic scalar potential

ψ Magnetic flux

Ω Spatial domain of model

Ω_c The domain of conducting material

Ω_n The domain of non-conducting material

ω Angular frequency

1 Introduction

1.1 Background

The therapeutic medical technique known as magnetic stimulation [1] involves passing pulses of high magnitude electric current through a coil of metal. The coil is held in close proximity to an area of a human patient's body and the electric field that surrounds the coil, owing to the changing magnetic field around the coil which in turn is due to the changing current in the coil, induces small currents within the tissue in proximity to the coil. The technique is used to effect current impulses in the nerves in the tissue which serve to help patients with disorders of the neuromuscular system or those that benefit from excitation of sensory nerves within the brain. The act of inducing such current pulses within the body is termed stimulation.

A problem with magnetic stimulation is that the profile of the electric field around a stimulation coil is typically quite broad and nerve structures other than those which are intended to be exercised are stimulated. In addition, energy is wasted in the field which is concentrated all around the coil rather than in one area. This thesis concerns work which is intended to find a novel way to improve the focality of the electric field around a stimulation coil by searching for a more suitable coil geometry.

Background information regarding the biology of stimulation is presented in Appendix A. This chapter begins by discussing some of the background to magnetic stimulation. It then continues by considering the equipment used in stimulation, some of the effects which arise within stimulation coils, the focality of coils and an approach to finding more focal coils. In the next chapter, coil focality is discussed in greater depth, particularly with reference to exactly what electrical quantity lies at the centre of focality. This leads to a novel method of finding new coil geometries being proposed. This method relies on two methods of simulating the electric fields around coils and the use of a mathematical technique known as optimisation.

Chapters 3, 4 and 5 present the field simulation techniques used in this work in considerable detail and introduce some novel aspects relating to the work. Chapter 6 discusses optimisation at length and shows for the first time how a particular combination of field simulation and optimisation techniques can be used to solve a problem involving a magnetic stimulation coil. Finally, Chapter 7 shows how this work's chosen simulation and optimisation methods can be combined to produce computer software intended to implement the method of finding new coil geometries presented in Chapter 2. New coil geometries will be presented and field measurements will be taken from two shapes to verify that the field simulation software is working correctly.

1.2 Magnetic Stimulation

The physical basis for magnetic stimulation lies in the principle of electromagnetic induction which was investigated by and report on by Michael Faraday in 1831. This is centred around the observation that a changing current in a wire, or a moving wire carrying a steady current, induces a current in a nearby wire. In magnetic stimulation a current pulse through a stimulation coil (of around 5 kA in maximum magnitude) changes over its duration and induces much smaller currents in body tissue which is close to the location where the coil is held.

An alternative to magnetic stimulation is electrical stimulation where electrodes are inserted into the body. Magnetic stimulation offers a pain free alternative to electrical stimulation since it is able to stimulate tissue below the surface without stimulating the pain receptors in the skin at the surface. This is because the pain receptors have a higher stimulation threshold [7].

Bickford and Fremming [8] were the first to report magnetic stimulation of peripheral nerves in humans and animals in 1965 and demonstrated the non-invasive magnetic stimulation of facial nerves. However, they were frustrated by their inability to take accurate measurements of the induced electrical behaviour and their work was not pursued further.

Magnetic stimulation was next reported upon by Polson, Barker and Freeston in 1982 [9] where they discussed the production of a magnetic stimulator of peripheral nerves and were the first to record a magnetically evoked muscle potential. This stimulator design was then further improved upon on by Jalinous [10].

Perhaps the landmark paper on magnetic stimulation came in 1995 from Barker et. al. [11]. In it they described how they had achieved magnetic stimulation of the human motor cortex. Here, it was found that it was possible to position a stimulating coil above a patient's head and, by passing pulses of current through the coil, cause a peripheral part of the body to move.

Since then there has been a steady stream of interest in magnetic stimulation in the form of research publications, development of therapeutic applications and improvements in manufacturing techniques. By today, a number of companies manufacture commercial stimulators including the Magstim Co. Ltd., Neuronetics, Medtronic and Neotonus.

The publication [12] offers a good summary of the uses of magnetic stimulation at the moment. It may be found that single pulse stimulation systems have a number of applications in the diagnosis of many degenerative neurological diseases. For example transcranial magnetic stimulation has been used in the early diagnosis of multiple sclerosis, central motor disorders and motor neurone disease. Single pulse systems have been used for cortical mapping, functional assessment of central motor pathways and general brain research. Additionally, stimulation has been used to induce speech difficulties and brain lesions to investigate brain function [13][14]. Applications of stimulation in peripheral parts of the body include for spinal injury and the treatment of urinary incontinence [15].

Systems involving repetitive trains of current pulses in the stimulation coil are also very useful and the Magstim Rapid^2 stimulator is an example of a machine capable of producing pulse trains at rates of between 1 and 100 pulses per second. The uses of such a stimulator lie in the field of repetitive transcranial magnetic stimulation (rTMS). Uses for rTMS include in cognitive neuroscience which includes the investigation of learning, memory, speech, hearing, perception and functional

connection; in psychiatry including the treatment of depression [16] and schizophrenia [17], and to influence brain function within the dorsoleteral prefrontal cortex; in neurophysiology where it is used in the stimulation of the peripheral and central nervous pathways; and for rehabilitation including muscle recovery and the relief of spasticity.

Despite the successful applications of magnetic stimulation listed above, the technique is not without its problems. Aside from problems associated with the lack of focus of the electric field around the coil and the energy wasted in a lot of the field around the coil, other problems exist. Firstly, the stimulation coil heats quite rapidly during use meaning that energy is wasted as heat and the coil itself becomes hot. This is undesirable for something that is in contact with the body (although a thin plastic insulating shell exists around the coil) and places a limit on the duration that repetitive stimulation pulse trains may be used for. Some coils have ventilation fans attached to them to try and reduce the heating effect during application.

The other main problem with magnetic stimulation is with aspects of the technique itself. Single pulse stimulation is considered to be a safe procedure with little in the way of side-effects [18]. However rTMS is capable of producing dangerous side effects such as epileptic seizures if it is not administered in a considered and careful manner [18]. Advice for what is a safe dosage for rTMS appears in [18].

Despite the above difficulties, magnetic stimulation has found numerous applications where it is successfully and safely used.

1.3 Stimulating Machines

Essentially, other than the patient, three items are involved in the process of magnetic stimulation. These are the stimulating coil itself, a box containing all the electrical and electronic components to generate the current pulse in the coil known as a stimulator, and a cable to connect the coil and the stimulator together. This section is concerned with the two main types of stimulator.

The first type of stimulator, which is the type involved in single pulse stimulation, is known as a monophasic stimulator. A simplified circuit diagram of a monophasic stimulator [19] is shown in Figure 1.1. The stimulator includes a large capacitor which can be charged, via a separate circuit, to a voltage typically as high as about 3 kV. When the clinician is ready to discharge the current pulse, the switch is closed and current begins to flow into the coil which can be thought of as a resistor and inductor in series. The current through the system can be as high as about 5 kA. The current then returns from the coil and passes through the high voltage diode then reaches the stimulator's resistor where the returning energy is dissipated as heat. The capacitor is then recharged incase a further pulse is required by the clinician.

A magnitude normalised illustration of a current pulse due to a Magstim 200 monophasic stimulator is shown in Figure 1.2. It may be seen that the current rapidly rises to a maximum value then diminishes in magnitude more slowly as energy is dissipated in the coil and more so in the stimulator's resistor. This pulse shape has a flat frequency spectrum until about 10 kHz, above which the frequency content falls off quite quickly [20]. This is seen in Figure 1.3.

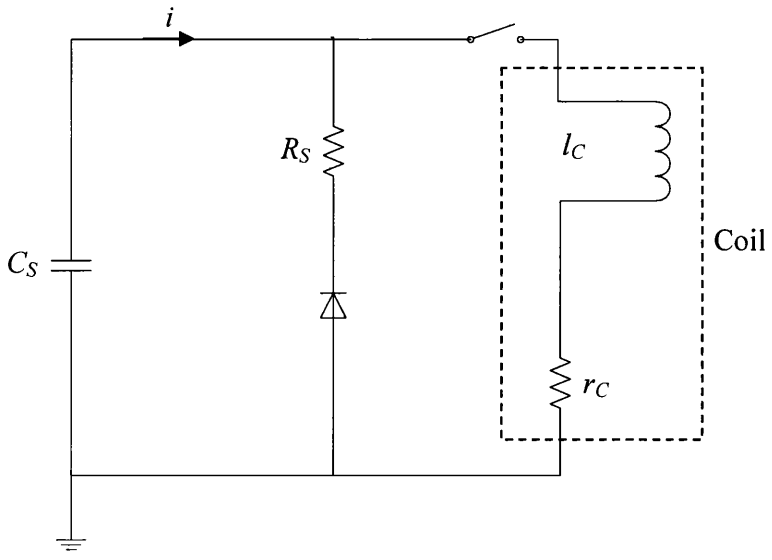

Figure 1.1 - A simplified circuit diagram of a monophasic stimulator

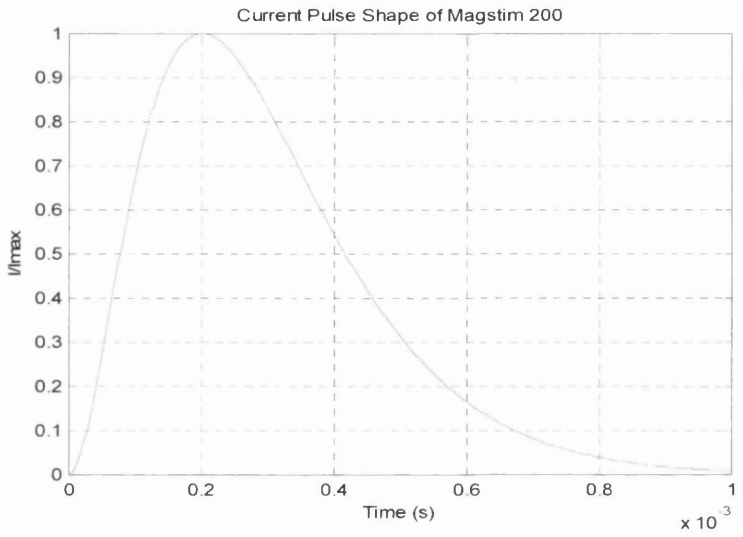

Figure 1.2 - The time domain current pulse shape of the Magstim 200 monophasic stimulator

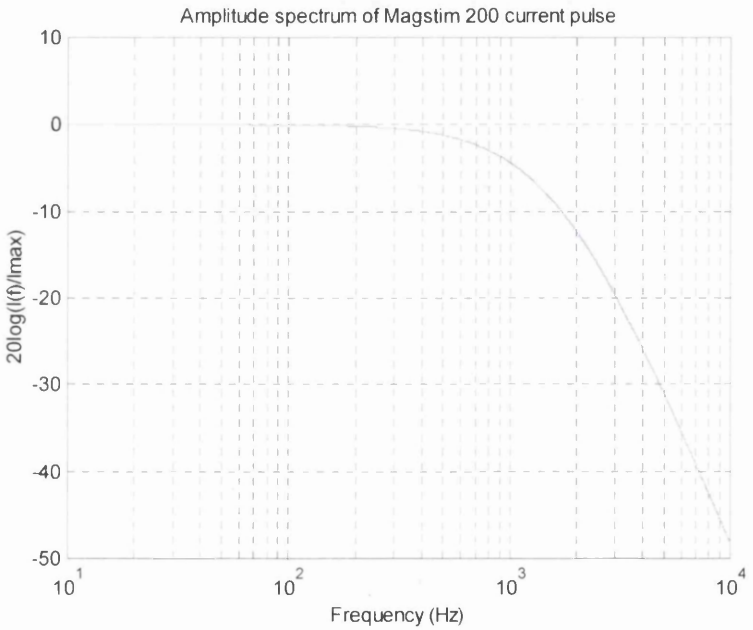

Figure 1.3 - The frequency spectrum of a current pulse due to a Magstim 200 monophasic stimulator

The stimulator type used for repetitive pulse trains is known as a biphasic stimulator. (It should be noted that a typical biphasic stimulator, such as the Magstim Rapid^2, is also capable of being set to single pulse mode.) A simplified circuit diagram of a biphasic stimulator [21] is shown in Figure 1.4. Here, the stimulator consists of a large capacitor which may be charged to a high voltage; in the case of the Magstim Rapid^2 this is 1700 V. When the clinician closes the switch, the capacitor discharges

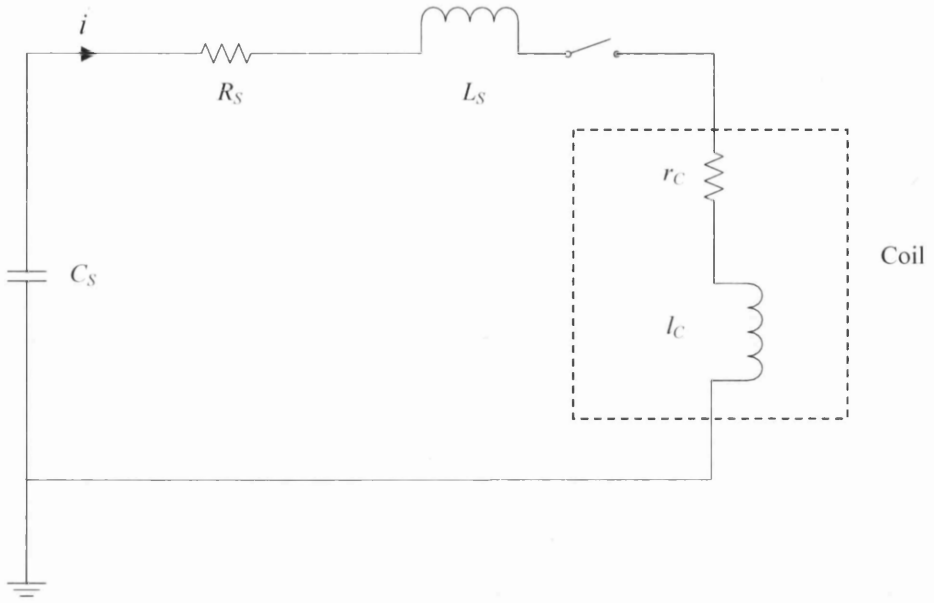

Figure 1.4 - A simplified ciruit diagram of a biphasic stimulator

into the coil which behaves as an inductor and resistor in series. However, unlike in a monophasic stimulator, there is no large resistor within the stimulator (only a small residual series resistance and inductance), and the current from the coil flows back to recharge the capacitor with the opposite polarity to before. Once the capacitor has recharged, it immediately discharges back through the coil, after which the capacitor recharges with the same polarity as at the beginning. An electronic switch is then opened to end this oscillatory behaviour. The capacitor is then charged to its original state. After a short period of time has passed which depends on the pulse train selected, if the clinician keeps the switch pressed, the next pulse then begins. A plot of one biphasic pulse is shown in Figure 1.5. It may be seen that a biphasic pulse, due to its oscillatory origination, is a simple damped sinusoid with a single frequency component. The energy lost in the system is from the resistive coil, the connecting cable joining the stimulator to the coil, and the small residual resistance in the stimulator.

In a biphasic stimulator, a sizeable fraction of the energy initially discharged from the capacitor is recaptured by the end of the pulse. This has been measured for a Magstim Rapid^2 with a Magstim HP90 coil to be around 48% [22]. Thus a biphasic system can, in a way, be considered less wasteful than a monophasic one where all the capacitor's energy is lost either in the coil, the leads or the stimulator's internal resistor.

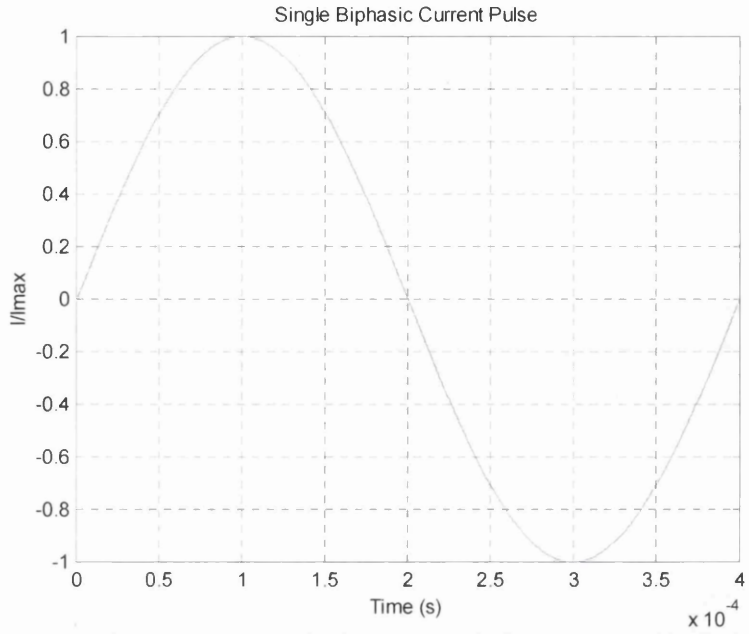

Figure 1.5 - The time domain normalised current waveform due to a Magstim Rapid² biphasic stimulator

It can be noted that the circuit shown in Figure 1.4 may be described by the following second order differential equation:

$$L_{tot}\frac{d^2i}{dt^2} + R_{tot}\frac{di}{dt} + \frac{1}{C_S}i = 0 \tag{1.1}$$

where $R_{tot} = R_S + r_C$ and $L_{tot} = L_S + l_C$. The initial conditions for the circuit are [23]:

$$i\Big|_{t=0} = 0 \tag{1.2}$$

$$\left.\frac{di}{dt}\right|_{t=0} = \frac{-V_0}{L_{tot}} \tag{1.3}$$

where V_0 is the initial voltage across the stimulator's capacitor. The above equations may be combined when converted into the Laplace domain [23] as:

$$I(s) = \frac{-V_0}{L_{tot}s^2 + R_{tot}s + 1/C_S} \tag{1.4}$$

This may be expressed as partial fractions and when performing an inverse Laplace Transform, the following expression for the current in the circuit as a function of time, assuming the system is underdamped, may be obtained:

$$i(t) = \frac{-V_0}{\omega L_{tot}} \exp\left(\frac{-R_{tot} t}{2L_{tot}}\right) \sin(\omega t) \tag{1.5}$$

Here, ω is the system resonant frequency and may be given in radians per second as:

$$\omega = \sqrt{\frac{1}{L_{tot} C_S} - \frac{R_{tot}^2}{4L_{tot}^2}} \tag{1.6}$$

1.4 The Skin and Proximity Effects

Owing to two electromagnetic effects, the resistance and inductance of conductors carrying current as alternating current are altered when compared to the values which they take when the conductors carry direct current. These effects are known as the skin and proximity effects and will be examined below.

When a conductor carries alternating current, a changing magnetic field arises around the current. This changing magnetic field induces new currents in nearby conducting material including the conductor itself. The currents are 90° out of phase with the original current and these secondary currents, which are themselves alternating, induce tertiary current which are 180° out of phase with the original current. These effects tend to be strongest towards the centre of a conductor where magnetic coupling is greatest.

The effects within a conductor itself are termed the skin effect since the net current through the conductor appears to be pushed towards the outside of the conductor. This effect is illustrated in a circular wire in Figure 4.8 of Section 4.11 at 4 kHz. At very high frequencies, the skin effect becomes very pronounced and only the surface or skin of a conductor appears to conduct at all.

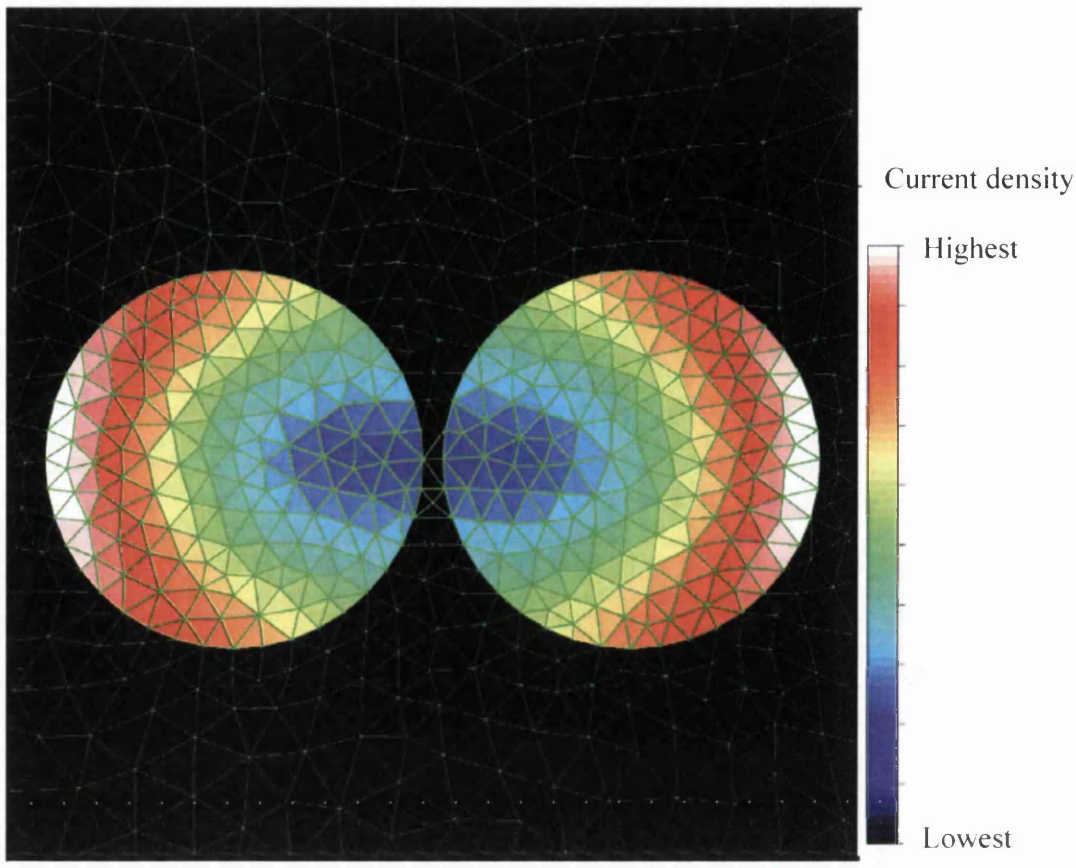

Figure 1.6 – A model of the current density distribution within two parallel circular conductors carrying current at 4 kHz in the same direction

The induction effect described above when the current in one conductor induces currents in a neighbouring conductor is termed the proximity effect. Figure 1.6 illustrates this effect in two circular wires running in parallel and carrying current at 4 kHz in the same through direction. It may be seen that the proximity effect causes the current in the wires to be pushed away from the neighbouring conductor and to concentrate at the sides of the wires furthest from their neighbour. Obviously the skin effect is also present to some degree in the conductors.

Given that the skin and proximity effects influence how much current is present in different areas of conductors it should be clear that both the resistance and inductance of the conductors change when carrying alternating current compared to the case at 0 Hz when the current distribution will be even across the conductor cross section. The resistance with alternating current will be greater than with direct current since the through current will be confined to a smaller area. It will be seen later in this work

that the skin and proximity effects change the resistance and inductance of magnetic stimulation coils and that these changes are important when making calculations involving coil resistance and inductance.

1.5 Focality

As has already been discussed in this work, one of the greatest problems with magnetic stimulation is the lack of focus of the electric field around stimulation coils and the consequent issue of mistaken stimulation of neural structures that were not intended to be stimulated. This has been studied by a number of workers and the term focality has been used in the past to refer to the desirability of the electric field profile of a stimulation coil [24]. A good precis of the work that has been done on the focality of stimulation coils was given in [25] and this is summarised below together with extra comments and the noting of additional work.

Firstly it can be noted that several workers have attempted to quantify the degree of localisation of the electric field below a magnetic stimulation coil. Mouchawar et al [26], Carabunaru and Durand [27] and Hsu [28] all define quantities which are the same as the region in a plane below the base of a coil over which the magnitude of the electric field falls to $1/\sqrt{2}$ of its peak value. The distance across this region can be thought of as the focality of the coil and may be termed the half-power region.

The stimulation coil reported upon by Barker et al in 1985 [11] was a flat spiral coil and further work by others [29][30][26] has found that coils with small diameters have more focal field profiles. Nevertheless, the field due to small coils does not penetrate so deeply into tissue [31] and therefore the depth below a coil where stimulation is desired to take place must be taken into account when attempting to design a coil with as great a focality as possible for stimulation to take place at a particular depth.

Normally, a standard single spiral coil such as the Magstim HP90 coil is oriented during stimulation such that the plane of the coil is tangential to the tissue surface at

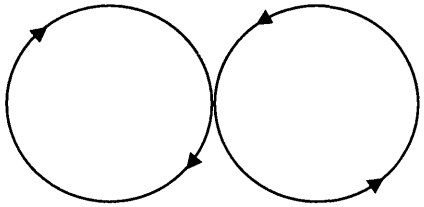

Figure 1.7 - The current flow in a double spiral coil

the location where stimulation is desired to take place. However, it has been found that orienting such a coil so that its plane is perpendicular to the tissue leads to a more focal induced field [24][28]. Nevertheless, this can cause a build up of electric charges to build up at the air - tissue interface which causes the electric field inside the body to be less than it would otherwise be [32]. This is discussed in greater length in Section 3.10.

In 1988 Ueno et al [33] reported upon a coil design which consisted of two flat spiral coils placed side-by-side with one another. Here, current was passed along the spirals so that it flowed in the opposite direction in one spiral when compared to the other. This resulted in the current in the parts of the spirals which were closest to the other spiral being in the same direction as in Figure 1.7.

Ueno at al found that the maximum current density induced by the double spiral coil was located beneath the central area of the coil where the spirals' currents flowed in the same direction. This maximum current density was about two to three times that in the regions which were not the target for stimulation. Thus it was found that the double spiral coil possessed superior focality to the single spiral coil. Cohen at al [34] considered the field due to a double spiral coil theoretically. They also found that the maximum electric field due to such a coil occurred under its centre and at a clearly defined point.

Ueno et al went on to investigate whether the space between the spirals making up the double spiral coil had an influence on focality. They found that the closer the spirals the greater the ratio of the peak current density induced beneath the coil when

compared with the current density in the regions which were not the target for stimulation.

Cohen at al also considered the effects of tilting the spirals making up a double spiral at various angles when compared to the horizontal such that the double spirals looked like a V when viewed side on. They found that the focality of the field due to the coil increased with increasing spiral angles from the horizontal. However, although the magnitude of the electric field immediately below the coil centres was the same regardless of coil angles, it was found that the magnitude of the field at this point contained greater z components compared to x and y plane components with increasing coil angle. It was thought that this could alter the coil's stimulation effectiveness.

Esselle and Stuchly [35] reported on a variety of coil geometries by using an analytical coil model of the electric field induced in a human arm represented as a homogeneous cylindrical conductor. They assumed that the activation function, i.e. what leads to stimulation occurring, is the size of the spatial derivative of the electric field in the direction of a nerve. In their model, the arm had a long straight nerve. They modelled the electric field due to a double square coil – i.e. a coil like the double spiral but with squares of conducting material rather than circular spirals. Esselle and Stuchly found that such a coil had a superior focussing of the activation function when the angle between the coil's square wings was increased.

Roth et al [36] and Esselle and Stuchly [35] both reported on a four leaf coil design and again took the spatial derivative of the electric field as the activation function leading to stimulation in a nerve. They found that the four leaved design had a well-defined location of stimulation directly under the centre of the coil where the 'leaves' met. Additionally, Esselle and Stuchly suggested that the activation function magnitude could be increased by tilting the leaves away from the horizontal plane.

Ren at al [37] presented a coil design based on the shape of a slinky coil. Here, a double spiral coil had five additional spirals added so that the whole structure formed a semi-circle and resembled a slinky toy when that is opened such that both ends of it are located next to each other on a floor. The objective of this 'slinky coil' was to

reduce the magnitudes of the two side peaks located on other side of the main electric field peak due to a double spiral coil. Ren at al found that the slinky coil design resulted in an increased central field peak and reduced side peaks. However, the central peak was made broader in the slinky coil design.

In 2001, Hsu and Durand [28] reported on a so-called three dimensional differential coil. This shape resembled a slinky coil with only the two horizontal spirals and the vertical spiral present. In addition two new spirals were added side-on and in the same plane as the vertical spiral. The objective of this design was to produce a coil with a narrower central electric field peak than both the slinky and double spiral coil designs. In this respect the design was a success achieving a significantly narrower central peak and a half-power region 35% more localised than the double spiral coil; the slinky coil in comparison was 16% less localised. However, Hsu and Durand found that their new coil design required that the stimulator capacitor be charged to two or three times the level required with the double spiral coil for stimulation to take place.

Cohen et al [24][34] also go on to discuss double spiral coils where the spirals have an angle between them so that the structure appears as an *inverted* V when viewed side-on. Such coil shapes mean that the coil can 'curve' around the skull convexivity when the coil is used for cortical stimulation. Cohen et al find that such coils have an increased maximum induced electric field when compared to flat double spiral coils and can therefore be considered as more efficient. However these angled coils have reduced focality due to the increase in influence of the coil elements away from the coils' central axes.

Lontis et al also considered inverted V coils in their paper of 2006. Here, two inverted V coils were compared to their equivalent flat coils. The coils chosen for comparison were the Medtronic-Dantec B70, where the parts of the loops of each spiral which are closest to the neighbouring spiral are moved inwards compared to a standard double spiral coil so that these inner parts are stacked on top of those of the neighbouring spiral, and a Medtronic-Dantec B80 which is more like a conventional inverted V coil except that the wings are wound so that they are not exactly spirals but have turns which form a shape more like a cone. This is illustrated in Figure 1.8 and Figure 1.9.

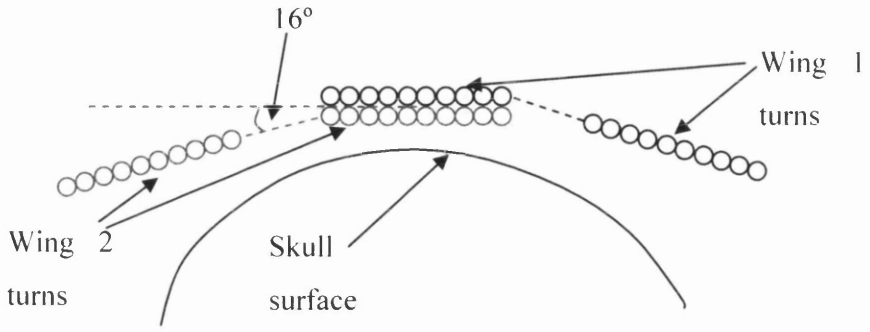

Figure 1.8 - A vertical cut of a Medtronic B70 coil above a skull showing the turns making up each wing of the coil, the overlap of the wings and the angle of the wings away from the horizontal

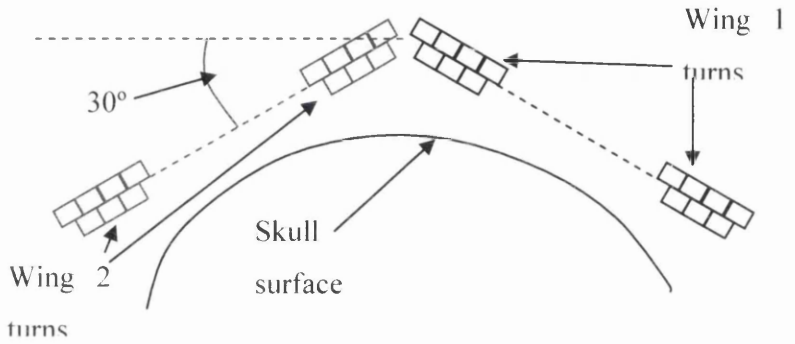

Figure 1.9 - A vertical cut of a Medtronic B80 above a skull showing the turns making up each wing of the coil stacked in a way resembling a cone and the angle of the wings away from the horizontal

Lontis et al used electromagnetic models to evaluate the electric field that would be induced in a homogeneous approximation of the human cortex by the coils under consideration. They found that the B70 coil had a marginally improved focality over its flat equivalent coil, but that the B80 coil had a noticeably worse focality than its flat equivalent. They suggested that the causal factors in these results were the actual wing geometries and relative positions of the wings.

Lontis et al went on to state that the width of the main electric field peak below the coils was what characterises the spread of induced currents below the junction between the coil wings and is therefore a better metric of field localisation than the half-power region. Given this, they reported on the widths of the main electric field

peak below the coils. Here, the B70 had a peak width marginally narrower than its flat equivalent. However, both had widths noticeably narrower than the B80 which in turn was marginally narrower than the flat version of the B80. The wing geometries and relative wing positions were cited as the significant factors in influencing electric field peak lobe width rather than the angle of bending of the coil wings.

In 2001, Al-Mutawaly et al [39] presented work on a proposed new coil shape. This resembled a slinky coil where the conductor loop which was at 90° to the plane of the coil base was replaced by three conductor loops. The coil then consisted of three sections namely the three new loops and the sections of the slinky at either side of the new loops. The electricity supply of each section could reportedly be independently controlled. Al-Mutawaly et al also presented on a version of this new coil shape which had a core of ferromagnetic material placed through the loops of conducting material making up the coil. They found that the new coil shape without the ferromagnetic material, when compared to a flat double spiral coil, had improved focality of *magnetic* flux density, improved magnitude magnetic flux density at the site of stimulation and greater induced current density when the site of stimulation (in the upper arm) was modelled using a Finite Element Method program. The coil with ferromagnetic material notably improved on the performance of the coil without the material on all three counts.

Finally, in 2006, Kim et al [40] authored a paper in which the focality of a double spiral coil was compared to that of a double spiral coil with a plate of copper between it and the human head. The focalities of the coils were assessed using a Finite Element Method model of the human head built up from magnetic resonance data where the focality was evaluated as the half power region of the electric field induced in the head by the coil. The effects of varying the size of a square gap in the plate were evaluated. It was found that, with focality measured along a line 40 mm below the coil and when the gap in the plate was a 60 mm by 30 mm rectangle below the centre of the coil, the focality of the coil with the plate was 54% smaller than that of a standard double spiral coil. The mean spiral diameters in all cases were 70 mm.

1.6 Optimisation and the Approach to Finding More Focal Coils

Perhaps the ideal way of finding the most focal magnetic stimulation coil for a particular situation would be if it were possible to design a computer program that could take a certain target location for stimulation as input and then solve Maxwell's equations to come up with a coil geometry as output that would result in stimulation at the desired location only. Unfortunately there are two things that make this approach impractical.

The first problem is that solving Maxwell's equations in situations where a current carrying conductor geometry is already known, and one desires to know what the field distribution owing to that geometry is, becomes very difficult indeed for anything but the most straightforward geometry and normally requires recourse to some numerical technique such as the Method of Moments or the Finite Element Method. Therefore solving Maxwell's equations in an inverse way, like that required for the ideal method described in the last paragraph, where one has to go from a desired field distribution to a coil geometry that would produce that distribution, is impossibly difficult.

The second problem is that, in 1992, Heller and van Hulsteyn [41] proved theoretically that it is not possible, by the superposition of any external current sources such as the elements of a stimulation coil, to produce a three dimensional localized maximum region of electric field inside the brain. Thus, the goal of producing stimulation at depth within the brain, whilst not stimulating some adjacent tissue in any direction, is not possible to meet by simply choosing a particular shape of stimulation coil if the electric field is to be the metric of whether stimulation has occurred.

As a result of the two problems described above, the approach to finding more focal coil shapes taken in this work is firstly to attempt to find coil shapes that are more focal, as quantified by the half power region introduced in the last section, in two dimensions. This is of practical use, and such coils are desirable to clinicians. Thus the focality will be assessed in planes below the coil, and coils that are more focal in a nominated plane will be determined.

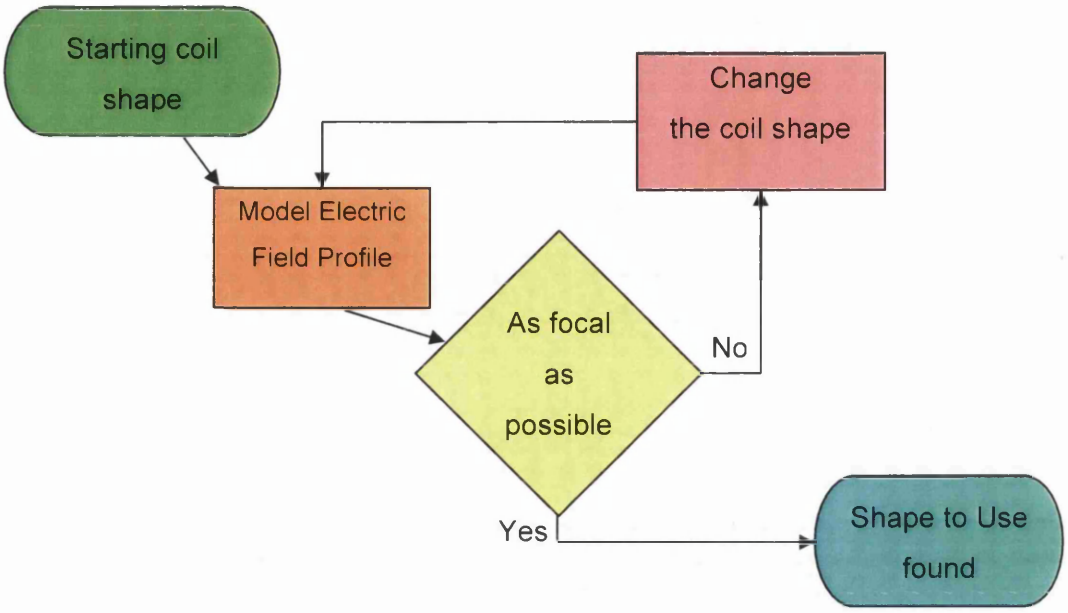

Figure 1.10 - Overview of the optimisation procedure to be used in this work

Secondly, the approach to finding more focal coil shapes will make use of the mathematical technique of optimisation [42]. The exact technique and the method of application to this work will be discussed in Chapters 2, 6 and 7, however the overall process can be thought of as avoiding the solution of inverse Maxwell equations by starting with a coil shape then solving an electromagnetic model of that coil to obtain its electric field profile before making a controlled change to the shape of the coil before solving another electromagnetic model. This is repetitively done in an iterative cyclical manner such that the controlled shape changes drive the coil shape to the most focal shape possible. The process is illustrated in Figure 1.10.

As far as has been possible in this work, no previous work has been found in which the mathematical technique of optimisation has been applied to the task of improving the geometry itself of magnetic stimulation coils in order to achieve a more focal electric field profile. Thus, the work to be presented in the forthcoming chapters is novel. Nevertheless work has been published in which the term optimisation appears in relation to coil geometry. However, upon investigation, either this optimisation merely relates to the fact that a coil shape with improved properties is suggested in the

work (and it does not imply that systematical mathematical optimisation has been applied to the task of finding new coil shapes) or something other than coil geometry in relation to its electric field profile was optimised for. Additionally, other works including the term optimisation refer to improving other aspects of stimulation equipment such as the amount of energy wasted in the process.

For example, Ruohonen et al [43] report on the application of Rosenbrock's Search Method to the optimisation of one limited aspect of the geometries of two coil shapes in order to minimise the peak magnetic energy required to achieve a fixed rate of change of electric field with respect to space. This thesis, however, will present an optimisation process in which the focality of the electric field itself is optimised and in addition will allow a target value of nerve membrane potential to be met, albeit at present as a normalised value.

In [44] and [45] Ravazzani et al publish reports that make reference to the optimisation of coils. However, these works are actually reports on how the current pulse frequency content in magnetic stimulation affects the skin effect, proximity effect and dissipated energy in coils of certain geometries. In addition, the cross-section of some coil conductors are reported on and the influence of cross-section on skin effect, proximity effect and dissipated energy noted. Also analytical expressions are presented for the skin effect in conductors of round and rectangular cross-section together with the proximity effect in round cross-sectioned conductors. Sadly, no expression is included for the proximity effect in rectangular conductors such as those typically used in most stimulation coils.

The paper of [46] by Sekino et al makes reference to an optimum current distribution in transcranial magnetic stimulation. This work again does not make use of the mathematical technique of optimisation. Instead, this work makes use of a Finite Element Method model of the human head to compute the current distribution induced in the head due to different sizes of double spiral coils, coils held at different angles to the head and the current magnitudes in the stimulation coils. The results include the difference between the induced current density with magnetic stimulation as compared to that achieved using electroconvulsive therapy.

Mathematical optimisation is however used by Onuki et al [47] but not to optimise the actual geometry of a stimulation coil. Instead, they use the genetic optimisation algorithm to optimise stimulation using a three coil system where a main coil and two sub-coils are located above human tissue. The objective is to be able to use a three stimulation coil system to enable magnetic flux to penetrate more deeply into tissue than with a single coil. Optimisation is used together with a Finite Element Method model of tissue to establish the optimal current to be used in the three coils and the relative locations of the two sub-coils in relation to the main coil so that improved induced current density is achieved in a particular tissue location. The paper of Ruohonen and Ilmoniemi [48] takes the concept of using multiple stimulation coils further by considering large arrays of up to 37 coils.

The part that optimisation will take in this work will be considered at a high level in the next chapter. Optimisation will be considered in detail in Chapters 6 and 7.

2 The Tri-Modular Approach

2.1 Background

In Chapter 1 the technique of magnetic stimulation was described, and it was seen in Appendix A that the objective of stimulation is to cause the nerve membrane potential in a certain area of tissue to exceed a threshold value thus generating an 'action potential' signal in the associated nerve. It was also seen that, at the same time, it is important to try and stop unwanted action potentials from being generated in adjacent nerves, and the associated concept of coil focality was discussed.

As was mentioned, the chief objective of this work is to develop a way of using optimisation techniques to find more focal coil shapes, and the reasoning behind and overall structure of the proposed method are described in this chapter. The chapter begins by describing an expression for the potential across a nerve membrane in terms of convenient quantities relevant to the operation of a magnetic stimulation system. It outlines what the quantities are, discusses the problems associated with obtaining some of the quantities in practical situations, and explains how the expression, together with a simpler form that uses assumed values for the problematic quantities, can be applied to finding a more focal stimulation coil.

However, there is a very real danger that in combining optimisation with numerical techniques of electromagnetic modelling that a method is developed that has unrealistically large computational requirements. Another important part of this work is to find a way around this problem, and this chapter outlines a proposed method. It will be seen why focality can be reduced to just considering peak values of electric field, and that it is best to separate the tasks of improving focality and meeting a required nerve membrane potential level.

This separation results in a proposed solution having three separate computer programs, or modules, and this chapter goes on to describes the purpose and functionality of each module. Finally, the chapter ends with a summary of the novel

aspects of this work, before the subsequent chapters offer a detailed insight into the work.

2.2 Expressions for the Nerve Membrane Potential

As was discussed in Appendix A, when determining the efficacy of magnetic stimulation it is necessary to consider the response of a neural structure to the field generated by the stimulation system – i.e. whether an action potential is triggered or not. This response can most conveniently be considered by developing an expression for the potential across a nerve membrane in terms of parameters that describe the stimulation system.

2.2.1 An Equivalent Electrical Circuit of a Nerve Fibre

In [49] Davey and Epstein present an equivalent electrical circuit, reproduced in Figure 2.1, of a nerve fibre. The circuit consists of a capacitor C_m in parallel with a resistor R_m (to represent the nerve membrane), which are in series with a resistor $R_e + R_i$ that represents the resistance of the axon's extra and intra cellular space. V_m is the potential across the nerve membrane itself, while V_{ind} is the total potential induced at the target stimulation site and is proportional to the electric field at the target site.

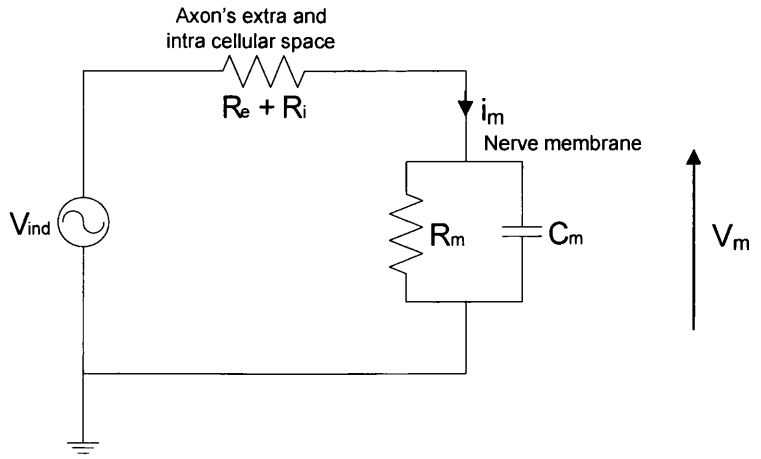

Figure 2.1 - Equivalent electrical circuit of a nerve axon

The nerve membrane time constant $\tau_m = R_m C_m$ has been found by Barker et al [50] to be approximately 150μs for cortical stimulation.

By analysing the circuit in Figure 2.1, it can be seen that the current through the nerve membrane is given by:

$$i_m(t) = C_m \frac{dV_m}{dt} + \frac{V_m}{R_m} \tag{2.1}$$

To obtain the potential across the nerve membrane at a time t_1, given an initial potential $V_m = 0$, (2.1) can be integrated between the time limits $t = 0$ and $t = t_1$ giving:

$$V_m(t_1) = \frac{1}{C_m} \exp\left(\frac{-t_1}{R_m C_m}\right) \int_0^{t_1} \exp\left(\frac{t}{R_m C_m}\right) i_m(t)\, dt \tag{2.2}$$

It can also be seen that, if the resistance of the axon's extra and intra cellular space is much larger than the nerve membrane's impedance [49], the current through the nerve membrane $i_m(t)$ will be directly proportional to the induced potential V_{ind} which is in turn directly proportional to the induced electric field at the target site $E(t)$.

2.2.2 Extending the Nerve Equivalent Circuit Model

To develop (2.2) into an expression for the nerve membrane potential in terms of parameters describing the whole stimulation system, it should first be noted that the electric field at the target site is a function of the rate of change of magnetic flux at the site, and that that function is directly proportional to the rate of change of current flowing through the stimulation coil. This can be expressed as:

$$E(t) = k_1 \frac{\partial \psi}{\partial t} = k_2 \frac{di}{dt} \tag{2.3}$$

where k_1 and k_2 are constants of proportionality, ψ is the magnetic flux, and i is the coil current. k_1 may be treated as a constant since this is equivalent to what is done in the derivation of a different expression for the nerve membrane potential in [49] which is briefly discussed later in this section. Since di/dt is directly proportional to $k_1 \, d\psi/dt$, then k_2 is, by implication, also a constant. However in Section 3.10 of this thesis it is contended that treating k_1 as a constant is not quite correct. Nevertheless, since, as will be seen, this does not alter the work that will be produced in this thesis, k_1 and hence k_2 will be regarded as constants in the derivation that follows.

Next, it is necessary to consider the equation for the current through the stimulating machine. To illustrate the process, the biphasic stimulator described in Section 1.3 will be used, for which the corresponding current equation is (1.1). By combining (1.5) with (2.3), and taking the derivative with respect to time, the electric field induced at the target site becomes:

$$E(t) = \frac{-k_2 V_0}{L_{tot}} \exp\left(\frac{-R_{tot} t}{2L_{tot}}\right)\left(\left(\frac{-R_{tot}}{2L_{tot}\omega}\right)\sin(\omega t) + \cos(\omega t)\right) \tag{2.4}$$

where V_0, R_{tot}, L_{tot} and ω are as in Section 1.3.

At time $t = 0$, (2.4) reduces to the coefficient $-k_2 V_0 / L_{tot}$ which represents the peak electric field E_0. This occurs at the beginning of the stimulation pulse, before the effects of resistive decay are manifested.

By making use of $i_m(t) = k_3 E(t)$, then, if (2.4) is substituted into (2.2), the following is obtained:

$$V_m(t) = k_3 E_0 \frac{\left[\frac{2R_m C_m - R_{tot} C_S}{\sqrt{4C_S L_{tot} - C_S^2 R_{tot}^2}}\right]\exp\left(\frac{-R_{tot} t}{2L_{tot}}\right)\sin(\omega t) + \exp\left(\frac{-R_{tot} t}{2L_{tot}}\right)\cos(\omega t) - \exp\left(\frac{-t}{R_m C_m}\right)}{\frac{1}{R_m C_m} + \frac{R_m C_m - R_{tot} C_S}{C_S L_{tot}}}$$

(2.5)

where C_S is the capacitance of the stimulating machine. An equivalent expression to (2.5) for monophasic stimulators can be obtained via a similar derivation process that uses non time harmonic terms.

(2.5) is a powerful and useful equation since it expresses the nerve membrane potential only in terms of quantities that describe the electrical properties of the nerve and stimulation system. These are:

- $R_m C_m = \tau_m$, the nerve membrane time constant enumerated by Barker et al.
- C_S, the stimulating machine capacitance, which is a known quantity for a particular machine model.
- R_{tot} and L_{tot}, which are the total resistance and inductance of the stimulating machine, connecting leads and coil combination. The resistance and inductance of a stimulating machine and its leads can be measured quite easily, as can the resistance and inductance of a pre-existing coil. However, the resistance and inductance of a hypothetical coil would need to be obtained via a modelling technique – this will be discussed at length later in this thesis.
- ω and E_0, the resonant frequency and initial peak induced electric field, both of which can be measured for pre-existing coils, but would also need to be obtained via modelling for a hypothetical coil.
- The constant of proportionality k_3. This arose from using $i_m(t) = k_3 E(t)$, and the constant clearly relates the magnitude of the membrane current to the electric field induced from the coil at the target site. As will be explained later, k_3 will not be used for the work described in this thesis, and, therefore, no attempt will be made to gain a deeper understanding of it beyond a brief discussion in Section 3.3. It should be obvious though that, if one wanted to quantify k_3, a study of the tissue at the site of stimulation would need to be undertaken, quite likely involving an electromagnetic model of the tissue. k_3 is not, however, a function of the characteristics of the coil or stimulating machine themselves.

In [49], Davey and Epstein present their Equation 16, which is similar in form and derivation to (2.5). The chief differences are that their equation for the nerve membrane voltage includes terms for the energy delivered to the stimulator/coil circuit, the reluctance of the coil, and the fraction of the total magnetic flux from the coil that interacts with the stimulation site of interest. No term for the peak electric field, or a term directly equivalent to k_3 in (2.5) are included.

Davey and Epstein's equation offers an illuminating insight into the effects of changing various quantities on nerve membrane voltage. In [49] they use the equation to outline how the efficiency of the stimulation process can be improved by judicious choice of parameters. However, in this thesis, it is the focality of nerve stimulus that is of interest, and some of the terms in Davey and Epstein's equation, notably the flux fraction, make the analysis of focality more difficult than it need be. Therefore, this thesis's work will make use of (2.5), which, although based on Davey and Epstein's nerve equivalent circuit, uses a different derivation process to arrive at the nerve membrane voltage, and avoids having to consider what fraction of a coil's magnetic flux interacts with a target stimulation site.

2.3 Using the Nerve Membrane Potential Expression

In this work, (2.5) will be the equation that forms the basis of the coil optimisation procedure outlined in Chapter 1. Variables that describe the coil geometry will be systematically altered and the equation revaluated at each iteration of the optimisation loop to obtain the nerve membrane potential at several points along a line at a desired stimulation depth. Part of this information will be used to evaluate coil focality, and the optimisation process will be explained in detail later in this chapter and in Chapters 6 and 7.

The chief difficulty in using (2.5) lies with the fact that in order to quantify the constant of proportionality k_3, an electromagnetic model of the tissue at and around the site of stimulation would need to be solved. This model would likely have to be of

a three dimensional finite element type, and its solution would be a lengthy and computationally demanding affair.

However, in this work, the main objective is to develop a way to improve the focality of a stimulating coil, and it obviously would be simpler to analyse the focalities of different coils by comparing their performance in a uniform tissue region rather than separate tissue regions having different electrical properties. For this reason it is intended to develop the optimisation procedure introduced in this work with a uniform tissue region as the stimulation target. After this work is complete, the computer programs that are produced could be extended so that they couple in some way to full electromagnetic models of more realistic tissue as part of future work. This means that, for now, it will be assumed that the tissue in this work's optimisation process has some arbitrary electrical properties, and that those same properties exist at every point along the line at which the nerve membrane potential is evaluated as part of the process. Constant k_3 could therefore be chosen to always be some convenient value, e.g. unity, each time (2.5) is evaluated, and a measure of coil focality could be calculated. As was seen in Section 1.5, earlier researchers have reported coil focality in regions having uniform properties – usually air.

By letting $k_3 = 1$ in (2.5) a normalised nerve membrane potential is thus obtained:

$$V_{mn}(t) = E_0 \frac{\left[\frac{2R_mC_m - R_{tot}C_S}{\sqrt{4C_SL_{tot} - C_S^2R_{tot}^2}}\right]\exp\left(\frac{-R_{tot}t}{2L_{tot}}\right)\sin(\omega t) + \exp\left(\frac{-R_{tot}t}{2L_{tot}}\right)\cos(\omega t) - \exp\left(\frac{-t}{R_mC_m}\right)}{\frac{1}{R_mC_m} + \frac{R_mC_m - R_{tot}C_S}{C_SL_{tot}}} \tag{2.6}$$

It should be noted that, other than time and $R_mC_m = \tau_m \approx 150\mu s$ for cortical stimulation, all the terms on the right hand side of (2.6) relate to the stimulation system itself, and will need to be obtained at each iteration of the optimisation process by solving a model of the system that includes the coil geometry that has arisen at that iteration.

2.4 Modelling the Stimulation System

In Section 2.2.2, it was noted that R_{tot} and L_{tot} in (2.6) are respectively the resistance and inductance of the stimulating machine, connecting leads and coil combination, and that the resistance and inductance of the machine and leads can be measured relatively straightforwardly. However, as was explained in Section 1.4, the resistance and inductance of a stimulating coil carrying an alternating current are influenced by the skin and proximity effects, and are therefore dependent on the coil shape and the frequency content of the current that results from using the coil in combination with the stimulating machine and leads. As a consequence, in order to establish the resistance and inductance of a coil shape that arises out of an iteration of the optimisation process, a computer model of the coil, stimulator and leads combination must be solved.

Such a model would need to be capable of representing the distribution of current within the coil's conductors, the interaction of the fields due to the current in the various sections of the coil, and the operation of the circuit formed by the stimulating machine, connecting leads and coil. Additionally, the frequencies that arise in a stimulation system current pulse are typically less than about 10 kHz, i.e. wavelengths greater than about 30 km. These factors suggest that the model should comprise of an electromagnetic model of the coil structure coupled to a lumped circuit element model of the stimulator and leads. An overview of different detailed electromagnetic modelling techniques is given in Chapter 4 together with an explanation of why the Finite Element Method (FEM) will be the technique used in this work.

2.5 The Approach Towards the Optimisation Process

2.5.1 Background

As was discussed in Section 2.3, the ideal aim in this work would be to devise an optimisation process where a set of variables describing coil geometry were altered at

each iteration of the process in an attempt to drive the coil geometry towards a more focal shape. The focality would be defined in terms of the normalised nerve membrane potential, V_{mn} in (2.6), which would need to be revaluated at each iteration at several points on the line along which focality was being assessed. Each evaluation would require that (2.6) be solved and this would require that an FEM model of the coil coupled to a model of the stimulator circuit be solved at each iteration in order to obtain the required coil resistance and inductance.

In theory there is nothing wrong with the approach described above. However, in practise, the approach would be problematical due to the length of time it would take to solve the FEM models. Solving one FEM model could take several minutes in the case of a fairly simple axisymmetric coil shape for which one could use a two dimensional model, and this would likely extend to several hours for non-axisymmetric shapes requiring three dimensional models, even using advanced types of computers. (For example, the solution of one circuit coupled two dimensional axisymmetric FEM model of the gull-wing shaped coil seen in Chapter 7 takes some 23 minutes using the FEM code developed in this work on a Pentium 4 1.8 GHz personal computer.) Given that many FEM models would need to be solved over the course of the optimisation procedure, then it could be that many hours or even days could pass before a 'solution' coil shape would be obtained for a particular problem.

In this work it is desired by the eventual users of the computer programs developed to be able to find more focal coil shapes without regularly encountering such lengthy solution times. Therefore, an important goal of this work is to devise a procedure which could still make use of optimisation techniques to find more focal coil shapes, but which limits the use of FEM models whilst maintaining accurate results. Solution coil shapes should be obtained within minutes or a few hours rather than many hours or days. The remainder of this chapter discusses the background to the procedure proposed in this work.

2.5.2 A Closer Examination of Focality

The right hand side of (2.6) can be considered to consist of two significant terms, namely the peak electric field, E_0, and everything to its right. It is the term to the right of E_0 which contains the resistance and inductance values, which must be obtained by solving an electromagnetic model. If focality is to be assessed by taking the ratios of V_{mn} at the point along a line at which it is a maximum against V_{mn} at other points along the line then calculating focality clearly involves dividing V_{mn} values at different points. From (2.6) it can be seen that dividing V_{mn} values will result in the elimination of the term to the right of E_0 (this term contains no spatially dependent values if we accept that $R_m C_m$ is the same throughout the cortex), reducing focality to be dependent on the ratios of different E_0 values along the line. This definition of focality would agree with the definition used by earlier researchers as outlined in Section 1.5.

So, at this stage in our considerations, it would appear that, if we are constructing an optimisation procedure to find a more focal coil, we could assess focality by just calculating E_0 values rather than V_{mn} values. This would obviate the need to run FEM models to obtain coil resistance and inductance, meaning that the reason for running the models would be to obtain E_0 itself. If it were possible to calculate E_0 using a quicker and simpler modelling method than the FEM then the iterative optimisation procedure would be speeded up considerably.

It is the case that the peak electric field E_0 at a point around a stimulation coil is directly proportional to the maximum rate of change of current within the coil. Given the passive nature of the stimulator / coil circuit and that the stimulator and coil are resistive, and therefore exhibit gradual energy loss, the maximum rate of change of current within a coil occurs at the beginning of the pulse of current which is discharged into the coil – i.e. as soon as the trigger switch is pressed. Since no current is actually flowing in the coil at the instant the switch is pressed, no skin or proximity effects are present within the coil at that instant. This means that the resistance and

inductance of the coil could be calculated using a simpler modelling technique that doesn't take skin or proximity effect into account. These values for resistance and inductance could then be used in a simple circuit model of the stimulator and coil to calculate the rate of change of current at the instant the switch is pressed. A suitable modelling technique and the simple circuit model are described in detail in Sections 7.3 and 7.4.

However, even if the maximum rate of change of current within a coil can be calculated, then some method is still required to obtain the value of the peak electric field E_0 around the coil. It turns out that earlier researchers have successfully modelled stimulation coils with known rates of change of current as infinitesimally thin wires in order to obtain their electric fields. No time consuming FEM modelling is required. This is discussed in more detail in Chapter 3.

By combining the above technique to obtain the maximum rate of change of current with a modelling technique that approximates the stimulation coil as a thin wire, it is possible to calculate the peak electric field E_0 around a new coil shape without resorting to using FEM modelling. Therefore it would appear that it should be possible to devise an optimisation process to improve the focality of stimulation coils by defining focality in terms of E_0 and using simpler modelling techniques to model E_0 rather than the FEM required to model V_{mn}. Such a process would not require exceedingly long computation times.

Unfortunately, whilst it is reasonable to define coil focality by just considering the peak electric field E_0 as the earlier researchers have, it must be remembered that the objective of magnetic stimulation is to ensure that a nerve action potential is triggered at a certain point – i.e. that V_{mn} reaches some specified threshold value. Examination of (2.6) reveals that the normalised nerve membrane potential V_{mn} is zero when $t = 0$, i.e. when the coil rate of change of current is at its peak, so no nerve action potential can be generated at that time. The first peak in V_{mn} occurs some time into the duration of the coil current pulse, and it has been shown in [63] that the largest peak in nerve membrane potential with a biphasic pulse is the second peak. Therefore, there is a

very real danger that in devising an optimisation scheme that iterates towards the most focal coil in terms of E_0 that the resulting coil may have resistive and inductive properties such that V_{mn} is too small throughout the current pulse to ever trigger an action potential.

Thus it is important that the optimisation scheme considers not only focality of stimulation but also whether the values of V_{mn} obtained with a stimulator / coil combination are suitable. Unfortunately, this suggests that values of V_{mn} would need to be calculated at each iteration of the optimisation process after all, meaning that time consuming FEM models rather than the quicker thin wire E_0 models discussed above would need to be solved. In the next section a novel way around this difficulty is proposed.

2.5.3 The Proposed Approach

In the previous section it was established that it is reasonable to define focality of stimulation in terms of the peak electric field around a coil and that fairly quick methods exist to model the peak electric field around new coil shapes. This means that an iterative optimisation scheme set up purely to find more focal shapes should not take an excessive amount of time or computer resources to run. However, it was also established that in order to ensure that the nerve membrane potential due to a new coil is large enough to trigger an action potential, an electromagnetic model of the new shape coupled to a stimulator circuit would need to be solved. This suggests that it is impossible to devise an optimisation process that doesn't require lengthy FEM models to be solved at each iteration. It could be noted that, even if the optimisation process involved the finding of the most focal coil for a particular problem then increasing the current in the coil until the required nerve membrane potential was met, the calculation of the nerve membrane potential value would still require the knowledge of coil resistance and inductance values which could only be obtained from FEM models of the coil.

In this work it is accepted that, although an optimisation process involving repeated FEM modelling could yield the most optimal coil shapes, such a process with its lengthy solution times would be unsuited to the application intended in this work given the speed and capacity of computers available today and likely to be available in the immediate future. Instead, an approach is proposed in which the more general task of using optimisation to find more focal coil shapes is separated from the more practical task of using optimisation to answer the question 'what is a coil shape with good focality that meets a required normalised nerve membrane potential level?' The solution based on this approach consists of three computer programs or modules which are outlined in the following sub-sections.

2.5.3.1 The New Shape Module

This is a program which will make use of an iterative optimisation procedure to find new stimulating coil shapes that have improved focality. Focality will be defined in terms of the peak electric field generated by the coil when used with a stimulator, and the focality will be measured along a straight line at a distance below the coil specified by the program's user. Thus the program's design will acknowledge the fact that different coil shapes will yield the best focality at different distances below the coil. The program will not attempt to calculate normalised nerve membrane potential values and, hence, time consuming FEM models will not be used.

The peak electric field values will be calculated using the thin wire coil modelling method outlined in Chapter 3. The repetitive use of modelling during the optimisation process should not therefore cause the whole process to take an unfeasibly long time to complete.

Whilst the mathematical technique upon which the optimisation process in this module will be based – Simulated Annealing – is not new [64], its application to the problem of finding a more focal coil and its use with the electric field modelling method of Section 3.8 are new to this work. In this work a way is developed to define a set of variables that describe a coil's shape so that the variables can be systematically altered in the optimisation process, and these variables' values at each

iteration used to set up an electric field model. The electric field focality as returned by the model is then converted into a measure of the coil shape's 'goodness' at that iteration which is used by the optimisation process to drive the variables iteratively towards values that end up at the most focal coil. The background to the optimisation process is discussed in Chapter 6, and its application to this work and results obtained from its use are described in Chapter 7.

2.5.3.2 The Other Two Modules

Whilst the task of finding new more focal coil shapes is to be the realm of the New Shape Module, the remaining two modules exist so that a user can find a coil shape with good focality that meets a required normalised nerve membrane potential level at a certain distance below the coil. Together they are intended to offer a novel way around the problem of having to run time consuming FEM models at each iteration of an optimisation process which has to repeatedly calculate normalised nerve membrane potential values.

2.5.3.2.1 The Main Module

This is intended to be the program that a user who wants to find a coil shape with good focality that meets a required normalised nerve membrane potential level (V_{mn}) would run most often and is therefore known as The Main Module. A user would enter a required V_{mn} value together with the distance below the coil at which this value is required, and the program would then use an iterative optimisation process to find the coil shape that can generate the required V_{mn} value that is also the most focal it can find.

Clearly V_{mn} needs to be calculated for the coil shape that arises at each iteration of the optimisation process. The way out, proposed in this work, of the need to run FEM models to obtain V_{mn} at each iteration begins with the definition a set of 'basic shapes'.

The phrase 'basic shape' refers to the general topology of a coil and, from amongst coils that are manufactured at the moment, examples of basic shapes would be a single spiral coil, a double spiral coil, and a double cone coil, all of which can be seen in [65]. For each basic shape a set of size governing variables can be defined, e.g. for the single spiral coil these could be the number of turns, the turn separation distance and the radius of the inner turn. Thus each type of basic shape can exist in many different sizes.

Now, for a particular basic shape type, it should be possible to establish how its resistance and inductance changes when used with a particular stimulator as its size governing variables are altered. This could be done by running stimulator circuit coupled FEM models of the coil at several different size variable values and recording the coil resistance and inductance. Interpolation could then be used to generate expressions for the coil resistance and inductance values in terms of the size governing variables. It could be noted that the resistance of a HP90 coil changes form 8 mΩ at DC to 16 mΩ at its resonant frequency when used with a Magstim Rapid^2 stimulator.

In the Main Module it is proposed to restrict the program to offering solution coil shapes from amongst a set of basic shapes for which resistance and inductance versus size variable expressions have been established. The program would work towards a solution coil shape by taking each basic shape type in turn, and, using a revised version of the optimisation algorithm from the New Shape Module which was restricted to only altering the size variables of the basic shape under consideration, would calculate the most optimal size of each basic shape in terms of achieving the required V_{mn} value with the smallest focality. The most optimal size of the basic shape having the smallest focality that met the V_{mn} requirement would be the eventual solution coil. The change in a coil's resistance from DC to AC mentioned in the last paragraph is significant enough for it too be felt that just estimating a coil's resistance, rather than using interpolated expressions derived from FEM models, could lead to erroneous values of V_{mn} being arrived at. This could lead one to believe that the use of a coil would lead to stimulation taking place when in fact it does not or vice versa.

The field modelling method used in the Main Module would be identical to that used in the New Shape Module except that the expressions for resistance and inductance versus size variables would be used together with the peak electric field calculation in (2.6) to obtain V_{mn} values. Thus the optimiser can work with V_{mn} values rather than just electric field as in the New Shape Module.

This approach to the Main Module has several advantages. Firstly, time consuming FEM modelling during the optimisation process is avoided. Secondly, the optimisation and field modelling program code from the New Shape Module can be re-used with some minor modifications. Thirdly, the user of the Main Module need have no knowledge of setting up FEM models.

2.5.3.2.2 The Finite Element Module

This is the program that facilitates the finding of the expressions required for the Main Module of how the resistance and inductance of each basic shape changes as its size governing variables are altered. The program will consist of a Finite Element electromagnetic modeller into which a model of a basic shape at a certain size can be entered, coupled to a lumped element model of a stimulating machine circuit. It is important that the FEM model be circuit coupled since the circuit will influence the frequency content of the current pulse that will occur in a stimulating coil, which influences the magnitude of the skin and proximity effects, which in turn affect the coil's resistance and inductance.

Using the Finite Element Module will involve entering a mesh and running the program for a particular size of a basic shape. The model must then be solved and the resistance and inductance of the coil recorded. The user must then repeat this process for several different values of each variable that has been chosen to describe the size of the basic shape. Interpolation must then be used to form the resistance and inductance versus size variable expressions required. Clearly this could involve having to enter and solve quite a number of FEM models. However, this should be many fewer than would be solved in an optimisation loop that included FEM modelling at each iteration. Additionally, once a basic shape and its resistance /

inductance expressions have been added to the Main Module's 'database' of shapes there will be no need to solve FEM models for any sizes of that shape in the future, thus avoiding potentially solving FEM models for similar coil geometries which may arise many times that an FEM based optimiser is run.

Whilst literature exists on using the FEM to model the effects in tissue of magnetic stimulation coil fields, little, if anything, has been written on applying the FEM to modelling the fields and currents of the coil itself. Nevertheless it is known that work has been undertaken in the University of Sheffield, UK where a finite element formulation known as **A**-V was used with standard nodal finite elements to model the current distribution in a single spiral coil using two dimensional axi-symmetric models [213].

In this work, it is desired to use an FEM formulation that allows coil models to be solved as efficiently as possible, and that can be straightforwardly applied to modelling coils in three dimensions. It is important that the coil models can easily be coupled to a lumped circuit model of a stimulating machine, and that the models can deal with stimulators having biphasic and other pulse shapes. For these reasons it has been decided to use a **T**-Φ FEM formulation with edge based finite elements in the time domain. Whilst this formulation and element type are not new, there is no record of them having been applied to modelling stimulating coils. Therefore, their application to this end and the reporting of issues that arose during their application is new to this work. The background to and the results from the FEM modelling undertaken in this work appears in Chapters 4 and 5. Additionally, it is explained in Section 4.9 why it was decided to write an original FEM modelling program for use in this work rather than use a commercially available program.

2.5.3.3 The Three Modules Taken Together

Taken together, the three modules represent a solution that allows users to search for new more focal coil shapes that meet their requirements without running an optimisation program that uses an impossibly large number of time consuming FEM models to find a solution.

The Main Module could be regarded as being a database of basic shapes that are known to have good focality at certain sizes. In normal use it is intended that the New Shape and FEM modules would first be used to find a group of perhaps ten basic shapes with good focality and their associated resistance / inductance expressions, and then these shapes added to the Main Module database. Less specialised practitioners could then use the Main Module to obtain a suggested coil shape /size for their needs within a sensible time scale.

In this work it is intended to demonstrate that this tri-modular solution process can work. To that end, use of and results from using the New Shape Module are presented in Chapter 7. Also in that chapter the process of using FEM modelling to obtain expressions for the resistance and inductance of various sizes of a basic shape obtained from the New Shape Module is reported upon. Using that basic shape in the Main Module to meet a user's normalised nerve membrane potential requirements is then described.

2.6 A Summary of the Novel Aspects of This Work

The remainder of this thesis describes the work outlined in the first two Chapters in more detail. In summary, the novel aspects of the work presented in the following chapters are as follows:

a) A three program modular method to combine optimisation and electromagnetic modelling to search for more focal magnetic stimulation coils, and to allow users to search for coils with better focality that meet a required nerve membrane potential level. The method avoids the problems associated with solving Finite Element Method models at each iteration of the optimisation process.
b) The application of optimisation to improving the focality of a magnetic stimulation coil by changing its geometry. The work reports on the choice of an optimisation method and develops a way to describe a coil's geometry using a set of variables. A connection is made between the variables and a measure of focality 'goodness', and a means shown whereby that measure can

be incorporated into the optimisation process. It is shown where electromagnetic modelling fits in to the procedure.

c) The reporting of new coil shape designs obtained from the optimisation program. One shape is constructed and experimental measurements are presented to verify that its electric field is modelled correctly in the computer program and that its field is indeed more focal than a pre-existing coil.

d) A report on incorporating the constructed new shape as a basic shape type in the Main Module of the tri-modular computer program system. This illustrates how the tri-modular system works as a complete entity.

e) The use of the **T**-Φ FEM formulation to model magnetic stimulation coils. Results are presented from using this formulation in both the frequency and time domains, together with results from combining the time domain models with lumped circuit element models of a stimulating machine. Issues relating to time step size are discussed and suitable time step sizes suggested. Vector based finite elements are used, and model boundary conditions described. A method of running a circuit coupled time domain **T**-Φ FEM model followed by one run of a frequency domain **T**-Φ FEM model in order to obtain the resistance and inductance of a coil when used with a biphasic stimulator is suggested and demonstrated in Chapter 5.

f) Data to show the results of **T**-Φ FEM modelling that illustrate that the resistance and inductance of a spiral stimulation coil change with time when a biphasic stimulator is used.

g) The reporting of results to quantify the difference in electric field values generated when a spiral coil is modelled as a coil of thin wire. Additional results are presented to quantify the further error introduced by modelling a spiral as concentric loops of thin wire.

h) As an addendum, in Chapter 8, the results of an experiment to assess whether, in use, coil heating affects the electric field around a coil are mentioned.

3 The Electromagnetic Modelling of Stimulation Coils as Thin Wires

3.1 Background

In Chapter 2 it was mentioned that several earlier researchers have modelled the electric and magnetic fields around stimulating coils by approximating them as coils of infinitesimally thin wire. In these cases the current or rate of change of current through the coil is already known, and the modelling technique provides a comparatively simple and computationally inexpensive way to get knowledge of the fields from these quantities.

In this work it is proposed to use an optimisation technique to obtain coil shapes that have improved focality. During the optimisation process, new coil geometries will arise at each iteration of the process for which the rate of change of current through the coil will be unknown. This would seem to suggest that it would not be possible to use the thin wire technique to gain the knowledge of electric field distribution required for the optimisation algorithm to establish whether a change in coil geometry leads to improved focality or not. However, a way around this apparent difficulty is proposed and discussed in Chapter 2 – the 'tri-modular' approach. Both the New Shape and Main modules of the tri-modular approach make use of thin-wire modelling to obtain the electric fields of new coil geometries for which the peak rate of change of current has already been obtained using the techniques outlined in Chapter 2.

This chapter concentrates on the thin-wire modelling method and begins by explaining how the method works with reference to earlier researchers' work. It works through the derivation of the method's electromagnetic formulation from Maxwell's equations before describing two ways that general coil geometries can be represented in three dimensions as thin wires in a computer program.

When a coil composed of metal that has an actual cross-section is approximated as being made of wire that is infinitely thin, one would expect there to be some error in the field obtained from a model using that approximation, particularly if the points at which the field is to be evaluated are close to the coil. Although the thin-wire field modelling method has been used quite widely by earlier researchers, there appears to be no published data that quantifies the error in field values associated with the method. Given the reliance of this work's optimisation programs on that method, it would be desirable to have justifiable confidence in the values that can be obtained from it. Therefore, in this chapter, some work is presented to quantify the errors in electric field values that are obtained from both described computer implementations of the thin-wire modelling method

It will be seen that, although one implementation makes a greater approximation to a coil's shape than the other, it can be computationally much faster. This chapter goes on to outline the limitations of the faster implementation and to consider whether it is suitable for use in the optimisation work reported later in this thesis.

Finally, when working through the derivation of the thin-wire method's electromagnetic formulation it will be seen that consideration of one of the terms that arises offers a fresh insight into a term in (2.5) in Section 2.2.2. This insight will lead to a contention in Section 3.10 that there is a discrepancy in results previously published by another research group.

3.2 Electromagnetism and Magnetic Stimulation

Electromagnetic phenomena have been well understood since the nineteenth century when James Clerk Maxwell presented his famous equations in complete form which included a term for the displacement current density [2]. These equations are presented below in differential form appended by the two vector constitutive relations required to ensure that there are sufficient equations to solve for the unknown quantities:

$$\begin{aligned}
\nabla \cdot \mathbf{D} &= \rho \\
\nabla \times \mathbf{E} &= -\frac{\partial \mathbf{B}}{\partial t} \\
\nabla \cdot \mathbf{B} &= 0 \\
\nabla \times \mathbf{H} &= \mathbf{J} + \frac{\partial \mathbf{D}}{\partial t} \\
\mathbf{D} &= \varepsilon \mathbf{E} \\
\mathbf{B} &= \mu \mathbf{H}
\end{aligned} \tag{3.1}$$

In (3.1), ρ is the volume density of free electric charges, **D** is the electric flux density, **E** is the electric field intensity, **B** is the magnetic flux density, **H** is the magnetic field intensity, **J** is the electric current density, ε is the material permittivity and μ is the material permeability.

At low frequencies, i.e. below about 10 kHz, the second term in Maxwell's magnetic curl equation, $d\mathbf{D}/\partial t$, may safely be omitted from calculations involving that equation [3][4] because the density of free charges varies slowly with time. This similarity in the equation's form to the direct current case leads to the low frequency situation being referred to as the quasi-static state. The quasi-static form of Maxwell's equations which may be used in solving problems at low frequencies are therefore:

$$\begin{aligned}
\nabla \cdot \mathbf{D} &= \rho \\
\nabla \times \mathbf{E} &= -\frac{\partial \mathbf{B}}{\partial t} \\
\nabla \cdot \mathbf{B} &= 0 \\
\nabla \times \mathbf{H} &= \mathbf{J} \\
\mathbf{D} &= \varepsilon \mathbf{E} \\
\mathbf{B} &= \mu \mathbf{H}
\end{aligned} \tag{3.2}$$

Given that the frequency content of the current pulses typically used for neural magnetic stimulation is less than 10 kHz [5], it will be the quasi-static form of Maxwell's equations which will form the basis of the techniques that will be used to simulate magnetic stimulation coils' behaviour later in this work.

3.3 Introduction to Thin Wire Modelling

The thin wire method of modelling the field around a magnetic stimulation coil involves representing the coil as a coil of infinitesimally thin wire rather than one composed of wire having an actual cross-sectional size and shape. Perhaps the earliest reported use of the method to model the electric field was in the work of Roth et al [66], where the method is discussed in some detail and applied to calculating the electric field induced in a flat tissue surface and a cylindrical volume conductor which is meant to represent an arm containing peripheral nerves.

The method is subsequently used by Cohen et al [67] to model the electric field around coils of different geometries, and by Roth and Basser [68] to model the electric field in work examining the physics of peripheral nerve action potentials. It is used by Mouchawar et al [69] to investigate magnetic stimulation of the cardiac system, and by Garnham et al [70] to investigate the combination of magnetic stimulation with electrode stimulation.

The slightly simpler form of the method needed to model the magnetic field is used by De Leo et al [71] in a computer model of magnetic stimulation of cortical nerves, and by Cerri et al [72] to expand the computer model of [71] to three dimensions. Both the magnetic and electric field variants of the thin wire method are also used by several other researchers, and continue to be regularly used until the present day. Thus it can be seen that the method is widely accepted by the magnetic stimulation research community.

To understand the method we must first consider Maxwell's equations and their associated constitutive relations. When modelling the electric field, it is possible to make use of the fact that **B** is divergence free and express **B** as the curl of another vector field **A**, i.e. $\mathbf{B} = \nabla \times \mathbf{A}$, where **A** is known as the magnetic vector potential [73]. If this is then substituted into Faraday's Law, the second equation in (3.2), manipulation leads to:

$$\nabla \times \mathbf{E} = -\frac{\partial}{\partial t}(\nabla \times \mathbf{A})$$

$$\nabla \times \left(\mathbf{E} + \frac{\partial \mathbf{A}}{\partial t} \right) = 0 \tag{3.3}$$

Since the curl of the parenthesised terms in (3.3) is zero then, because a curl-free vector field can be expressed as the gradient of a scalar field [74], (3.3) can be expressed as:

$$\mathbf{E} + \frac{\partial \mathbf{A}}{\partial t} = -\nabla \phi$$

$$\mathbf{E} = -\frac{\partial \mathbf{A}}{\partial t} - \nabla \phi \tag{3.4}$$

where ϕ is the electric scalar potential [75] and (3.4) is known as the electric field potential function.

From (3.4) it can be seen that the electric field is composed of two components. The first term on the right hand side accounts for the portion of the electric field that is due to electromagnetic induction resulting from the changing coil magnetic field, and the second term accounts for the portion due to static electric charges.

As explained earlier, magnetic stimulation occurs at frequencies that are low enough for the quasi-static approximation to Maxwell's equations to apply, and the fourth equation in (3.1) reduces to Ampere's Circuital Law, $\nabla \times \mathbf{H} = \mathbf{J}$. This, together with the facts that the stimulation coils under consideration are composed of single continuous lengths of conductor, that there is no initial distribution of static electric charges on a stimulation coil, and that the air around a stimulation coil is non-conductive, means that the only place in or around a coil where accumulation of static electric charges could occur is within the tissue itself. (The tissue is composed of conductive layers.) This, in turn, means that the static charge term in (3.4) is only required if one wishes to include tissue in the electromagnetic model.

Given the problems and computational cost associated with fully modelling the attributes of particular areas of particular people's tissue (everyone's tissue configuration is slightly different) and that it is desired to find new coil geometries that are generally more focal, it was explained in Section 2.3 that it is not intended to run electromagnetic models of tissue in this thesis. By extension, this means that it is not intended to include the contribution of static charges to the electric field in any models. Therefore, in this work, (3.4) can be reduced to:

$$\mathbf{E} = -\frac{\partial \mathbf{A}}{\partial t} \tag{3.5}$$

Now the magnetic vector potential, **A**, at a point due to a coil of thin wire, as in Figure 3.1 reproduced from [66], can be shown to be [79]:

$$\mathbf{A} = \frac{\mu_0 I}{4\pi} \int \frac{1}{|\mathbf{r} - \mathbf{r}'|} d\mathbf{l}' \tag{3.6}$$

where **r** is the position vector where **A** is to be calculated, **r'** is the position vector of a differentially small segment of the coil, d**l'** is a vector tangent to the coil at **r'**, I is the current magnitude in the coil, and μ_0 is the permeability of free space. Taking the partial time derivative of (3.6) and combining with (3.5) yields the following expression for the electric field due to induction from a stimulating coil represented as a thin-wire:

$$\mathbf{E} = -\frac{dI}{dt}\frac{\mu_0}{4\pi} \int \frac{1}{|\mathbf{r} - \mathbf{r}'|} d\mathbf{l}' \tag{3.7}$$

Thus, so long as the rate of change of current through the coil is known, the electric field can be calculated using (3.7).

In order for (3.7) to be used more practicably, the continuous integral around the coil is normally approximated as a summation of discrete values. To do this the coil is

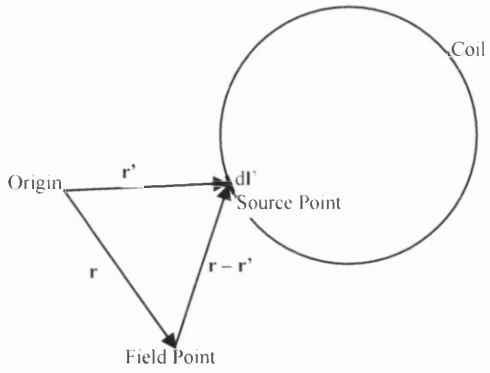

Figure 3.1 – Calculating the magnetic vector potential for a coil of wire

represented as being composed of a large number of short straight line segments, along each of which (3.7) can be more easily evaluated. The total electric field is then the vector summation of the contribution from each segment [66][70].

The question then arises of how many segments the coil should be split into. This depends on the level of accuracy required from the coil model, but, for example, in [70] a 21 turn spiral coil is said to be modelled using 100 linear segments. That value appears to be low, and greater accuracy would be desirable in this work. Therefore, in Section 3.7, some work is undertaken to try to establish the segment length that should be used to obtain a certain level of electric field accuracy from discretised thin-wire models.

A difference exists between researchers as to how spiral sections of coil are represented in thin-wire models. Some researchers, e.g. [69], keep the coil as a true spiral which is then discretised into linear segments. Others, e.g. [70], approximate a spiral coil as a series of concentric rings, and the field from each is then calculated and summed. No discussion appears in the literature as to the accuracies of either method, and, therefore, in Sections 3.7 and 3.8, the accuracies of both methods are reported upon when modelling the electric field due to a 14 turn spiral coil.

3.4 Computer Implementation of the Thin-Wire Modelling Technique

Implementing the thin-wire technique as a computer program chiefly involves evaluating the contribution of each short straight line wire segment to the field. To do this, the procedure used by the code developed in this work begins by allocating a local coordinate system to each straight segment, as shown in Figure 3.2.

The electric field at the 'field point', i.e. the point where it is desired to know the field, due to a segment is then given by:

$$\mathbf{E} = -\mathbf{k}\frac{dI}{dt}\frac{\mu_0}{4\pi}\int_{z_1}^{z_2}\frac{1}{|\mathbf{r}|}dz' \tag{3.8}$$

where **k** is a unit vector in the z direction. This formula still contains an integral, and a method must be chosen to evaluate it numerically. In this work, the method used is to evaluate $|\mathbf{r}|$ at the midpoint of the wire segment and complete the integration by multiplying the reciprocal of $|\mathbf{r}|$ by the segment length. (3.8) therefore becomes:

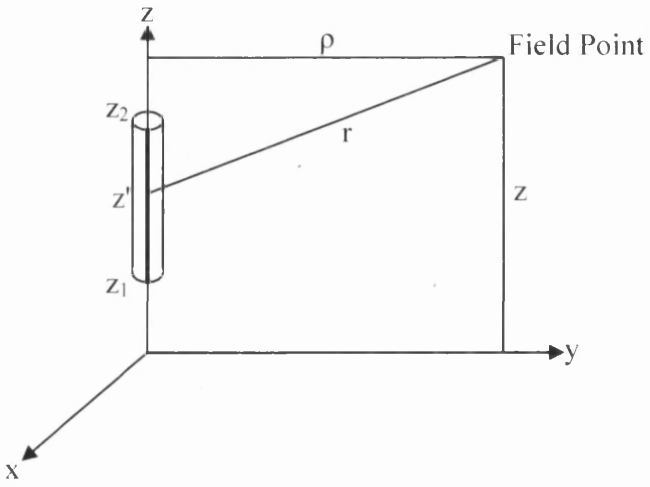

Figure 3.2 - Calculating the field from a straight thin wire segment

$$\mathbf{E} = -\mathbf{k}\frac{dI}{dt}\frac{\mu_0}{4\pi}\frac{1}{|\mathbf{r}_{\text{midpoint}}|}(z_2 - z_1) \tag{3.9}$$

An alternative would be to evaluate $|\mathbf{r}|$ at several points on the wire and combine these using a weighted average system. However, that approach has been rejected in this work since the additional accuracy offered can also be achieved by simply using a slightly higher number of straight line segments. Additionally, since the current magnitude does not vary along the length of a wire segment, as is the case in high frequency work, the incentive for using a weighted average system for the current in a segment that exists in such high frequency work is absent from this work.

Once (3.9) has been evaluated, the field obtained is converted into the global coordinate system by projecting the local **k** unit vector onto the global system unit vectors at the field point and multiplying by the magnitude of the field calculated in (3.9). After this has been done for each straight line segment, the total electric field is obtained by vector addition of the contributions from each segment.

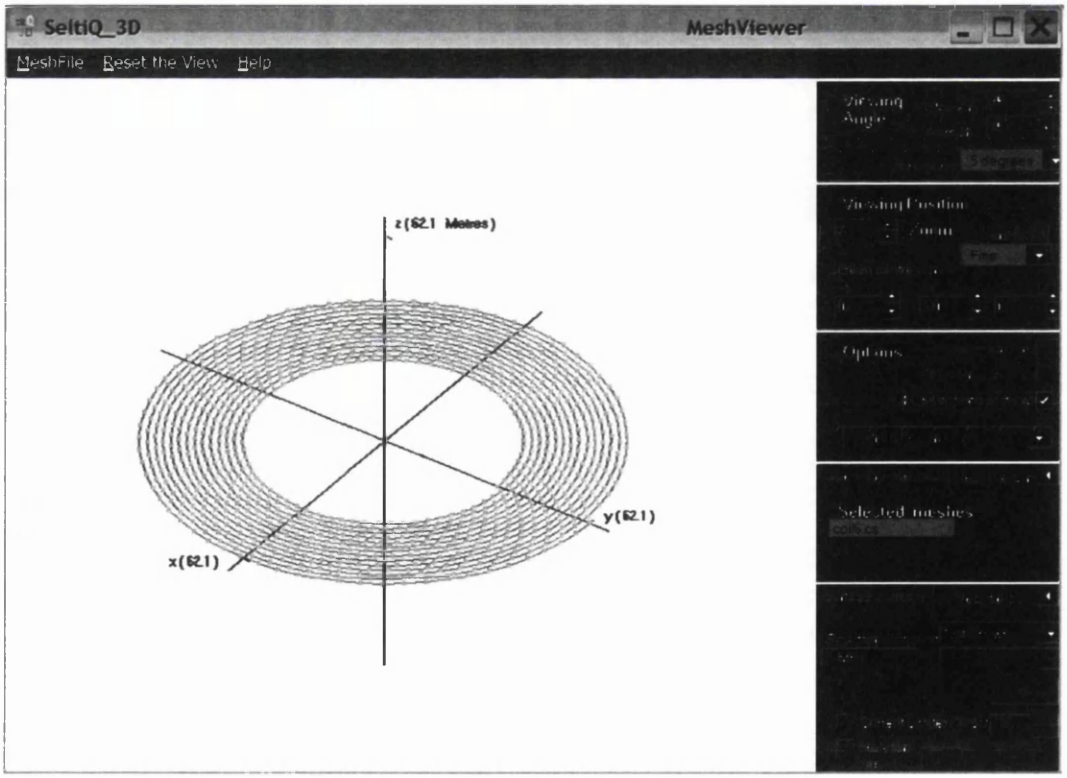

Figure 3.3 - A discretised thin-wire spiral in the graphical interface of SeltiQ_3D

Luckily, a program already existed at Swansea University (SeltiQ_3D) which included a graphical interface for entering wire geometries and discretising them into straight line segments for use in radio frequency analyses. That program was therefore used as a basis in the work that follows to evaluate the accuracy of the thin-wire modelling technique, and routines for undertaking the low frequency electric field calculations described above were added to the program using the FORTRAN77 language. A screenshot of the program with a discretised thin-wire representation of a 14 turn single spiral stimulating coil is shown in Figure 3.3.

3.5 The Electric Field Due to a Thin Wire Circular Loop

Before making full use of the thin-wire modelling program described in the previous section, it was necessary to verify that the program could correctly evaluate the electric fields from geometries whose fields are already known. This was done for several different geometries including straight lines, polygonal loops and circular loops, and a comparison of the field obtained from a discretised circular loop with the analytical solution for such a loop is presented in the next section. This geometry is chosen for presentation because, as will be seen later, that analytical solution method will prove to have a wider use in this project's work. In the remainder of this section an analytical solution for the electric field from a thin-wire loop is described.

Finding the magnetic field or magnetic vector potential due to a circular loop of wire is a problem commonly discussed in book on electromagnetics. Unfortunately, the analytical formulae derived therein only apply either when the field point is far from the loop, or for field points along the loop's axis. However, Shadowitz [80] derives an expression for the magnetic vector potential, **A**, anywhere in space due to a circular thin-wire loop. With reference to Figure 3.4, this potential is given in the spherical coordinate system [81] by:

$$\mathbf{A} = \Phi \frac{\mu_0 I}{2\pi} \sqrt{\frac{a}{r_r}} \left[\left(\frac{2}{k} - k \right) K(k) - \frac{2}{k} E(k) \right] \tag{3.10}$$

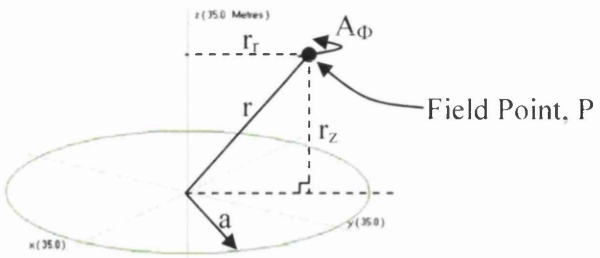

Figure 3.4 - The magnetic vector potential due to a circular thin-wire loop

where

$$k = \sqrt{\frac{4r_r a}{r_z^2 + (r_r + a)^2}} \tag{3.11}$$

and $\boldsymbol{\Phi}$ is the unit vector in the Φ direction at the field point, K is an elliptic integral of the first kind and E is an elliptic integral of the second kind [82]. Given that the electric field due to induction is the negative time differential of **A**, the electric field due to the circular loop is given by:

$$\mathbf{E} = -\boldsymbol{\Phi}\frac{dI}{dt}\frac{\mu_0}{2\pi}\sqrt{\frac{a}{r_r}}\left[\left(\frac{2}{k} - k\right)K(k) - \frac{2}{k}E(k)\right] \tag{3.12}$$

The only terms in (3.12) which are not straightforward are the elliptic integrals. Of course one could obtain values for these from published mathematical tables, but, as will be seen later, it will prove to be useful in this work to write a computer program to evaluate (3.12) for any size of circular wire loop. Algorithms are therefore required to solve the integrals for different values of k.

Such algorithms have been described by Carlson [83], and Carlson, Notis and Pexton have written FORTRAN routines to perform the integrals which are publicly available as part of the SLATEC library. These routines, specifically versions drf and drd have

been used in slightly modified forms to evaluate (3.12) in this work. The modifications merely relate to changing the tolerance values at which the iterative algorithms stop so as to reflect the accuracy level available from double precision data in a 32 bit personal computer processor.

3.6 The Reliability of the Electric Field Obtained from the Discretised Thin-Wire Loop Modelling Program

The reliability of the thin-wire loop modelling program discussed in Section 3.4 will be verified in this section by comparing the results obtained from it when modelling a circular loop of wire to those obtained by using the analytical formula (3.12) from the previous section. To do this, a circular loop of 50mm radius was entered into the modeller, and discretised into N straight line segments of equal lengths. Assuming a rate of change of current of 1A/s, models were solved using different values of N and hence different segment lengths. Choosing to model the electric field magnitude at a point 30mm from the loop's axis on a plane 30mm below the loop's plane (this would be a typical magnetic stimulation position in relation to a coil), the percentage errors in the values obtained from the models compared to the value of 112.4 nV/m obtained using the analytical formula (3.12) are shown in Figure 3.5.

From Figure 3.5 it can be seen that the error between the modelled values and the value obtained using (3.12) reduces asymptotically towards zero as the number of segments in the circular loop model is increased. This suggests that the discretised thin-wire loop electric field modelling program is working correctly, and is yielding reliable results. This was confirmed by performing similar analyses on other shapes as outlined at the beginning of the previous section.

It can also be seen from Figure 3.5 that the accuracy of the results obtained from the modelling program is dependent on the number of straight line segments used. When running other models, it was found that long segments could be safely used in long straight sections of shapes like a square loop of wire without impacting on accuracy. However, in shapes having curved sections, the number of segments used to represent

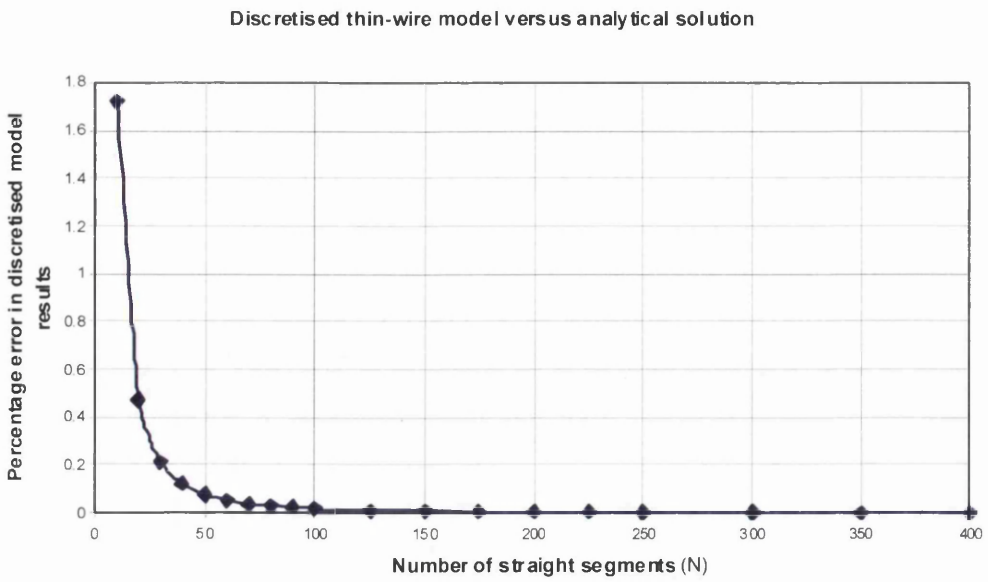

Figure 3.5 - The percentage error in electric field magnitude due to modelling a circular loop using N straight line segments

the curves is clearly important. Care must therefore be taken when using the modeller to ensure that accuracy is maintained. This accuracy is discussed in greater detail in the next section.

3.7 The Accuracy of the Electric Field From a Thin-Wire Model of a Spiral Coil

In Section 3.3 it was seen that the practise of modelling magnetic stimulation coils as coils of infinitesimally thin wire in order to obtain the fields surrounding them has been frequently used by earlier researchers. However, no data appears to have been published with regard to how accurate this practise actually is. Given that a coil is actually composed of wire that has a cross-section (e.g. 6mm x 1.75mm in the HP90 coil produced by the Magstim Co. Ltd. of Whitland, UK) and that tissue to be stimulated is typically located only some 20mm - 60mm below a coil, one would expect the accuracy of the thin wire approximation to suffer somewhat. The next section reports on whether that is the case or not when a spiral coil is represented as concentric circular loops of thin wire. However, in this section, the accuracy of

modelling a spiral Magstim HP90 stimulation coil as a spiral of thin wire is investigated.

Since it is the accuracy of representing something made of wire having an actual cross-section using thin wire that is of interest in this section, it will be important to try to reduce the error in the thin wire models due to the use of straight line segments to a very small level. Therefore this section begins by trying to ascertain the number of segments that would be required to adequately represent the HP90 in the model. To do this, representations of the coil discretised into N segments along its length were entered into the modeller, and preliminary models were solved to obtain the electric field magnitude at a point 60mm from the coil's axis in a plane 15.5mm below the coil's plane for different values of N. An assumed rate of change of current value of 1A/s was used in these models. The dimensions of the modelled HP90 were based on physical measurements of an actual HP90, which was found to be a constantly tapering spiral of 14 turns with the centres of the innermost and outermost conductors at radii of 34.375mm and 62.125mm respectively. The distance between the centres of adjacent turns was 1.982mm. The results of these models appear in Figure 3.6.

Figure 3.6 shows that the modelled electric field magnitude tends asymptotically towards a value of 2.9676μV/m as N is increased. Figure 3.7 shows the times taken to solve the HP90 models on a computer having a Pentium 4 1.8GHz processor, the only

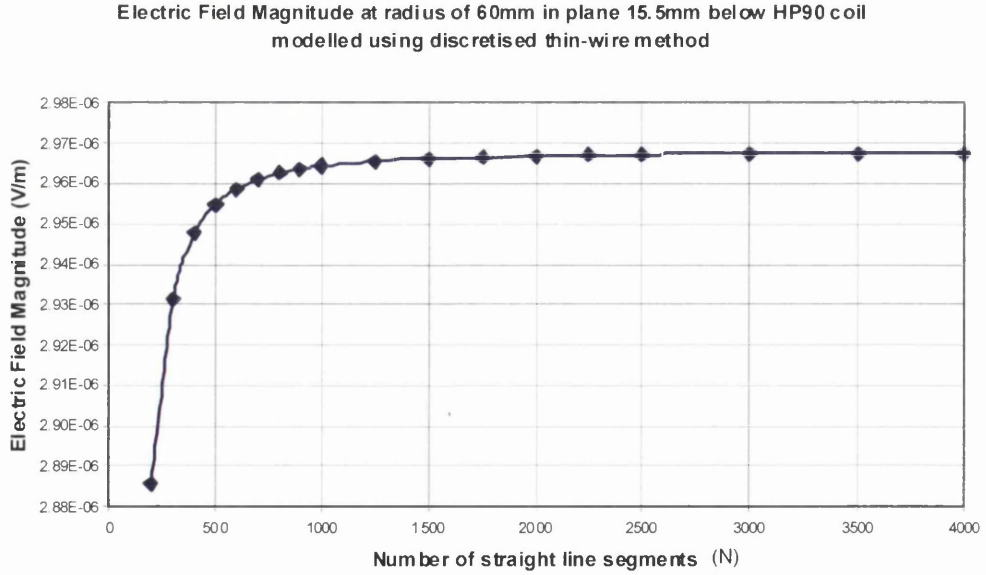

Figure 3.6 - The electric field magnitude due to thin-wire models of the HP90 having different numbers of segments

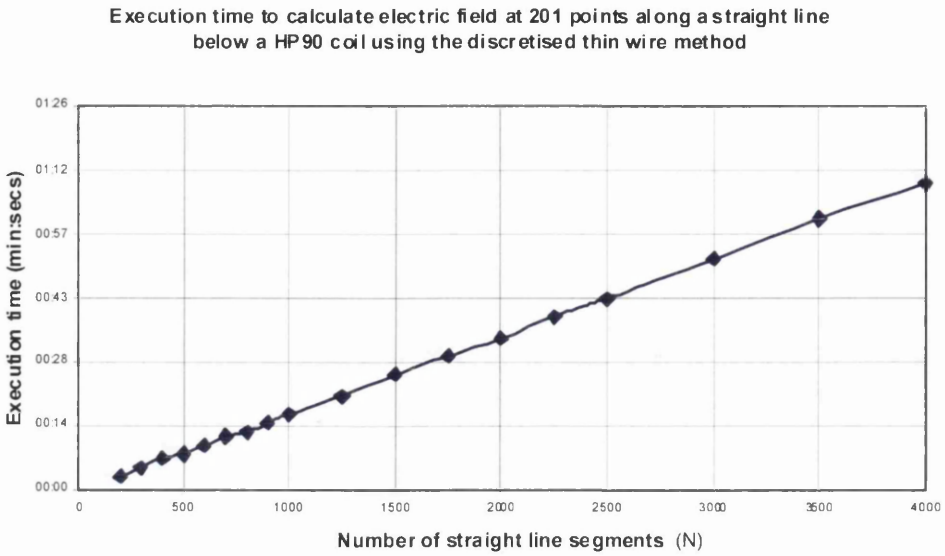

Figure 3.7 - The time taken to solve for the electric field due to discretised thin-wire models of the HP90 having different numbers of segments

difference being that the electric field magnitude is computed at 201 points along a line in the plane 15.5mm below the coil. This configuration of points was chosen because that will be typical of the type of modelling required to ascertain the focality of coils during the iterative optimisation process that will be developed later in this work.

From Figure 3.6 and Figure 3.7 it can be seen that a trade-off exists between solution accuracy and solution time when choosing the number of segments to use in the model of the HP90. For the solution to become stable to within four significant figures, the solution time for the 201 field points was 1 minute and 1 second. That high level of accuracy is desirable for the modelling work in the remainder of this section. However, whilst that solution time is not excessively long for a model that is only intended to be to run once, it implies that the overall solution time could be lengthy when many models are solved during an iterative optimisation sequence. Perhaps during the optimisation process it would be better off settling for accuracy within three significant figures. For the solution to become stable to that tolerance, the solution time in Figure 3.7 was 21 seconds. That would be more acceptable and the segment length ratio used to represent the curves in the corresponding model was 70.35μm per mm radius of curvature. It is therefore suggested that this segment length

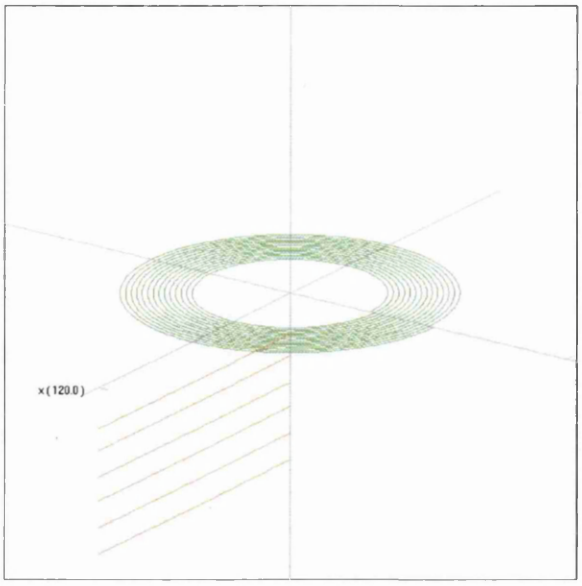

Figure 3.8 - Electric field points lying along lines below the spiral HP90 coil

ratio be used to represent curves if discretised thin-wire models are to be used during an optimisation sequence. In this section, to obtain results accurate to within four significant figures, the results of the preliminary models suggest that the HP90 should be split into 3500 segments with the segment length ratio used to represent the curves being 25.13μm per mm radius of curvature.

The Magstim Co. Ltd. was kind enough to supply data relating to the peak electric field from a HP90 coil when used with a Magstim Rapid^2 biphasic stimulator for the purpose of comparison against modelled results. The data consisted of measurements of the electric field magnitude taken at regular points along lines parallel to the plane of the coil which were located at distances of 12.5mm, 20.8mm, 30.8mm, 39.9mm, 50.0mm and 60.0mm below the coil. This configuration is illustrated in Figure 3.8. The measurements were taken with an electric field probe using the same apparatus used to take field measurements from a new coil shape later in Chapter 7.

To compare the field from a thin-wire model of the HP90 to the Magstim supplied data, knowledge of the peak rate of change current through the coil when used with a Rapid^2 stimulator will be required. As will be explained in Chapter 7, this can be calculated as:

$$\left.\frac{di}{dt}\right|_{peak} = \frac{V_c}{L_s + L_c} \tag{3.13}$$

where V_c is the potential across the charging capacitor in the stimulating machine, and L_s and L_c are the inductances of the stimulating machine and coil respectively. In the Magstim data, V_c = 1530V, and L_s and L_c were measured using a Wayne Kerr 6425 impedance bridge to be 1μH and 23μH respectively. Therefore the peak rate of change of current would be 63.75MA/s.

To investigate the accuracy of modelling a HP90 coil as a spiral of thin wire, the discretised representation of the coil was entered into the modelling program together with the peak rate of change of current and solved to give the electric field magnitude along the same lines below the coil as the Magstim supplied data. A comparison of the results is shown in Figure 3.9. There is, in general, good agreement between the thin-wire results and the measured data. The thin-wire field magnitudes are a little less than the measured data for points within about 45mm of the coil's axis, and, beyond there, are a little higher than the measured data. This agreement is surprisingly good

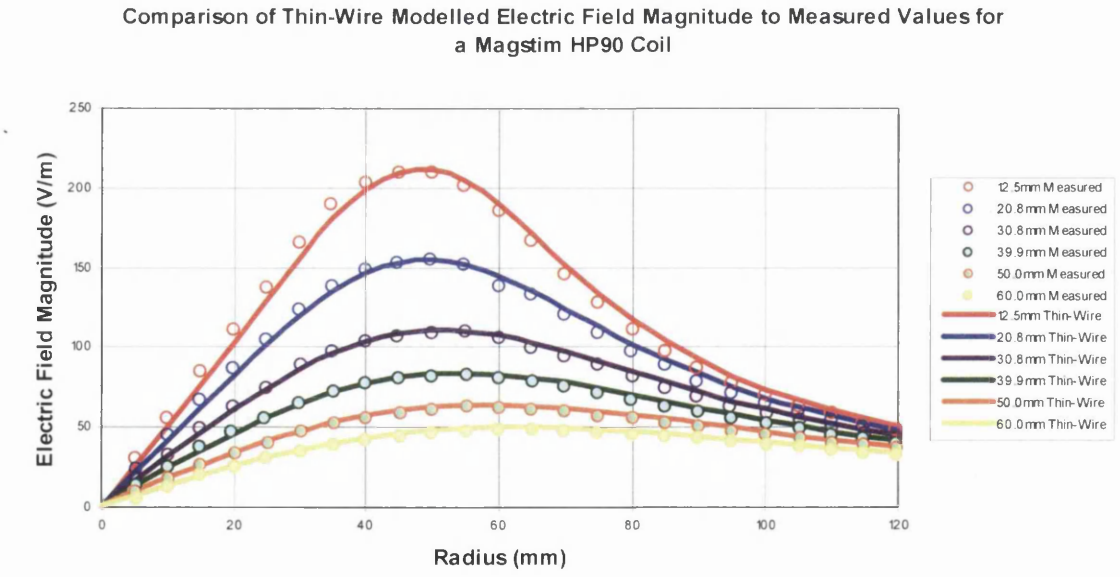

Figure 3.9 - A comparison of the results from modelling a HP90 coil as a spiral of thin wire compared to measured electric field values

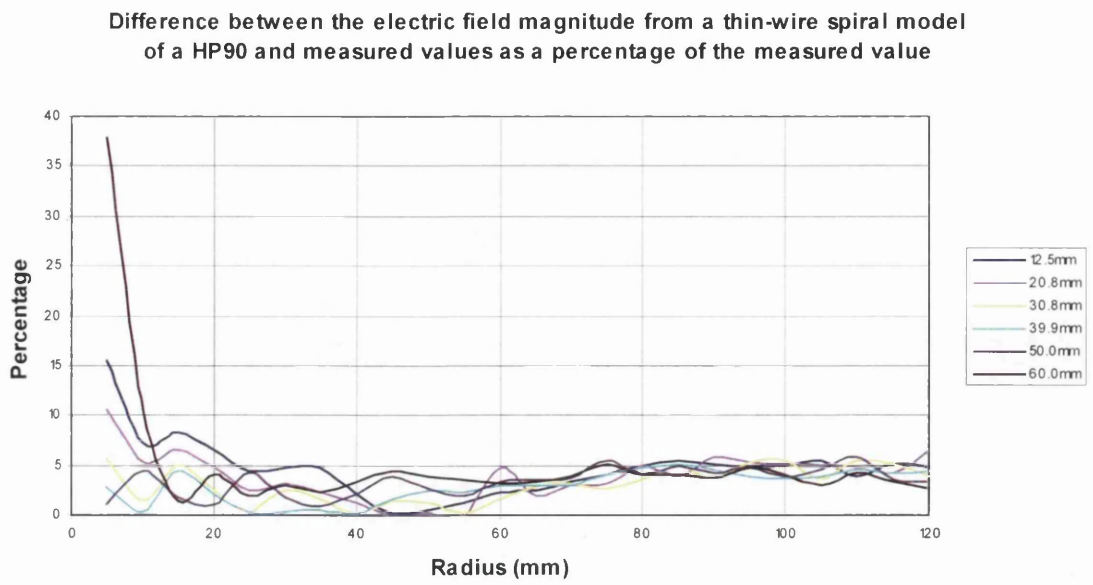

Figure 3.10 - The difference between the thin-wire and measured data as a percentage of the measured data

given how close the field points are to the coil.

Figure 3.10 shows the difference between the electric field magnitude obtained from the spiral thin-wire model of the HP90 and the measured data as a percentage of the measured data. As can be seen, for field points at radii between 25mm and 75mm, the difference is 5% or less, but, beyond 75mm, the difference becomes consistently closer to 5%, fluctuating to a high of 6.5% at one point. For radii less than 25mm, the percentage difference increases beyond the values at 25mm, and, at 12.5mm and lower, the percentage difference increases asymptotically. This occurs as the measured electric field magnitude (the denominator in the percentage calculation) becomes small, tending to zero at zero radius.

The results obtained in this section give more confidence in the accuracy of the thin-wire modelling technique than if it were just accepted because earlier researchers use it. But, are the larger differences between the modelled electric field and the measured data as a percentage of the measured data seen at radii below 25mm a problem? For a single spiral coil, like the HP90, the answer is no. This is because, although the percentage difference is not small, the field magnitude at these radii is low – very low

near to zero radius. The focality of a coil is assessed by examining the electric field magnitude along a line below a coil, starting at zero radius and working away from the coil's axis, looking for the largest peak encountered, then finding the radius beyond the peak at which the field falls to -3dB of its peak value. If there is a discrepancy in modelling the field values at radii less than the radius of the peak field, then the calculated focality should not be altered, so long as the discrepancy is not large enough to cause a false peak to occur. As can be seen from Figure 3.8, the discrepancy is nowhere near that large.

For a coil composed of several spiral sections, like that of Hsu and Durand [85], focality is assessed by considering a line of field points below the *whole* coil. The percentage difference issues referred to above with thin-wire modelling at radii below 25mm under a single spiral would only become relevant if a field point happened to be located at a radius below 25mm in relation to a spiral section. Even then, the contribution to the field from that spiral at that point should be low enough for the small discrepancy in its value not to cause undue worry.

From the results presented in this section, it can be concluded that the thin-wire modelling technique is accurate enough to be used as part of the coil optimisation programs described later in this thesis. These programs were outlined in Chapter 2.

3.8 The Accuracy of the Electric Field from a Thin-Wire Model of a Spiral Coil Modelled as Concentric Circular Loops

In the previous section it was seen that good values for the electric field from a spiral coil can be obtained by modelling it as a spiral of infinitesimally thin wire. However, in Section 3.3 it was noted that some researchers have modelled spiral coils by approximating them as concentric circular loops of thin wire. In this section it is intended to report on the accuracy of modelling a spiral Magstim HP90 stimulation coil in this way.

It was also seen in the previous section that modelling a coil of the size of a HP90 using discretised thin wires results in there being a need for many straight wire segments. This meant that having to calculate the contribution to the field from each segment caused the solution time for the model to be not insignificant. However, in Section 3.5, an analytic formula was reproduced for calculating the electric field from a circular thin-wire loop without having to discretise it into straight segments – this is computationally very fast. Given the potential time saving involved, the electric field in the concentric circular loop model of the HP90 in this section will be calculated by applying the analytic formula to each loop and summing the answers rather than by discretising the loops into segments.

To this end a new FORTRAN program was written that allowed its user to specify any combination of circular thin wire loops and field calculation points in 3D space, and would apply (3.12) and the elliptic integral algorithm referred to in Section 3.5 to calculate the electric field at each point due to all the loops. The user could specify the rate of change of current through the coil.

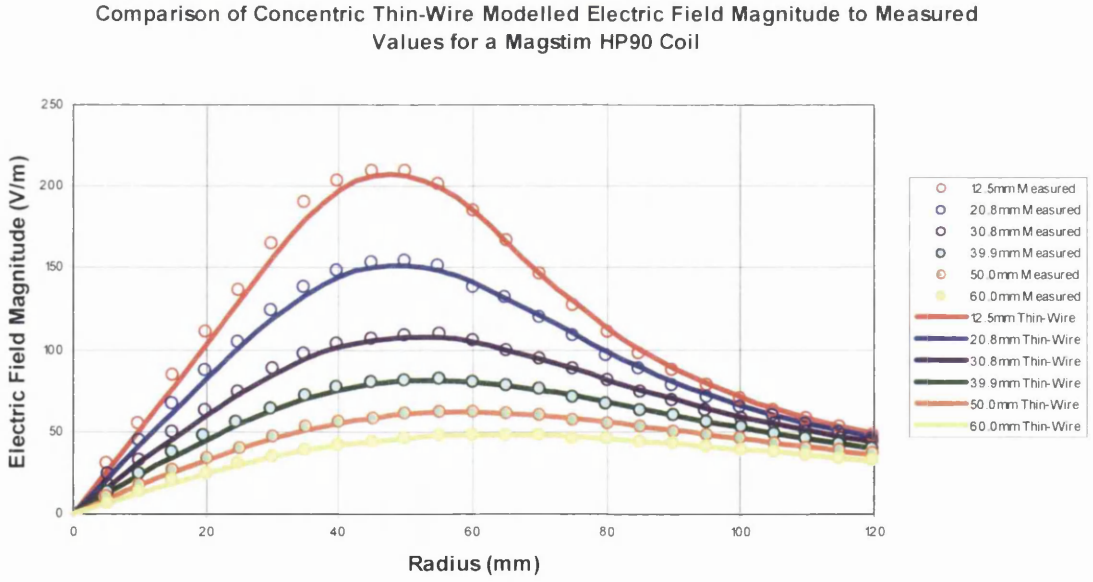

Figure 3.11 - A comparison of the results from modelling a HP90 coil as concentric circular loops of thin wire compared to measured electric field values

Into this program a representation of the HP90 was entered as 14 regularly spaced concentric thin-wire loops, with the inner loop having a radius of 34.875mm, and each remaining loop having a radius 2.05mm larger than its predecessor. The rate of change of current calculated in the previous section of 63.75MA/s was used. The same field points as were used in the previous section were entered, allowing comparison of the field obtained from this model with the measured electric field data provided by the Magstim Co. Ltd. that was described in the previous section.

As can be seen in Figure 3.11, the results from this model are also in good agreement with the measured data. At radii from the coil axis less than about 55mm, the results are not as close to the measured data as the results obtained by modelling the coil as a thin-wire spiral in the previous section. However at radii beyond 55mm, the results are in better agreement with the measured data than the spiral model results! This analysis is confirmed by looking at the differences between the modelled electric field and the measured data as a percentage of the measured data shown in Figure 3.12.

The improved correlation with the measured data for radii beyond 55mm could be due to the error involved in approximating a spiral coil as concentric loops compensating for the error involved in approximating a coil of wire that has an actual cross-section as a thin-wire coil. The same reasoning as was used in the last section can be applied when judging the significance of the percentage figures at radii near the coil's axis seen in Figure 3.12. This suggests that there is no cause for concern. This is borne out by the graph of Figure 3.13 which plots the difference between the electric field due to the concentric loop model of the HP90 and the measured values as a percentage of the measured peak electric field value on each line. It may be seen that the percentage difference is always below 5%.

The results of the modelling work undertaken in this section suggest that spiral coil sections can be reliably modelled by approximating them as concentric loops of thin-wire. It should be noted that the time taken by the concentric loop modelling program to solve for the field at the 174 points needed to produce the plots in this section was less than one second.

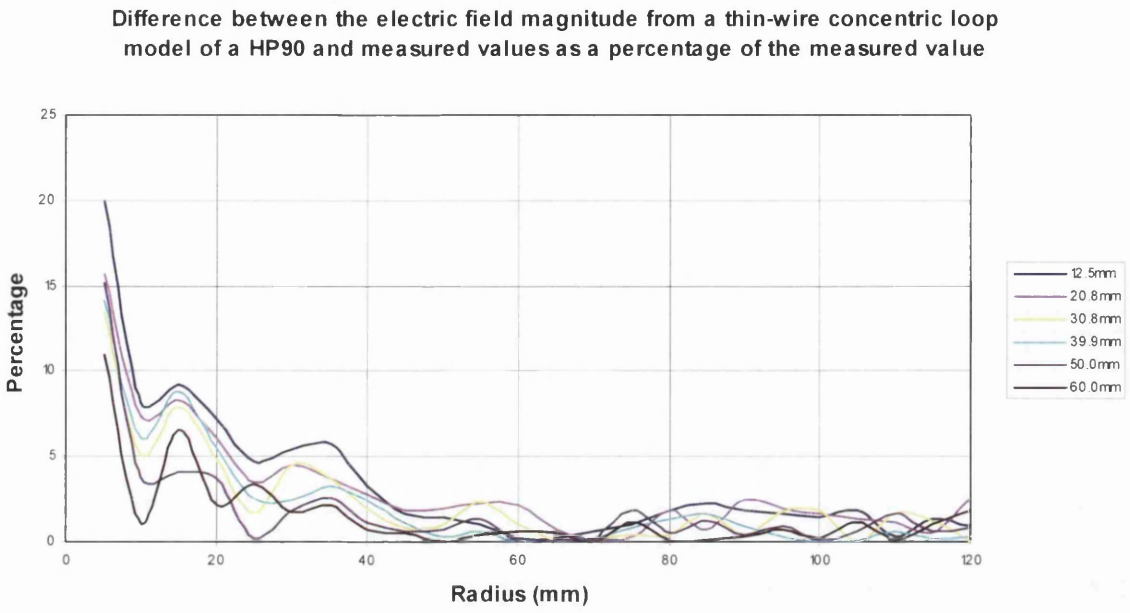

Figure 3.12 - The difference between the concentric loop thin-wire and measured data as a percentage of the measured data

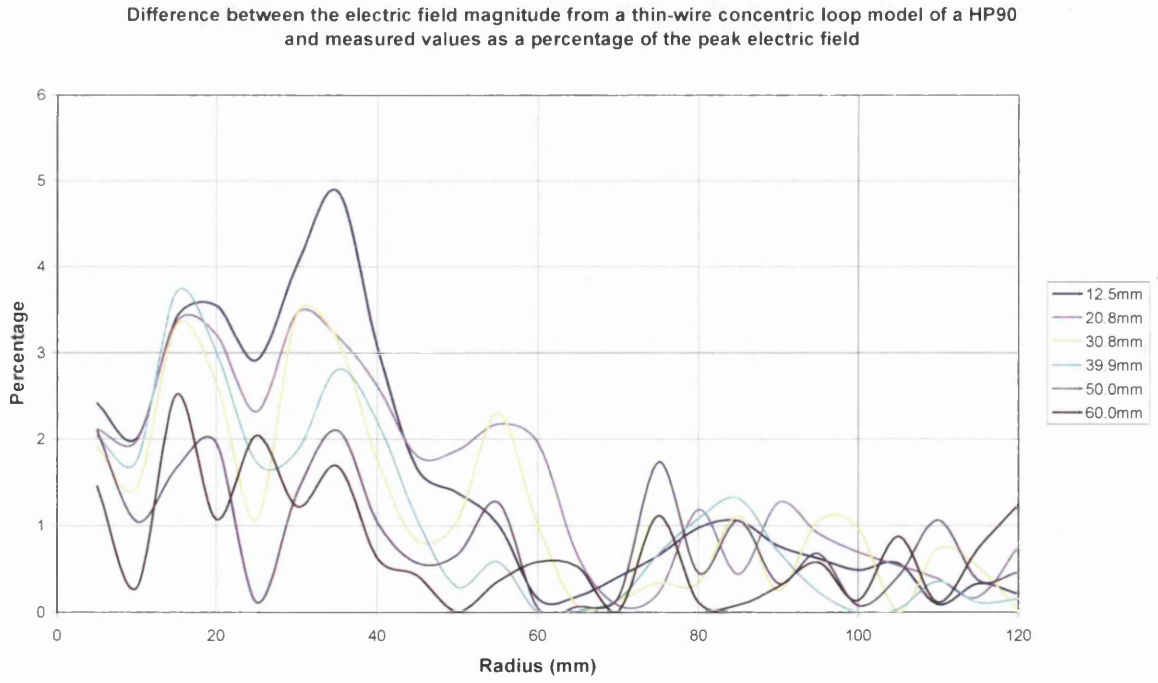

Figure 3.13 - The difference between the concentric loop thin-wire as a percentage of the peak electric field at each line

3.9 Thin-Wire Modelling in the Remainder of this Thesis

In Section 3.7 it was seen that a good approximation to the electric field due to a stimulation coil can be obtained by modelling it as being made of infinitesimally thin wire. In that section, a spiral Magstim HP90 was modelled as a spiral of thin-wire, and similar results have also been obtained, but are not reported in this thesis, by comparing the fields obtained from measurements or Finite Element Method (FEM) models of other coil geometries to those obtained from thin-wire models. These other shapes include a conical helix and rings of wire stacked vertically.

Whilst they are relatively fast when compared to models that include the wire cross-section, like FEM models, the discretised thin-wire models still have computation times that are several seconds long. Given that it is intended to solve many thin-wire models in the optimisation programs that are described later in this thesis, the overall solution time could become lengthy. There is therefore an incentive, where it is valid to do so, to apply the much faster technique used in Section 3.8 of approximating a coil as concentric loops of thin-wire and using the analytical formula to solve the model.

In Section 3.8 it was seen that approximating a flat spiral coil, like the HP90, using concentric thin-wire loops gave acceptable electric field values. This has also proven to be the case with related coil geometries. For example, in Chapter 7, good agreement is shown between measured and coaxial thin-wire loop modelled field values for a new coil design developed in this work. That coil design could be thought of as a conical helix whose tapering sides exhibit two changes in the degree of taper. Furthermore, in Figure 3.14 and Figure 3.15, good agreement is seen between electric field values for a helix when modelled as vertically stacked coaxial loops of thin-wire and, using the discretised method, as a helix of thin-wire. The geometry of the model is given in Appendix B.

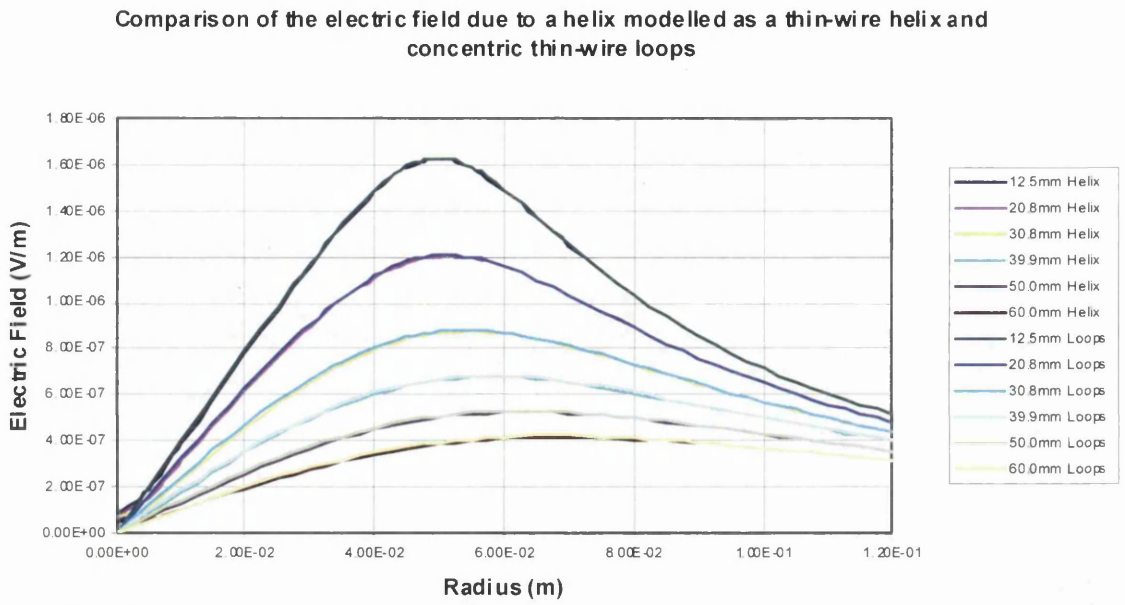

Figure 3.14 - The electric field due to a discretised thin-wire model of a helix and the helix modelled using concentric circular thin-wire loops

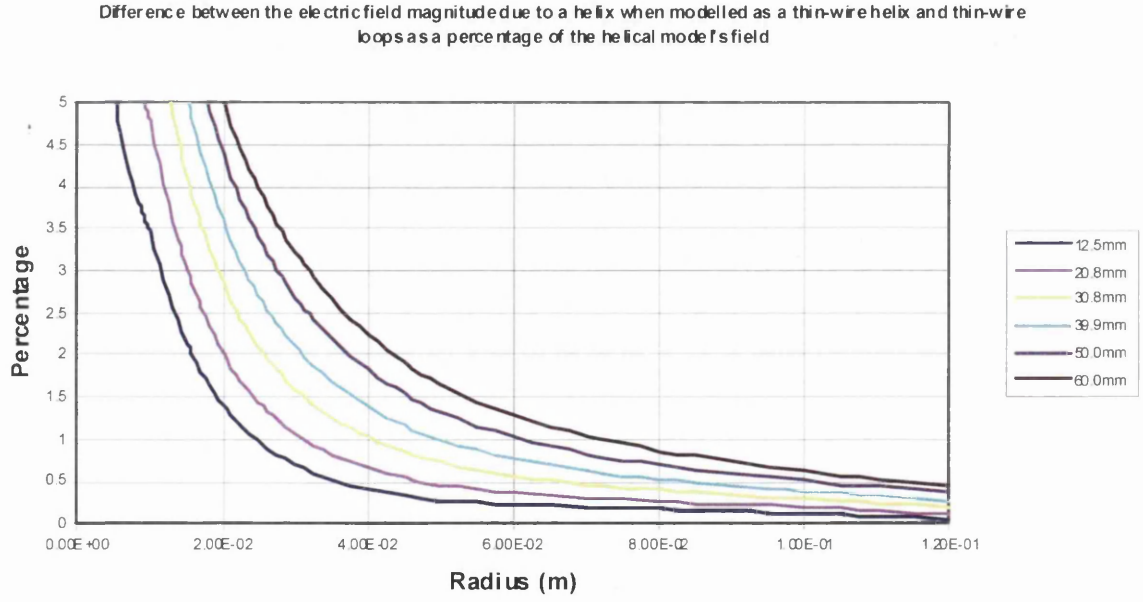

Figure 3.15 - The difference between the electric fields obtained from discretised thin-wire and concentric circular thin-wire loops of a helix as a percentage of the field from the discretised model

Given the good results achieved with the coaxial loop and analytical formula method, and its significant speed advantage, it has been decided to use this modelling method during the development of the optimisation programs in this work. However, choosing this method means that the optimisation programs will be restricted to considering coil geometries that have sections whose shapes can be approximated using coaxial loops in a similar fashion to flat spirals or helices. This does not render the remainder of this thesis an academic exercise. The manufacturing processes for stimulation coils are already chiefly geared towards the production of coil sections that can be approximated as coaxial loops, and there is much interest in whether the design of these coils can be improved without requiring expensive capital outlay on radically different manufacturing equipment. Also, after an optimisation approach and program code have been successfully developed in this work, they could, as part of future work, be extended to consider more diverse shapes by changing the field modelling computer program subroutines from ones using coaxial loops to ones using true shape discretised thin-wire representations.

3.10 Static Electric Charges and Magnetic Stimulation

In Section 3.3 it was mentioned that static electric charges accumulate in tissue as a result of exposure to the electromagnetic fields from a nearby stimulation coil. Although, as was explained, it is not intended to include charge accumulation in this thesis's modelling work, this section offers a brief description of the phenomenon before suggesting that, in failing to take it into account, another research group's reported results must contain a discrepancy.

Roth et al [66] and Mouchawar et al [76] explain that the electric field (due to induction) around a coil is in the opposite direction to the current flow around the coil at a particular time – this is shown in Figure 3.16. These field lines pass through both the air and tissue that surrounds the coil. Now, the air is an insulator but the tissue is conductive, and this causes electric charges to flow through the tissue in the direction of the field lines and accumulate at the air-tissue interface as shown in Figure 3.17.

The static charges that appear at the interface have polarities such that their fields oppose the direction of the induced electric field around the coil. This means that the electric field that appears in the tissue due to the coil is effectively somewhat reduced in magnitude. It can also be seen by considering Figure 3.17 that, if the coil were held parallel to the air-tissue interface, its induced electric field lines would not cut through the interface, and no static charges would be directed along the lines to accumulate at

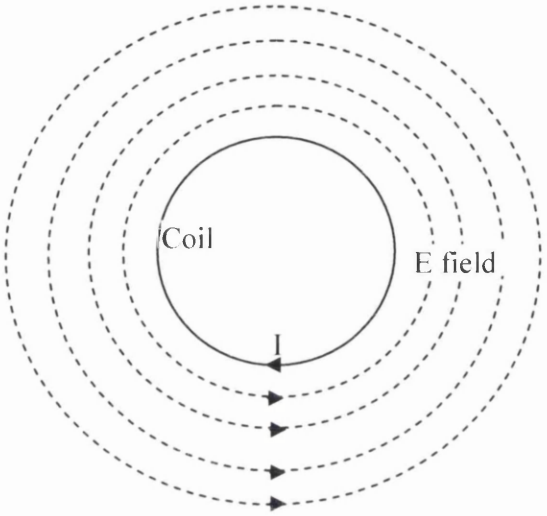

Figure 3.16 – Electric field direction around a simple coil

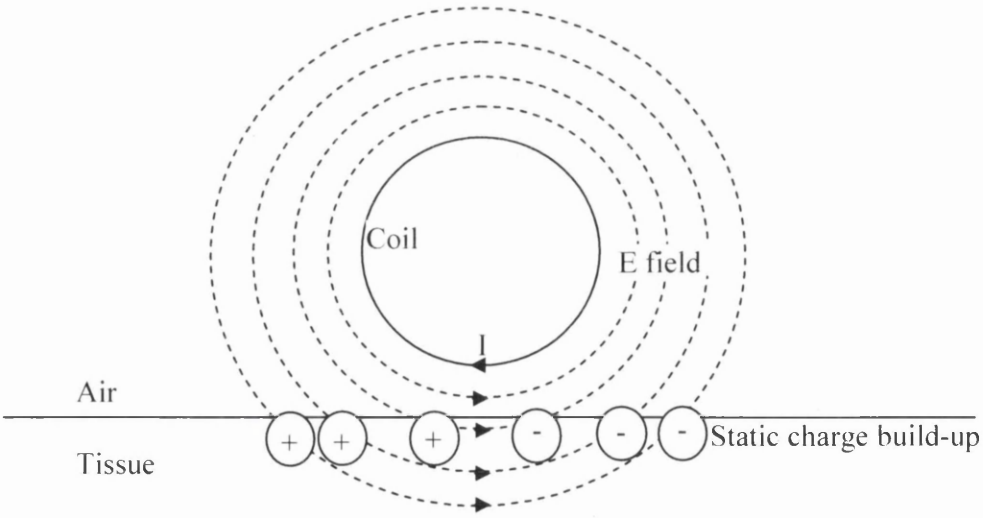

Figure 3.17 – Static charge accumulation at air –tissue interface

the interface. This would mean that the induced field would not be opposed by static charges' fields. Therefore, the orientation of a coil relative to the air-tissue interface has an influence on the electric field that arises in the tissue.

Additionally, Mouchawar et al [77] report that charge accumulation also occurs at the interfaces of regions of tissue having different conductivities, and it is known that many different regions exist within the body, often closely packed in concentrated areas such as the brain. Further, the inter-tissue interfaces are in slightly different locations for different people, all of which suggests that predicting the electric field that will arise in a person's tissue due to a particular coil held at a particular angle is far from straightforward. Wagner et al [78] and others are adamant that tissue boundary layers do measurably alter induced electric field.

In [66] and [76], the authors include expressions to evaluate the contribution made to the electric field at a point in tissue due to the accumulation of charges at the air-tissue interface. However, they make no attempt to take into account the multi-region nature of human tissue and the accumulation of charges at region boundaries. Later works like [71] or [78] that include multi-region tissue models make use of equivalent circuit or Finite Element Method (FEM) tissue models rather than closed expressions for the charges. So, to fully model the electric field that will arise in real tissue requires that charge accumulation in the tissue be modelled, and to do this correctly requires that a complex model of the tissue, probably using the FEM, be solved.

Section 2.2.2 introduced an expression for nerve membrane potential, (2.5), which is reproduced below as (3.14).

$$V_m(t) = k_3 E_0 \frac{\left[\frac{2R_mC_m - R_{tot}C_S}{\sqrt{4C_SL_{tot} - C_S^2R_{tot}^2}}\right]\exp\left(\frac{-R_{tot}t}{2L_{tot}}\right)\sin(\omega t) + \exp\left(\frac{-R_{tot}t}{2L_{tot}}\right)\cos(\omega t) - \exp\left(\frac{-t}{R_mC_m}\right)}{\frac{1}{R_mC_m} + \frac{R_mC_m - R_{tot}C_S}{C_SL_{tot}}} \tag{3.14}$$

Consideration of (3.14) reveals that, taken together, the terms to the right of k_3 relate to the magnitude, at a certain time, of the component of the electric field that arises due to electromagnetic induction – i.e. the first term on the right hand side of (3.4). In Section 2.2.2 it was explained that k_3 is a property of the tissue at the location being stimulated, and, in the light of the discussion in the previous paragraphs, it can be seen that it must include the influence on the nerve membrane potential of the component of the electric field that is due to build up of static charges in the surrounding tissue.

As has been seen, the accumulation of static charges is dependent on the size of the electric field due to induction. This means that k_3 cannot be a constant and that its value must vary in some way with the electric field due to induction. If one follows the origin of k_3 in (2.5) back through the derivation in Section 2.2.2, it can be seen that the term k_1 in (2.3) cannot be a constant, but must vary in some way with the rate of change of magnetic flux term.

Since k_1 was chosen to be constant as a result of the work of Davey and Epstein [49], it follows that there is a discrepancy in that work. Specifically, Davey and Epstein claim to have derived an expression for nerve membrane potential, but, since they omit to take static charges into account, the expression is not complete. In the work, no mention at all is made of static charges, and no statement is made that their contribution to the membrane potential has been assumed to be constant or deliberately omitted for simplicity's sake. One must therefore presume that Davey and Epstein erroneously believe their expression to be complete, and it must be pointed out in this work that the values of nerve membrane voltage that they go on to calculate and report cannot be entirely correct.

4 Finite Element Method Modelling

4.1 Background

In Section 2.5.3.2.2, it was explained that, as part of the tri-modular computer program approach proposed in this work as a method of finding more focal stimulation coil geometries, a Finite Element Method (FEM) program would be required whose function would be to calculate the resistance and inductance of new coil geometries whilst correctly taking into account the skin and proximity electromagnetic effects introduced in Section 1.4. The FEM program would implement a detailed electromagnetic model of the coil, and in Section 2.4 it was explained why a detailed model that includes the coil's interior is required.

This chapter develops the FEM modelling work undertaken during this project, and begins by explaining why the FEM was chosen as a detailed electromagnetic modelling technique. The chapter then goes on to introduce a chosen FEM formulation – the **T-Φ** method – and explains why it was selected. Aspects related to the accurate and efficient application of the **T-Φ** method to this work are discussed in some detail, and the associated frequency domain matrix equations are formulated.

Unfortunately, hardly any literature exists discussing FEM modelling of the actual internal structure of magnetic stimulating coils. In addition, no literature at all exists on using the **T-Φ** method to do this although literature exists illustrating the use of this method for general eddy current analysis such as Rodger and Atkinson [100], Carpenter and Wyatt [96], and Preston and Reece [99]. Therefore, once it has been shown that the FORTRAN based FEM program developed in this work is functioning correctly, work is presented to show that, using the particular form of electrical current drive chosen, the **T-Φ** method is capable of accurately modelling the current density within and the magnetic field around a Magstim HP90 coil used with a Magstim Rapid^2 stimulator.

4.2 Computational Electromagnetic Modelling Techniques

4.2.1 Background to Detailed Electromagnetic Modelling

Electromagnetic (EM) phenomena are completely described by Maxwell's equations and their associated constitutive relations [2]. Unfortunately, other than in a few simple cases, it is difficult or impossible to find closed form analytical solutions to problems involving Maxwell's equations, and recourse to some method of finding an approximate solution is often required. In the past, this would frequently involve lengthy analytical manipulations, using techniques that were chosen to suit the particular problem's geometry, followed by the use of a numerical method to solve a complicated integral or infinite series. However, as fast digital computers have become widely available, more generally applicable, but computationally intensive, methods have seen widespread use. The three most commonly used computational methods are the Finite Difference (FD) Method, the FEM and the Boundary Element Method (BEM).

4.2.2 The Finite Difference Method

In the FD Method, the continuous differential form of Maxwell's equations are converted into a discrete set of algebraic equations by first placing a regular grid of points throughout and around the space occupied by the bodies involved in an EM problem, and approximating the spatial derivatives as differences between quantities at adjacent points divided by the distance between the points. Then, if the problem is not a static one, the time derivatives are approximated (after discretising time into regular intervals) as the differences between quantities at the same grid point at adjacent time steps divided by the time step size. This usually leads, after taking boundary and initial conditions into account, to a situation where a matrix equation must be solved at each time step to obtain the values of the quantities being solved for at each grid and time point. The values of the unknown quantities at intermediate spatial and temporal points can then be obtained by interpolation.

The FD Method is well understood and has been successfully applied to a wide range of EM problems with accurate results; however, several difficulties arise. Firstly, it is difficult to closely match irregular boundaries using regular grid points without resorting to having a fine grid throughout the problem's domain; this increases the sizes of the matrix equations. Secondly, material interfaces, symmetry conditions, and coupling to equations representing external systems are not straightforward to deal with. Finally, although accuracy can be improved by using higher order Taylor series rather than simple differences to represent derivatives, these series cannot be straightforwardly used either.

Owing to the drawbacks inherent in the FD Method, it will not be used for the EM modelling described in this thesis, and will not be discussed in greater detail. However, the method is comprehensively treated in [53].

4.2.3 The Finite Element Method

This method is again based on electromagnetic equations in their differential form, but includes attempts to circumvent some of the problems associated with the FD Method. To obtain an approximate solution to an EM equation involving spatial derivatives using this method, one would begin by discretising the space in and around the bodies involved in a problem with a mesh of shapes – usually triangles or quadrilaterals in two dimensional problems and tetrahedra or hexahedra in three dimensions. This mesh would generally be of the unstructured type – i.e. it would be irregular, which would allow a greater density of shapes, or elements, to be used in regions having a complex geometry.

Then, a system of 'basis functions' are defined on the mesh. These functions, which are non-zero in only a few adjacent elements, are typically low-order polynomials. The basis functions are used to define an approximation to the required solution across the mesh so that, for example, a solution function f may be approximated as:

$$f(\mathbf{x}) \approx \sum_{i=1}^{n} f_i N_i(\mathbf{x}) \tag{4.1}$$

where **x** is a location on the mesh, f_i is the value of the solution function at the i'th of n pre-defined locations on the mesh, and $N_i(\mathbf{x})$ is the value of the i'th of n basis functions at **x**. The n pre-defined locations are normally the corners, or nodes, of each element, although, as will be seen in Section 4.4, this is not always the case. It is the coefficients f_i that are eventually solved for in the FEM.

Two procedures are then available to obtain the solution function. The process of using variational functionals is explained in detail in [86], but will not be made use of in the finite element modelling work of this thesis. Instead, the more generally applicable method of weighted residuals will be used. Here, a 'residual' is defined, which, for a general differential equation $L(f)=s$ having a solution function f, differential operator L, and source quantity s, is $r=L(f)-s$. This residual will only be zero when an approximate solution is equal to the exact solution to a problem. Of course, this will generally not be the case and the aim when using the FEM is usually to try to set a weighted average of the residual across the region covered by the mesh to be zero.

To this end, a set of weighting, or test, functions are then defined, and there should be as many functions as there are unknown coefficients (f_i in (4.1)) to be solved for. If the weighting functions are chosen to be the same as the basis functions, then the method is known as Galerkin's Method.

The weighted residuals are then set to be zero, and a system of integral equations results. For (4.1), the system of integral equations would then resemble:

$$\int_{\Omega} w_i \cdot \left[L(f) - s \right] d\Omega = 0, \qquad i = 1 \text{ to } n \tag{4.2}$$

where w_i is the i'th weighting function and Ω is the domain of the problem. Numerical integration schemes, like Gaussian Quadrature [54], together with the approximate representation of the solution, as in (4.1), are then used to transform the integral equations into a system of algebraic simultaneous equations. This system of

equations can then be solved to obtain the required unknown approximate solution coefficients. These values can then be used in the approximate representation of the solution to calculate the value of the solution function anywhere on the mesh.

The FEM is, by now, also a very well established computational method and numerous books and papers have been written explaining how the method can be applied to various types of EM problem. Comprehensive treatments are provided in [55]-[59] and [211].

When the FEM is applied to an EM problem, any time derivatives are generally dealt with in one of two ways. If a problem is known to be purely time harmonic, i.e. fields vary linearly with their sinusoidal sources, the time derivative $\partial/\partial t$ is replaced by $j\omega$, where $j=\sqrt{-1}$ and ω is the angular frequency. Solving the problem then involves following the procedure described above for problems having spatial derivatives. Obviously, any solution is composed of complex numbers in the form of peak or RMS values depending on the source values used.

Alternatively, if a problem is not purely time harmonic, time is discretised into short steps, and the time derivatives are approximated either in a similar way to that used with the FD Method, or by representing time itself as a one dimensional FE mesh. These methods of representing time derivatives are discussed in more detail in Chapter 5. However, both methods result in a system of algebraic simultaneous equations having to be solved at each time step. Therefore, this time-domain FEM is normally much more computationally intensive than the frequency-domain version discussed in the previous paragraph.

The FEM has several advantages over the FD Method. Firstly, by allowing the use of an irregular mesh, a greater density of solution points can be positioned in areas of complex geometry, and only a few points need be placed in areas of simple, monotonous geometry. This leads to more accurate and computationally efficient solutions.

Secondly, by including the basis functions in the computational procedure, an interpolation of the solution function across the mesh elements is included in the process of finding the value of the solution at the solution points themselves. This leads to more accurate solutions, and, by choosing higher order polynomials for the basis functions, the practitioner can further increase accuracy. Often, when using higher order basis functions, a less dense mesh can be used to achieve a similar solution accuracy as that obtained with lower order basis functions and a denser mesh; however, even though this is computationally more efficient, the problem becomes more difficult to program.

Thirdly, material interfaces are much more straightforward to deal with. Depending on the FEM formulation used, this may involve no more than recording the electromagnetic properties of each mesh element, e.g. relative permeability.

Finally, coupling the EM model to equations representing external systems, e.g. drive circuitry, is more straightforward in the FEM than the FD Method. The exact method of coupling depends on the FEM formulation and the nature of the problem, but this issue is discussed in more detail in Chapter 5.

However, the FEM has a few disadvantages in comparison to the FD Method. Firstly, the method is more complex to understand and more difficult to work with. The method requires some skill when deciding what shape of mesh to use, which basis functions to use, which formulation is best suited to a problem, how to handle time derivatives, and in actually writing the computer program.

Secondly, time domain simulations can take longer with the FEM than the FD Method. With the FD Method it is sometimes possible to derive explicit formulae for updating quantities at each time step without a system of simultaneous equations having to be solved at each step. In the FEM, this is not generally possible, and time domain FEM models therefore require more computer memory and consume more processor cycles.

Nevertheless, the advantages of the FEM are such that it is chosen over the FD Method by many practitioners. The FD Method generally is used when simplicity of

implementation is important, or when its time domain efficiency can be taken advantage of. The latter property most readily applies to EM problems at micro-wavelengths.

4.2.4 The Boundary Element Method

The Boundary Element Method (BEM) differs from the FD Method and the FEM in two important ways. The first is that the underlying EM equations are cast in their integral form. The second is that after, making use of Green's functions, such as in [60], only active material regions or, for magnetically linear materials material boundaries, need to be discretised with a mesh of points. In high frequency work, a form of the BEM known as the Method of Moments is used.

The remainder of the solution process for the BEM is similar to that used in the FEM. Typically an approximate solution function is defined using basis functions that exist on elements of the mesh. A residual is defined, and the procedure continues by using weighting functions to ensure that a weighted average of the residual across the mesh is zero. Again, a set of algebraic simultaneous equations arise which must then be solved. Detailed accounts of the BEM appear in [56][61][62].

The BEM has several advantages when compared with the FD Method or the FEM. Firstly, only boundaries need to be discretised and included in the models. This is particularly useful in large three dimensional problems, and in problems having large expanses of linear material.

Secondly the BEM readily deals with the open outer boundaries of problems. These cause problems in the differentially based methods, where special techniques have to be employed so that errors do not occur due to the mesh abruptly ending. This will be discussed in more detail in Section 4.3.

Thirdly, the fields obtained as solutions to problems using the BEM are generally smoother than those obtained from the differential methods. This implies that there are not localised zones where the solution is quite inaccurate.

Finally, techniques exist to represent wires as thin wire approximations which are discretised along their length rather than their surfaces being discretised. This leads to further efficiency savings in computational costs.

However, there are a few drawbacks to the BEM. Firstly, the system of simultaneous equations that must be solved leads to a full matrix expression. The differential methods have sparsely filled matrices and these can conventionally be solved with less computational effort. Therefore a practitioner must weigh-up the relative merits of the BEM's small mesh but full matrix against the differential methods' larger mesh but sparse matrix. However, with the rise in multi-core processors and hence in parallel processing, the BEM may gain an advantage since this type of processing can handle full matrices more efficiently. Secondly, the BEM tends to lead to singular matrices and matrix ill-conditioning [212].

Thirdly, since the BEM only consists of a mesh on the boundaries within a problem, it is therefore ill-suited to problems containing volumes of non-linear materials [212].

4.2.5 The Choice of a Detailed EM Modelling Technique

Sections 4.2.2 - 4.2.4 summarised the three main computational methods used to model electromagnetic problems. A choice must therefore be made of which of the three methods is the most appropriate to make use of in the EM models of the stimulating coil structures that will arise during the optimisation procedure described in this thesis.

The method chosen must be able to model the interaction of the fields due to the current in the various sections of the coil and correctly model the skin and proximity effects, described in Section 1.4, that occur at the frequencies that are likely to arise within the coil. The BEM, since it has difficulties in modelling problems containing volumes of non-linear material and it may be desired to include such material in the problems to be solved using this work's chosen EM method at some stage in the future, it was decided that the BEM would not be chosen for the EM modelling work

of this work. An additional reason was because of the dense matrices associated with the BEM. A differential method like the FD Method or FEM must therefore be used.

It is also important that the method chosen should allow the model to be easily coupled to a circuit model of the stimulating machine and connecting leads, and that the regions of conducting and surrounding materials that make up the EM model can be easily joined together. Also, since the coils are expected to have several turns and that it is important to be able to model the activity at depth in each of these turns in detail, it is likely that a sizeable mesh of points will be required. It would therefore be useful to be able to take advantage of the FEM's facility for having irregular meshes and basis functions between mesh points in order to make the process of computing a solution more accurate and efficient. For these reasons the computational method chosen for the full EM models of the coils in this work is the FEM.

4.3 The Choice of Finite Element Method Formulation

Given that it has been decided to use the FEM for the detailed EM models that will be solved in this work, the question then arises as to which differential equation or equations should be used in conjunction with the method. This may, at first, seem obvious since Maxwell's equations in differential form together with their associated constitutive relations could indeed be used [87]. These equations were introduced in Chapter 3 and are reproduced below.

$$\begin{aligned}
&\nabla \cdot \mathbf{D} = \rho \\
&\nabla \times \mathbf{E} = -\frac{\partial \mathbf{B}}{\partial t} \\
&\nabla \cdot \mathbf{B} = 0 \\
&\nabla \times \mathbf{H} = \mathbf{J} + \frac{\partial \mathbf{D}}{\partial t} \\
&\mathbf{D} = \varepsilon \mathbf{E} \\
&\mathbf{B} = \mu \mathbf{H} \\
&\mathbf{J} = \sigma \mathbf{E}
\end{aligned} \tag{4.3}$$

Since Maxwell's equations specify the divergence and curl of the electric and magnetic fields [88] and, according to Helmholtz's Theorem [89], vector fields are determined to within an additive constant if their divergence and curl are specified everywhere, unique solutions can be obtained to EM problems formulated using Maxwell's equations if appropriate boundary and initial conditions are applied to these fields. Suitable boundary conditions are discussed in [90].

Nevertheless, solving systems of multiple coupled equations having several variables can be difficult using the FEM [91], and, over the years, practitioners have derived more convenient formulations from Maxwell's equations. Some of these involve deriving a wave equation from one of Maxwell's curl equations by differentiation and substitution, so that one is left with a single equation in which the only remaining vector quantity is the electric or magnetic field, which is then solved for. The wave equation is sometimes recast into two equations so as to remove the double curl operator that arises in the single equation form. Wave equation formulations are described in [92].

Potential based formulations are also commonly used. These typically begin by using vector identities and substitution to recast one of Maxwell's curl equations into a form where the electric or magnetic field is expressed as equivalent to the sum of two potential functions – one a vector and the other a scalar. For the electric field this would follow the same process as was used to obtain (3.4) in Section 3.3. Then, Maxwell's other curl equation is used together with the constitutive relations and a vector identity to eliminate the fields from the formulation entirely. This is shown in detail later in this section. One is then left with a formulation containing only material properties and the vector and scalar potentials which are then solved for. A commonly used EM FEM formulation is the **A**-V formulation using the magnetic vector and electric scalar potentials. Potential based formulations are explained in [93].

Other types of formulations also exist, for example some require solving for a mixture of field and potential terms. Also, it can be convenient to use different formulations in different regions of a model, and coupling techniques are then required to mathematically join these regions. An example of a formulation involving the magnetic field and a magnetic scalar potential at frequencies similar to those encountered in this work appears in [94], and a good survey of potential based

formulations together with the coupling of formulations in different regions exists in [95], again at frequencies relevant to this work.

Choosing which formulation to use involves considering a number of factors. These include the number of variables that must be solved for, the computer memory and processing demands of the formulation, how easily the formulation can be implemented as computer code, how numerically stable the formulation is, how easy it is to implement boundary and initial conditions, how efficiently any pre or post processing routines related to the input and output from the model can be implemented and how easily the FEM model can be coupled to external lumped element electrical circuit models.

In this work it has been decided to use a potential based formulation most often known as the **T-Ω** method, but also referred to as **T-Φ** so as to avoid confusion with the Ω label commonly used to refer to the spatial domain of a model. Slightly different forms of the formulation will be used in conducting and non-conducting model regions, and careful coupling will be required between them. The formulation will first be described and then the reasons for choosing it given.

The **T-Φ** method was first introduced by Carpenter and Wyatt [96] and was subsequently further elucidated upon by Carpenter [97], Preston and Reece [98][99], and Rodger and Atkinson [100] amongst others. Its original application was in modelling eddy-currents that would be induced in conductive sections in machinery such as generators that operate at fairly low frequencies where the quasi-static approximation to Maxwell's equations, discussed in Chapter 1, apply. These conductive sections would not be primary carriers of current through the machine, so any currents in them would be of the secondary induced eddy type. Derivation of the formulation begins with the quasi-static from of Maxwell's equations together with their associated constitutive relations which are reproduced below:

$$\begin{aligned}
\nabla \times \mathbf{H} &= \mathbf{J} \\
\nabla \times \mathbf{E} &= -\frac{\partial \mathbf{B}}{\partial t} \\
\nabla \cdot \mathbf{B} &= 0 \\
\nabla \cdot \mathbf{D} &= \rho \\
\mathbf{J} &= \sigma \mathbf{E} \\
\mathbf{B} &= \mu \mathbf{H}
\end{aligned} \tag{4.4}$$

Now, the principle of conservation of electric charge is expressed mathematically by the equation of continuity:

$$\nabla \cdot \mathbf{J} = -\frac{\partial \rho}{\partial t} \tag{4.5}$$

However, since, as was discussed in Section 3.2, under quasi-static conditions displacement currents may be omitted from calculations, (4.5) reduces to:

$$\nabla \cdot \mathbf{J} = 0 \tag{4.6}$$

The divergence free nature of **J** means that it can be expressed as the curl of another vector, **T** say, such that:

$$\mathbf{J} = \nabla \times \mathbf{T} \tag{4.7}$$

Substitution of (4.7) into Maxwell's magnetic field curl equation yields:

$$\nabla \times \mathbf{H} = \nabla \times \mathbf{T} \tag{4.8}$$

$$\nabla \times (\mathbf{H} - \mathbf{T}) = \mathbf{0} \tag{4.9}$$

Since a curl-free vector field can be expressed as the gradient of a scalar field, (4.9) implies that it is possible to introduce a scalar quantity, Φ, and say:

$$\mathbf{H} - \mathbf{T} = -\nabla \Phi \tag{4.10}$$

$$\mathbf{H} = \mathbf{T} - \nabla \Phi \tag{4.11}$$

Thus, (4.11) expresses the magnetic field **H** as the sum of two potential functions namely **T**, the electric or current vector potential, and Φ, the magnetic scalar potential [99]. It should be noted that **T** could be chosen to have an arbitrary divergence.

Then, from Maxwell's electric field curl equation, substitution of the constitutive relations yields:

$$\nabla \times \mathbf{E} = -\frac{\partial \mathbf{B}}{\partial t} \tag{4.12}$$

$$\nabla \times \left(\frac{1}{\sigma} \mathbf{J} \right) = -\frac{\partial}{\partial t} \mu \mathbf{H} \tag{4.13}$$

Combining (4.7), (4.11) and (4.13) then yields:

$$\nabla \times \left(\frac{1}{\sigma} \nabla \times \mathbf{T} \right) = -\frac{\partial}{\partial t} \mu \left(\mathbf{T} - \nabla \Phi \right) \tag{4.14}$$

Also, Maxwell's magnetic flux density divergence equation, after substitution of the constitutive relations and (4.11), gives:

$$\nabla \bullet \mathbf{B} = 0 \tag{4.15}$$

$$\nabla \bullet \mu \mathbf{H} = 0 \tag{4.16}$$

$$\nabla \bullet \mu \left(\mathbf{T} - \nabla \Phi \right) = 0 \tag{4.17}$$

Equations (4.14) and (4.17) are the governing equations of the **T**-Φ method, and represent the two equations which are solved simultaneously to give the values of the two unknowns **T** and Φ throughout a problem's domain. It should be noted that in non-conductive regions, where the magnetic field is entirely curl-free and can be represented purely as the gradient of a scalar potential, **T** can be assigned a zero value [101], which means that only a reduced form of (4.17) needs to be solved there:

$$\nabla \bullet \mu \left(-\nabla \Phi \right) = 0 \tag{4.18}$$

Thus, making use of the **T**-Φ method in this form first involves defining one or more conductor geometries which do not carry through current surrounded by a non-conducting zone such as air. A time-changing magnetic field would then be defined around the periphery of the non-conducting zone as values of the magnetic scalar potential. The problem could then be solved as a boundary value problem to obtain the values of Φ and, in the conductors, **T** that would arise within the problem's domain. These values could then be post-processed to obtain other values, for example the induced eddy-current density vectors in the conductors by taking the curl of **T** as in (4.7). Typically the boundary values of Φ would arise from knowledge of the magnetic field due to conductors carrying through current which would be beyond but in the vicinity of the **T**-Φ geometric domain.

Boundary conditions would also need to be defined on the boundaries between the conducting and non-conducting zones within the **T**-Φ domain. These inner boundary conditions follow from the implications of Maxwell's equations with respect to the magnetic field [90] and are that the normal component of $\mu\mathbf{H}$ is continuous across the boundary and that the tangential component of **H** is discontinuous by an amount corresponding to any surface current on the conductor. The first condition would normally be enforced via a particular choice of finite element discretisation. To understand the second condition, one must first appreciate that surface currents can only exist on ideal perfect conductors or superconductors [102], and that, for almost all physical media, the tangential component of **H** would be continuous across the conductor's surface. In the **T**-Φ method this continuity would be ensured by choosing a finite element discretisation such that $-\nabla\Phi$ was tangentially continuous and by forcing the tangential component of **T** to be zero at the conductor surface since **T** would be zero in the non-conducting zone. Finite element discretisation will be discussed in the next section.

The main advantage of the **T**-Φ method is that it has been shown to be computationally very efficient whilst maintaining a high level of accuracy [103]. This computational efficiency arises chiefly because only the magnetic scalar potential must be solved for and stored in computer memory for non-conducting regions rather than a multi-component vector quantity, as would be the case with a field based formulation or the **A**-V potential based formulation referred to earlier. A comparison

of the accuracies and efficiencies of various formulations suited to eddy-current analysis appears in [103].

The comparative efficiency of the **T**-Φ method led researchers to investigate whether it could be extended from a method which allows one to model the secondary currents induced in conductors due to external magnetic fields, to a method that can additionally model the secondary currents that would arise in conductors due to one or more of them carrying prescribed amounts of primary through current. This would, for example, allow one to model the skin and proximity effects that arise in current carrying conductors that were discussed in Section 1.4. The main difficulty in extending the method is that having to enforce the tangential component of **T** to be zero at the conductor surfaces also has the effect of enforcing the net through current in the conductor to be zero [104]. Several techniques were initially suggested to circumvent this problem such as those in [105] and [106], but these were problematic to implement. A much more successful approach was later developed, and this was proposed, seemingly independently, by Nakata et al [107] and Biro et al [104].

The approach of Nakata et al and Biro et al is to split **T** into two components:

$$\mathbf{T} = \mathbf{T}_s + \mathbf{T}_e \tag{4.19}$$

such that:

$$\mathbf{H} = \mathbf{T}_s + \mathbf{T}_e - \nabla\Phi \tag{4.20}$$

$\mathbf{T}_s$ is effectively the input to the model, is defined across the whole of the model's spatial domain, must be calculated before starting to solve the model, and is a magnetic field pattern that 'could' arise due to the conductors carrying the prescribed amount of through current at some randomly chosen frequency. This is normally chosen to be the magnetic field due to the conductors carrying the prescribed current as direct current since this is relatively inexpensive to calculate. The problem then becomes one of solving for $\mathbf{T}_e - \nabla\Phi$ which, given the boundary conditions described below, is effectively a corrective magnetic field representing the difference between the $\mathbf{T}_s$ magnetic field and the magnetic field that would arise with the conductors

carrying the prescribed through current and associated induced secondary currents at the true frequency of operation. The final 'true' magnetic field is then obtained by summing all components as in (4.20) and may be post-processed as required to obtain quantities such as the current distribution across the conductor cross-sections.

The above approach has the advantage that it retains the main strength of the original **T**-Φ method in that only the scalar Φ must be solved for in non-conducting regions and $\mathbf{T}_e$ is confined to regions where the **H** field can have curl – i.e. the conductors. The tangential component of $\mathbf{T}_e$ can safely be set to zero on conductor surfaces since that merely imposes the condition that the total of the distribution correcting currents and induced secondary currents at the true frequency of operation through a conductor are zero; it is $\mathbf{T}_s$ that imposes how large the total through current is.

The governing equations of this revised form of the **T**-Φ method are in conducting regions:

$$\nabla \times \left(\frac{1}{\sigma} \nabla \times \left(\mathbf{T}_s + \mathbf{T}_e \right) \right) = -\frac{\partial}{\partial t} \mu \left(\mathbf{T}_s + \mathbf{T}_e - \nabla \Phi \right) \tag{4.21}$$

and

$$\frac{\partial}{\partial t} \nabla \cdot \mu \left(\mathbf{T}_s + \mathbf{T}_e - \nabla \Phi \right) = 0 \tag{4.22}$$

and in non-conducting regions:

$$\frac{\partial}{\partial t} \nabla \cdot \mu \left(\mathbf{T}_s - \nabla \Phi \right) = 0 \tag{4.23}$$

These governing equations arise from substituting (4.19) into (4.14) and (4.17) taking into account that $\mathbf{T}_e$ only exists in conductors. A slight difference between the revised **T**-Φ method and its original form is the taking of time derivatives in (4.22) and(4.23). This is done to maintain the symmetry of the eventual discretised finite element equation system given that the time derivative of $\mathbf{T}_s$ appears by necessity in (4.21) [108].

The boundary conditions in this formulation are:

$$\frac{1}{\sigma}(\nabla \times \mathbf{T}_e) \times \mathbf{n} = \mathbf{0} \qquad \text{on } \Gamma_E \tag{4.24}$$

$$\mu(\mathbf{T}_s + \mathbf{T}_e - \nabla\Phi)\cdot\mathbf{n} = 0 \qquad \text{on } \Gamma_E \tag{4.25}$$

$$\mathbf{T}_e \times \mathbf{n} = \mathbf{0} \qquad \text{on } \Gamma_{cn} \tag{4.26}$$

$$\Phi = 0 \quad \text{on } \partial(\Omega_c + \Omega_n) \tag{4.27}$$

$$\Phi \text{ and } \mu(\mathbf{T}_s - \nabla\Phi)\cdot\mathbf{n} \text{ are continuous on } \Gamma_{cn} \tag{4.28}$$

where $\mathbf{n}$ is an outwardly directed unit vector normal to a conductors surface at any point, Γ_E are the end faces of conductors where through current enters or exits, Γ_{cn} are the surfaces of conductors (where the conductive material meets the surrounding non-conductive material), and $\partial(\Omega_c + \Omega_n)$ is the far outer boundary of the space included in the model.

(4.24) is required so as to impose the condition that there are no surface secondary currents on the end faces of the conductors (a similar condition for the through current will have been imposed when calculating $\mathbf{T}_s$). (4.25) ensures that the normal component of $\mu\mathbf{H}$ is continuous on the conductor end faces. (4.26) ensures that $\mathbf{H}$ is tangentially continuous across conductor/non-conductors boundaries since $\mathbf{T}_e$ is zero in non-conductors, $\mathbf{T}_s$ is tangentially continuous by prior calculation, and $-\nabla\Phi$ is ensured to be tangentially continuous by selection of the finite element discretisation. (4.27) is a Dirichlet boundary condition [109] that ensures that the model is physically realistic by setting the magnetic scalar potential to zero at the outer far boundary of the model. (4.28) ensures that the normal component of $\mu\mathbf{H}$ is continuous across conductor/non-conductors boundaries given that $\mathbf{T}_e$ is zero in non-conductors.

These boundary conditions serve to ensure that any solution obtained from using the $\mathbf{T}$-Φ formulation is physically realistic by ensuring the uniqueness of the magnetic field which can be obtained using the potentials involved in the method from (4.20). To ensure the numerical stability of the method it is also necessary to ensure that the

potentials themselves are unique. The uniqueness of the scalar potential in the **T-Φ** method is ensured up to a constant value, so long as the magnetic field is unique [110] – the constant value is fixed by virtue of the boundary condition (4.27). However, although the curls of $\mathbf{T}_s$ and $\mathbf{T}_e$ are fixed by virtue of (4.19) and (4.7), their divergences are not, and they are therefore not uniquely defined. To remedy this, any divergence can be chosen at will without affecting the physical problem in a process known as gauging [110]. Several gauging methods exist for vector potentials including the Coulomb, Lorentz and Diffusion gauges [111]. In this work it will prove most convenient to partly implement the Coulomb gauge, namely:

$$\nabla \cdot \mathbf{T}_e = 0 \tag{4.29}$$

since the finite element discretisation chosen for $\mathbf{T}_e$ can be made intrinsically divergence-free within elements. However it should be noted that this discretisation will not enforce the divergence-free condition between elements. $\mathbf{T}_s$ will be divergence free by calculation.

The main advantage of the **T-Φ** formulation, namely its computational efficiency, has already been discussed. Another advantage of the method is that it allows one to define the through primary current in conductors as the starting point for calculating $\mathbf{T}_s$. This means that the input to the method can be thought of as the through current, which makes it relatively easy to couple FEM models that use this formulation to external lumped parameter electrical circuit models in terms of the current. This will prove useful when coupling FEM coil models to stimulating machine circuit models in this work – the coupling is discussed in the next chapter. It would also prove useful if the FEM models were used to investigate the effects of sending different current pulse shapes through coils, although that study will not be undertaken in this work. Due to these advantages it has been decided to use the **T-Φ** formulation as the basis of the FEM models in this work.

4.4 The Choice of FEM Basis Functions

In Section 4.2.3 it was explained that basis functions must be defined on an FEM mesh and are used to construct the approximate solution across the mesh to the function being computed as summarised in (4.1). Normally, basis functions are associated with the nodes of elements and are typically low order polynomial functions, often linear functions. For example, for a two dimensional mesh, elements will usually be chosen to be triangular or quadrilateral, and triangular elements would have linear basis functions like those in Figure 4.1.

It will be seen that the nodes have numbers which are local to the element and local x-y and ξ-η coordinate systems are defined within the element whose relationship is defined in [112]. The basis functions are then defined in terms of ξ and η as:

$$\begin{aligned} N_1 &= 1-\xi-\eta \\ N_2 &= \xi \\ N_3 &= \eta \end{aligned} \tag{4.30}$$

Across the whole element:

$$N_1 + N_2 + N_3 = 1 \tag{4.31}$$

Thus each node, *i*, of the element has an associated basis function, N_i, which is unity valued at node *i* and zero at the other two nodes. The global basis function associated with node *i* , for use in (4.1), is obtained by the summation of the local basis functions associated with that node in adjacent elements. Clearly, care has to be taken within the computer program implementing the FEM to correctly convert the local node numbers from each element to global numbers for use in (4.1).

Nodal basis functions are successful when the function being computed is a scalar one, and have also been used successfully to approximate vector functions by representing each vector component as a separate scalar function with (4.1) being implemented for each component. Nevertheless, it can be advantageous to solve for

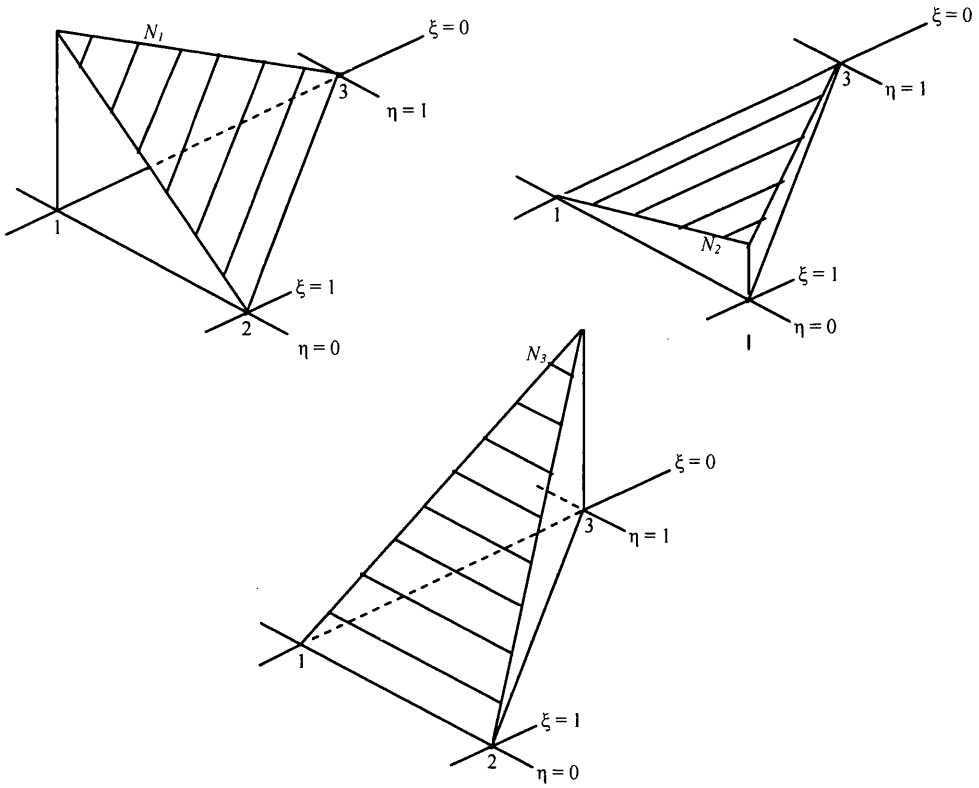

Figure 4.1 - Nodal basis functions for use with triangular elements in two dimensional meshes

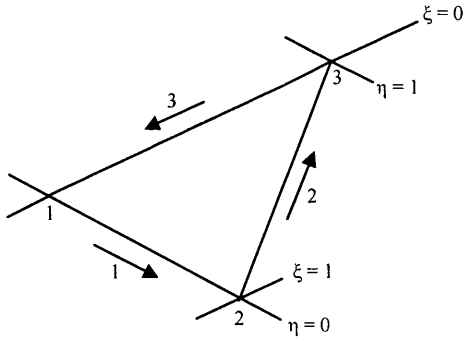

Figure 4.2 - Triangular finite element showing ξ-η coordinate system and edge numbers next to arrows

vector functions in FEM problems using special vector, or edge, basis functions. When speaking of finite elements in relation to edge basis functions, they are termed edge elements.

Edge elements were first suggested by Whitney [113] and have seen a slow rise in use by the engineering community since the late 1970's, particularly after the publication of Nedelec's paper [114]. Rather than being scalar, each edge basis function within an element is itself a vector which, at the edge with which it is associated, is at its maximum magnitude and has a direction tangent to that edge. That basis vector's magnitude decreases as one moves away from its associated edge, and, depending on the element shape, its direction may also change. Illustrations of edge element basis function magnitude and direction changes are given for square and triangular elements in [115] and [116]. The magnitude of an edge vector basis function is such that the tangent line integral along its associated edge has unity value.

A vector function's value within an element can be approximated using edge basis functions as:

$$\mathbf{f}(\mathbf{x}) \approx \sum_{i=1}^{n} f_i \mathbf{N}_i(\mathbf{x}) \tag{4.32}$$

where n is the number of edges in the element, $\mathbf{N}_i$ are the edge based vector basis functions and f_i are the coefficients associated with each edge that are eventually solved for. It should be noted that the coefficients themselves are scalar quantities.

In extending (4.32) to the global representation of a vector function, n becomes the number of edges in the whole mesh. The global vector basis function for an edge is obtained by the summation of the local basis functions associated with that edge in adjacent elements.

With reference to Figure 4.1, Figure 4.2 and the linear nodal basis functions described above, a set of first order linear edge basis functions for a triangular element in a two dimensional mesh can be defined as follows:

$$\begin{aligned} \mathbf{N}_1 &= N_1\nabla N_2 - N_2\nabla N_1 \\ \mathbf{N}_2 &= N_2\nabla N_3 - N_3\nabla N_2 \\ \mathbf{N}_3 &= N_3\nabla N_1 - N_1\nabla N_3 \end{aligned} \tag{4.33}$$

There are several advantages in using edge elements when solving for a vector function in an FEM model. These are discussed in the points below.

As can be seen in (4.32), only a single scalar coefficient needs to be solved for each edge in the simultaneous equation system that arises as part of the FEM solution process. When using nodal elements to solve for a vector function, coefficients for each component of the vector must be solved for at each node. Edge elements therefore have an intrinsic computational performance and storage advantage in this scenario.

By virtue of the fact that an edge scalar coefficient is shared by the basis functions in neighbouring elements that meet at a common edge, and that the tangent line integrals of the basis function vectors along that edge are equal, tangential continuity of the vector function being calculated is naturally ensured from element to element. This is advantageous when the vector function is known to be physically continuous in this way. The **T** vectors in the **T**-Φ method described in the previous section exhibit natural tangential continuity since they are components of the magnetic field vector **H**.

Edge elements do not, however, enforce normal continuity of the vector function being calculated [95], which is advantageous when working with a vector quantity that naturally behaves in that way. The **T** vectors in the **T**-Φ method do not necessarily exhibit normal continuity since they are components of **H**, and it is μ**H** which is normally continuous [90] – **H** is therefore normally discontinuous when the permeability, μ, of a material changes.

Using nodal elements to represent vector functions unnaturally enforces normal continuity of the vector function, and this causes problems when the function is a vector potential, such as **T**, and a sharp corner must be modelled. The normal continuity causes the curl of the potential, the current density **J** in the case of **T**, to take on an unnatural zero value at the corner [95]. This problem is avoided with edge elements.

The edge elements described above are naturally divergence free within elements. This is useful because it allows the Coulomb gauge condition discussed in the previous section to be naturally partly implemented without further amendments to a formulation. It can also deal with the problem of spurious non-physical solutions which can occur because of inadequacies in the implementation of the Coulomb gauge when using nodal elements to represent vector functions [117]. It could be noted though that the use of nodal elements does not necessarily in of itself imply a lack of gauge : a weak gauge can be implied in some cases when the time derivative term in a formulation is non-zero. However when the time derivative term is zero, an external gauge can also be imposed.

Because of the advantages of edge elements, they will be used to form the approximation to $\mathbf{T}_c$ in the **T**-Φ method FEM models of this work. Section 4.6 will explain why it will be useful to also express the input function $\mathbf{T}_s$ in terms of edge basis functions. The magnetic scalar potential, Φ, will be approximated using nodal basis functions.

4.5 T-Φ Method Galerkin Equations

In Section 4.2.3 it was explained that, when solving an FEM model using the system of weighted residuals, a set of weighting functions must be defined and these then multiplied against the main formulation before being integrated across the problem's spatial domain as in (4.2). This section aims to develop the integral equations equivalent to (4.2) for the **T**-Φ formulation to be used in this work. The Galerkin

method of choosing weighting functions to be the same as basis functions will be used, and the integral equations are therefore known as Galerkin equations. The same notation for the problem's boundaries as was given after (4.28) in Section 4.3 will be used together with Ω_c and Ω_n to represent the conducting and non-conducting regions respectively.

For governing equation (4.21), which will only be used in conductors, the weighting functions will be the set of edge element basis functions $\mathbf{w}_i$ where $i = 1$ to n_e, and n_e is the number of edges whose unknown coefficients must be calculated. This then leads to:

$$\nabla \times \left(\frac{1}{\sigma} \nabla \times \left(\mathbf{T}_s + \mathbf{T}_e \right) \right) = -\frac{\partial}{\partial t} \mu \left(\mathbf{T}_s + \mathbf{T}_e - \nabla \Phi \right) \tag{4.34}$$

$$\int_{\Omega_c} \left[\nabla \times \left(\frac{1}{\sigma} \nabla \times \left(\mathbf{T}_s + \mathbf{T}_e \right) \right) + \frac{\partial}{\partial t} \mu \left(\mathbf{T}_s + \mathbf{T}_e - \nabla \Phi \right) \right] \bullet \mathbf{w}_i d\Omega = 0 \tag{4.35}$$

$$\int_{\Omega_c} \nabla \times \left(\frac{1}{\sigma} \nabla \times \left(\mathbf{T}_s + \mathbf{T}_e \right) \right) \bullet \mathbf{w}_i d\Omega + \int_{\Omega_c} \frac{\partial}{\partial t} \mu \left(\mathbf{T}_s + \mathbf{T}_e - \nabla \Phi \right) \bullet \mathbf{w}_i d\Omega = 0 \tag{4.36}$$

Then, using the vector identity:

$$\nabla \times \mathbf{A} \bullet \mathbf{B} = \mathbf{A} \bullet \nabla \times \mathbf{B} - \nabla \bullet \left(\mathbf{B} \times \mathbf{A} \right) \tag{4.37}$$

(4.36) becomes:

$$\begin{aligned} &\int_{\Omega_c} \left(\frac{1}{\sigma} \nabla \times \left(\mathbf{T}_s + \mathbf{T}_e \right) \right) \bullet \left(\nabla \times \mathbf{w}_i \right) d\Omega - \int_{\Omega_c} \nabla \bullet \left(\mathbf{w}_i \times \frac{1}{\sigma} \nabla \times \left(\mathbf{T}_s + \mathbf{T}_e \right) \right) d\Omega \\ &+ \int_{\Omega_c} \frac{\partial}{\partial t} \mu \left(\mathbf{T}_s + \mathbf{T}_e - \nabla \Phi \right) \bullet \mathbf{w}_i d\Omega = 0 \end{aligned} \tag{4.38}$$

Using the divergence theorem [118], (4.38) becomes:

$$\int_{\Omega_c}\left(\frac{1}{\sigma}\nabla\times\left(\mathbf{T}_s+\mathbf{T}_e\right)\right)\bullet\left(\nabla\times\mathbf{w}_i\right)d\Omega-\int_{\Gamma_{cn}}\mathbf{n}\bullet\left(\mathbf{w}_i\times\frac{1}{\sigma}\nabla\times\left(\mathbf{T}_s+\mathbf{T}_e\right)\right)d\Gamma$$
$$+\int_{\Omega_c}\frac{\partial}{\partial t}\mu\left(\mathbf{T}_s+\mathbf{T}_e-\nabla\Phi\right)\bullet\mathbf{w}_i d\Omega=0 \tag{4.39}$$

where **n** is an unit vector outward normal at any point on a conductor's surface. However, from the discussion in Section 4.3, it is known that no surface currents can exist on a conductor's surface, and therefore $\nabla\times\left(\mathbf{T}_s+\mathbf{T}_e\right)$ must always be zero on Γ_{cn}. The second integral in (4.39) also must always be zero. The Galerkin equation for this governing equation is therefore:

$$\int_{\Omega_c}\left(\frac{1}{\sigma}\nabla\times\left(\mathbf{T}_s+\mathbf{T}_e\right)\right)\bullet\left(\nabla\times\mathbf{w}_i\right)d\Omega+\int_{\Omega_c}\frac{\partial}{\partial t}\mu\left(\mathbf{T}_s+\mathbf{T}_e-\nabla\Phi\right)\bullet\mathbf{w}_i d\Omega=0 \tag{4.40}$$

For governing equation (4.22), which also will only be used in conductors, the weighting functions will be the set of nodal element basis functions w_i where i = 1 to n_n, and n_n is the number of nodes whose unknown coefficients must be calculated. This then leads to:

$$\frac{\partial}{\partial t}\nabla\bullet\mu\left(\mathbf{T}_s+\mathbf{T}_e-\nabla\Phi\right)=0 \tag{4.41}$$

$$\int_{\Omega_c}\frac{\partial}{\partial t}w_i\nabla\bullet\mu\left(\mathbf{T}_s+\mathbf{T}_e-\nabla\Phi\right)d\Omega=0 \tag{4.42}$$

However, there exists a vector identity:

$$\nabla\bullet\left(f\mathbf{v}\right)=\left(\nabla f\right)\bullet\mathbf{v}+f\left(\nabla\bullet\mathbf{v}\right) \tag{4.43}$$

$$f\left(\nabla\bullet\mathbf{v}\right)=\nabla\bullet\left(f\mathbf{v}\right)-\left(\nabla f\right)\bullet\mathbf{v} \tag{4.44}$$

This identity means that (4.42) can be expressed:

$$\int_{\Omega_c} \nabla \bullet \frac{\partial}{\partial t} w_i \mu \left(\mathbf{T}_s + \mathbf{T}_e - \nabla \Phi \right) d\Omega - \int_{\Omega_c} \nabla \frac{\partial}{\partial t} w_i \bullet \mu \left(\mathbf{T}_s + \mathbf{T}_e - \nabla \Phi \right) d\Omega = 0 \qquad (4.45)$$

Applying the divergence theorem to the first integral in (4.45) leads to:

$$\int_{\Gamma_{cn}} \mathbf{n} \bullet \frac{\partial}{\partial t} w_i \mu \left(\mathbf{T}_s + \mathbf{T}_e - \nabla \Phi \right) d\Gamma - \int_{\Omega_c} \nabla \frac{\partial}{\partial t} w_i \bullet \mu \left(\mathbf{T}_s + \mathbf{T}_e - \nabla \Phi \right) d\Omega = 0 \qquad (4.46)$$

where **n** is an unit vector outward normal at any point on a conductor's surface. (4.46) is the Galerkin equation for governing equation (4.22).

For governing equation (4.23), which will only be used in the non-conducting region, the weighting functions will be the set of nodal element basis functions w_i where i = 1 to n_n, and n_n is the number of nodes whose unknown coefficients must be calculated. This leads to:

$$\frac{\partial}{\partial t} \nabla \bullet \mu \left(\mathbf{T}_s - \nabla \Phi \right) = 0 \qquad (4.47)$$

$$\int_{\Omega_n} \frac{\partial}{\partial t} w_i \nabla \bullet \mu \left(\mathbf{T}_s - \nabla \Phi \right) d\Omega = 0 \qquad (4.48)$$

Application of identity (4.44) then leads to:

$$\int_{\Omega_n} \nabla \bullet \frac{\partial}{\partial t} w_i \mu \left(\mathbf{T}_s - \nabla \Phi \right) d\Omega - \int_{\Omega_n} \nabla \frac{\partial}{\partial t} w_i \bullet \mu \left(\mathbf{T}_s - \nabla \Phi \right) d\Omega = 0 \qquad (4.49)$$

Since the non-conducting region has boundaries with conductors and a far outer boundary where the model's spatial domain ends, applying the divergence theorem to the first integral in (4.49) yields:

$$\begin{aligned} &\int_{\Gamma_{cn}} \mathbf{n} \bullet \frac{\partial}{\partial t} w_i \mu \left(\mathbf{T}_s - \nabla \Phi \right) d\Gamma + \int_{\partial(\Omega_c + \Omega_n)} \mathbf{n} \bullet \frac{\partial}{\partial t} w_i \mu \left(\mathbf{T}_s - \nabla \Phi \right) d\Gamma \\ &- \int_{\Omega_n} \nabla \frac{\partial}{\partial t} w_i \bullet \mu \left(\mathbf{T}_s - \nabla \Phi \right) d\Omega = 0 \end{aligned} \qquad (4.50)$$

where **n** are unit vectors outward normal at any point on the non-conducting region's boundary – i.e. the conductor/non-conductor surfaces in the first integral and the far outer boundary in the second integral. (4.50) is the Galerkin equation for governing equation (4.23).

Consider now the boundary condition (4.27). If Φ is set to zero at all nodes along $\partial(\Omega_c+\Omega_n)$, then, since each w_i associated with nodes other than those on $\partial(\Omega_c+\Omega_n)$ are zero on $\partial(\Omega_c+\Omega_n)$, any integral of $\frac{\partial}{\partial t}w_i\mu(-\nabla\Phi)$ along $\partial(\Omega_c+\Omega_n)$ will also be zero. If, as will be shown in Section 4.8, $\mathbf{T}_s$ is chosen to be zero along $\partial(\Omega_c+\Omega_n)$, then any integral of $\frac{\partial}{\partial t}w_i\mu(\mathbf{T}_s)$ will be zero. Therefore, in this situation, it is possible to omit the second integral from (4.50).

Further, consider the second term in boundary condition (4.28). Given that the unit normal vectors along Γ_{cn} in the first integrals in (4.46) and (4.50) are exactly opposite in direction, and that $\mathbf{T}_e$ is zero in the non-conducting region, then the boundary condition will be fulfilled in an average sense around the whole boundary if those integrals are equal in magnitude. (Summing (4.46) and (4.50) would lead to the contribution from those integrals cancelling owing to the opposing directions of the normal vectors.) Therefore, if those integrals are omitted from (4.46) and (4.50), then the boundary condition becomes naturally enforced.

By following a similar line of reasoning it is possible to see that by virtue of the absence of normal component line integrals around the perimeter of the finite elements within the regions covered by (4.46) and (4.50), the continuities of the normal components of $\mu(\mathbf{T}_s+\mathbf{T}_e-\nabla\Phi)$ and $\mu(\mathbf{T}_s-\nabla\Phi)$ respectively are ensured from element to element – this ensures inter-element continuity of the normal component of $\mu\mathbf{H}$. Inter-element continuity of the tangential component of **H** is, for the **T** components, ensured by the natural tangential continuity of edge elements discussed in the previous section, and, for the $-\nabla\Phi$ component by the fact that, so long as a potential is continuous, then nodal elements will ensure that the associated

field quantity is tangentially continuous [119]. The continuity of the potential Φ can be ensured by choosing nodal elements with linear basis functions such as those described in the previous section [120][121].

Finally, the revised forms of the Galerkin equations (4.46) and (4.50) are therefore:

$$-\int_{\Omega_c} \nabla \frac{\partial}{\partial t} w_i \bullet \mu \left(\mathbf{T}_s + \mathbf{T}_e - \nabla \Phi \right) d\Omega = 0 \tag{4.51}$$

and

$$-\int_{\Omega_n} \nabla \frac{\partial}{\partial t} w_i \bullet \mu \left(\mathbf{T}_s - \nabla \Phi \right) d\Omega = 0 \tag{4.52}$$

4.6 Obtaining $\mathbf{T}_s$

A feature of edge elements is that the curls of the edge basis functions are not linearly independent even though the basis functions themselves are [95]. This means that in this work, when solving the **T**-Φ formulation using the elements and equations described in the previous sections, a singular finite element curl-curl matrix would occur due to the first integral in Galerkin equation (4.40) when the final system of FEM equations is written. It could be noted that a singular equation system could be avoided if the Coulomb gauge was imposed between elements in addition to the natural divergence free nature of the edge elements to be used in this work. This could be done by using a tree-cotree gauging method such as that used in [210]. In this work such a gauging method will not be adopted and the singular equation system will be solved using an iterative rather than a direct Gaussian method. Some of the issues resulting from this decision will be reported on. Such an iterative solution would only be possible if the right-hand side of the equation system were consistent. The right-hand side will be formed, as shown in the next section, by transferring the $\mathbf{T}_s$ terms across. Consistency can be assured if the same linear interdependence exists between the right hand sides of the FEM equations as the left hand sides [95]. One way of

achieving this is if the input function $\mathbf{T}_s$ is expressed in terms of the same edge basis functions as $\mathbf{T}_e$, that is:

$$\mathbf{T}_s \approx \sum_{i=1}^{n_e} T_{si} \mathbf{N}_i \tag{4.53}$$

This means that before starting to solve a problem using the **T-Φ** formulation and edge elements, $\mathbf{T}_s$ must first be calculated and converted into the form of (4.53).

Biro et al [122] discuss a way of effecting this conversion. Remembering that $\mathbf{T}_s$ is a magnetic field pattern that 'could' arise due to the conductors carrying the prescribed amount of through current at some frequency, an arbitrary infinitesimally thin wire (like the thin wire discussed in the previous chapter) is defined to run somewhere within each conductor along its length, carrying the prescribed amount of through current. In the non-conducting region, the magnetic fields due to each wire are calculated using the Biot-Savart Law [123] and summed to give the total magnetic field. The coefficients T_{si} for (4.53) are then calculated as the line integral of the component of the magnetic field tangential to each edge.

In the conductors, the magnetic field that would arise within them due to the prescribed amount of through current being carried as direct current is calculated. This is a simple boundary value problem, with the magnetic field on the edges making up the conductor/non-conductor boundaries having already been calculated using the method described in the last paragraph. A small FEM boundary problem is then solved using only edge elements to represent $\mathbf{T}_s$ to obtain the coefficients T_{si} on each edge within the conductors. This may be solved using either a direct Gaussian or iterative method. The formulation, using previously defined notation, is simply:

$$\nabla \times \left(\frac{1}{\sigma} \nabla \times \mathbf{T}_s \right) = 0 \qquad \text{in } \Omega_c \tag{4.54}$$

$$\mathbf{T}_s \times \mathbf{n} \quad \text{as defined on } \Gamma_{cn} \tag{4.55}$$

$$\frac{1}{\sigma}\nabla\times\mathbf{T}_s\times\mathbf{n}=0 \qquad \text{on } \Gamma_E \tag{4.56}$$

Clearly, having to solve this smaller FEM problem to obtain the input function $\mathbf{T}_s$ for the main **T-Φ** formulation FEM problem adds to the overall solution time. Nevertheless, when solving the main problem by time-stepping in the time domain, the input function must only be calculated at the beginning, and adds little to the overall solution time. When solving the main problem in the frequency domain, the situation is not quite so clear cut. Then, so long as most of the problem's space is composed of non-conducting material (as is often the case), the efficiency advantage of the **T-Φ** formulation over others means that the penalty incurred by having to initially solve for $\mathbf{T}_s$ is not prohibitive. The method outlined in this section will be used to obtain $\mathbf{T}_s$ for the FEM models solved in this work.

4.7 The FEM Equation System in the Frequency Domain

Now that the Galerkin equations and the method of representing $\mathbf{T}_s$ have been established, it is possible to express the actual equation system that will be solved in the **T-Φ** formulation FEM models of this work. Starting with the first governing equation (4.40) and with weighting functions where j = 1 to n_e,

$$\int_{\Omega_c}\left(\frac{1}{\sigma}\nabla\times\left(\mathbf{T}_s+\mathbf{T}_e\right)\right)\bullet\left(\nabla\times\mathbf{w}_j\right)d\Omega+\int_{\Omega_c}\frac{\partial}{\partial t}\mu\left(\mathbf{T}_s+\mathbf{T}_e-\nabla\Phi\right)\bullet\mathbf{w}_j d\Omega=0 \tag{4.57}$$

As will be discussed in Section 4.9, the models presented in this chapter will be solved in the frequency domain and, therefore, (4.57) becomes:

$$\int_{\Omega_c}\left(\frac{1}{\sigma}\nabla\times\left(\mathbf{T}_s+\mathbf{T}_e\right)\right)\bullet\left(\nabla\times\mathbf{w}_j\right)d\Omega+\int_{\Omega_c}j\omega\mu\left(\mathbf{T}_s+\mathbf{T}_e-\nabla\Phi\right)\bullet\mathbf{w}_j d\Omega=0 \tag{4.58}$$

$$\int_{\Omega_c}\left[\left(\frac{1}{\sigma}\nabla\times\mathbf{T}_e\right)\bullet\left(\nabla\times\mathbf{w}_j\right)+j\omega\mu\mathbf{T}_e\bullet\mathbf{w}_j\right]d\Omega+\int_{\Omega_c}\left[j\omega\mu\left(-\nabla\Phi\right)\bullet\mathbf{w}_j\right]d\Omega=$$
$$-\int_{\Omega_c}\left[\left(\frac{1}{\sigma}\nabla\times\mathbf{T}_s\right)\bullet\left(\nabla\times\mathbf{w}_j\right)+j\omega\mu\mathbf{T}_s\bullet\mathbf{w}_j\right]d\Omega \tag{4.59}$$

By representing $\mathbf{T}_s$, $\mathbf{T}_e$ and Φ in terms of the relevant basis functions discussed in Section 4.4 and the weighting functions using the edge vector functions discussed in that section, (4.59) then becomes:

$$\int_{\Omega_c}\left[\left(\frac{1}{\sigma}\nabla\times\sum_{i=1}^{n_e}T_{ei}\mathbf{N}_i\right)\bullet\left(\nabla\times\mathbf{N}_j\right)+j\omega\mu\left(\sum_{i=1}^{n_e}T_{ei}\mathbf{N}_i\right)\bullet\mathbf{N}_j\right]d\Omega$$
$$-\int_{\Omega_c}j\omega\mu\left(\nabla\sum_{i=1}^{n_n}\Phi_i N_i\right)\bullet\mathbf{N}_j d\Omega= \tag{4.60}$$
$$-\int_{\Omega_c}\left[\left(\frac{1}{\sigma}\nabla\times\sum_{i=1}^{n_e}T_{si}\mathbf{N}_i\right)\bullet\left(\nabla\times\mathbf{N}_j\right)+j\omega\mu\left(\sum_{i=1}^{n_e}T_{si}\mathbf{N}_i\right)\bullet\mathbf{N}_j\right]d\Omega$$

Owing to the linearity of the curl operator, (4.60) can be rearranged as:

$$\sum_{i=1}^{n_e}\left\{T_{ei}\int_{\Omega_c}\left[\left(\frac{1}{\sigma}\nabla\times\mathbf{N}_i\right)\bullet\left(\nabla\times\mathbf{N}_j\right)+j\omega\mu\mathbf{N}_i\bullet\mathbf{N}_j\right]d\Omega\right\}$$
$$-\sum_{i=1}^{n_n}\left\{\Phi_i\int_{\Omega_c}j\omega\mu\left(\nabla N_i\right)\bullet\mathbf{N}_j d\Omega\right\}= \tag{4.61}$$
$$-\sum_{i=1}^{n_e}\left\{T_{si}\int_{\Omega_c}\left[\left(\frac{1}{\sigma}\nabla\times\mathbf{N}_i\right)\bullet\left(\nabla\times\mathbf{N}_j\right)+j\omega\mu\mathbf{N}_i\bullet\mathbf{N}_j\right]d\Omega\right\}$$

The second governing equation (4.51) with weighting functions where j = 1 to n_n is:

$$-\int_{\Omega_c}\nabla\frac{\partial}{\partial t}w_j\bullet\mu\left(\mathbf{T}_s+\mathbf{T}_e-\nabla\Phi\right)d\Omega=0 \tag{4.62}$$

which in the frequency domain becomes:

$$-\int_{\Omega_c} \nabla j\omega w_j \bullet \mu\left(\mathbf{T_s} + \mathbf{T_e} - \nabla\Phi\right) d\Omega = 0 \tag{4.63}$$

$$-\int_{\Omega_c} \nabla j\omega w_j \bullet \mu \mathbf{T_e} d\Omega - \int_{\Omega_c} \nabla j\omega w_j \bullet \mu\left(-\nabla\Phi\right) d\Omega = \int_{\Omega_c} \nabla j\omega w_j \bullet \mu \mathbf{T_s} d\Omega \tag{4.64}$$

By again representing $\mathbf{T_s}$, $\mathbf{T}_e$ and Φ in terms of the relevant basis functions and using the nodal weighting functions discussed in Section 4.4, (4.64) then becomes:

$$\begin{aligned} &-\int_{\Omega_c} \nabla j\omega N_j \bullet \mu \sum_{i=1}^{n_e} T_{ei} \mathbf{N_i} d\Omega + \int_{\Omega_c} \nabla j\omega N_j \bullet \mu\left(\nabla \sum_{i=1}^{n_n} \Phi_i N_i\right) d\Omega = \\ &\int_{\Omega_c} \nabla j\omega N_j \bullet \mu \sum_{i=1}^{n_e} T_{si} \mathbf{N_i} d\Omega \end{aligned} \tag{4.65}$$

Due to the linearity of the gradient operator, (4.65) may be rearranged as:

$$\begin{aligned} &-\sum_{i=1}^{n_e}\left\{T_{ei}\int_{\Omega_c} j\omega\mu \mathbf{N_i} \bullet \nabla N_j d\Omega\right\} + \sum_{i=1}^{n_n}\left\{\Phi_i \int_{\Omega_c} j\omega\mu \nabla N_i \bullet \nabla N_j d\Omega\right\} = \\ &\sum_{i=1}^{n_e}\left\{T_{si}\int_{\Omega_c} j\omega\mu \mathbf{N_i} \bullet \nabla N_j d\Omega\right\} \end{aligned} \tag{4.66}$$

The derivation process for the third governing equation (4.52) is similar to that for the second and

$$-\int_{\Omega_n} \nabla \frac{\partial}{\partial t} w_j \bullet \mu\left(\mathbf{T_s} - \nabla\Phi\right) d\Omega = 0 \tag{4.67}$$

becomes:

$$\sum_{i=1}^{n_n}\left\{\Phi_i \int_{\Omega_n} j\omega\mu \nabla N_i \bullet \nabla N_j d\Omega\right\} = \sum_{i=1}^{n_e}\left\{T_{si}\int_{\Omega_n} j\omega\mu \mathbf{N_i} \bullet \nabla N_j d\Omega\right\} \tag{4.68}$$

Thus (4.61), (4.66) and (4.68) together represent the system of equations that will be solved in the frequency domain FEM models of this work. These may be represented in matrix form as:

$$\begin{bmatrix} \mathbf{A} & \mathbf{B} \\ \mathbf{B}^{\mathbf{T}} & \mathbf{C} \end{bmatrix} \begin{bmatrix} \mathbf{E} \\ \mathbf{\Phi} \end{bmatrix} = \begin{bmatrix} \mathbf{S}_1 \\ \mathbf{S}_2 \end{bmatrix} \tag{4.69}$$

$$A_{ij} = \int_{\Omega_c} \left[\left(\frac{1}{\sigma} \nabla \times \mathbf{N}_i \right) \bullet \left(\nabla \times \mathbf{N}_j \right) + j\omega\mu \mathbf{N}_i \bullet \mathbf{N}_j \right] d\Omega \tag{4.70}$$

$$B_{ij} = -\int_{\Omega_c} j\omega\mu \nabla N_i \bullet \mathbf{N}_j d\Omega \tag{4.71}$$

$$C_{ij} = \int_{\Omega_c + \Omega_n} j\omega\mu \nabla N_i \bullet \nabla N_j d\Omega \tag{4.72}$$

$$E_i = T_{ei} \tag{4.73}$$

$$\Phi_i = \Phi_i \tag{4.74}$$

$$\left(S_1\right)_j = -\sum_{i=1}^{n_e} \left\{ T_{si} \int_{\Omega_c} \left[\left(\frac{1}{\sigma} \nabla \times \mathbf{N}_i \right) \bullet \left(\nabla \times \mathbf{N}_j \right) + j\omega\mu \mathbf{N}_i \bullet \mathbf{N}_j \right] d\Omega \right\} \tag{4.75}$$

$$\left(S_2\right)_j = \sum_{i=1}^{n_e} \left\{ T_{si} \int_{\Omega_n} j\omega\mu \mathbf{N}_i \bullet \nabla N_j d\Omega \right\} \tag{4.76}$$

It is in this matrix form that the equations will be represented in the computer program that will be used to solve them.

4.8 Infinite Elements

When solving FEM models of the type that will be used in this work (involving conductors surrounded by a non-conducting region), for the models to be as realistic as possible, the meshes should ideally continue for a very long, if not infinite, distance from the conductors before the Dirichlet condition of $\Phi = 0$ is imposed at the far boundary. Unfortunately, this would lead to impossibly large meshes and equation systems.

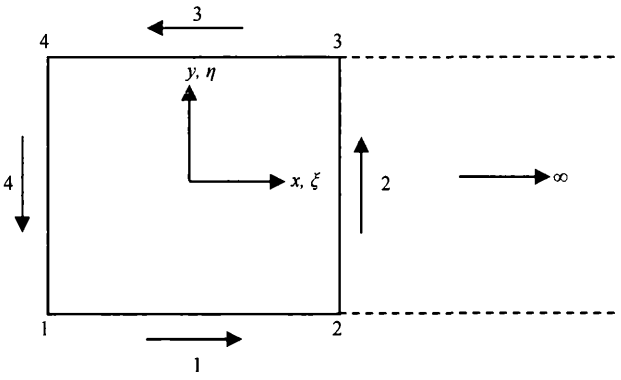

Figure 4.3 - A quadrilateral infinite element

One way around this problem would be to terminate a mesh at some distance away from the conductors and impose the Dirichlet boundary condition there. Whilst, so long as the mesh does not end too close to the conductors, this can give reasonably good results, it will still be the case that a certain amount of error will have been introduced into the model's results. With the T-Φ formulation this error will result in the magnetic field calculated from the potentials always being tangent to the far boundary at the location where the mesh is terminated, with the amount of error decreasing as one moves inwards from the boundary. In this work, to keep mesh sizes and therefore equation systems as small as possible, it will be desirable to terminate meshes relatively close to the coils being simulated. This, if additional action were not taken, could result in the current distribution in a coil being adversely affected and erroneous values obtained for the coil resistance and inductance.

A better solution is possible if so-called infinite elements are placed around a mesh's far boundary. These are special finite elements which have some nodes shared with a mesh based finite element on the traditional far boundary and have their other nodes located at infinity.

An example of a two dimensional infinite element is shown in Figure 4.3. This is based on a standard quadrilateral finite element [125], but has its nodes 2 and 3 located at infinity. The value of the quantity being modelled is always zero at nodes 2 and 3, and therefore the nodal basis functions associated with those nodes are always zero – i.e. $N_2 = N_3 = 0$. The other nodal basis functions are:

$$N_1 = \frac{1-\eta}{1-\xi}, \qquad N_4 = \frac{1+\eta}{1-\xi} \tag{4.77}$$

It is also possible to have infinite edge elements. For quadrilaterals, in this case, edge 2 is always at infinity and the scalar coefficient associated with that edge is always zero. Thus, any vector quantity being represented using the infinite edge element is zero at infinity. Suitable edge basis functions would be:

$$\begin{aligned} \mathbf{N}_1 &= \frac{1}{2}(1-\eta)\hat{\mathbf{x}}, & \mathbf{N}_2 &= \frac{1}{2}(1+\xi)\hat{\mathbf{y}} \\ \mathbf{N}_3 &= -\frac{1}{2}(1+\eta)\hat{\mathbf{x}}, & \mathbf{N}_4 &= -\frac{1}{2}(1-\xi)\hat{\mathbf{y}} \end{aligned} \tag{4.78}$$

where $\hat{\mathbf{x}}$ and $\hat{\mathbf{y}}$ are unit vectors in the local x and y coordinate system of the element.

4.9 FEM Modelling Work in This Thesis

The features described in the preceding sections – i.e. the **T**-Φ formulation and equation system, the method of obtaining $\mathbf{T}_s$ from a prescribed current, the mixed use of edge and nodal elements, and the use of infinite elements – will form the basis of the FEM modelling of stimulation coils to be undertaken in this work. A FORTRAN computer program was developed during this work to implement this modelling system.

As was stated in Chapter 2, it could be expected that even a single full FEM model of a coil would take some time to solve. Given that several of these models will need to be solved both during the development of the FEM computer code itself and subsequently when using the FEM code to model different sizes of coil shapes to obtain the expressions for coil resistance and inductance discussed in Sections 2.5.3.2.2 and 2.5.3.3, it would be desirable to try to restrict the execution times of each FEM model in some way. Additionally, reasons were given in Section 3.9 for choosing to restrict the optimisation programs that will be developed in this work to consider coil geometries that have sections whose shapes can be approximated using

concentric or co-axial loops of wire, including reasons for why this is valuable work. Now, a coil that can be approximated as co-axial circular loops having a single axis, like the helix of Section 3.9 or the new shape proposed in Section 7.8, can be considered as exhibiting axial symmetry, and a detailed electromagnetic model of the coil could be obtained from a two dimensional axi-symmetric FEM model of the loops. Therefore it has been decided to take advantage of the shorter computational speed of such a model, restrict the FEM modelling work undertaken in this thesis to coils whose shapes can be approximated as co-axial loops having a single axis, and attempt to meet the commercial desire to find improved coils of that type. In this thesis, work will be presented to demonstrate how accurate such an FEM representation of that coil type is when used with the **T-Φ** formulation - in this chapter and the next comparisons will be made of modelled and measured magnetic field values due to a single spiral Magstim HP90 coil. Clearly, as part of future work, the FEM program developed could be extended from 2D axi-symmetric to full 3D whilst retaining most of the computer code and allowing a full range of shape types to be modelled.

In Section 2.4 it was explained that, in order to find the resistance and inductance of a stimulating coil when used in combination with a stimulating machine and connecting leads, an FEM model of the coil structure coupled to a lumped circuit element model of the stimulator and leads needs to be solved in order that the frequency content of the current that would arise in the whole system is correctly modelled. In fact, so long as there is no non-linear magnetic material in the coil's vicinity, the current pulse through a biphasic stimulator and coil, as in Figure 1.4, is a single period of a slightly damped sine wave, and the system may be thought of as having current at a single resonant frequency. Unfortunately, since this resonant frequency is not known for a new coil shape, it would be difficult to use the faster frequency domain form of the FEM to model a new shape. Whilst there is a way around this issue, it involves running several separate frequency domain FEM models and circuit models to iteratively 'find' the resonant frequency, and, even then, the method fails when non-linear magnetic material is present. Given that it is desired for the FEM technique used in this work to be generally applicable to both biphasic and monophasic stimulators (which have current pulses with more complex frequency content), and that the speed advantage of frequency domain over time domain FEM modelling is

eroded when several frequency domain models have to be solved, most of the FEM work reported in this thesis will consist of an FEM model of the coil structure coupled to a lumped circuit element model of the stimulator and leads solved in the time domain. Time domain modelling is discussed in the next chapter. Nevertheless, in order to demonstrate that the **T-Φ** formulation FEM models are working adequately without the additional complication of the lumped circuit models, some results obtained from solving FEM models in the frequency domain will be presented in the remainder of this chapter.

Finally, it is important to consider why a new FEM computer program was developed for this work given that there are successful commercial FEM packages available. There are several reasons for this, and these include:

1) The FEM models to be solved in this work are potentially large due to the density of finite elements required within conducting regions to adequately model the skin and proximity effects and the amount of free space between different conducting sections of coils. This would be particularly so for full 3D models. Therefore it would be beneficial to have maximum control over the FEM process to ensure that a particular choice of formulation, finite element type, discretisation, and equation solver could be made in an attempt to control the efficiency of the whole procedure.

2) Hardly any published work exists on the FEM modelling of the internal structure of stimulation coils. Given the potential efficiency of the **T-Φ** formulation, it was desired to report in this work on the stability and suitability of the formulation to modelling stimulation coils. In particular it is desired to know whether the method of deriving $\mathbf{T}_s$ from a prescribed current causes problems – especially in stimulator circuit coupled time domain models, and also when used in 2D axi-symmetric models given that the literature on this method refers to 3D modelling.

3) Given that stimulator circuit coupled time domain models are to be solved, it was desired to also have maximum control over how this circuit coupling is to

be implemented. Particularly, it was desired to be able to control how the equations of the coupled system impact on one another, which electrical quantities would link the two sections, whether explicit or implicit time-stepping should be used, and what time-step size would be permissible.

4) In the future, it may be desired to move beyond the tri-modular approach of this work to a position where an optimisation algorithm directly incorporates running FEM models. This would require the algorithm to repetitively run FEM models whilst making step-by-step mesh changes. It would therefore be desirable to develop a particularly efficient FEM program that could be incorporated at a later time into such an optimisation program.

5) A version of the **T**-Φ formulation, without **T** split into $\mathbf{T}_s$ and $\mathbf{T}_e$ has been successfully used by others [78] to model the secondary currents induced in tissue due to the fields from stimulation coils which were themselves modelled using a simpler method than the FEM models of this work because their frequency of operation and peak through currents were already known. In the future it could be useful to run FEM models that include both the internal structures of a stimulator coupled coil and tissue, and, since using the same formulation for both structures would be beneficial, it would be useful to show in this work that the **T**-Φ formulation can adequately model a coil's structure.

4.10 Amendment to the FEM Formulation for 2D Axi-Symmetry

In order to use the **T**-Φ formulation in a 2D axi-symmetric FEM model, some factors need to be considered. The first is that, since the potentials together represent the magnetic field as given by (4.20), for the magnetic field to be truly axi-symmetric, it must have no component normal through the axis of symmetry. Actually, this condition can be naturally ensured by simply terminating the mesh at the axis of symmetry. This is a side effect of ensuring the inter-element continuity of $\mu\mathbf{H}$ by always not including in the formulation the integrals:

$$\int_{\Gamma} \mathbf{n} \bullet \frac{\partial}{\partial t} w_i \mu \left(\mathbf{T}_s + \mathbf{T}_e - \nabla \Phi \right) d\Gamma \tag{4.79}$$

or

$$\int_{\Gamma} \mathbf{n} \bullet \frac{\partial}{\partial t} w_i \mu \left(\mathbf{T}_s - \nabla \Phi \right) d\Gamma \tag{4.80}$$

around the outside of every conducting or non-conducting element respectively (as discussed in Section 4.5). By also always not performing these integrals along the sides of elements that abut the axis of symmetry, the value of the integrals, and hence the normal component of the magnetic field, will always be zero. (Initial conditions are that the magnetic field is zero.)

The second consideration is whether any change needs to be made to the equation system that must be solved to account for 2D axi-symmetry. The paper by Hiptmair and Ledger [126] discusses the 2D axi-symmetric FEM equations for use with a high frequency formulation where both edge and nodal finite elements are used. Careful consideration of the paper reveals that for the low frequency problem in this work where the quasi-static approximation to Maxwell's equations applies, and no build up of static electric charges are to be modelled, the equation system (4.69)-(4.76) simply becomes:

$$\begin{bmatrix} \mathbf{A} & \mathbf{B} \\ \mathbf{B}^{\mathrm{T}} & \mathbf{C} \end{bmatrix} \begin{bmatrix} \mathbf{E} \\ \mathbf{\Phi} \end{bmatrix} = \begin{bmatrix} \mathbf{S}_1 \\ \mathbf{S}_2 \end{bmatrix} \tag{4.81}$$

$$A_{ij} = \int_{\Omega_c} \left[\left(\frac{1}{\sigma} r \nabla \times \mathbf{N}_i \right) \bullet \left(\nabla \times \mathbf{N}_j \right) + j\omega\mu r \mathbf{N}_i \bullet \mathbf{N}_j \right] d\Omega \tag{4.82}$$

$$B_{ij} = -\int_{\Omega_c} j\omega\mu r \nabla N_i \bullet \mathbf{N}_j d\Omega \tag{4.83}$$

$$C_{ij} = \int_{\Omega_c + \Omega_n} j\omega\mu r \nabla N_i \bullet \nabla N_j d\Omega \tag{4.84}$$

$$E_i = T_{ei} \tag{4.85}$$

$$\Phi_i = \Phi_i \tag{4.86}$$

$$(S_1)_j = -\sum_{i=1}^{n_e}\left\{T_{si}\int_{\Omega_c}\left[\left(\frac{1}{\sigma}r\nabla\times\mathbf{N}_i\right)\bullet\left(\nabla\times\mathbf{N}_j\right)+j\omega\mu r\mathbf{N}_i\bullet\mathbf{N}_j\right]\mathrm{d}\Omega\right\} \quad (4.87)$$

$$(S_2)_j = \sum_{i=1}^{n_e}\left\{T_{si}\int_{\Omega_n} j\omega\mu r\mathbf{N}_i\bullet\nabla N_j\,\mathrm{d}\Omega\right\} \quad (4.88)$$

where r is the perpendicular distance from the axis at a point. When comparing with the work in [126] it should be noted that high-frequency related modes are absent in this work. Additionally, the $1/r$ singularities that occur in [126], arising from that work's Equation 6, do not occur in this problem because, if one imagines a cylindrical coordinate system with the z axis corresponding to a coil's axis of symmetry, the curl of the magnetic field is always along the θ direction and has no component in the problematic r or z directions. It is the amended 2D axi-symmetric form of the **T-Φ** formulation described here that will be used in the FEM models of this work, other than in the test model reported upon in the next section.

4.11 The Current Distribution Across a Single Round Wire

As has been mentioned, the ultimate purpose of the FEM models in this work will be to provide results – the magnetic field **H** – that can be processed to obtain the resistance and inductance of new coil geometries when used with a particular stimulating machine. That post-processing will be discussed in Chapter 5. However, it is first necessary to demonstrate that the frequency domain **T-Φ** formulation FORTRAN FEM program mentioned in the previous section works correctly. Obviously, several tests were undertaken to verify the program's results, however, in this section, results will be presented to validate the FEM code and in particular to show that, with suitable post-processing, the program can be used to correctly model the low frequency current density distribution on the cross-section of a long straight circular conductor.

The problem of finding this current density distribution is one that has an analytical solution. With reference to Figure 4.4, this is given in [127] as:

$$J_z = I\frac{j^{3/2}k}{2\pi r_w J_1\left(j^{3/2}kr_w\right)}J_0\left(j^{3/2}kr\right) \tag{4.89}$$

where I is the total current through the wire; r is the distance from the wire's centre to an observation point; r_w is the wire's radius; $k^2 = \omega\sigma\mu$ where ω is the angular frequency, σ is the conductivity and μ is the permeability; and $J_n\left(j^{3/2}kr\right)$ is an n'th order Bessel function of the first kind. Such a Bessel function may be expressed as:

$$J_n\left(j^{3/2}kr\right) = \mathrm{ber}_n(kr) + j\,\mathrm{bei}_n(kr) \tag{4.90}$$

where

$$\mathrm{ber}_n(kr) = \sum_{m=0}^{\infty}\frac{(-1)^m\left(\frac{kr}{2}\right)^{n+2m}}{m!\Gamma(n+m+1)}\cos\frac{3}{4}(n+2m)\pi \tag{4.91}$$

$$\mathrm{bei}_n(kr) = \sum_{m=0}^{\infty}\frac{(-1)^m\left(\frac{kr}{2}\right)^{n+2m}}{m!\Gamma(n+m+1)}\sin\frac{3}{4}(n+2m)\pi \tag{4.92}$$

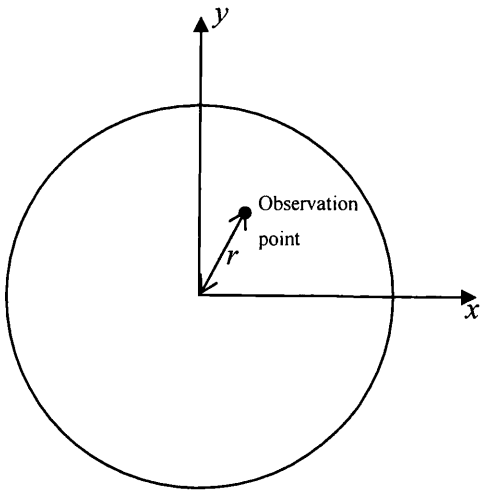

Figure 4.4 - A long straight round wire parallel to the z axis

in which $\Gamma(n+1)$ is the Gamma function.

The problem to be investigated is that of finding the current distribution across a 2mm radius circular wire of conductivity $\sigma = 5\text{x}10^7$S/m carrying a 3 kA current at 4 kHz. For comparison with the FEM modelled results, a computer program implementing the analytical formula described above was written, and used to obtain the distribution shown in Figure 4.7. It should be noted that the results in the figure are shown on a mesh purely for ease of comparison with the FEM modelled results – no mesh is required with the analytical formula. Although any points could be chosen, the analytical formula was used to obtain the current densities at points equivalent to the centroids [128] of the mesh elements, and these values are shown across the whole of each element in Figure 4.7.

For the FEM model, the frequency domain **T**-Φ formulation with edge and nodal elements as described in this chapter was used together with a 2D triangular element mesh. The mesh was generated using the MeshAdapt original 2D algorithm of the program known as gmsh [133]. The whole mesh, including the non-conducting space around the wire is shown in Figure 4.5, and Figure 4.6 shows a close-up of the wire in the centre portion of the mesh. As the wire is long and straight, the axi-symmetric modifications to the formulation described in the previous section were not used. Although planar symmetry exists in this test problem, no lines of symmetry were implemented in order exclude potential sources of error. A current value of 3 kA was used to obtain $\mathbf{T}_s$ using the method of Section 4.6, the formulation solved to obtain $\mathbf{T}_e$ and Φ, and the current densities at the centroids of each element obtained by post-processing using $\mathbf{J} = \nabla \times \mathbf{H} = \nabla \times (\mathbf{T}_s + \mathbf{T}_e - \nabla\Phi)$. These centroid values are shown across each element in Figure 4.8.

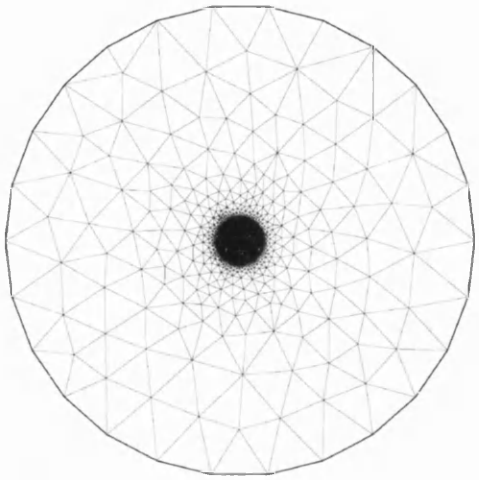

Figure 4.5 - Complete FEM mesh

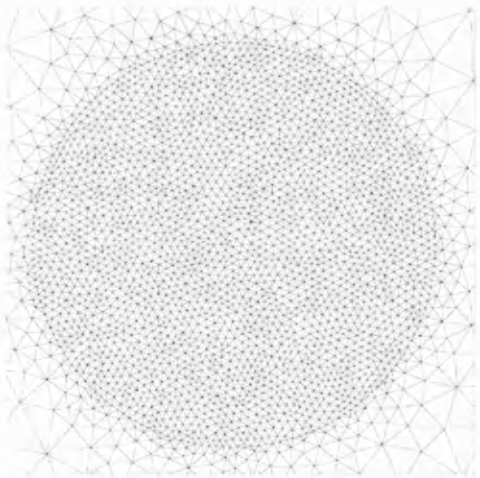

Figure 4.6 - Close-up of the wire in the FEM mesh

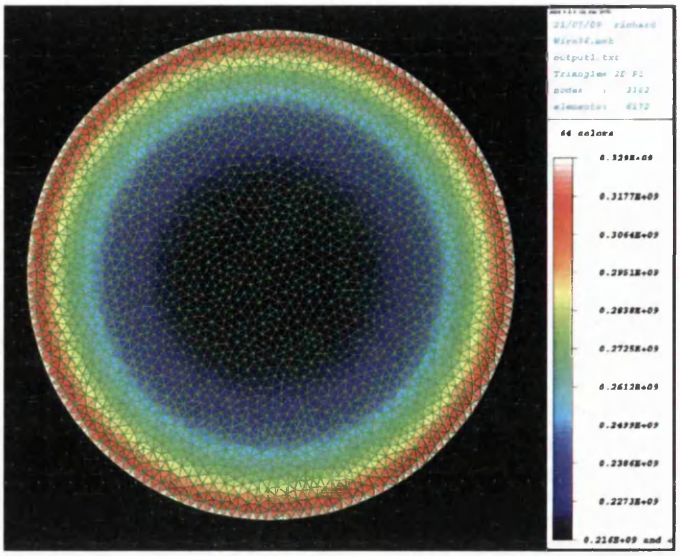

Figure 4.7 - Current density in A/m^2 at element centroids due to analytical formula

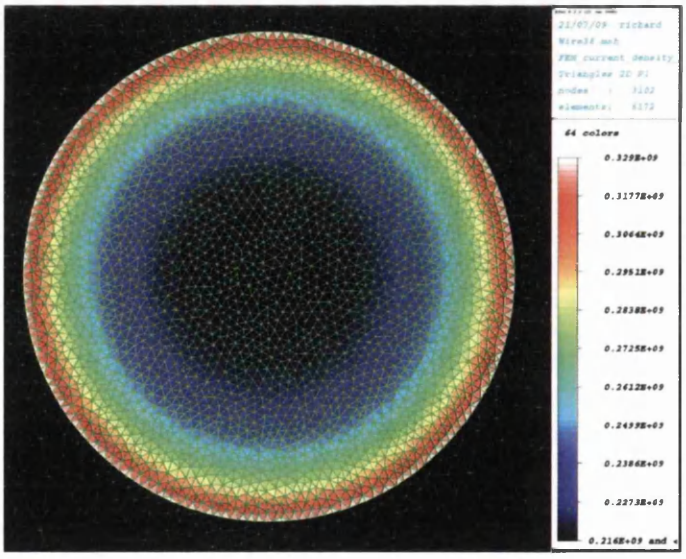

Figure 4.8 - Current density in A/m^2 at element centroids due to FEM model

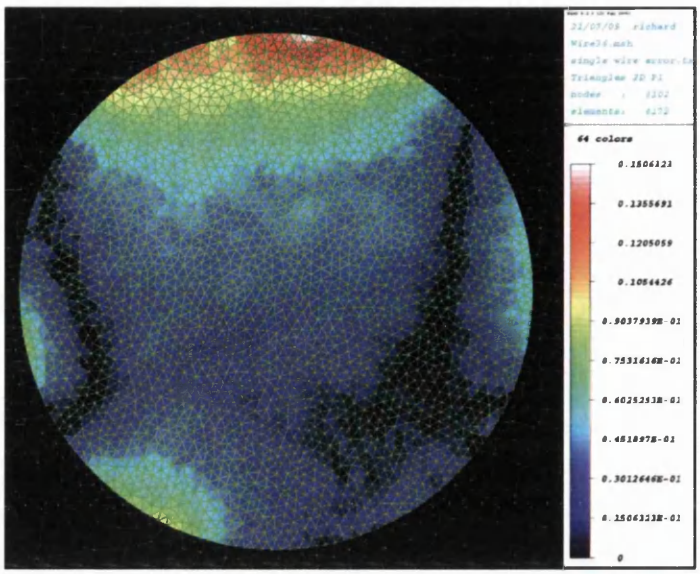

Figure 4.9 - Percentage error in FEM model at element centroids

Figure 4.9 shows the percentage error between the centroid FEM and analytical values as percentages of the analytical values. As can be seen, the percentage error is low – 0.15% or less – which, together with the closeness in values and distributions observed in Figure 4.7 and Figure 4.8, suggests that the FEM program is functioning correctly. This was borne out by the results from other test models. It could be noted here that the problem of a single long straight conductor is not wholly realistic since there should strictly be a current return path defined somewhere in the problem space. The lack of a defined return path, together with the use of infinite elements that impose no current return path at infinity, means that solving the problem leads to an implied return path being distributed across the problem space elements. Nevertheless, as seen in Figure 4.9, this does not lead to a significant error in the results obtained from solving the problem, and the solution is good enough to be considered to have validated the FEM program's performance. It is interesting to note that, here, the higher error values were associated with elements whose edges had higher $\mathbf{T}_e$ coefficient reference numbers in the FEM equation system. When running more practically useful FEM models, a coarser mesh leading to somewhat less accurate results but faster solution times would be acceptable.

As was mentioned in Section 4.6, the FEM equation system being solved is singular, but should be solvable using an iterative method. The solver used to obtain the above results was the symmetric matrix three-term recurrence without look-ahead version of QMRPACK. This is a type of Krylov Method solver and is discussed in [129]. The solver was chosen because, as discussed in Section 4.3 and 4.4, this formulation is used without explicitly enforcing a gauge condition, which is known to greatly reduce the number of iterations with Krylov solvers [130]. This solver will be used for the remainder of the FEM models in this work. In the model reported above, which contained 10409 unknown coefficients, the solver calculated a solution after 1497 iterations in 1 minute 43 seconds on a Pentium 4 1.8GHz personal computer.

It should be reported that, before using the QMRPACK solver in this work, an attempt was made to solve the FEM equation system in several models using a Gaussian elimination direct solver, but with the addition of a wholly real regularisation term:

$$\alpha \int_{\Omega_c} \mathbf{N}_i \cdot \mathbf{N}_j d\Omega \tag{4.93}$$

to the first term in the integral on the right hand side of (4.70) in an attempt to remove the singularity by making the equations linearly independent. The parameter α would be some chosen small value. However, this did not prove successful, and, although broadly realistic solutions of models were obtained, the magnetic field was composed of spurious values in a small, but significant, proportion of mesh elements. Ultimately these spurious values were due to the singular FEM equation system whose solution was being sought. As discussed in Section 4.6, the equation system was singular because a decision was taken not to fully implement the Coulomb gauge. The iterative solver somewhat obscures the lack of gauge in the system in its solutions whereas the direct solver reveals it as spurious values.

4.12 An FEM Model of a Magstim HP90 Coil

In this section, the 2D axi-symmetric frequency domain **T**-Φ formulation FORTRAN FEM program will be used to solve a model of a flat single spiral Magstim HP90 coil

represented as concentric circular loops in the manner outlined in Section 4.9. The purpose of this work is firstly to confirm that the program is working correctly when more than one conducting section appears in a 2D mesh and secondly to present original work on the accuracy of the current density and magnetic field values obtained from the frequency domain **T-Φ** formulation when a spiral stimulating coil is approximated as concentric circular loops in a 2D axi-symmetric model.

The geometric dimensions of a HP90 were given in Section 3.7, and the wire cross-section given there was used for each concentric circular loop in this section's model. A 2D axi-symmetric mesh of triangular elements was constructed in a similar manner to the mesh of the last section using the gmsh program. The centres of each concentric loop were the same as those used for the concentric thin-wire loop model of Section 3.8. The mesh used is shown in Figure 4.10, and a magnified view of the region containing the conducting loops is shown in Figure 4.11. It will be seen that the mesh

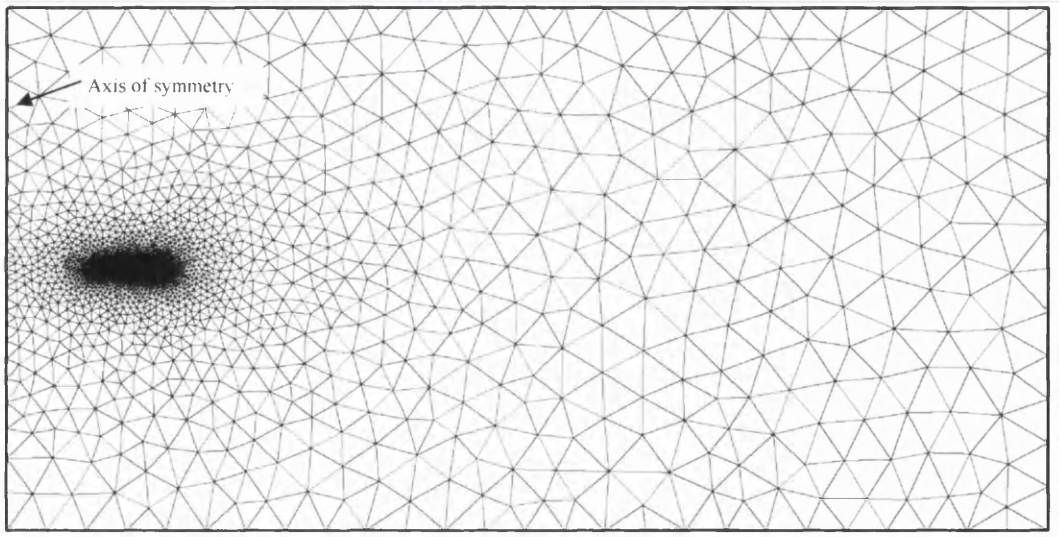

Figure 4.10 - Mesh used for HP90 FEM model

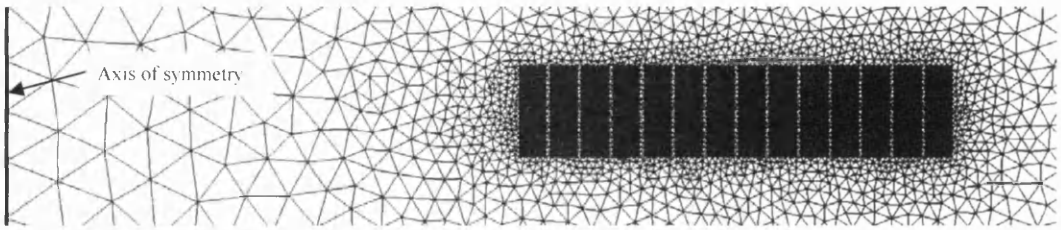

Figure 4.11 - Close-up of region containing concentric conducting loops in mesh of HP90 coil

is finest in and around the conductors in order to capture in detail both the skin and proximity electromagnetic effects. The mesh can be quite coarse at distance from the conductors without significantly affecting what is modelled within the conductors. The reason that the mesh was extended so far from the conductors was so that the magnetic field values required for the plots presented later in this section could be calculated.

In order for a frequency domain model to be valid, the HP90 will be considered to be attached to a Magstim Rapid^2 biphasic stimulator meaning that, as discussed in Section 4.9, the frequency content of the current through the coil will consist of one component. By experimentally measuring the potential across the discharge capacitor of a Rapid^2 stimulator when connected to a HP90 using a Tektronix TDS3014 oscilloscope, the circuit formed by the pair was found to be resonant at 2.5kHz. The FEM model was therefore driven at that frequency.

The equation for the current through a biphasic stimulator is given in Section 1.3 as (1.5) and is reproduced below:

$$i(t) = \frac{-V_0}{\omega L_{tot}} \exp\left(\frac{-R_{tot}t}{2L_{tot}}\right) \sin(\omega t) \tag{4.94}$$

where V_0 is the initial voltage across the stimulator's discharge capacitor, and $R_{tot} = R_s + R_c$ and $L_{tot} = L_s + L_c$ are the total resistance and inductance of the stimulator (with connecting leads) and coil at the frequency of operation. By taking the time derivative of (4.94) the following is obtained:

$$\frac{di}{dt} = \frac{-V_0}{\omega L_{tot}} \left[\exp\left(\frac{-R_{tot}t}{2L_{tot}}\right) \omega \cos(\omega t) - \sin(\omega t) \frac{R_{tot}}{2L_{tot}} \exp\left(\frac{-R_{tot}t}{2L_{tot}}\right) \right] \tag{4.95}$$

Now, the peak current through the coil will arise at the time when di/dt is zero. From (4.95) this occurs when:

$$\omega\cos(\omega t) = \frac{R_{tot}}{2L_{tot}}\sin(\omega t) \tag{4.96}$$

$$\frac{2\omega L_{tot}}{R_{tot}} = \tan(\omega t) \tag{4.97}$$

$$t = \frac{\arctan\left(\frac{2\omega L_{tot}}{R_{tot}}\right)}{\omega} \tag{4.98}$$

Measurements were taken from an actual HP90 coil at a frequency of 2.5kHz using a Wayne Kerr Analyser 6425 impedance bridge, leading to values of $R_c = 16\text{m}\Omega$, $L_c = 23\mu\text{H}$. Additionally, values of $R_s = 25\text{m}\Omega$ and $L_s = 1\mu\text{H}$ were supplied for the resistance and inductance of the Rapid^2 stimulating machine and connecting cables at 2.5kHz by the Magstim Company Ltd. Using this information, (4.98) can be evaluated to give $t = 9.639\text{x}10^{-5}\text{s}$. Substituting these values back into (4.94), together with an initial capacitor voltage of 1530V, gives the maximum peak current through the coil as 3.88kA. It is this current value that was used as the through current value for each conductor in the FEM model in this section in order to obtain the function $\mathbf{T}_s$ using the method of Section 4.6.

Once $\mathbf{T}_s$ was obtained, the FEM program proceeded to solve the main **T-Φ** formulation using the 2D axi-symmetric equation system of Section 4.10. In total, the mesh described above resulted in an equation system of 8032 unknown coefficients which took 6 minutes 39 seconds to solve on a Pentium 4 1.8GHz personal computer using the QMRPACK solver described in the previous section.

To help verify that the program was working correctly, the Magstim Company Ltd supplied data relating to the current density distribution across the conductor cross-sections in a HP90 coil obtained by solving a 2D axi-symmetric FEM model in the commercial package Ansys [131]. The same concentric loop coil geometry was used in the Ansys model as the **T-Φ** model presented in this section, but the Ansys model was solved using purely nodal finite elements and the **A-V** formulation referred to in

Section 4.3. Since an initial capacitor voltage of 1530V was used in the Magstim model, this is the value used above in deriving the peak coil current for the **T-Φ** model. The results from the **T-Φ** model were post-processed to obtain the conductor current densities using $\mathbf{J} = \nabla \times \mathbf{H} = \nabla \times (\mathbf{T}_s + \mathbf{T}_e - \nabla\Phi)$, and the results of this calculation are shown in Figure 4.12 with the current densities in A/m^2 at the element centroids shown across the elements. The Magstim supplied Ansys data is shown in Figure 4.13 for comparison.

As can be seen from Figure 4.12 and Figure 4.13, the current density values and distribution obtained from the **T-Φ** model agree closely with the Ansys derived data supplied by Magstim. This, together with other tests conducted, suggests that the FORTRAN based 2D axi-symmetric frequency domain **T-Φ** based program is working correctly, and is properly modelling both the skin and proximity effects. Inspection of the magnetic field data from the **T-Φ** model (before any post-processing is applied) revealed that the calculated field is always stable, and has no spurious values.

In addition to considering the current density in the coil, the magnetic field was also calculated at points along several lines below the coil using the **T-Φ** model's results. These lines extended away from the coil's axis, along its radius and were parallel to its plane, in a manner similar to the lines in Figure 3.8 in Section 3.7. The field was calculated by reconstructing $\mathbf{T}_s, \mathbf{T}_e$ and Φ from the solved finite element coefficients at each field observation point and performing the sum $\mathbf{H} = \mathbf{T}_s + \mathbf{T}_e - \nabla\Phi$. Plots of the radial and vertical components of the magnetic flux density $\mathbf{B} = \mu\mathbf{H}$ are shown in Figure 4.14 and Figure 4.15.

Although the results in Figure 4.14 and Figure 4.15 appear to be broadly realistic, the flux density magnitudes can be seen to fluctuate quite seriously along each line. This is because the finite element discretisation in the mesh described above is relatively

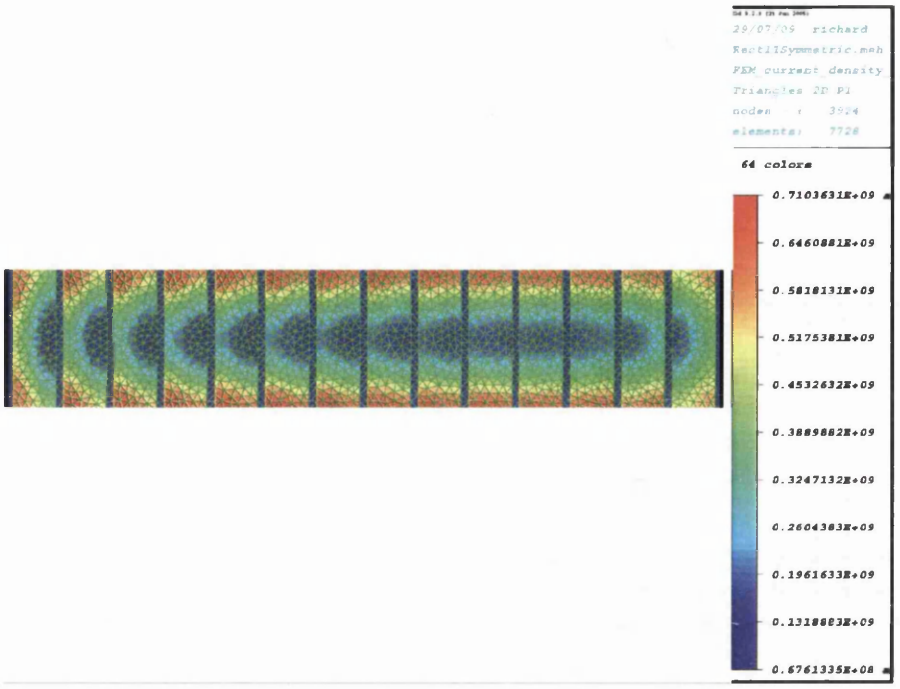

Figure 4.12 - Current densities across the conductor cross-sections of a HP90 coil obtained from the T-Φ model

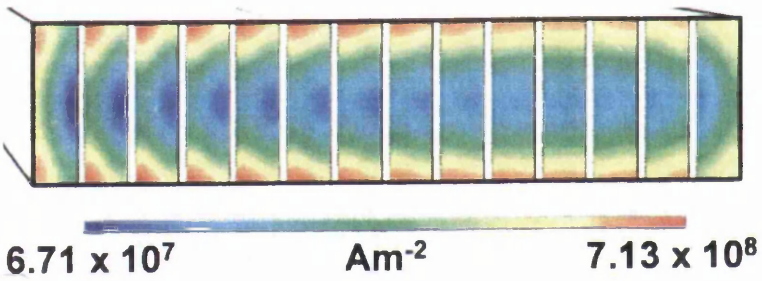

Figure 4.13 - Current densities in Magstim supplied FEM data across the conductors of a HP90 coil

coarse at these distances away from the coil. This distant coarseness has little effect on the current density seen in Figure 4.12, and if one is only interested in ensuring that the skin and proximity effects are adequately modelled so that an electromagnetic quantity like the current density, or the coil's AC resistance or inductance, can be reliably modelled, then this type of mesh is sufficient.

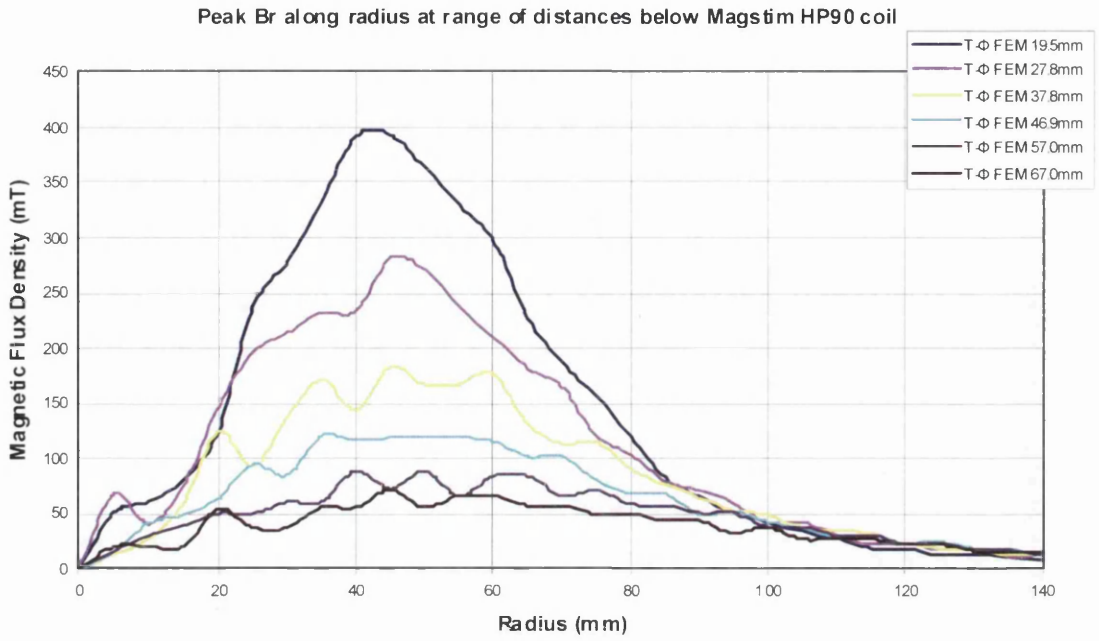

Figure 4.14 - The radial component of the magnetic flux density at points on lines at various distances below a HP90 coil calculated using the T- Φ model

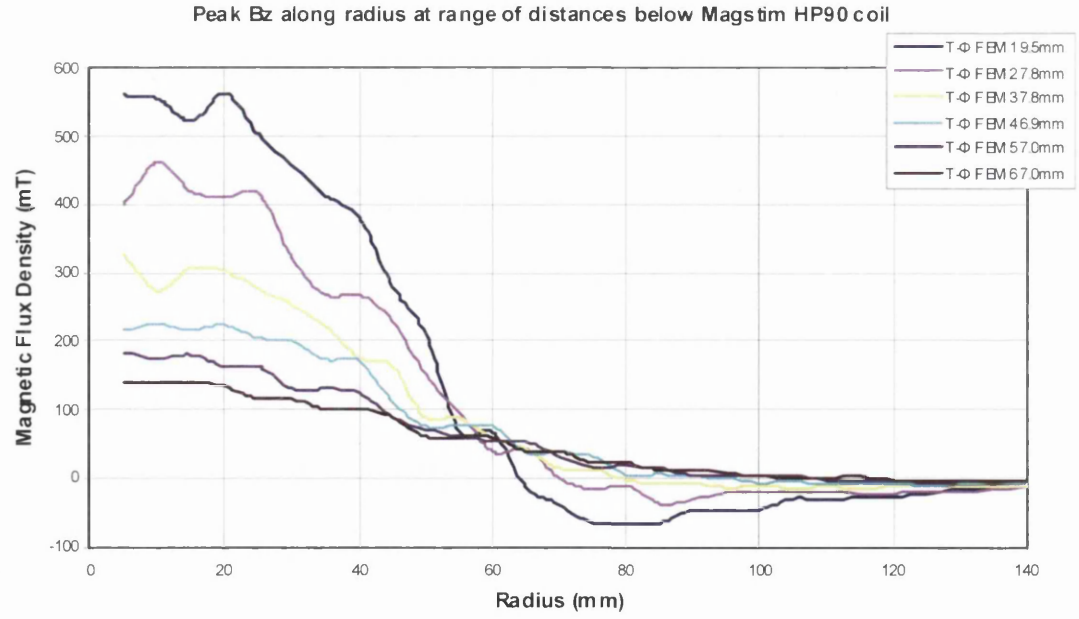

Figure 4.15 - The vertical component of the magnetic flux density at points on lines at various distances below a HP90 coil calculated using the T- Φ model

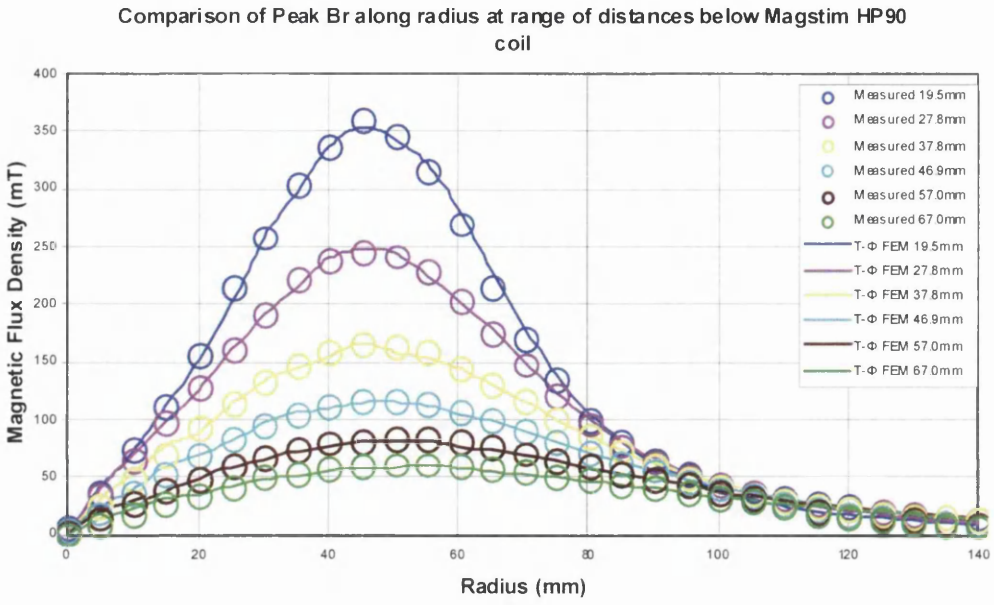

Figure 4.16 - Comparison of radial component of magnetic flux density on lines below HP90 coil due to T- Φ model and measured data

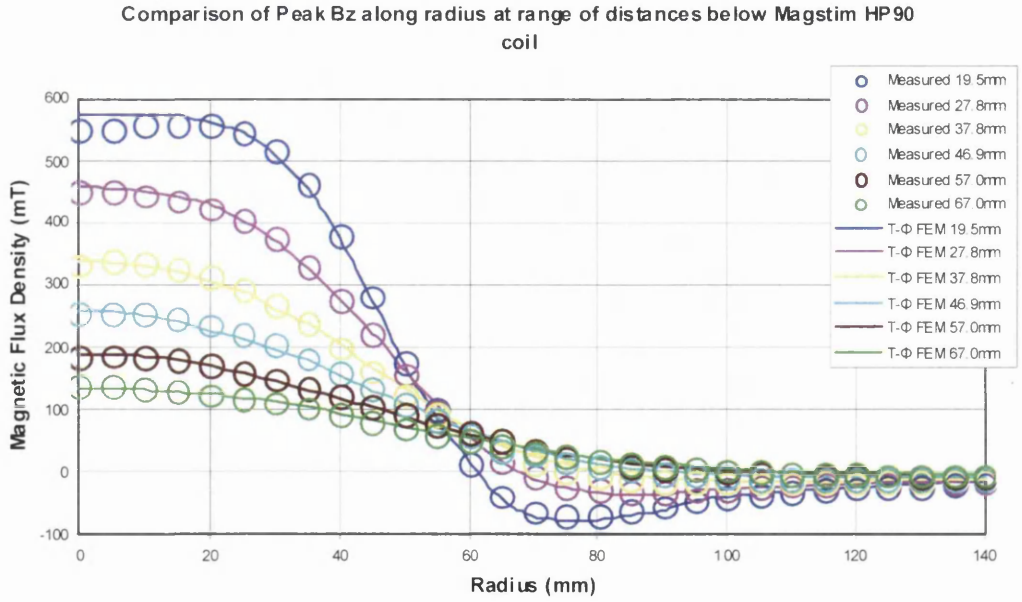

Figure 4.17 - Comparison of vertical component of magnetic flux density on lines below HP90 coil due to T- Φ model and measured data

In order to obtain better flux density values at distance from the coil, the mesh was revised so that a thin layer of finer mesh existed for 1.5mm above and below each line containing field observation points. The remainder of the mesh remained the same, and the **T-Φ** model was re-run. The Magstim Company Ltd supplied data consisting of radial and vertical magnetic flux density component measurements at points along each line taken using a 10mm diameter calibrated search coil having an accuracy of ± 2% [132]. These measurements are shown in Figure 4.16 and Figure 4.17 together with the results from the re-run model.

As can be seen from Figure 4.16 and Figure 4.17, the modelled magnetic flux density varies much more smoothly from point to point along each line when the revised mesh is used. There is also good agreement between the modelled and Magstim supplied measured data.

From the above results it can be seen that the 2D axi-symmetric frequency domain **T-Φ** formulation FEM method described in this chapter can be applied to successfully model the magnetic field around a stimulation coil such as a spiral. However, care needs to be taken to ensure that the mesh is relatively fine in the vicinity of any points at which the field is to be evaluated, even if distant from the coil. An alternative would be to keep a less fine mesh but evaluate the field at Gaussian points within the elements containing the points at which it is desired to know the field, then project the field values back onto the elements' nodes. The nodal shape functions could then be used to interpolate the field onto the points at which it is desired to know the field. A possibility would be to use a combination of this field smoothing and a finer mesh. A further alternative, since the field is due to the current within the coil, could be to perform Biot-Savart integrals over the coil geometry itself to obtain the field at the desired points. This would, however, involve more evaluations than the other methods mentioned above, so would be a less desirable post-processing technique.

4.13 Conclusions for the FEM Work in the Remainder of This Thesis

In this chapter it has been shown for the first time that the 2D axi-symmetric frequency domain **T-Φ** formulation FEM method can be used to successfully model

the skin and proximity electromagnetic effects in a coil that can be approximated as being axi-symmetric. This has been demonstrated by the production of reliable values for the current density in the HP90 coil, and magnetic field values that compare closely to experimentally measured values. Of course this modelling relied on *a-priori* knowledge of the current magnitude and frequency that arose when the HP90 coil was used with a particular biphasic stimulator. In the next chapter, the model will be expanded into a stimulator circuit coupled time domain form so that, if desired, a near axi-symmetric coil could be modelled when used with either a biphasic or monophasic stimulator. That work will then lead on to a point where the AC resistance and inductance of a coil can be obtained through post-processing of modelled results and used in the tri-modular optimisation scheme described in Chapter 2.

Finally, it could be noted that, although an assumed DC current distribution was used in the conductors in the FEM models in order to obtain the source function $\mathbf{T}_s$, a different assumed current distribution could have been used instead. For the modelling to work as intended though, it would be necessary to ensure that the total through current in the conductors would be the same as that used in the DC distribution model. If an alternative $\mathbf{T}_s$ distribution were decided to be used, the solution functions $\mathbf{T}_e$ and Φ would be different to those obtained from the DC distribution model although the final total magnetic field function $\mathbf{H} = \mathbf{T}_s + \mathbf{T}_e - \nabla\Phi$ would be expected to be the same.

5 Time Domain Finite Element Modelling

5.1 Background

Section 2.5 and its subsections introduced this work's proposed tri-modular scheme to find improved magnetic stimulation coil shapes whilst avoiding the repetitive running of time consuming Finite Element Method (FEM) electromagnetic models during an iterative optimisation algorithm. There, it was explained that the New Shape Module would use optimisation to search for coil geometries having a better peak electric field focality and that the simpler thin-wire electric field modelling technique can be used as part of this task. However, it was also explained that, in practise, although it is desirable to use a focal coil, it is also desirable to know whether a particular coil is capable of stimulating the intended nerve tissue which is at a certain distance below the coil.

This work's Main Module was proposed (which also uses optimisation and thin-wire field modelling) in order to offer a way to find the most focal coil geometry from a set of basic shape topologies which is also able to meet a specified normalised nerve membrane potential value at a certain distance below the coil. In Section 2.5.2, it was explained that the peak nerve membrane potential value may not occur until some time into the current pulse being discharged through the coil; this peak may be calculated for coils used with a biphasic stimulator by evaluating (2.6) during the current pulse. However, in order to use (2.6), it is necessary to know the resistance and inductance of the coil, which are values that depend on the skin and proximity electromagnetic effects that arise within the coil when it is used with a particular stimulator.

In Chapter 4 it was demonstrated that a 2D axi-symmetric **T**-Φ FEM formulation can be used in the frequency domain to model the skin and proximity electromagnetic effects in coil shapes that are suited to being represented as concentric circular loops. Clearly, in order to undertake a frequency domain simulation, it is necessary to know the frequency at which to run the model. Unfortunately, the frequency content of the

current pulse that arises when a new coil geometry (that may have arisen during an optimisation iteration) is used with a particular stimulator is not known *a priori*, meaning that the FEM program of Chapter 4 cannot be directly used in this work. Therefore, this chapter investigates how the 2D axi-symmetric **T**-Φ FEM formulation program may be extended to work in the time domain and coupled to a lumped element circuit model of a stimulating machine so that the resistance and inductance of new coil geometries may be established. It will be seen that, for a biphasic stimulator, the frequency domain program still has a supporting role in the process.

It is intended that the final form of the circuit coupled time domain FEM program reported on in this chapter together with the supporting frequency domain routine be this work's FEM Module. The FEM Module may then be used in the way outlined in Section 2.5.3.2.2 to obtain expressions for the resistance and inductance of the basic coil shapes in terms of the basic shapes' size governing variables. Use of the FEM Module to do this is examined in Section 7.12. The Main Module's optimisation therefore involves taking one or more basic coil shape topologies and finding the size governing variable values that optimise a shape's focality whilst meeting the normalised nerve membrane potential requirement. There, use is made of thin-wire electric field modelling to assess focality and to partially calculate (2.6) to obtain the membrane potential; the remainder of (2.6) is calculated making use of the expressions for resistance and inductance for the basic shape obtained via the FEM Module. The Main Module is discussed in greater detail in Chapter 7.

The present chapter begins by showing that the quasi-static frequency (less than 10 kHz) electromagnetics that underlie the technique of magnetic stimulation are an example of a diffusion process. Armed with that knowledge, an appropriate time stepping method for the time domain FEM coil model is identified and its stability discussed. The time domain FEM formulation is then shown to be able to adequately model a Magstim HP90 coil. Subsequently, a method for coupling the FEM model to a circuit model of a biphasic stimulator is presented, before this chapter closes by reporting how the coupled model can be used to accurately predict the resistance and inductance of a HP90 coil when used with a Magstim Rapid^2 biphasic stimulator.

5.2 The Quasi-Static Electromagnetic Problem as a Diffusion Process

The physical process of diffusion accounts for the way in which something, e.g. heat, particles, a field, etc., flows from regions of greater concentration to regions of lesser concentration. According to Fick's Law [142], the net movement of the diffusing quantity per unit area is proportional to its concentration gradient, and the constant of proportionality, known as the diffusion coefficient or diffusion constant, depends on the diffusing quantity's nature and the medium through which the diffusion takes place. Since concentration involves a first order spatial derivative of the quantity of interest and diffusion involves the gradient of the concentration, it is no surprise to find that the Diffusion Equation [143] contains the Laplacian operator:

$$\frac{\partial u}{\partial t} = c^2 \nabla^2 u \tag{5.1}$$

$$\frac{\partial u}{\partial t} = c^2 \left[\frac{\partial^2 u}{\partial x^2} + \frac{\partial^2 u}{\partial y^2} + \frac{\partial^2 u}{\partial z^2} \right] \tag{5.2}$$

where c^2 is the diffusion constant and u is the diffusing quantity.

The property known as the diffusion length is a measure of how far the diffusing quantity has propagated in a straight line via a diffusion process in a certain time t, and may be expressed as:

$$L = \sqrt{4c^2 t} \tag{5.3}$$

This may be rearranged as:

$$t = \frac{L^2}{4c^2} \tag{5.4}$$

to give the time taken for a quantity to diffuse a certain distance.

Consider now the **T**-Φ formulation to be used in the FEM models of this work. It may be seen that governing equations (4.22) and (4.23) are obtained by taking the divergence of governing equation (4.21) which represents the physics of the problem. If (4.21) is applied in a spatial sub-domain of a problem having uniform scalar material properties (where, given its definition, $\mathbf{T}_e$ is zero if the sub-domain is non-conducting) and use is made of (4.20), the constitutive relation $\mathbf{B} = \mu\mathbf{H}$ from (4.4), and the fact that the gradient of a scalar field has no curl, (4.21) may be developed:

$$\nabla\times\left(\frac{1}{\sigma}\nabla\times\left(\mathbf{T}_s+\mathbf{T}_e\right)\right)=-\frac{\partial}{\partial t}\mu\left(\mathbf{T}_s+\mathbf{T}_e-\nabla\Phi\right) \tag{5.5}$$

$$\frac{1}{\sigma}\nabla\times\nabla\times\left(\mathbf{T}_s+\mathbf{T}_e\right)=-\frac{\partial}{\partial t}\mu\left(\mathbf{T}_s+\mathbf{T}_e-\nabla\Phi\right) \tag{5.6}$$

$$\frac{1}{\sigma}\nabla\times\nabla\times\mathbf{H}=-\frac{\partial}{\partial t}\mu\mathbf{H} \tag{5.7}$$

$$\frac{1}{\sigma\mu}\nabla\times\nabla\times\mathbf{B}=-\frac{\partial}{\partial t}\mathbf{B} \tag{5.8}$$

Using the vector identity $\nabla\times\nabla\times\mathbf{A}=\nabla\left(\nabla\bullet\mathbf{A}\right)-\nabla^2\mathbf{A}$, (5.8) becomes:

$$\frac{1}{\sigma\mu}\nabla\left(\nabla\bullet\mathbf{B}\right)-\frac{1}{\sigma\mu}\nabla^2\mathbf{B}=-\frac{\partial}{\partial t}\mathbf{B} \tag{5.9}$$

However, from Maxwell's equations (4.4), $\nabla\bullet\mathbf{B}=0$. This means that (5.9) becomes:

$$\frac{1}{\sigma\mu}\nabla^2\mathbf{B}=\frac{\partial}{\partial t}\mathbf{B} \tag{5.10}$$

$$\frac{1}{\sigma\mu}\left[\frac{\partial^2\mathbf{B}}{\partial x^2}+\frac{\partial^2\mathbf{B}}{\partial y^2}+\frac{\partial^2\mathbf{B}}{\partial z^2}\right]=\frac{\partial}{\partial t}\mathbf{B} \tag{5.11}$$

By comparing (5.10) and (5.11) to (5.1) and (5.2) it is possible to see that, within such an uniform sub-domain, the quasi-static electromagnetic models being solved in this work represent a diffusion process where the diffusing quantity is the magnetic flux density **B**, and the diffusion constant is $1/\sigma\mu$. If this constant is used in (5.4), the following is obtained:

$$t = \frac{L^2 \sigma \mu}{4} \tag{5.12}$$

which represents the time taken for the magnetic flux density to diffuse over a distance L. By virtue of their having zero conductivity, diffusion is instantaneous across ideal non-conductors, but takes increasingly longer as the conductivity σ is increased.

Now, when solving FEM models in the time domain, different techniques exist of converting time derivatives into equations which must be solved at discrete time steps. If the simplest techniques could be used, models using this work's formulation would have unstable solutions if the time step used were longer than the time it takes given (5.12) for **B** to diffuse across some fraction of the smallest conducting element. This restriction is a consequence of the work of Courant et al [144], and the relevance of the associated quantity known as the 'Courant number' to time-stepping general convective and diffusive FEM problems is discussed in [145]. In the next sections, different time stepping techniques will be examined, and it will be considered whether the restriction consequent of Courant's work can be avoided in this work.

5.3 Differenced Time Stepping

In Section 4.3 it was seen that the governing equations (4.21) - (4.23) for the **T**-Φ FEM formulation used in this work contain, at most, first order time derivatives. Perhaps the simplest form of problem involving a first order time derivative would take the form of:

$$G(f) = \frac{\partial f}{\partial t} \tag{5.13}$$

where f is the function to be solved for and G is some spatial operator. Obviously, (5.13) relates to time as a continuum, and a straightforward time discretisation of the equation would be:

$$G\left(f^{(n)}\right) = \frac{f^{(n+1)} - f^{(n)}}{\Delta t} \tag{5.14}$$

where n is a time step number, $f^{(n)}$ is the value of f at the n'th time step, and Δt is the time between two steps. The scheme in (5.14) is known as forward differencing, and a similar scheme known as backward differencing also exists. A slightly more complex, but more accurate, scheme known as central differencing is also often used by practitioners, and all three schemes are discussed in [134].

The solution to (5.14) at step n+1 can readily be seen to be:

$$f^{(n+1)} = \Delta t G\left(f^{(n)}\right) + f^{(n)} \tag{5.15}$$

This has the advantage of being fast to compute since the spatial operator represented by G would simply constitute a matrix multiplication against stored $f^{(n)}$ values in an FEM implementation, and no matrix inversion would be required at each time step. A disadvantage is that, for the reason outlined in the previous section with regard to diffusion, the solution can become numerically unstable if a sufficiently small time step is not chosen. The specific limit on step size can be established using a technique such as von Neumann's stability analysis. Despite this restriction, the fact that no matrix inversion is required means that this type of time-stepping yields solutions relatively quickly, and it is known as explicit time-stepping.

Unfortunately, analysis of the governing equations for the FEM models in this work reveals that matrix inversion must be performed at every time step, which is known as implicit time-stepping. Consider again the first governing equation (4.21) which is reproduced below:

$$\nabla\times\left(\frac{1}{\sigma}\nabla\times\left(\mathbf{T}_s+\mathbf{T}_e\right)\right)=-\frac{\partial}{\partial t}\mu\left(\mathbf{T}_s+\mathbf{T}_e-\nabla\Phi\right) \tag{5.16}$$

$$\nabla\times\left(\frac{1}{\sigma}\nabla\times\mathbf{T}_e\right)+\frac{\partial}{\partial t}\mu\left(\mathbf{T}_e-\nabla\Phi\right)=-\nabla\times\left(\frac{1}{\sigma}\nabla\times\mathbf{T}_s\right)-\frac{\partial}{\partial t}\mu\mathbf{T}_s \tag{5.17}$$

When (5.17) is implemented as an FEM model using the mixed edge and nodal element spatial discretisation described in Section 4.4, and the Galerkin weighting system of Section 4.5, a matrix equation resembling the following will result:

$$\mathbf{S}\mathbf{f}(t)+\mathbf{M}\frac{\partial\mathbf{f}(t)}{\partial t}=-\mathbf{A}\mathbf{s}(t)-\mathbf{B}\frac{\partial\mathbf{s}(t)}{\partial t} \tag{5.18}$$

where $\mathbf{f}$ is a column matrix containing the edge and vector coefficients of $\mathbf{T}_e$ and Φ; $\mathbf{s}$ is a column matrix containing the (already known) $\mathbf{T}_s$ edge coefficients which are the input to the system; and $\mathbf{S}$, $\mathbf{M}$, $\mathbf{A}$, and $\mathbf{B}$ are matrices containing zeros and entries arising from the spatial discretisation of each term in (5.17). A forward differenced time stepping scheme based on (5.18) would resemble:

$$\mathbf{S}\mathbf{f}^{(n)}+\mathbf{M}\frac{\left(\mathbf{f}^{(n+1)}-\mathbf{f}^{(n)}\right)}{\Delta t}=-\mathbf{A}\mathbf{s}^{(n)}-\mathbf{B}\frac{\left(\mathbf{s}^{(n+1)}-\mathbf{s}^{(n)}\right)}{\Delta t} \tag{5.19}$$

$$\mathbf{M}\left(\mathbf{f}^{(n+1)}-\mathbf{f}^{(n)}\right)=-\Delta t\mathbf{S}\mathbf{f}^{(n)}-\Delta t\mathbf{A}\mathbf{s}^{(n)}-\mathbf{B}\left(\mathbf{s}^{(n+1)}-\mathbf{s}^{(n)}\right) \tag{5.20}$$

$$\mathbf{f}^{(n+1)}=\mathbf{f}^{(n)}+\mathbf{M}^{-1}\left[-\Delta t\mathbf{S}\mathbf{f}^{(n)}-\Delta t\mathbf{A}\mathbf{s}^{(n)}-\mathbf{B}\left(\mathbf{s}^{(n+1)}-\mathbf{s}^{(n)}\right)\right] \tag{5.21}$$

Thus to obtain $\mathbf{f}^{(n+1)}$ containing the edge and node element coefficients of $\mathbf{T}_e$ and Φ at the next time step, the matrix $\mathbf{M}$ must be inverted at each step. That inversion makes this form of implicit time-stepping computationally expensive in comparison with the explicit scheme referred to above, particularly when one remembers that similar restrictions apply with regards to time step size and numerical stability. The use of an implicit scheme in this work is, however, unavoidable.

5.4 Improved Implicit Time Stepping

Given the necessity of using implicit time stepping in this work, it would be useful if it were possible to keep computation time to a minimum by using as few time steps as possible – i.e. time steps that are as long as possible. In the differencing scheme of the previous section, numerical stability places a restrictive upper limit on step length. However, a way of circumventing this limit is described in this section.

In this scheme, the time derivatives in the governing equations are replaced, not by simple discrete time difference terms, but by approximating them using a one dimensional finite element scheme in time. The scheme is essentially an application of techniques similar to those of [136] and [137], and may be understood by considering the **T-Φ** formulation's first governing equation as expressed in (5.18) from the previous section and reproduced below:

$$\mathbf{S}\mathbf{f}(t) + \mathbf{M}\frac{\partial \mathbf{f}(t)}{\partial t} = -\mathbf{A}\mathbf{s}(t) - \mathbf{B}\frac{\partial \mathbf{s}(t)}{\partial t} \tag{5.22}$$

Approximations of $\mathbf{f}(t)$ and $\mathbf{s}(t)$ to a first order over the interval between the time steps at $t = t^{(n+1)}$ and $t = t^{(n)}$ may be expressed as:

$$\mathbf{f}(t) = (1-\tau)\mathbf{f}^{(n)} + \tau\mathbf{f}^{(n+1)} \tag{5.23}$$

$$\mathbf{s}(t) = (1-\tau)\mathbf{s}^{(n)} + \tau\mathbf{s}^{(n+1)} \tag{5.24}$$

where

$$\tau = \frac{t - t^{(n)}}{t^{(n+1)} - t^{(n)}} = \frac{t - t^{(n)}}{\Delta t} \tag{5.25}$$

and

$$\frac{\partial \mathbf{f}(t)}{\partial t} = \frac{\partial \mathbf{f}(t)}{\partial \tau}\frac{\partial \tau}{\partial t} = \frac{\mathbf{f}^{(n+1)} - \mathbf{f}^{(n)}}{\Delta t} \tag{5.26}$$

$$\frac{\partial \mathbf{s}(t)}{\partial t} = \frac{\partial \mathbf{s}(t)}{\partial \tau}\frac{\partial \tau}{\partial t} = \frac{\mathbf{s}^{(n+1)} - \mathbf{s}^{(n)}}{\Delta t} \tag{5.27}$$

In this scheme τ may be thought of as a basis function for the approximations of $\mathbf{f}(t)$ and $\mathbf{s}(t)$ with $\mathbf{f}^{(n+1)}$, $\mathbf{f}^{(n)}$, $\mathbf{s}^{(n+1)}$ and $\mathbf{s}^{(n)}$ as 1D finite element nodal values. If τ is also selected as a weighting function, then a Galerkin weighted residual method may be employed to set the weighted average residual error in the representations of $\mathbf{f}(t)$ and $\mathbf{s}(t)$ over the interval to zero:

$$\int_0^1 \left\{ \mathbf{S}\left[(1-\tau)\mathbf{f}^{(n)} + \tau\mathbf{f}^{(n+1)}\right] + \mathbf{M}\frac{\mathbf{f}^{(n+1)} - \mathbf{f}^{(n)}}{\Delta t} + \mathbf{A}\left[(1-\tau)\mathbf{s}^{(n)} + \tau\mathbf{s}^{(n+1)}\right] + \mathbf{B}\frac{\mathbf{s}^{(n+1)} - \mathbf{s}^{(n)}}{\Delta t} \right\} \tau d\tau = 0 \tag{5.28}$$

$$\frac{\mathbf{S}}{6}\mathbf{f}^{(n)} + \frac{\mathbf{S}}{3}\mathbf{f}^{(n+1)} + \frac{\mathbf{M}}{2\Delta t}\mathbf{f}^{(n+1)} - \frac{\mathbf{M}}{2\Delta t}\mathbf{f}^{(n)} + \frac{\mathbf{A}}{6}\mathbf{s}^{(n)} + \frac{\mathbf{A}}{3}\mathbf{s}^{(n+1)} + \frac{\mathbf{B}}{2\Delta t}\mathbf{s}^{(n+1)} - \frac{\mathbf{B}}{2\Delta t}\mathbf{s}^{(n)} = 0 \tag{5.29}$$

$$\mathbf{f}^{(n+1)}\left(\frac{\mathbf{S}}{3} + \frac{\mathbf{M}}{2\Delta t}\right) + \mathbf{f}^{(n)}\left(\frac{\mathbf{S}}{6} - \frac{\mathbf{M}}{2\Delta t}\right) + \mathbf{s}^{(n+1)}\left(\frac{\mathbf{A}}{3} + \frac{\mathbf{B}}{2\Delta t}\right) + \mathbf{s}^{(n)}\left(\frac{\mathbf{A}}{6} - \frac{\mathbf{B}}{2\Delta t}\right) = 0 \tag{5.30}$$

$$\mathbf{f}^{(n+1)} = \left(\frac{\mathbf{M}}{2\Delta t} + \frac{\mathbf{S}}{3}\right)^{-1}\left\{\mathbf{f}^{(n)}\left(\frac{\mathbf{M}}{2\Delta t} - \frac{\mathbf{S}}{6}\right) - \mathbf{s}^{(n+1)}\left(\frac{\mathbf{B}}{2\Delta t} + \frac{\mathbf{A}}{3}\right) + \mathbf{s}^{(n)}\left(\frac{\mathbf{B}}{2\Delta t} - \frac{\mathbf{A}}{6}\right)\right\} \tag{5.31}$$

Thus (5.31) represents a matrix equation which can be solved at each time step to obtain the vector matrix $\mathbf{f}^{(n+1)}$ containing the edge and node element coefficients of $\mathbf{T}_e$ and Φ at that time step.

This scheme can be seen to be a slightly different representation of that described in [138]. Consideration of the basis function τ in (5.25) reveals it to be the same as that

in Figure 10.3(e) of [138], when that reference's parameter Θ takes the value $\frac{2}{3}$. In a later section [139] in the same work, it is seen that the scheme is unconditionally stable when $\Theta \geq \frac{1}{2}$. Therefore the Galerkin time stepping scheme described in this section is numerically stable regardless of the time step size. The scheme that results from using $\Theta = \frac{1}{2}$ is known as the Crank-Nicolson scheme, and suffers from somewhat less truncation error than the Galerkin scheme [140]. However it is prone to exhibit oscillatory behaviour [141] and, since it was desired to avoid such behaviour whilst undertaking this work, it was decided to use the Galerkin scheme instead.

Since the Galerkin time stepping scheme is unconditionally numerically stable, it is possible to choose longer time steps than would be possible when using the differencing scheme of the previous section. This helps to alleviate the problem of lengthy program run times when using implicit time stepping. In theory, the choice of step size is then a trade-off between acceptable solution accuracy and program run time. Smaller time steps produce a more accurate FEM solution in a similar way to that in which a fine spatial mesh give better accuracy, but this is at the cost of greater computation time. The choice of step size is covered in detail in Section 5.7.

5.5 The Time Domain T-Φ Formulation Used in This Work

Given that the Galerkin time stepping scheme has been chosen, it is then possible to obtain the time domain equivalents of the frequency domain governing equations presented in Section 4.7 for the **T-Φ** FEM formulation used in this work. The amendments of Section 4.10 for 2D axi-symmetry will be included at the end of the presentation below.

Let τ be as in (5.25), the edge and nodal element coefficients of $\mathbf{T}_s$, $\mathbf{T}_e$ and Φ respectively be:

$$\mathbf{s}(t) = (1-\tau)\mathbf{s}^{(n)} + \tau\mathbf{s}^{(n+1)} \tag{5.32}$$

$$\mathbf{e}(t) = (1-\tau)\mathbf{e}^{(n)} + \tau\mathbf{e}^{(n+1)} \tag{5.33}$$

$$\mathbf{\Phi}(t) = (1-\tau)\mathbf{\Phi}^{(n)} + \tau\mathbf{\Phi}^{(n+1)} \tag{5.34}$$

and

$$\frac{\partial \mathbf{s}(t)}{\partial t} = \frac{\partial \mathbf{s}(t)}{\partial \tau}\frac{\partial \tau}{\partial t} = \frac{\mathbf{s}^{(n+1)} - \mathbf{s}^{(n)}}{\Delta t} \tag{5.35}$$

$$\frac{\partial \mathbf{e}(t)}{\partial t} = \frac{\partial \mathbf{e}(t)}{\partial \tau}\frac{\partial \tau}{\partial t} = \frac{\mathbf{e}^{(n+1)} - \mathbf{e}^{(n)}}{\Delta t} \tag{5.36}$$

$$\frac{\partial \mathbf{\Phi}(t)}{\partial t} = \frac{\partial \mathbf{\Phi}(t)}{\partial \tau}\frac{\partial \tau}{\partial t} = \frac{\mathbf{\Phi}^{(n+1)} - \mathbf{\Phi}^{(n)}}{\Delta t} \tag{5.37}$$

Let the first governing equation (4.21):

$$\nabla \times \left(\frac{1}{\sigma}\nabla \times (\mathbf{T}_s + \mathbf{T}_e)\right) = -\frac{\partial}{\partial t}\mu(\mathbf{T}_s + \mathbf{T}_e - \nabla\Phi) \tag{5.38}$$

$$\nabla \times \left(\frac{1}{\sigma}\nabla \times \mathbf{T}_e\right) + \frac{\partial}{\partial t}\mu\mathbf{T}_e - \frac{\partial}{\partial t}\mu\nabla\Phi + \nabla \times \left(\frac{1}{\sigma}\nabla \times \mathbf{T}_s\right) + \frac{\partial}{\partial t}\mu\mathbf{T}_s = \mathbf{0} \tag{5.39}$$

after spatial discretisation and spatial Galerkin weighting be represented as:

$$\mathbf{A}\mathbf{e}(t) + \mathbf{B}\frac{\partial \mathbf{e}(t)}{\partial t} - \mathbf{C}\frac{\partial \mathbf{\Phi}(t)}{\partial t} + \mathbf{D}\mathbf{s}(t) + \mathbf{E}\frac{\partial \mathbf{s}(t)}{\partial t} = \mathbf{0} \tag{5.40}$$

Temporal Galerkin weighting of (5.40), in the same manner as (5.28) – (5.29) in the previous section, leads to:

$$\begin{aligned}&\frac{\mathbf{A}}{6}\mathbf{e}^{(n)} + \frac{\mathbf{A}}{3}\mathbf{e}^{(n+1)} + \frac{\mathbf{B}}{2\Delta t}\mathbf{e}^{(n+1)} - \frac{\mathbf{B}}{2\Delta t}\mathbf{e}^{(n)} - \frac{\mathbf{C}}{2\Delta t}\mathbf{\Phi}^{(n+1)} + \frac{\mathbf{C}}{2\Delta t}\mathbf{\Phi}^{(n)} + \\ &\frac{\mathbf{D}}{6}\mathbf{s}^{(n)} + \frac{\mathbf{D}}{3}\mathbf{s}^{(n+1)} + \frac{\mathbf{E}}{2\Delta t}\mathbf{s}^{(n+1)} - \frac{\mathbf{E}}{2\Delta t}\mathbf{s}^{(n)} = 0\end{aligned} \tag{5.41}$$

$$\begin{aligned}&2\Delta t\mathbf{A}\mathbf{e}^{(n+1)} + 3\mathbf{B}\mathbf{e}^{(n+1)} - 3\mathbf{C}\mathbf{\Phi}^{(n+1)} \\ &= -2\Delta t\mathbf{D}\mathbf{s}^{(n+1)} - \Delta t\mathbf{D}\mathbf{s}^{(n)} - 3\mathbf{E}\mathbf{s}^{(n+1)} + 3\mathbf{E}\mathbf{s}^{(n)} - \Delta t\mathbf{A}\mathbf{e}^{(n)} + 3\mathbf{B}\mathbf{e}^{(n)} - 3\mathbf{C}\mathbf{\Phi}^{(n)}\end{aligned} \tag{5.42}$$

Applying a similar representation and then the temporal Galerkin processing sequence to the second governing equation (4.22) yields:

$$\frac{\partial}{\partial t}\nabla\bullet\mu\left(\mathbf{T}_s+\mathbf{T}_e-\nabla\Phi\right)=0 \tag{5.43}$$

$$\frac{\partial}{\partial t}\nabla\bullet\mu\mathbf{T}_e-\frac{\partial}{\partial t}\nabla\bullet\mu\left(\nabla\Phi\right)+\frac{\partial}{\partial t}\nabla\bullet\mu\mathbf{T}_s=0 \tag{5.44}$$

$$\mathbf{F}\frac{\partial\mathbf{e}(t)}{\partial t}-\mathbf{G}\frac{\partial\mathbf{\Phi}(t)}{\partial t}+\mathbf{H}\frac{\partial\mathbf{s}(t)}{\partial t}=0 \tag{5.45}$$

$$\frac{\mathbf{F}}{2\Delta t}\mathbf{e}^{(n+1)}-\frac{\mathbf{F}}{2\Delta t}\mathbf{e}^{(n)}-\frac{\mathbf{G}}{2\Delta t}\mathbf{\Phi}^{(n+1)}+\frac{\mathbf{G}}{2\Delta t}\mathbf{\Phi}^{(n)}+\frac{\mathbf{H}}{2\Delta t}\mathbf{s}^{(n+1)}-\frac{\mathbf{H}}{2\Delta t}\mathbf{s}^{(n)}=0 \tag{5.46}$$

$$3\mathbf{F}\mathbf{e}^{(n+1)}-3\mathbf{G}\mathbf{\Phi}^{(n+1)}=-3\mathbf{H}\mathbf{s}^{(n+1)}+3\mathbf{H}\mathbf{s}^{(n)}+3\mathbf{F}\mathbf{e}^{(n)}-3\mathbf{G}\mathbf{\Phi}^{(n)} \tag{5.47}$$

which contains the common coefficient of three in order that the $\mathbf{e}^{(n+1)}$ term has the same coefficient as the second $\mathbf{e}^{(n+1)}$ term in (5.42); this allows the eventual matrix equation to have a symmetric matrix

Similarly for the third governing equation (4.23):

$$\frac{\partial}{\partial t}\nabla\bullet\mu\left(\mathbf{T}_s-\nabla\Phi\right)=0 \tag{5.48}$$

$$-\frac{\partial}{\partial t}\nabla\bullet\mu\left(\nabla\Phi\right)+\frac{\partial}{\partial t}\nabla\bullet\mu\mathbf{T}_s=0 \tag{5.49}$$

$$-\mathbf{J}\frac{\partial\mathbf{\Phi}(t)}{\partial t}+\mathbf{K}\frac{\partial\mathbf{s}(t)}{\partial t}=0 \tag{5.50}$$

$$-\frac{\mathbf{J}}{2\Delta t}\mathbf{\Phi}^{(n+1)}+\frac{\mathbf{J}}{2\Delta t}\mathbf{\Phi}^{(n)}+\frac{\mathbf{K}}{2\Delta t}\mathbf{s}^{(n+1)}-\frac{\mathbf{K}}{2\Delta t}\mathbf{s}^{(n)}=0 \tag{5.51}$$

$$-\mathbf{J\Phi}^{(n+1)} = -\mathbf{Ks}^{(n+1)} + \mathbf{Ks}^{(n)} - \mathbf{J\Phi}^{(n)} \tag{5.52}$$

(5.42), (5.47) and (5.52) may now be combined with the frequency domain representation in Section 4.7 of the FEM equation system to be solved in this work to give the time domain version of the equation system. To do this, (5.42) is combined with (4.61), (5.47) with (4.66), and (5.52) with (4.68). When the amendment to the formulation for 2D axi-symmetry given in Section 4.10 is also included, and careful attention paid to minus signs from *both* sets of equations, the following equation system arises:

$$\begin{aligned}
&\sum_{i=1}^{n_e}\left\{T_{ei}^{(n+1)}2\Delta t\int_{\Omega_c}\left(\frac{1}{\sigma}r\nabla\times\mathbf{N_i}\right)\bullet\left(\nabla\times\mathbf{N_j}\right)\mathrm{d}\Omega\right\}+\sum_{i=1}^{n_e}\left\{T_{ei}^{(n+1)}3\int_{\Omega_c}\mu r\mathbf{N_i}\bullet\mathbf{N_j}\mathrm{d}\Omega\right\}\\
&-\sum_{i=1}^{n_n}\left\{\Phi_i^{(n+1)}3\int_{\Omega_c}\mu r\left(\nabla N_i\right)\bullet\mathbf{N_j}\mathrm{d}\Omega\right\}=\\
&-\sum_{i=1}^{n_e}\left\{T_{si}^{(n+1)}2\Delta t\int_{\Omega_c}\left(\frac{1}{\sigma}r\nabla\times\mathbf{N_i}\right)\bullet\left(\nabla\times\mathbf{N_j}\right)\mathrm{d}\Omega\right\}-\sum_{i=1}^{n_e}\left\{T_{si}^{(n)}\Delta t\int_{\Omega_c}\left(\frac{1}{\sigma}r\nabla\times\mathbf{N_i}\right)\bullet\left(\nabla\times\mathbf{N_j}\right)\mathrm{d}\Omega\right\}\\
&-\sum_{i=1}^{n_e}\left\{T_{si}^{(n+1)}3\int_{\Omega_c}\mu r\mathbf{N_i}\bullet\mathbf{N_j}\mathrm{d}\Omega\right\}+\sum_{i=1}^{n_e}\left\{T_{si}^{(n)}3\int_{\Omega_c}\mu r\mathbf{N_i}\bullet\mathbf{N_j}\mathrm{d}\Omega\right\}\\
&-\sum_{i=1}^{n_e}\left\{T_{ei}^{(n)}\Delta t\int_{\Omega_c}\left(\frac{1}{\sigma}r\nabla\times\mathbf{N_i}\right)\bullet\left(\nabla\times\mathbf{N_j}\right)\mathrm{d}\Omega\right\}+\sum_{i=1}^{n_e}\left\{T_{ei}^{(n)}3\int_{\Omega_c}\mu r\mathbf{N_i}\bullet\mathbf{N_j}\mathrm{d}\Omega\right\}\\
&-\sum_{i=1}^{n_n}\left\{\Phi_i^{(n)}3\int_{\Omega_c}\mu r\left(\nabla N_i\right)\bullet\mathbf{N_j}\mathrm{d}\Omega\right\}
\end{aligned} \tag{5.53}$$

$$\begin{aligned}
&-\sum_{i=1}^{n_e}\left\{T_{ei}^{(n+1)}3\int_{\Omega_c}\mu r\mathbf{N_i}\bullet\nabla N_j\mathrm{d}\Omega\right\}+\sum_{i=1}^{n_n}\left\{\Phi_i^{(n+1)}3\int_{\Omega_c}\mu r\nabla N_i\bullet\nabla N_j\mathrm{d}\Omega\right\}=\\
&\sum_{i=1}^{n_e}\left\{T_{si}^{(n+1)}3\int_{\Omega_c}\mu r\mathbf{N_i}\bullet\nabla N_j\mathrm{d}\Omega\right\}-\sum_{i=1}^{n_e}\left\{T_{si}^{(n)}3\int_{\Omega_c}\mu r\mathbf{N_i}\bullet\nabla N_j\mathrm{d}\Omega\right\}\\
&-\sum_{i=1}^{n_e}\left\{T_{ei}^{(n)}3\int_{\Omega_c}\mu r\mathbf{N_i}\bullet\nabla N_j\mathrm{d}\Omega\right\}+\sum_{i=1}^{n_n}\left\{\Phi_i^{(n)}3\int_{\Omega_c}\mu r\nabla N_i\bullet\nabla N_j\mathrm{d}\Omega\right\}
\end{aligned} \tag{5.54}$$

$$\sum_{i=1}^{n_n}\left\{\Phi_i^{(n+1)}\int_{\Omega_n}\mu r\nabla N_i\bullet\nabla N_j\mathrm{d}\Omega\right\}=\sum_{i=1}^{n_e}\left\{T_{si}^{(n+1)}\int_{\Omega_n}\mu r\mathbf{N_i}\bullet\nabla N_j\mathrm{d}\Omega\right\}$$
$$-\sum_{i=1}^{n_e}\left\{T_{si}^{(n)}\int_{\Omega_n}\mu r\mathbf{N_i}\bullet\nabla N_j\mathrm{d}\Omega\right\}+\sum_{i=1}^{n_n}\left\{\Phi_i^{(n)}\int_{\Omega_n}\mu r\nabla N_i\bullet\nabla N_j\mathrm{d}\Omega\right\} \quad (5.55)$$

In (5.53), (5.54) and (5.55) notation is as in Section 4.7 except for r, which is as in Section 4.10, and the superscripts and Δt, which have the same time stepping meaning as earlier in this section.

This is the equation system that will be solved at each time step in the 2D axi-symmetric FEM models in the remainder of this work to give the values of the edge and nodal element coefficients of $\mathbf{T_e}$ and Φ at each time step. Together with the edge coefficients of the known input function $\mathbf{T_s}$ at the same time step, these may be used to obtain the magnetic field at that time step using (4.20), which may be post-processed as required. The FORTRAN FEM program developed in this work and referred to in Section 4.9 was extended to incorporate time domain modelling using this equation system. The infinite finite elements referred to in Section 4.8 were retained, and the symmetric matrix three-term recurrence without look-ahead version of the QMRPACK iterative solver referred to in Section 4.11 was also retained albeit using double precision rather than complex variables.

5.6 $\mathbf{T_s}$ in the Time Domain and Initial Conditions

In Section 4.3 it was explained that, in the T-Φ FEM formulation used in this work, the model's input, $\mathbf{T_s}$, is chosen to be the magnetic field that would arise due to the conductors carrying their prescribed through currents at DC. The problem, due to the governing equations, boundary conditions and AC nature of the problem, then becomes one of solving for the corrective magnetic field $\mathbf{T_e} - \nabla\Phi$ which, when added to $\mathbf{T_s}$, gives the true AC magnetic field as in (4.20). In Section 4.6 it was shown how

to obtain $\mathbf{T}_s$, and this method was then used to obtain the input for the frequency domain models in the remainder of Chapter 4.

When modelling in the time domain, it is required that the total current through a coil be able to vary according to some arbitrary current drive function in time so that the coil's model can eventually be coupled to a lumped circuit model of a stimulator, for the reasons explained in Section 4.9. From the previous section, it can be seen that the edge element coefficients of $\mathbf{T}_s$ are required to be known at every time step. These can be obtained at every time step by using knowledge of the value of the total current through the coil at a time $t = t^{(n+1)}$ to calculate a DC magnetic field distribution as in Section 4.6, thus giving the input coefficient $T_s^{(n+1)}$ for each edge at that step. The problem is then one of solving for the corrective magnetic field $\mathbf{T}_e^{(n+1)} - \nabla\Phi^{(n+1)}$ given the boundary conditions, the current time step DC field $\mathbf{T}_s^{(n+1)}$, and the total AC field at the last time step $\mathbf{T}_s^{(n)} + \mathbf{T}_e^{(n)} - \nabla\Phi^{(n)}$, using the equations (5.53), (5.54) and (5.55) from the last section.

Having to calculate $\mathbf{T}_s^{(n+1)}$ at every time step may seem cumbersome, but, in reality, it is only necessary to solve the DC FEM problem of Section 4.6 once using a through current of 1A. Edge coefficients for $\mathbf{T}_s^{(n+1)}$ may then be obtained by simply multiplying each T_s edge coefficient at 1A by the through current at $t = t^{(n+1)}$. The time spent solving a single smaller FEM problem to obtain the distribution of $\mathbf{T}_s$ is therefore very little in comparison to the time taken to solve the main time stepped **T-Φ** formulation FEM problem. Thus the benefits of using **T-Φ** given in Section 4.3 are not outweighed by the cost of having to calculate $\mathbf{T}_s$.

The initial conditions for the main **T-Φ** formulation problem must also be considered. Given that current is deemed to first flow in the coil at time $t = 0$, the conditions at time $t = (0 - \Delta t)$ are simply $\mathbf{T}_s^{(0-\Delta t)} = \mathbf{T}_e^{(0-\Delta t)} = \mathbf{0}$ and $\Phi^{(0-\Delta t)} = 0$. The model can then get underway in a physically realistic manner at $t = 0$ by solving for $\mathbf{T}_e^{(0)} - \nabla\Phi^{(0)}$

given that a through current has just started flowing whose DC distribution $\mathbf{T}_s^{(0)}$ is calculated via the method described in this section.

5.7 Equation System Conditioning and Establishing a Suitable Time Step Size

In Section 5.4, it was seen that the Galerkin based implicit time stepping scheme to be used in this work is numerically stable for any choice of time step size. It was also explained that, with the scheme, smaller time step sizes should improve solution accuracy in a similar manner to that in which a finer spatial mesh gives better accuracy. In this section, the question of what is an appropriate time step size to be used in the remainder of this work will be addressed, and it will be seen that this is somewhat linked to the conditioning of the resulting matrix equation system.

To illustrate this analysis, consider the meshes of Figure 5.1 which show a radially axi-symmetric torus of conducting material discretised at two levels of fineness surrounded by air. The torus has a radius of 4.1mm and the conductor cross-section has a radius of 2mm. In the analysis, a current of 3000A is to flow through the torus at a frequency of 4kHz. The task will be to use this work's time domain FEM program to obtain the magnetic field magnitude at an arbitrary point within the conductor with cylindrical coordinates r=5.9941358mm z=0.18687051mm given that the torus's centre is at r=z=0, and the z axis corresponds to the torus's axis.

To undertake the analysis, frequency domain models of both meshes were first solved using the axi-symmetric **T**-Φ FEM formulation FORTRAN program whose equations appear in Section 4.10, and the magnetic field magnitude at the point obtained. Then, the time domain FORTRAN code discussed in Section 5.5 was run for both meshes using several different time step values. A current function of $3000\sin(2\pi \cdot 4000t)$ was used to drive the time domain models and the magnetic field magnitude at the point was calculated after two and a quarter periods of the sine wave had passed,

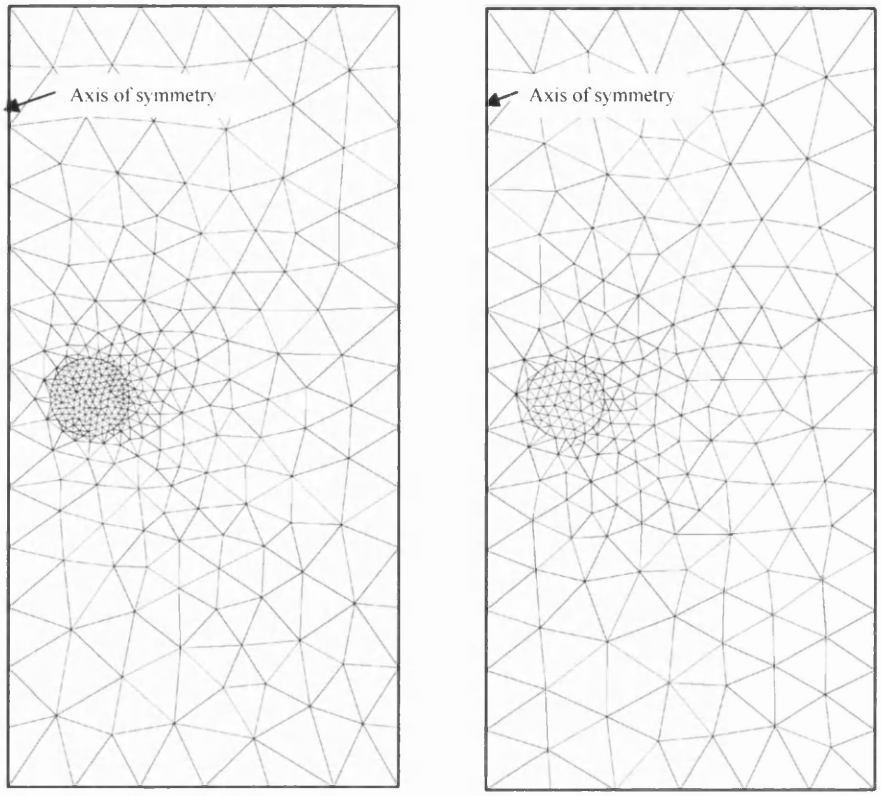

Figure 5.1 - Fine and coarse meshes for axi-symmetric torus

when the current would equal 3000A, so that a direct comparison of the frequency and time domain results could be made.

As reported in Section 4.6, a singular finite element curl-curl matrix arises within the FEM equation system to be solved in this work. This leads the system to be very ill-conditioned, which can result in difficulties when solving problems, including the one discussed in this section. An estimation of the 1-norm condition number [152] for the fine mesh problem of Figure 5.1 obtained using a double precision version of the CON routine from the publicly available NAPACK library (part of NETLIB) was 2.25×10^{21}, and 5.07×10^{21} for the coarse mesh, indicating that the overall equation system is almost singular. When trying to solve both meshes, it was found that, whatever time step size was used, ill-conditioning led the time domain QMRPACK solver, referred to in Section 5.5, to stop processing after five iterations and report that an A-invariant subspace had been found. According to [146], the occurrence of that report means that the solver should have been able to proceed to the correct solution, but that the report arose because either the user defined convergence tolerance was

too strict (too low), or the check for invariant subspaces was too loose (too high). In this work, it was found that the solver terminated early due to an A-invariant subspace even when high convergence tolerance numbers, e.g. 0.1, were used or the tightest possible tolerance parameter for invariant subspace checking was used, i.e. the machine epsilon value [147] for IEEE double precision arithmetic (2^{-52}). This was ultimately due to the nature of the problem's ill-conditioning which caused the number calculated by QMRPACK in order to judge whether an invariant subspace had occurred to be much lower than the epsilon value for double precision arithmetic even though the solver had not yet converged on a valid solution.

Several methods could be used to deal with QMRPACK's invariant subspace report. One method would be to increase the arithmetic precision used for calculations thereby reducing the machine epsilon value, and allowing a smaller/tighter tolerance parameter for invariant subspace checking to be used. Fortran 90 allows precision greater than double to be used and, since the source code for QMRPACK is available in the public domain, this could be converted to work in higher precision. This is undesirable, however, since computation time and computer memory storage requirements are increased.

Another method, would be to divide the equation system (5.53), (5.54) and (5.55) throughout by Δt. This changes the nature of the ill-conditioned system to the extent that QMRPACK is able to solve for and obtain valid solutions for some time values, even though the system is still ill-conditioned – condition numbers for the 4kHz problems in Figure 5.1 were then 2.34×10^{21} and 9.99×10^{20} for the fine and coarse meshes respectively. For the coarse mesh, valid solutions that compared well with the frequency domain solution were obtained in this way with time step sizes of 1.75×10^{-5} s and larger, and 1.25×10^{-5} s and larger for the fine mesh. Below these time step sizes, the solution varied widely and unpredictably. In this method, the invariant subspace report is avoided, but the equation system is still ill-conditioned and valid solver convergence is particularly sensitive to the magnitudes of the values in the matrix, which depend on time step size and mesh geometry (in general, the finer the mesh, the smaller the time step size that can be used). Additionally, valid solver convergence may be impossible at time step sizes that are low enough to adequately represent high quasi-static frequencies (i.e. up to 10kHz) with some geometries.

Therefore, this method of avoiding the invariant subspace report will not be used in this work.

A more reliable method would be to improve the condition of the equation system by using an algorithm known as a pre-conditioner. Many different algorithms exist [149], and different ones are better suited than others to certain problems. Each algorithm involves the cost of some additional computation on the equation system, but this must be weighed against the improvement in solution convergence. The exact choice of the most optimal pre-conditioning technique for this work's FEM formulation could be the subject of lengthy work in its own right, and, in order to have time to complete the other work reported upon in this thesis, such an investigation was not undertaken. Instead, a decision was made to use the two-sided ILUT preconditioning algorithm [150] for the reasons that it is included in some distributions of QMRPACK, a pre-compiled processor optimised version was readily available at hand, and reliable results have been reported when it has been used with QMRPACK for other problems e.g. [151]. A problem with ILUT is that it destroys the symmetry of the equation system, and this meant that the less efficient non-symmetric version of the QMRPACK solver routine had to be used for the remainder of this work. However, with this work's 2D axi-symmetric models, computation times increase by

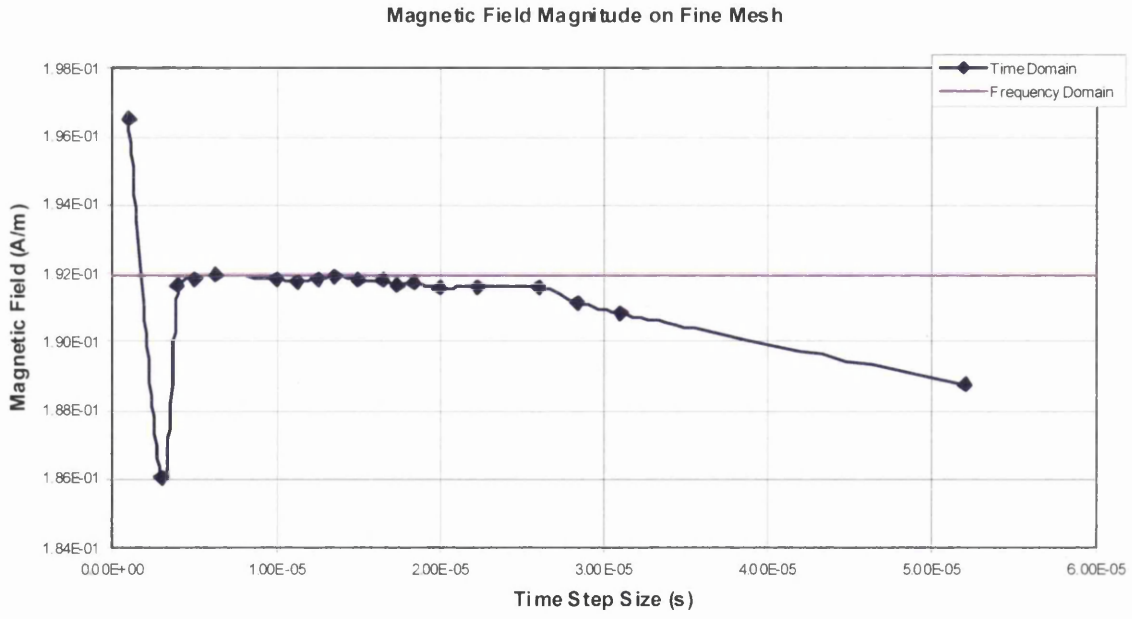

Figure 5.2 - Magnetic field magnitude at point within torus modelled using a fine mesh

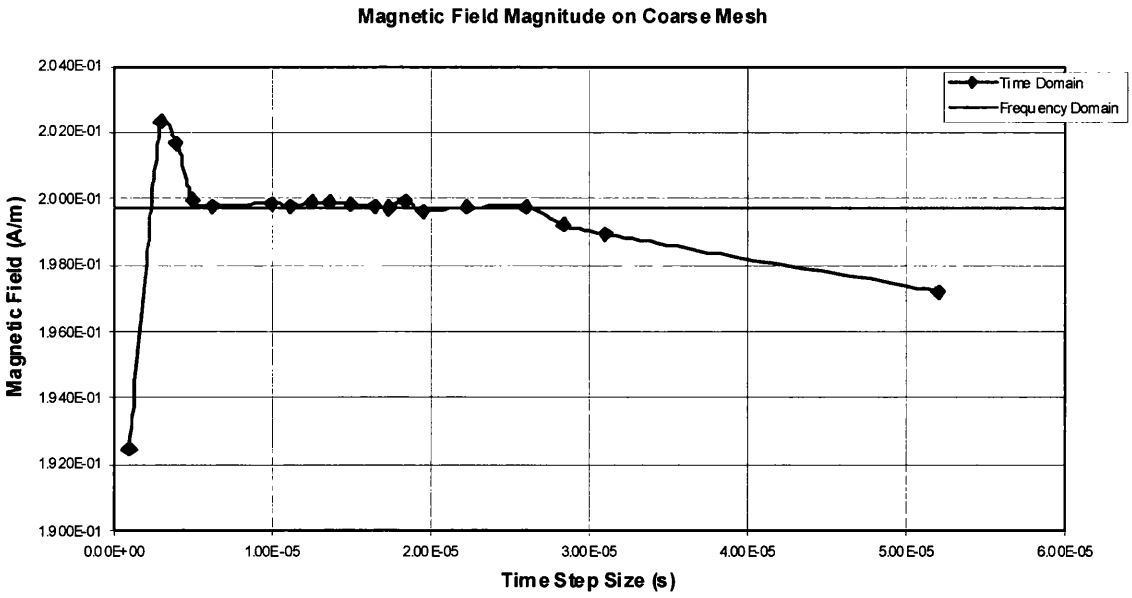

Figure 5.3 - Magnetic field magnitude at point within torus modelled using a coarse mesh

only a small percentage when ILUT and the non-symmetric solver are used instead of the symmetric solver.

Figure 5.2 and Figure 5.3 show the calculated magnetic field magnitudes at the nominated observation points in the fine and coarse mesh models of the problem specified earlier in this section. The time domain lines show the values calculated using the ILUT preconditioner with the non-symmetric QMRPACK solver, and the values calculated using the frequency domain code based on the equations of Section 4.10 (single values for each mesh) are shown as horizontal lines to make comparison with the time domain easier. It can immediately be seen from the figures that, not unexpectedly, the frequency domain modelled field magnitudes differ between the two meshes by some 4% (1.920×10^{-1} V/m on the fine mesh and 1.997×10^{-1} V/m on the coarse mesh) because of the meshes' different spatial discretisation.

However, with both meshes, it can also be seen that, as the time step size is reduced, the time domain field magnitude values converge gradually onto the frequency domain values before remaining very close to those values as the time step is further reduced until a critical point is reached where the time domain values diverge dramatically. It is noticeable that convergence to the frequency domain value occurs at the same time step value of 2.6×10^{-5}s in both meshes. This confirms that the mesh

density had no influence on convergence, and that convergence occurs when the time step size is small enough to adequately represent the frequency content of the current through the conductor, i.e. 4kHz in this example. Repeating the analysis at 10kHz, it was found that convergence occurred at 1.0×10^{-5}s.

Even when using the ILUT preconditioner, QMRPACK iterative solver convergence is still somewhat sensitive to matrix values, but less so than when the equation system (5.53), (5.54) and (5.55) was divided throughout by Δt. In the above example, with ILUT, the time domain solutions are seen to diverge from the frequency domain solutions at time step sizes below 5.0×10^{-6}s and 6.25×10^{-6}s respectively for the fine and coarse meshes. Below 1.0×10^{-6}s, either the solver cannot converge on a solution or an A-invariant subspace error is again reported. Therefore, it can be seen that both time step size and particular spatial mesh density affect matrix conditioning and solution convergence. If higher precision arithmetic is used, valid solutions can be obtained, confirming that the formulation itself is not at fault. However, as it is not desired to use greater than double precision arithmetic in this work, the time step size used should not be too low given the mesh density that is to be used.

In Section 4.12, it was seen that good results were obtained for the current density distribution and the magnetic field around a Magstim HP90 coil with the frequency domain FEM program developed in this work and the particular mesh used. This means that the skin and proximity effects referred to in that section were adequately represented in the model. Therefore, it is proposed to use meshes having the same spatial density within conductors, and in their vicinity, in the coil models of the remainder of this work. That spatial mesh density is the same as that used in the conductor in the fine mesh in this section, and can be selected by using a value of 3.0×10^{-4} for the characteristic length parameter of each point used to define a conductor's geometry in the gmsh meshing program.

Now, since it is desired to be able to represent frequencies up to 10kHz in the models of new coil shapes later in this work, the results of this section suggest that, if results of a similar accuracy to those from a frequency domain model of a coil resonant at a single frequency are desired, a time step no larger than 1.0×10^{-5}s be used. Additionally, to avoid solver convergence problems with the mesh density proposed

for use, the results above suggest that a time step larger than 5.0 $x10^{-6}$s should be used. Therefore, it is proposed to use a time step of 1.0 $x10^{-5}$s with the time domain axi-symmetric **T-Φ** FEM formulation FORTRAN program in the remainder of this work.

Given that dependable results had been obtained using the iterative solver for the time step size that is intended for use in this work it was decided to retain this method of solution for the remainder of this work. This was in preference to implementing the tree-cotree Coulomb full gauging method referred to earlier which would remove the singularity form the equation system being solved.

5.8 A Time Domain FEM Model of a Magstim HP90 Coil

In this section, in order to verify this work's time domain FEM program, the results of using the program to solve an equivalent time domain model of the HP90 coil to that solved in the frequency domain in Section 4.12 will be presented. In the model, the same mesh was used, and two and a quarter periods of the current function $3880\sin(2\pi \cdot 2500t)$ were used to drive the model so that the results, at peak current, could be compared directly with those of the frequency domain model. The time step used was 1.0 $x10^{-5}$s for the reasons explained in the previous section.

The magnetic field was calculated at points along several lines below the coil using the time domain FEM program in a manner similar to that done with the frequency domain program. The mesh described in Section 4.12 with thin layers of finer mesh for 1.5mm above and below each line containing field observation points was used in this analysis. The magnetic flux density was calculated using $\mathbf{B} = \mu\mathbf{H}$ so that a comparison could be made with the measured flux density data supplied by The Magstim Company Ltd that is discussed in Section 4.12 for a HP90 connected to a Magstim Rapid^2 biphasic stimulator resonant at 2.5kHz. Plots of the radial and vertical components of the magnetic flux density are shown in Figure 5.4 and Figure 5.5, where it can be seen that the values computed using the time domain FEM program compare well with the Magstim supplied measured values. It can also be

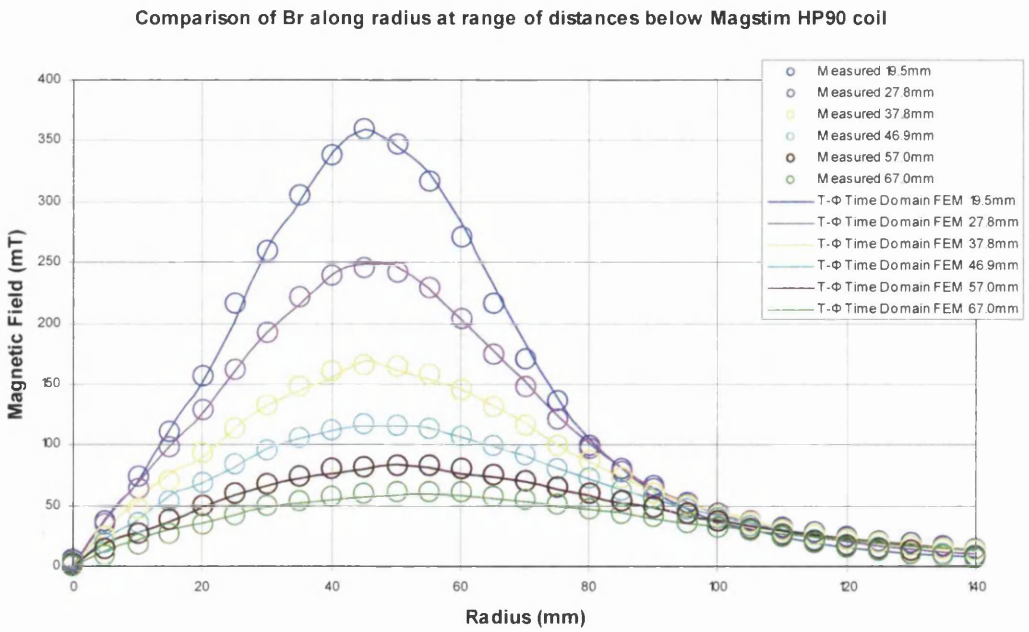

Figure 5.4 - Radial component of the magnetic flux density at points on lines below A HP90 coil calculated using the time domain T-Φ model compared with experimentally measured values

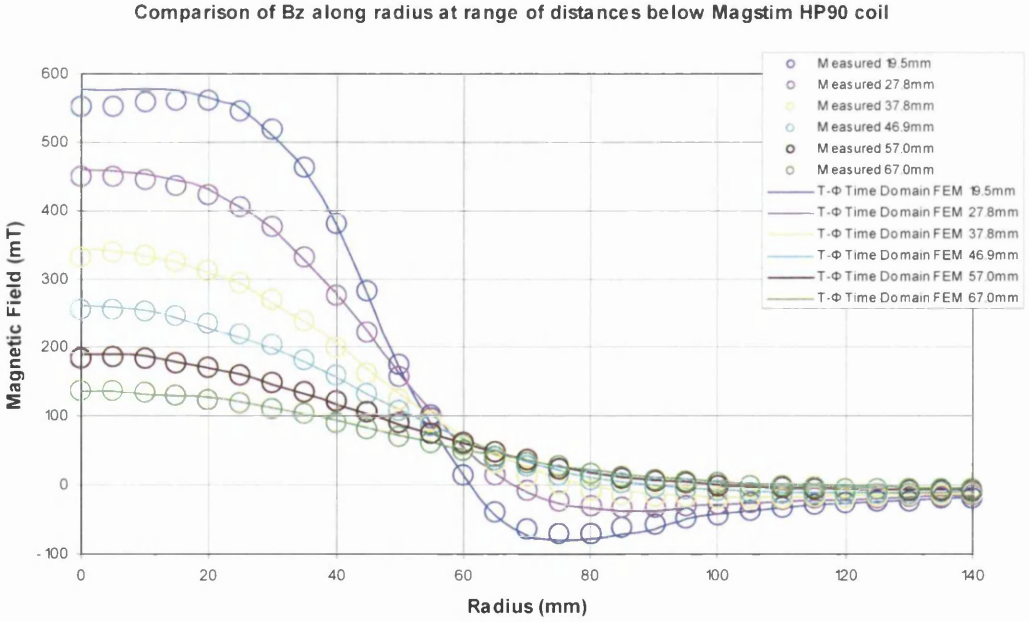

Figure 5.5 - Vertical component of the magnetic flux density at points on lines below a HP90 coil calculated using the time domain T-Φ model compared with experimentally measured values

seen, by comparing Figure 5.4 and Figure 5.5 to Figure 4.16 and Figure 4.17 in Section 4.12 that the flux density values obtained using the time and frequency domain programs compare favourably.

Thus, in this section, it has been demonstrated for the first time that the time domain 2D axi-symmetric **T-Φ** formulation can be used successfully to model the skin and proximity electromagnetic effects in appropriate coil shapes by approximating them as groups of concentric loops. In the above example a sine wave current function was used as input so that the results could be compared to those of the frequency domain program. However, any current function could be used, e.g. the wideband pulse due to a monophasic stimulator, so long as frequency components above the quasi-static limit of 10 kHz are not present.

Nevertheless, in the previous section, it was seen that matrix conditioning is an important issue in the time domain, and that scope exists for future work to identify optimal preconditioning methods for this problem. However, given the successful results presented in this section and the last, it was decided that the time domain FORTRAN program developed in this work would form the basis for the stimulator circuit coupled FEM simulation program that will be the subject of the remainder of this chapter.

5.9 Background to Coupling a T-Φ FEM Coil Model to a Lumped Circuit Stimulating Machine Model

The particular problem of having to solve an FEM model of a stimulation coil coupled to a lumped circuit model of a magnetic stimulation machine falls into the general category of problems known as coupled field-circuit problems and more broadly into the category of FEM problems referred to simply as coupled systems. Previous literature exists discussing both problem categories, examples of which will be given below.

In [153], Tsukerman et al review methods and accomplishments in dealing with two dimensional coupled field-circuit problems for eddy currents, although the discussion does not specifically involve the **T-Φ** FEM formulation. Bedrosian [154] presents a new circuit coupling method applicable in two and three dimensions, but the discussion is confined to the **A-V** potential based FEM formulation. Dular et al [155] report a method which may be used to naturally couple field and circuit models, and it may be seen that this is directly relevant to the **T-Φ** FEM formulation in both two and three dimensions. Also, Zhou et al of Ansoft Corporation present two quite different methods [156], [157] of coupling FEM models of transients in multi winding power machines to circuit models, and the method of [156] is applied in three dimensions using the **T-Φ** formulation.

From the above and other literature, it may be seen that coupled field-circuit problems may be solved using one of two methods. In the so-called direct method, the equations describing the lumped circuit model are incorporated into the FEM equation system and the whole system is then solved simultaneously. Alternatively, in the indirect method, the FEM model and the circuit model are solved as distinct systems which exchange key parameters sometimes known as coupling coefficients with each other in a time stepping procedure.

Both the direct and indirect coupling methods have advantages and disadvantages. The direct method's chief advantage lies with computational stability and efficiency. In the method, only one time stepping procedure applies to the whole coupled system and, if a time stepping process such as the Galerkin method of Section 5.4 were employed, then unconditional stability of the system could be ensured. Nevertheless, in the direct method, the circuit model's equations are embedded into the part of the FEM computer program that assembles the FEM matrix equation system.

The indirect method's advantages are that the circuit and FEM equation systems are quite separate from one another and are therefore conceptually clearly delineated and understood. Both parts of a coupled model may be specified separately from one another, and changes may be made to the circuit equation model without interfering with the FEM model's equation system. This separate specification extends to the nature of the time stepping technique used, and different stepping techniques and time

step sizes could be used for the circuit and FEM models. This flexibility led to the indirect coupling method being adopted in the remainder of this work.

The indirect method's main disadvantage is that the choice of what would seem like the most optimal time stepping technique or time step size for one part of the coupled model could cause the whole model to become numerically unstable. This is similar to the case of the coupled FEM systems discussed by Zienkiewicz and Taylor [158], where two FEM models are indirectly coupled via coupling coefficients which act as boundary conditions in the models. In that work [159], the authors show that, if implicit time stepping schemes such as the Galerkin or Crank-Nicholson schemes discussed in Section 5.4 are used in both parts of the coupled model, the whole system is unconditionally stable. However, if only one half of the coupled model uses such a scheme, stability in the coupled system requires that stability is ensured in the part of the system not using such a scheme by appropriate choice of time step size when that model part is considered without its coupling terms. As has previously been seen in this chapter, the time stepping scheme to be used in the remaining FEM models of this work is the unconditionally stable Galerkin scheme. Therefore, in this work, the lumped circuit model must be made either unconditionally stable or stable when considered as a separate entity for a certain time step size. The particular time stepping technique to be used for the circuit models in the coupled models of this work will be presented in the next section and it is considered to be stable for the time step chosen, thus ensuring stability of the coupled models.

5.10 A Time Stepping Scheme for the Stimulator Circuit Model

In this section, the time stepping scheme to be used in the stimulating machine circuit models that will form part of the coupled coil / stimulator circuit models in the remainder of this work will be described. Since, it is only intended to present later in this thesis examples of the coil geometry optimisation process involving coils being used with a Magstim Rapid^2 biphasic stimulator, the derivation that follows in this section will only be given for a biphasic stimulator, and will be specific to that stimulator type. Nevertheless, it is quite possible to derive a time stepping scheme for a monophasic stimulator circuit.

Consider the circuit of Figure 5.6 which is a simplified representation of a biphasic stimulator coupled to a stimulating coil. In the circuit, R_S and L_S represent the equivalent resistance and inductance of the stimulating machine and the lead connecting it to the coil, C_S is the stimulator's main discharge capacitor, and r_C and l_C are the resistance and inductance of the coil (which change over time during the current pulse through the coil because of the skin and proximity effects described in Section 1.4 and are related to the frequency content of the current pulse). The total resistance and inductance in the circuit at a particular time would be given by:

$$r(t) = R_S + r_C(t) \tag{5.56}$$

$$l(t) = L_S + l_C(t) \tag{5.57}$$

By applying Kirchhoff's Current Law [203] in the circuit, the following may be obtained:

$$i(t) = -C_S \frac{d}{dt}\left[l(t)\frac{di(t)}{dt} + r(t)i(t) \right] \tag{5.58}$$

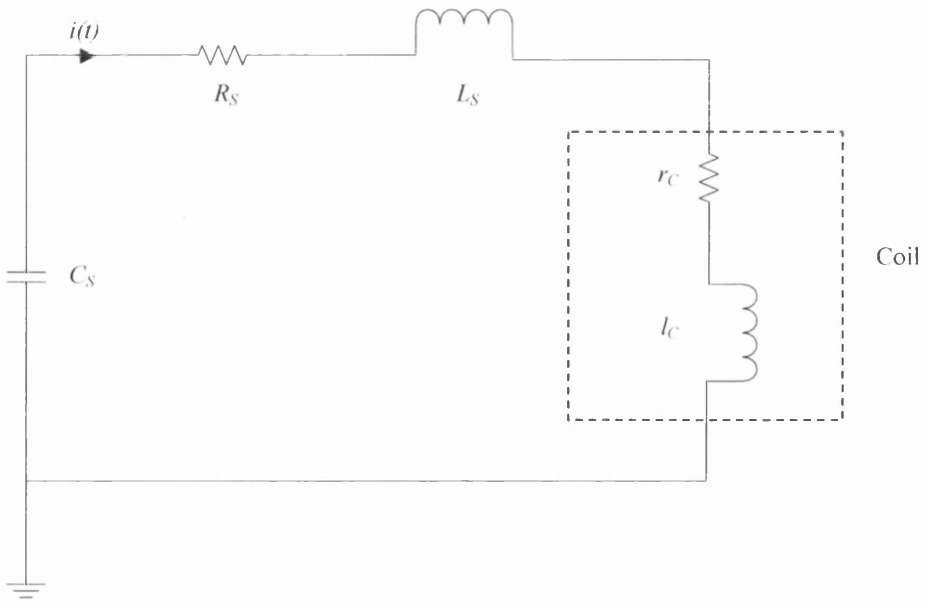

Figure 5.6 - Simplified circuit representation of a biphasic stimulating machine and coil

$$\frac{1}{C_S} i(t) + \frac{d}{dt}\left[l(t)\frac{di(t)}{dt} + r(t)i(t) \right] = 0 \tag{5.59}$$

$$\frac{1}{C_S} i(t) + \frac{d}{dt}\left[l(t)\frac{di(t)}{dt} \right] + \frac{d}{dt}\left[r(t)i(t) \right] = 0 \tag{5.60}$$

$$\frac{1}{C_S} i(t) + l(t)\frac{d^2 i(t)}{dt^2} + \frac{di(t)}{dt}\frac{dl(t)}{dt} + i(t)\frac{dr(t)}{dt} + r(t)\frac{di(t)}{dt} = 0 \tag{5.61}$$

The objective in the circuit model will be to calculate $i(t)$ at the next time step given knowledge of what the other circuit parameters are (including the most up to date values of r and l and their derivatives). Therefore, let the continuous current derivatives in (5.61) be converted into discrete time stepped form using a central differenced approximation for the second derivative and a forward differenced approximation for the first derivative:

$$\left.\frac{d^2 i(t)}{dt^2}\right|_{t=t_{n+1}} \approx \frac{i_{n+1} - 2i_n + i_{n-1}}{(\Delta t)^2} \tag{5.62}$$

$$\left.\frac{di(t)}{dt}\right|_{t=t_n} \approx \frac{i(t_{n+1}) - i(t_n)}{\Delta t} \tag{5.63}$$

where n refers to the time step number and Δt to the time step size. Let also the values of r_C and l_C used to obtain r and l be the values obtained from post-processing the results of the coil FEM model at the most recently completed time step – i.e. step n. Finally, let the values of r and l at the two most recently completed time steps – i.e. steps n and n-1 – be used to convert the continuous r and l derivatives in (5.61) into discrete form using the backward differenced approximations:

$$\left.\frac{dr(t)}{dt}\right|_{t=t_n} \approx \frac{r(t_n) - r(t_{n-1})}{\Delta t} \tag{5.64}$$

$$\left.\frac{dl(t)}{dt}\right|_{t=t_n} \approx \frac{l(t_n)-l(t_{n-1})}{\Delta t} \tag{5.65}$$

If (5.62) to (5.65) are substituted into (5.61), the following is obtained:

$$\frac{1}{C_S}i_{n+1} + l_n\left(\frac{i_{n+1}-2i_n+i_{n-1}}{\Delta t^2}\right) + \left(\frac{i_{n+1}-i_n}{\Delta t}\right)\left(\frac{l_n-l_{n-1}}{\Delta t}\right) + r_n\left(\frac{i_{n+1}-i_n}{\Delta t}\right) + i_{n+1}\left(\frac{r_n-r_{n-1}}{\Delta t}\right) = 0 \tag{5.66}$$

$$i_{n+1} = \frac{i_n\left(\frac{2l_n}{(\Delta t)^2} + \left(\frac{l_n-l_{n-1}}{(\Delta t)^2}\right) + \frac{r_n}{\Delta t}\right) - i_{n-1}\left(\frac{l_n}{(\Delta t)^2}\right)}{\frac{l_n}{(\Delta t)^2} + \left(\frac{l_n-l_{n-1}}{(\Delta t)^2}\right) + \frac{r_n}{\Delta t} + \left(\frac{r_n-r_{n-1}}{\Delta t}\right) + \frac{1}{C_S}} \tag{5.67}$$

Thus, in this work, the above circuit will be coupled to a time domain FEM coil model with the coil drive current (i_{n+1}), r_C and l_C as the coupling parameters. At the instant the simulation begins, just before the stimulator capacitor starts to discharge into the coupled circuit, no current will be present in the coil and r_C and l_C assume values reflecting the fact that no skin or proximity effects are present in the coil. Then, as current flow progresses, the secondary currents induced in the coil would change depending on the magnitude of the coil's through current and the rate of change of through current at a particular time. Thus, as stated above, the instantaneous r_C and l_C values differ at different times – this behaviour, although known of, has not been explicitly reported upon before in relation to stimulation coils and is illustrated for the first time in that context in Appendix C. The inductance of a coil is in fact a property of the coil's geometry; however, here, the secondary currents have the effect of changing the geometry of a coil from an electrical point of view meaning that inductance changes with the secondary currents.

In light of the above, the solution process for the coupled circuit FEM models in this work will be as follows:

1) Calculate r_C and l_C for the situation where no skin and proximity effects exist using the FEM program and the procedure detailed in the next section – this may be done by stopping the FEM program after the DC equivalent $\mathbf{T}_s$ distribution has been derived for a dummy current of 1A and using $\mathbf{H} = \mathbf{T}_s$ and a 1A current in the procedure detailed.

2) Use the calculated r_C and l_C values to derive the drive current for the FEM program for the first time step using (5.67) given that the current at the preceding time step ($t = 0$) was zero.

3) Solve the time domain FEM model and post-process the results as explained in the next section to obtain the latest instantaneous r_C and l_C values.

4) Use these values in (5.67) to obtain the FEM model's drive current for the next time step, and then return to stage three.

This iterative process should be continued until the current pulse through the coupled biphasic system reaches its first peak. The time of this first peak represents $T_B/4$, i.e. one quarter of the resonant period in the biphasic circuit representation discussed in Section 1.3 upon which equation (2.6) in Section 2.3 is based. That equation will be used later in this work when illustrating the functioning of the Main Module of this work's proposed 'tri-modular approach', and it is for that equation that the interpolated values of coil resistance and inductance referred to in Section 2.5.3.2.1 are required. Therefore, after completing the circuit coupled time domain FEM model, it is necessary to convert knowledge of the coupled circuit's resonant frequency to knowledge of the coil's resistance and inductance at that resonant frequency which can later be used in constructing the interpolated values after models of different coil sizes have been run. To undertake this conversion, first calculate the biphasic resonant frequency:

$$f_B = 4 \times \frac{T_B}{4} \tag{5.68}$$

Then, at f_B, run one frequency domain FEM model of the coil using the equation system of Section 4.10 and a dummy 1A drive current. The results of that model should then be used to calculate the coil's resistance and inductance at f_B which are the values required from the FEM modelling to be undertaken in this work.

It will be noticed that the solution of (5.67) at stage two of the coupled circuit iterative process requires knowledge of the circuit current at the time step at $t = 0 - \Delta t$. Additionally, the current at $t = 0$ is zero. Clearly, no current flows in the circuit until the operator triggers the stimulator to begin discharging its capacitor. Nevertheless, for the circuit simulation to proceed, it is necessary for the current to possess some rate of change at $t = 0$. A suitable rate of change may be imposed by considering the circuit in Figure 5.6 at $t = 0$. Since there is zero current at that time, there is no voltage drop across the resistances. Therefore, if the initial voltage across the capacitor is V_0, Kirchhoff's voltage law gives:

$$L\frac{di(t)}{dt} - V_0 = 0 \tag{5.69}$$

Applying the differencing scheme of (5.63) then yields:

$$L\left(\frac{i_{t=0} - i_{t=0-\Delta t}}{\Delta t}\right) - V_0 = 0 \tag{5.70}$$

But $i_{t=0} = 0$, therefore:

$$i_{t=0-\Delta t} = -\frac{V_0 \Delta t}{L} \tag{5.71}$$

where $L = L_S + L_C$ uses a value of L_C for the coil having no skin or proximity effects – i.e. the same value calculated at stage one above. Thus the initial conditions for the biphasic stimulator lumped circuit model are $i_{t=0} = 0$ and (5.71).

Unfortunately, it is far from straightforward to undertake an exact stability analysis for the lumped circuit model encapsulated in (5.67) because the resistance and inductance terms will change with time. Nevertheless, given that it is intended to use the same time step of 1.0 $x10^{-5}$s as the time domain FEM model, it is anticipated that this should prove adequate to model the circuit given that the intended maximum frequency will be 10 kHz. For the reasons given in the previous section, if the circuit model of (5.67) is separately stable, then the coupled circuit and time domain FEM model should be stable.

It would also be possible to use coil drive current and coil voltage as coupling parameters in the biphasic coupled stimulator / circuit model with the drive current as input to the time domain **T-Φ** formulation FEM model, and coil voltage as input to the circuit model. A suitable formula for calculating the coil voltage at the end of each FEM time step appears as (27) in [162]. However, it was decided not to use that technique in this work since it involves applying similar integrals to the FEM model's results to those described in the next section for obtaining R_C and L_C.

5.11 Calculating the Coil Resistance and Inductance

In the previous section it was seen that, in this work, it is necessary to calculate the resistance and inductance of a stimulation coil both during the solution of a coupled coil FEM / biphasic stimulator circuit model and after the solution of a frequency domain FEM coil model at biphasic resonant frequency. This section details the FEM post-processing required to obtain these values, which is a development of the post-processing used to obtain resistances and inductances from frequency domain coil models in [161].

The power dissipated from a stimulation coil at a certain time (or at peak current in a frequency domain scenario) may be given by:

$$P = i^2 R_C \tag{5.72}$$

where i is the current in the coil and R_C its resistance. Alternatively, this may be expressed as an integral over the coil's conductors:

$$P = \int_{\Omega_c} \mathbf{J} \cdot \mathbf{E} \, d\Omega \tag{5.73}$$

where $\mathbf{J}$ is the current density and $\mathbf{E}$ the electric field. Using the constitutive relationship $\mathbf{J} = \sigma \mathbf{E}$, where σ is the conductivity, performing the dot product, and approximating using the FEM mesh discretisation, (5.73) implies:

$$P = \int_{\Omega_c} \frac{J^2}{\sigma} d\Omega \approx \sum_{\text{cond.elements}} \left(\int_{\Omega_{\text{elemnt}}} \frac{J^2}{\sigma} d\Omega \right) \tag{5.74}$$

Equating (5.72) with (5.74) yields:

$$R_C \approx \frac{\sum_{\text{cond.elements}} \left(\int_{\Omega_{\text{elemnt}}} \frac{J^2}{\sigma} d\Omega \right)}{i^2} \tag{5.75}$$

Thus, using (5.75), R_C may be obtained from this work's FEM models by post-processing the results of the FEM model solution using $\mathbf{J} = \nabla \times \mathbf{H} = \nabla \times \left(\mathbf{T}_s + \mathbf{T}_e - \nabla \Phi \right)$, and using the latest coil drive current for i. However, a volume integral must be performed in each conductive element. In the axi-symmetric models of this work this will be done by firstly integrating J^2 across the area of the finite element using the same weighted Gaussian quadrature process used to perform the integration of basis functions across finite elements when constructing the FEM matrix. Then, the same weighting will be used to obtain an average length for the element by firstly calculating at each weighting point the circumference of a circle whose radius is the radial distance from the point to the coil axis. The average element length is then the weighted average of these circumferences, and the required elemental volume integral is then the product of this average length and the J^2 area integration divided by the conductivity of the element.

Similarly, the magnetic energy of a stimulation coil may be given by:

$$W = \frac{1}{2} i^2 L_C \tag{5.76}$$

where L_C is the coil inductance. If the coil is assumed to be in free space, or that is a reasonable approximation, this energy may also be expressed as an integral across all space:

$$W = \frac{1}{2} \int_{\Omega_c + \Omega_n} \mathbf{B} \cdot \mathbf{H} \, d\Omega \tag{5.77}$$

where **B** is the magnetic flux density and **H** the magnetic field. Using the constitutive relationship $\mathbf{B} = \mu \mathbf{H}$, where μ is the permeability, performing the dot product, and approximating using the FEM mesh discretisation, (5.77) implies:

$$W = \frac{1}{2} \int_{\Omega_c + \Omega_n} \mu H^2 d\Omega \approx \frac{1}{2} \sum_{\text{all.elements}} \left(\int_{\Omega_{\text{elemnt}}} \mu H^2 \, d\Omega \right) \tag{5.78}$$

Equating (5.76) with (5.78) yields:

$$L_C \approx \frac{\sum_{\text{all elements}} \left(\int_{\Omega_{\text{elemnt}}} \mu H^2 \, d\Omega \right)}{i^2} \tag{5.79}$$

Thus, using (5.79), L_C may be obtained from this work's FEM models in a similar manner to R_C in (5.75). However, a similar volume integral procedure must be undertaken in all finite elements. Note that in the frequency domain, **J**, **E**, **B**, and **H** are complex.

5.12 Verification of the Circuit Coupled Time Domain FEM model

So that it could be used in the remainder of this work, the FORTRAN based time domain 2D axi-symmetric **T**-Φ formulation FEM program referred to earlier was

expanded to include coupling to a Magstim Rapid^2 biphasic magnetic stimulator using the coupling process described in Section 5.10. The method of calculating the coil resistance and inductance of the previous section was also incorporated. Additionally, the program was set-up to solve one frequency domain FEM model of a coil after obtaining its biphasic resonant frequency using the coupled model so that its resonant resistance and inductance could be calculated. In this section, it will be demonstrated that this particular configuration of circuit and FEM modelling techniques can correctly model a Magstim HP90 coil connected to a Rapid^2 stimulator.

In this section, the same FEM mesh was used as in Section 5.8. The same data regarding the Rapid^2 and its cables was used as was referred to in Section 4.12, specifically leading to the stimulator lumped circuit model having values $R_s = 25\text{m}\Omega$ and $L_s = 1\mu\text{H}$. As in Section 4.12, an initial stimulator capacitor voltage of 1530V was used. The Magstim Company also supplied data that the stimulator's capacitor has a nominal value of 185μF.

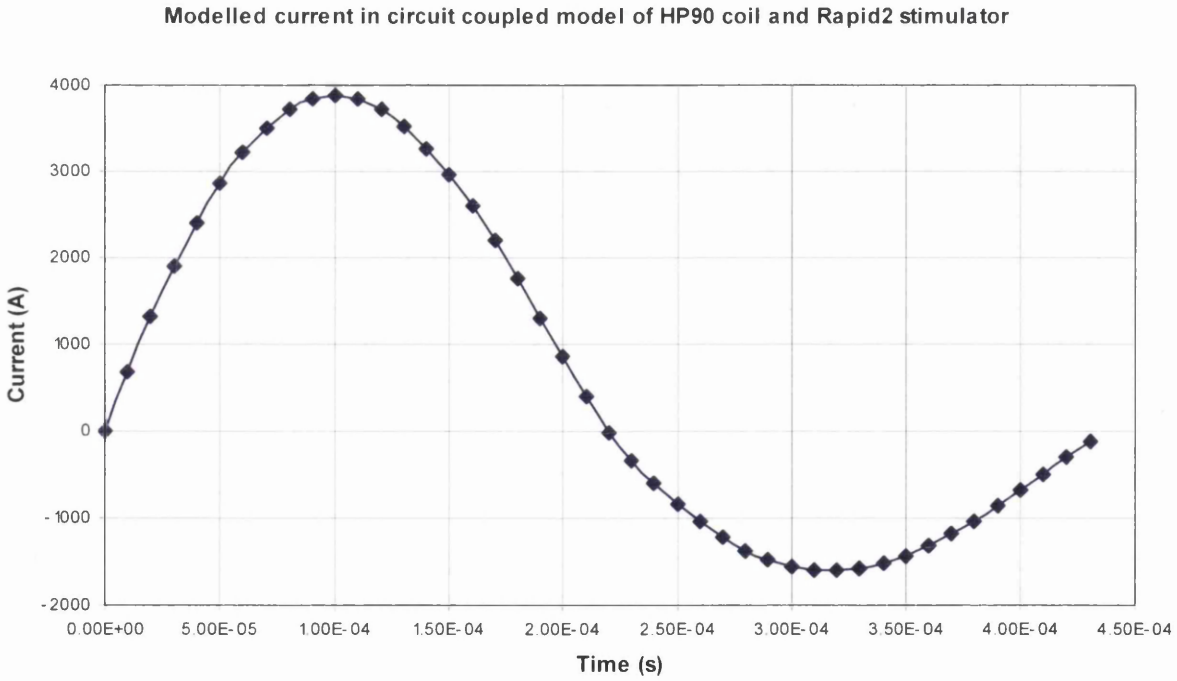

Figure 5.7 - Coil drive current calculated at each time step by the FORTRAN program for the circuit coupled model of a HP90 coil coupled to a Rapid^2 stimulator

Figure 5.7 shows a plot of the current used to drive the **T-Φ** formulation FEM model at each time step of the coupled model calculated by the program using (5.67). It may be seen that the first current peak occurs at time t=1x10^{-4}s. This implies that the biphasic resonant frequency is 2.5kHz. The program then solved a frequency domain model of the HP90 coil at 2.5kHz with a dummy current of 1A, which led to a current distribution identical to that in Figure 4.12 in Section 4.12, albeit with dummy current density values. Finally, the program post-processed this model using a 1A current in (5.75) and (5.79) to obtain values for the coil's resistance and inductance at a resonant frequency of 2.5kHz of 15.64 mΩ and 22.68 μH respectively.

From these results it may be seen that the biphasic resonant frequency for the Magstim Rapid^2 / HP90 coupled system predicted by the program's time stepped circuit coupled model matched the experimentally obtained value of 2.5kHz reported in Section 4.12. Additionally, the modelled values for the coil's resistance and inductance from the frequency domain model compare very favourably with the experimentally obtained values of 16 mΩ and 23 μH respectively. Therefore, it would appear that the expanded FORTRAN program is capable of satisfactorily obtaining the resistance and inductance values of coils appropriate for approximation as groups of concentric loops if they were used with a Magstim Rapid^2, as required for obtaining the interpolated resistance and inductance expressions referred to in Section 2.5.3.2.1.

5.13 Conclusions from Chapter 5

In Chapter 5 it has been shown for the first time that a time domain form of the 2D axi-symmetric **T-Φ** FEM formulation can be used to successfully model the electromagnetic behaviour of appropriate magnetic stimulation coils by approximating them as a collection of concentric circular loops. Good results were obtained for the current density distribution and magnetic fields around a Magstim HP90 coil carrying a through current at 2.5 kHz using an unconditionally stable Galerkin time stepping scheme. However, it was also found that the time domain formulation resulted in an ill-conditioned FEM matrix that required suitable preconditioning before it could be solved with the QMRPACK iterative solver. There

is scope for future identification of a more optimal preconditioning method. Alternatively, as discussed earlier, the formulation could have the Coulomb Gauge fully implemented, including between finite elements, meaning that the matrices to be solved are non-singular thus removing the concern surrounding ill-conditioning.

A method for coupling such a time domain FEM model to a biphasic stimulator circuit requiring the ongoing calculation of instantaneous coil resistance and inductance values from the FEM model has been presented. This method only requires that the coupled model be time stepped until the first biphasic current pulse peak, at which point the model's resonant frequency can be calculated. A frequency domain FEM coil model can then be used to obtain the biphasic resonant frequency resistance and inductance of the coil. This method has been demonstrated to accurately predict the resistance and inductance of a HP90 coil at 2.5 kHz, achieving values very close to experimentally measured ones.

Given the success of this work's FORTRAN program when the above features were added to it, and that it was capable of calculating the resistance and inductance values required of this work's FEM Module from Section 2.5.3.2.2, no further FEM development work was undertaken. In the remainder of this work the FORTRAN FEM program will be used for the purposes described in Chapter 2 of supporting the stimulating coil geometry optimisation procedure.

6 The Optimisation Process

6.1 Background

In Section 1.6 it was explained that one of the main objectives of this work is to develop a way of using optimisation techniques to find more focal magnetic stimulation coil shapes. This was discussed further in Chapter 2, in which it was elucidated upon why, although it is reasonable to define focality in terms of the peak electric field magnitude generated around a coil, it is also important to ensure that a coil is capable of inducing a certain nerve membrane voltage level at the desired location below the coil. In light of this, in Section 2.5 and its subsections, this work's novel tri-modular approach was proposed which avoids having to repetitively run detailed Finite Element Method electromagnetic models during a multi-cycle optimisation sequence. In this approach, optimisation is confined to the Main and New Shape Modules, and, in both modules, only the much faster and simpler thin-wire coil electric field modelling technique of Section 3.8 is used during the optimisation sequence.

There are many different types of techniques in existence that have been used to successfully apply optimisation to a wide variety of problems. A few of these techniques could be suited to the optimisation that must be undertaken in this work's Main and New Shape Modules; however, many other techniques would be unsuited for various reasons. Therefore, this chapter begins by summarising the different types of optimisation techniques available, and places them into several categories. This categorisation eases the task of identifying one particular technique for use in this work, and several reasons are given for the choice then made.

The Main and New Shape Modules both rely on the definition and presence of a set of variables (that are different in both modules) which together adequately describe the geometry of a stimulation coil. These variables are what are altered in the optimisation process, and the results of the optimisation are expressed as a set of particular variable values. Within the optimisation algorithm, strategic changes are

made to the variable values, and a decision made on whether to accept or reject a change based upon whether the change leads to an improvement in the value of a mathematical function. This function would, in the New Shape Module, act as a measure of the coil's focality, and, in the Main Module, would act as a combined measure of the coil's focality and whether a required normalised nerve membrane potential value was being achieved below the coil. Thus, for the chosen optimisation algorithm to work, a set of variables must be chosen, a function must be specified in terms of these variables, and a way must exist to translate a set of variable values into a particular function value. In this work, this translation will involve using the variables to run a thin-wire coil electric field model, then processing the results into a function value.

In this chapter, it is intended to show that the chosen optimisation technique is capable of functioning adequately when used in combination with a function that is defined in terms of a chosen set of coil geometry variables and that is evaluated via thin-wire modelling. To this end, a demonstration problem will be defined, followed by a set of variables and a function. These will be slightly different to those used in the Main and New Shape Modules, but will allow the combination's performance to be straightforwardly assessed. Both modules will be discussed in more detail in Chapter 7. This demonstration problem will be the first time that the combination of that optimisation technique together with such a function defined and evaluated in such a way will have been used to solve an optimisation problem involving the geometry of a stimulating coil.

6.2 Types of Optimisation Techniques

The mathematical process known as optimisation involves searching for the extreme, i.e. the maximum or minimum, value of some predefined function of a set of variables. This can, for minimisation, generally be expressed as:

$$\begin{array}{lll} \text{minimise} & f(\mathbf{x}) & \\ \text{subject to} & g_i(\mathbf{x}) \leq 0 & i = 1.....m \\ \text{and} & h_j(\mathbf{x}) = 0 & j = 1.....p \end{array} \qquad (6.1)$$

where f is the function to be optimised (the objective function), and $\mathbf{x}$ is a vector of n variable quantities (the design variables) which are attributes of the particular problem in hand. When the problem places no constraints on the permissible values of $\mathbf{x}$ (an unconstrained problem), no g or h functions are defined. However, it is common for some restriction to exist on the values that $\mathbf{x}$ may take, and one or more inequality constraint functions, g, or equality constraint functions; h, must then be defined.

Optimisation problems may be classified in several ways. These include, for example, the number of degrees of freedom in the equation system, the dimension of the vector $\mathbf{x}$, and the topography of the function $f(\mathbf{x})$ [163]. However, several important categories involving real valued functions and variables exist, the consideration of which will be helpful when choosing which of the many optimisation techniques should be applied to a problem. These categories will now be briefly discussed.

Perhaps the simplest category is one dimensional unconstrained optimisation which involves finding the optimum value of a function of a single variable without the existence of any constraint functions. Optimisation techniques in this category can be additionally useful as subroutines in techniques for multi-variable problems, and are generally of two types. The first, known as bracketing, involves evaluating the function for a few variable values, and ascertaining the variable interval between which the desired function extremum occurs. The procedure then concentrates on that interval only, and a similar process is followed to identify a smaller interval containing the extremum. Eventually, when the interval size is within some pre-defined tolerance, the extremum is deemed to have been found and the procedure stopped. Techniques of this type differ according to their complexity, stability, number of function evaluations required, speed of convergence, and whether polynomial curve fitting is used to reduce the interval size. Examples of these techniques include the Dichotomous Search Method [164], the Fibonacci Method

[165], the Golden Section Search Method [166], and Brent's quadratic interpolation and sectioning algorithm [167][168].

The second type of one dimensional unconstrained optimisation techniques are open methods. These do not involve interval identification, but rely on knowledge of the function's behaviour to move iteratively from an initial starting guess of the extremum location to its true value. Newton's Method [169] is an open method similar to the Newton-Raphson root finding technique [170] that requires knowledge of the function's first and second derivatives for its iterative procedure.

It should be noted that both the bracketing and open method technique types discussed above are suited to locating a local extremum of a function, e.g. a minimum point between two maxima. Indeed, the bracketing methods are intended for use over an initial function interval that contains no more than one extremum of the type being searched for. If more than one exists over the function interval under consideration, the techniques' behaviours would be unpredictable, possibly converging on one of the extrema, or quite likely not converging at all. The issue of function global and local minima with respect to optimisation is discussed in Sections 2.2 and 2.3 of [171], and Press et al [172] acknowledge that finding a global optimum is a difficult problem. This will be discussed further in Section 6.3.

The next optimisation category is multi-dimensional unconstrained optimisation, which obviously involves an objective function of more than one variable. Techniques in this category are of two types – direct methods which rely on the evaluation of the objective function and derivative methods which require knowledge of the function's first and sometimes second derivatives. Perhaps the simplest direct methods use brute force approaches such as that in the Random Search Method [173] where the function is evaluated at many randomly selected variable values until the extremum is eventually found. Such a method is clearly highly inefficient, but has the advantage, since a wide range of variable values are used, that it is not restricted to finding a local extremum.

More sophisticated search methods include the Cyclic Coordinate Search Method [174] and Powell's Conjugate Direction Method [175]. In these methods, a one

dimensional unconstrained optimisation technique, such as a bracketing method, is used to sequentially search in particular directions for a one dimensional extremum until the multi-dimensional extremum is found. In the cyclic method, these directions are the coordinate directions of the variable vector; however, use may be made of a pattern direction [176] amongst the one dimensional extrema to accelerate towards the multi-dimensional extremum. In Powell's method, pattern directions are used to form a series of conjugate directions in the variable space which are used for the one dimensional searches instead. A different approach is used in the Hooke and Jeeves Method [177] where jumps of a certain distance are made in each of the coordinate directions in a process called exploration instead of using a one dimensional optimisation technique to establish a pattern direction before a longer jump is made in that direction. Rosenbrock's Method [178] involves establishing sets of orthogonal directions for the exploratory jumps in preference to always using the coordinate directions. A further method is that of Nelder and Mead [179] in which a shape known as a simplex, which has one more corners than there are variables, is constructed in the variable space and, for minimisation, the corner where the function has its maximum value is eliminated before geometric transformations known as reflection, expansion or contraction are used to find a replacement point. The procedure of altering the simplex shape is continued cyclically until a small enough simplex surrounding the multi-dimensional extremum is arrived at.

Although the methods of the previous paragraph are usually more efficient than the Random Search Method, they are intended for finding a local rather than global extremum. These methods may, however, be adapted to find global extrema by the introduction of a degree of randomness. Press et al [172] state that this is usually done by either finding several local extrema starting from randomly chosen variable values and then selecting the most extreme, or by taking a finite step away from a local extrema and seeing if the method then proceeds to a more extreme value. Nevertheless, the newer method of Simulated Annealing [180][181] was devised as an improved way of finding the global optimum, and has been successfully applied to several problems. The method mimics the inherent randomness in the way that stored energy alters as a piece of metal cools (anneals), and is suitable for application even in problems where the global extrema is well hidden amongst a collection of local extrema [182]. This method will be discussed in detail in Section 6.4.

One other direct multi-dimensional optimisation technique is the Genetic Algorithm (GA) [183]. This was suggested by John Holland of the University of Michigan and, in its most common form, firstly involves representing each variable as a binary number of a particular number of bits. A random number generator is then used to create an initial 'population' of bits for each variable. These binary numbers are then subjected to a process akin to genetic reproduction with other binary numbers, and the bits making up the numbers are gradually altered in a 'survival of the fittest' process (in terms of whether the resulting variable values cause the function to move closer to an extrema) until no fitter collection of bits can be found for each variable. The final binary numbers for each variable can then be converted back to give the desired optimum values. The GA exists in several variant forms, each of which differs in terms of the number of function evaluations required, their efficiency, and applicability to particular problems. The GA is sometimes used to successfully find global optima, e.g. the example results in [183]; however, it does not always achieve this. Often, depending on the problem, it becomes trapped in a local extremum when the algorithm is unable to move beyond a particular peak in population genetic fitness. As discussed in the introduction of [184], the GA is often good at locating the general area of the global optimum, but then gets trapped in a nearby local optimum. Various techniques may be used to try to stop the GA from becoming trapped, usually involving some random process. These may involve the combination of the GA with another optimisation technique such as Simulated Annealing [184] or the two phase stochastic scheme of [185]. Alternatively, random searching may be incorporated into the GA's iterative procedure – the main work in [184] – or a method known as niching used which involves making efforts to maintain a genetically diverse population during the iterative procedure [186].

Derivative based multi-dimensional unconstrained optimisation techniques use knowledge of the objective function's derivatives to efficiently find an extremum. As in one dimension, the first derivative enables identification of an extremum of some kind, and in more than one dimension this derivative takes the form of a vector gradient in terms of the design variables. Often, when it is not known that the only extremum in the variable space is of the desired type, it is necessary to use the second derivative to establish whether a discovered extremum is a maximum or minimum. In multiple dimensions, this requires the evaluation of a matrix of second partial

derivatives known as the Hessian [187]. If derivatives are not known, it may be possible to calculate them using a numerical method such as the Finite Difference Method, although this may easily become computationally expensive. Frequently used examples of derivative methods include the Steepest Ascent Method [188], the Conjugate Gradient Method [189], Newton's Method [190], and quasi-Newton methods such as the Davidon-Fletcher-Powell and Broyden-Fletcher-Goldfarb-Shanno methods [191].

In practically based optimisation problems, it is often the case that some constraint functions are present, giving rise to the constrained optimisation problem category. Where the objective and constraint functions are linear, the well-known Linear Programming Method [192] may be used to efficiently solve problems having many design variables. With non-linear problems, if knowledge of the function's derivatives is available or not too expensively calculatable, use may be made of one of the methods in Chapter 5 of [193], namely the Generalised Reduced Gradient Method, Rosen's Gradient Projection Method, Zoutendijk's Method, or the Sequential Quadratic Programming Method, some of which convert the problem into an unconstrained form which may then be solved using a direct or gradient based method. However, when use of the function's derivatives is not to be made or is not possible, an indirect method of dealing with the constraints must be used. This is frequently through the use of a penalty function [194] which, constructed from the constraint functions, is added to the objective function and that causes the resulting composite function to become more or less optimal when subjected to an unconstrained optimisation method. Penalty functions will be returned to in Section 6.5. Penalty functions may also be used when a function's derivatives are available, allowing derivative based unconstrained optimisation methods to be used in problems where they behave more desirably than conventional derivative based constrained multi-dimensional optimisation methods.

6.3 Identification of an Appropriate Optimisation Scheme

The previous section offered a general overview of the mathematical procedure known as optimisation together with the main types of optimisation problem.

Furthermore, in Section 2.5.3 and its sub-sections, this work's proposed tri-modular scheme of using optimisation to find improved magnetic stimulation coils is described. There, it is explained that the Main Module will require an optimisation scheme in which certain size governing parameters of a coil having the same 'basic shape' can be varied in order to find the geometry of a coil of that basic shape that can generate a required normalised nerve membrane potential (V_{mn}) value that is also the most focal it can find. The New Shape Module will require an optimisation scheme in which coil geometry parameters that alter the basic coil shape can be changed in an effort to hunt for new basic shapes which minimise a coil's focality defined in terms of its peak electric field (E_0) profile along a straight line at a certain distance below the coil. This section will identify which of the previous section's optimisation techniques may be applied in this work.

To begin with, consider the Main and New Shape modules. From consideration of the previous paragraph, and the discussion in Section 2.5.2 explaining that it is reasonable to define coil focality by considering the E_0 rather than V_{mn} profile, it may be seen that both modules involve altering a set of (slightly different) design variables in order to minimise the E_0 focality. The objective function in both modules can therefore be thought of as the process that translates the design variables (e.g. coil inner turn radius, turn separation distance, etc.) into a representation of the spatial locations of the various turns that make up the coil, calculating the peak electric field at a set of points, then processing that information into the required measure of focality. Additionally, in the Main Module, an equality constraint exists in that the required V_{mn} value at a certain point below the coil (this will be more precisely defined in Section 7.13) must be met. (The V_{mn} would be calculated by multiplying the E_0 value computed from the design variables at the point by the remainder of (2.6) making use of coil resistance and inductance values obtained from the FEM Module.) In reality, this constraint may be converted into an inequality constraint ensuring that the V_{mn} value must be within a certain percentage of the required value. Despite the existence of a constraint in the Main Module, the similarity of the modules' objective functions means that the same optimisation technique will be used for both.

From the above, it should firstly be clear that there is more than one design variable, and that a multi-dimensional optimisation technique must be used. Additionally, it is also apparent that calculating the objective function is far from straightforward, involving several stages to get from the design variables (which are not simple spatial coordinates) to the measure of focality, via a modelling process to obtain E_0 at several points. (As explained in Sections 2.5.3.2.1, 2.5.3.2.2 and 3.9, it is the thin wire coil modelling procedure of Section 3.8 that will be used.) Thus, readily useable derivatives of the objective function in terms of the design variables would not be available and calculating these derivatives using a numerical procedure would be computationally expensive, complicated and impractical. Therefore, it is intended to use a direct multi-dimensional optimisation technique in this work rather than a derivative / gradient / Hessian based method.

Further, as will be discussed in Section 7.6, the objective function in this work could contain several local optima amongst which a global optimum is present. It would therefore be desirable to choose an optimisation technique that can straightforwardly cope with that situation. Although, as mentioned, several of the direct methods listed in the previous section can be adapted to search for global optima, most are inherently local methods. Given that the Simulated Annealing Method is a direct method that has been devised specifically to search for global optima, and that it has already been successfully applied to such problems, it is this method which is the optimisation technique chosen for use in this work. This is in preference to the various forms of the Genetic Algorithm because of the desire to avoid having to be concerned in this work with the various ways, outlined in the previous section, of stopping the algorithm from becoming trapped in a local optimum.

As mentioned, the Main Module's optimisation process will include a constraint function. In the previous section, it was seen that constraint functions may be incorporated into direct multi-dimensional optimisation techniques via a penalty function. Such a penalty function will be used in this work, and the particular form of the objective function, any penalty function and resulting composite functions of this work's Main and New Shape modules will be given in Sections 7.2, 7.5 and 7.13. In the remainder of this chapter, the Simulated Annealing Method will first be discussed

in more detail; a simple coil geometry optimisation problem will then be defined in terms of design variables and penalty function; then Simulated Annealing will be demonstrated to be able to solve the problem when combined with the thin wire electric field modelling technique of Section 3.8.

6.4 Simulated Annealing as Used in this Work

Simulated Annealing (SA) is a direct unconstrained multi-dimensional optimisation technique intended to robustly and efficiently seek a global minimum in a problem where several local minima may exist. Broadly speaking, it does this by sometimes, during an SA minimisation algorithm, accepting a change to the design variable values that results in a higher objective function value rather than always trying to progress to a lower value. Belegundu et al state in [181]: "A robust method for seeking a global minimum must adopt a strategy where a higher value of a function is acceptable under some conditions. Simulated Annealing provides such a strategy."

SA was first proposed by Kirkpatrick et al [195][196] and was based on the earlier work of Metropolis et al [197] which applied the principles of probabilistic thermodynamics to propose a modified Monte Carlo integration method for the computer simulation of fluid states. By now, several slightly different forms of SA are in use, and two such algorithms are described in [180] and [181]. It is the form proposed by Corona et al [198] and described by Belegundu et al in [181] that will be used in this work and the description is the basis for the algorithm's explanation that follows below.

When liquids are allowed to freeze and crystallise in a slow and controlled manner, or some molten material such as a metal or glass is similarly allowed to cool and solidify (anneal), the atoms making up the material lose thermal mobility and adopt positions such that a certain amount of energy is contained in the system. Sometimes during the annealing process, even while the trend is a net loss of energy, there may be an increase in energy. The probability of such an increase in energy ΔE is given by the Boltzmann probability distribution function:

$$p(\Delta E) = e^{-\frac{\Delta E}{kT}} \tag{6.2}$$

where k is Boltzmann's constant [199], and T is the material's temperature. It may be seen that the lower the material's temperature, the less likelihood there is of a large increase in energy occurring.

The above process may be applied to numerical calculations using Metropolis's Algorithm. During optimisation this has the effect that the problem may be considered to always be in some state of temperature, which is initially set to some chosen high value, then gradually reduced, mimicking the annealing process. If, at a step during a minimisation problem, a change is made to the design variables that causes the objective function to decrease, that change is always accepted. However, if the change causes the objective function to increase by a value Δf, the change is accepted with a probability based on (6.2) with Boltzmann's constant replaced by some chosen value, e.g. 1:

$$p(\Delta f) = e^{-\frac{\Delta f}{T}} \tag{6.3}$$

If the change is rejected, the design variables revert to their previous value, and the minimisation process proceeds to its next step when a different change to the variables is considered for acceptance in a similar fashion. The variable change acceptance probability is implemented by generating a random number between 0 and 1, and accepting the change only if the number is less than or equal to the probability value obtained from (6.3).

The SA algorithm used in this work is therefore as follows. An objective function (which, as discussed in the previous section, will be a composite function in the Main Module) is first defined, and this is a function of a set of n coil geometry describing design variables. Each design variable has an upper and lower value bound. The design variable vector $\mathbf{x}$ is initialised to random feasible values, the objective function value at $\mathbf{x}$, namely f, evaluated, and $\mathbf{x}_{\min}$ and $f_{\min}$ set equal to these values.

The algorithm will repeatedly consist of several function evaluations at a particular temperature followed by a reduction in temperature. Therefore, an initial value for the temperature T is defined, which is the first of several parameters within the algorithm which may be changed in order to adjust the algorithm's performance. A temperature reduction factor r_T (with $0 < r_T < 1$) is chosen, and the temperature reduced using $T^{new} = r_T T^{old}$ at the end of each temperature step. Additionally a vector of exploratory step sizes $\mathbf{s}$ is defined for the n variables, whose purpose is given in the next paragraph, and each value in $\mathbf{s}$ is initially set to be some sizeable fraction (e.g. 20%) of the difference between the upper and lower bound for that variable. At the end of each temperature step, the exploratory step sizes are reduced by a factor r_s (with $0 < r_s < 1$) using $\mathbf{s}^{new} = r_s \mathbf{s}^{old}$.

Within each temperature step, a group of N_I 'iterations' are performed, and each iteration involves N_C 'cycles'. During each cycle, an exploratory step is made in each design variable direction in turn, which, for the i'th variable, involves locating a new point in the design variable vector space using:

$$\mathbf{x}_{new} = \mathbf{x} + r s_i \mathbf{e}_i \tag{6.4}$$

where r is a random number between -1 and 1, s_i refers to the i'th element of $\mathbf{s}$, and $\mathbf{e}_i$ is an unit vector in the i'th variable direction. If $x_i + r s_i$ is out of the i'th variable's bounds then $x_{new,i}$ is chosen to be some random value within the bounds. f_{new} is then evaluated at $\mathbf{x}_{new}$ and, if this is less than or equal to f, the exploratory step is 'accepted'. If f_{new} is greater than f, $\Delta f = f_{new} - f$ is calculated, a random number from 0 to 1 generated, and the step accepted if the number is less than or equal to the probability calculated using (6.3). If a step is accepted, the following are updated: $\mathbf{x} = \mathbf{x}_{new}$, $f = f_{new}$; otherwise, $\mathbf{x}$ and f are retained. The next exploratory step in the cycle is then undertaken. Note that, if at an accepted step $f_{new} \le f_{\min}$, then $\mathbf{x}_{\min} = \mathbf{x}_{new}$, $f_{\min} = f_{new}$ are updated.

From the above description, it will be seen that, at higher temperatures before **s** becomes much reduced in sympathy with the temperature via use of the factor r_s, large exploratory steps are able to occur during cycles, and sizeable changes in the objective function's value may result. Any sizeable increase stands a reasonable chance of being accepted while the temperature is high because of (6.3). This gives the algorithm a good chance of escaping from large objective function troughs while searching long distances across the design variable space for regions where the function is low. As the temperature is reduced, the size of any function increase that stands a good chance of being accepted becomes progressively smaller; however, because of the sympathetic reduction in the magnitudes of the elements of **s**, smaller step sizes will occur for which less extreme changes in the objective function could be expected. Thus, the algorithm facilitates searching broadly for the area containing the global minimum at high temperature, then searching in gradually more localised areas as the temperature drops whilst all the time readily accepting some function increases which are of a size appropriate to the exploratory step size so as to try and avoid becoming trapped in a particularly local minimum. The global minimum should eventually be identified from amongst the various broad scale and more localised fluctuations of the objective function.

It may also be seen that the values used for the algorithm's controlling parameters (the initial temperature, r_T and r_s) will have an impact on the algorithm's performance that depends on the nature of the objective function – particularly, how large the fluctuations in its value are, and whether it has broad large scale peaks and troughs which contain more localised maxima and minima or whether it has no overall trend but simply many quite tightly packed extreme peaks and troughs. The way that the parameters are reduced during SA is known as the annealing schedule, and Press et al [200] acknowledge that the exact choice of schedule and meaning of 'high' and 'low' in the algorithm's description is problem dependent and may involve physical insight and trial and error to obtain satisfactory performance.

To help with the choice of step size, Corona et al's version of SA incorporates a technique to improve the exploratory step size whilst the algorithm is executing. This is the reason for the existence of N_I iterations consisting of N_C cycles at each

temperature step. The technique works by having a vector, **a**, whose elements are acceptance ratios for each of the design variables. These acceptance ratios are set equal to 1 at the beginning of each iteration. Then, when, during a cycle, a rejection occurs at an exploratory step involving the *i*'th variable, **a** is updated:

$$a_i = a_i - \frac{1}{N_C} \tag{6.5}$$

Thus, at the end of the N_C cycles in an iteration, each a_i is the ratio of acceptances to trials for that variable during that iteration. At that stage in the algorithm, if an a_i has a low value, it indicates that a relatively high number of rejections has occurred in that variable's exploratory steps, suggesting that the step size should be reduced so that less extreme changes in the objective function's value are encountered. The converse would apply to a high a_i value, and the ideal a_i value would be 0.5 indicating an equal number of acceptances and rejections for that variable. The vector **a** is then used at the end of an iteration to amend the exploratory step sizes **s** for the next iteration's cycles by applying to each variable the following formula shown for the *i*'th variable:

$$s_i^{new} = g(a_i)\, s_i^{old} \tag{6.6}$$

where g is a 'step multiplication factor' and takes the form [201]:

$$\begin{aligned} g(a_i) &= \frac{1}{1+2\dfrac{0.4-a_i}{0.4}} && a_i < 0.4 \\ &= 1 && 0.4 < a_i < 0.6 \\ &= 1+2\frac{a_i-0.6}{0.4} && a_i > 0.6 \end{aligned} \tag{6.7}$$

It should be emphasised that each a_i is reset to 1 at the beginning of each iteration and **s** is reset using $\mathbf{s}_{new} = r_s \mathbf{s}^{old\_orig}$ at the beginning of each new temperature step where $\mathbf{s}^{old\_orig}$ is the value of **s** at the beginning of the previous temperature step

before any step multiplication factors were applied. It is stated in [201] that the step multiplication factor system described above has been shown to work well in tests.

The algorithm may come to an end in several ways. The first is if the function minimum at the end of a temperature step is not less than the minimum at the end of the previous step or is less but only within some small margin. (The definition of a small margin depends on the problem being solved.) The second way is if more than a fixed number of temperature steps have been completed, thus stopping the algorithm from potentially executing indefinitely.

6.5 Definition of a Demonstration Problem

In Section 6.3, reasons were given for choosing Simulated Annealing (SA) as the optimisation technique to be used in this work, and, in the previous section, the particular type of SA to be used was discussed in some detail. In this section and the next, it will be shown that, after defining a set of design variables and a suitable constraint penalty function, this type of SA can be used together with the thin wire electric field modelling technique of Section 3.8 to solve a basic stimulation coil optimisation problem. This will serve to demonstrate that it is possible to construct a penalty function suitable for use with SA that is a function of some chosen coil geometry describing variables, that the SA algorithm is reliable when used with this type of penalty function, and that the thin wire modelling technique is suited to assimilation into this optimisation process. Thus, this will be the first time that this combination of a penalty function, SA and the thin wire modelling technique will be shown to be able to solve an optimisation problem involving the geometry of a magnetic stimulation coil.

First, it is necessary to define a problem to be solved. The initial step in this definition process is to state that, in the interest of simplicity, the problem will involve the peak electric field around a stimulation coil connected to a hypothetical stimulating machine that always generates a peak rate of change of current of 1 A/s through a coil. (The more realistic optimisation undertaken in the next chapter will involve a Magstim Rapid^2 biphasic stimulator.) Next, let the problem involve a single flat spiral

coil similar to the Magstim HP90 coil, and the problem be to find coil dimensions that would allow the coil, when it is used with the stimulator, to generate a peak electric field magnitude of at least a certain amount at one chosen point below the coil's plane, and no greater than some other amounts at two other points below the coil's plane.

Given that the spiral coil will be modelled as being composed of concentric circular loops of infinitesimally thin wire, and that the spacing between the spiral turns is to be regular, such a coil's geometry can be fully described by only three variables. These are: the turn separation distance, the number of turns, and a third variable which could be the inner turn's radius, the outer turn's radius, the average turn radius, etc. The radius and location of each loop making up the spiral coil model can be calculated from these variables. In this problem, the design variables will be the turn separation distance, the number of turns, and the inner turn's radius. The design variable limits will be:

Number of Turns:	7 – 28
Inner Radius:	10 – 80 mm
Turn Separation Distance:	1.8 – 3.5 mm

The three peak field measurement points will be on a line parallel to the coil's plane at a distance of 70mm below the coil since that represents a typical distance away from a coil's plane for a magnetic stimulation location. The task for the optimisation problem in this section will be to find a set of design variable values that would result in a single spiral coil capable of generating a peak electric field of at least 5.9×10^{-7} V/m at a radius of 70 mm, but no greater than 3.10×10^{-7} V/m and 4.66×10^{-7} V/m at radii of 20 mm and 120 mm respectively away from the coil's axis along the line 70mm below the coil. The field value constraints were chosen because, from the results of a preparatory investigation, it is known that the constraints may be achieved with several different values of the design variables – i.e. there is more than one valid solution to the problem – but most of the design variable space results in the constraints not being met; this is shown graphically later in this section.

A penalty function must now be constructed to incorporate the field value constraints given in the last paragraph. This is a function which will take on its minimum value – zero – when the constraints are met, but which becomes sharply more positive when a change in any of the design variables causes the peak electric field to be further away from the constraint values. For this sample problem a suitable penalty function would be:

$$P(\mathbf{x}) = c_p \left[\max\left(0, F_m - f_m(\mathbf{x})\right)^2 + \left[\sum_{i=1}^{2} \max\left(0, f_{s_i}(\mathbf{x}) - F_{s_i}\right)^2 \right] \right] \qquad (6.8)$$

In (6.8), **x** refers to the design variable vector, m to the spatial point at which the field must be at least 5.9 x 10^{-7} V/m, and s to the two points at which the field should be no greater than 3.10 x 10^{-7} V/m and 4.66 x 10^{-7} V/m respectively. Each F refers to the field constraint limit (greater than or less than as appropriate) at the point in question, and each f (**x**) to the peak electric field magnitude at the point in question given a particular set of design variables as obtained via the thin wire loop coil model of Section 3.8. It may be seen that the 'max' term involving point m takes on a zero value when the field magnitude at that point, f_m, is greater than or equal to the field magnitude constraint value, F_m, but takes on an increasingly positive value the more f_m is less than F_m. Conversely, the 'max' terms involving the s points are zero valued when the peak electric field magnitude, f_s, at the relevant point is less than or equal to the corresponding field magnitude constraint value, F_s, but takes on an increasingly positive value the more f_s is greater than F_s. The factor c_p governs how steeply the penalty function becomes positive when the constraints are broken, and its value may be chosen so as to result in an adequately performing algorithm in a similar way that the initial temperature, r_T and r_s may be chosen within the SA algorithm as described in the previous section.

In order to obtain a graphical plot of the penalty function as specified above, a combined C++ and FORTRAN program was authored that was capable of calculating (6.8) for a particular set of design variable values. This worked by calculating the radius and location of each loop in a thin-wire concentric loop model of the spiral coil

from the design variables, then solving the model to obtain f_m and the two f_s values. The program was run for a range of values across the design variable space. A value of 10^{15} was used for the factor c_p in (6.8).

It is obviously not possible to construct a single graph of a function of three independent variables. However, Figure 6.1 shows the penalty function as a function of the number of turns and the inner radius given a fixed turn separation distance of 2.65mm. It may be seen that the graph shows a distinct 'valley' running WSW-ENE, with a steep rise to a peak of 11233 at 28 turns, inner radius 80mm; a much less steep rise occurs at the graph's opposite corner to 290.832 at 7 turns, inner radius 10mm. The valley may be seen in greater detail by restricting the graph viewing software to a peak of 50, as in Figure 6.2. When viewing this graph it should be remembered that the number of turns is an integer variable, and this graph shows that for each discrete number of turns value, the penalty function forms a parabola against the inner radius value; the parabolas appear as V's for number of turns of 25 and above due to the graphing program having insufficient points with a penalty function value below 50 to

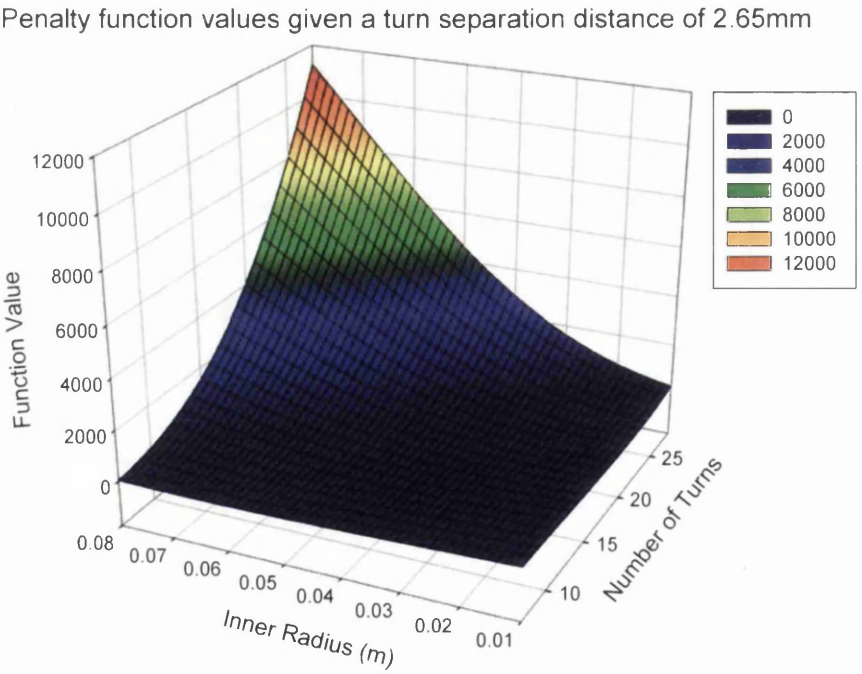

Figure 6.1 - The initial form of the demonstration problem penalty function when the turn separation distance is 2.65 mm

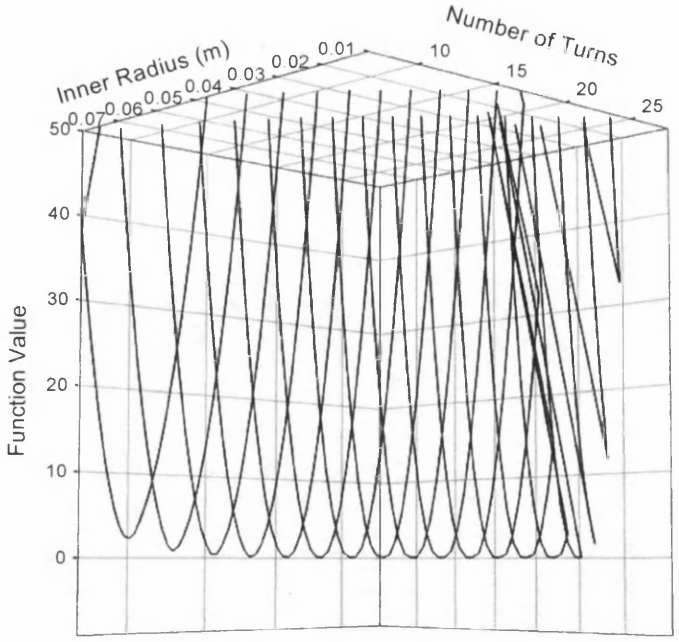

Figure 6.2 – The penalty function of Figure 6.1 when the graphing program is restricted to only show function values of 50 or less

correctly form parabolas. From Figure 6.2, it may be seen that the valley floor in Figure 6.1 is not flat, but is a minimum of zero only for number of turns values between 13 and 21.

Figure 6.3 offers an example of how the penalty function behaves against the third design variable – turn separation distance – when the other two variables are fixed. Here, there are 13 turns and an inner radius of 35.2 mm. The function is seen to behave essentially as a parabola, except that there is a flattened out region at the parabola's base where the function is minimal and zero valued. In fact, a similar parabolic type graph may be seen for the penalty function against turn separation distance when any values are used for the number of turns and inner radius; however, a flat zero valued base region only occurs when the combination of number of turns and inner radius are such that there is a range of turn separation distance values for which the problem's constraints are met. At number of turns and inner radius values for which no turn separation distance value leads to the constraints being met, the

graph of the penalty function against turn separation distance appears as a true parabola with a non-zero minimum value.

From consideration of the above discussion, it should not be surprising that the penalty function in its above specified form, when considered against all three design variables together, is a zero valued minimum across one restricted region of the design variable space, and is always increasing in any direction away from that region. However, in Section 6.3, it was stated that the optimisation technique to be used in this work must be able to deal with a function that has more than one separate local optimum amongst which a global optimum is present. Also, if that global optimum does spread over a region of the variable space rather than only be existent at one set of variable values, it would be desirable that this work's optimisation technique be able to correctly identify one set of design variables corresponding to that optimum.

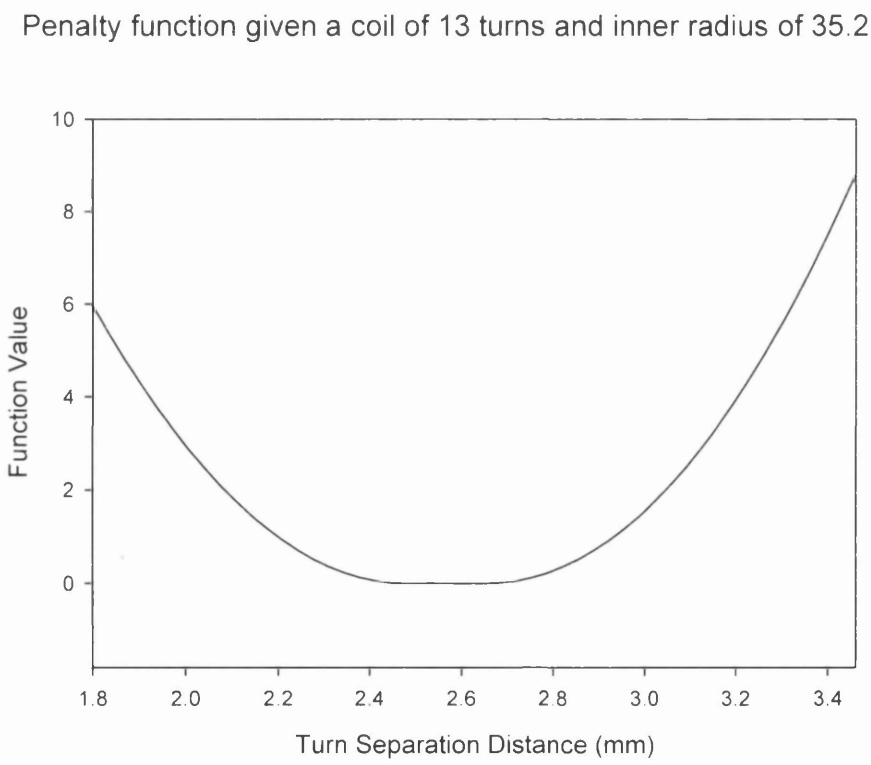

Figure 6.3 - The initial form of the demonstration problem penalty function when the number of turns is 13 and the inner radius is 35.2 mm

In order to demonstrate that the combination of SA, penalty function and thin wire modelling is capable of working with functions having the characteristics described in the previous paragraph, an amendment was made to the demonstration problem penalty function (6.8). The revised function is as follows:

$$P(\mathbf{x}) = c_p\left[\max\left(0, F_m - f_m(\mathbf{x})\right)^2 + \left[\sum_{i=1}^{2}\max\left(0, f_{s_i}(\mathbf{x}) - F_{s_i}\right)^2\right]\right] + \max\left(0, x_1 - 10\right)^2$$

when $x_1 \leq 16$

$$P(\mathbf{x}) = c_p\left[\max\left(0, F_m - f_m(\mathbf{x})\right)^2 + \left[\sum_{i=1}^{2}\max\left(0, f_{s_i}(\mathbf{x}) - F_{s_i}\right)^2\right]\right] + \max\left(0, 17 - x_1\right)^2$$

when $x_1 \geq 11$

(6.9)

where x_1 refers to the number of turns design variable.

The amended penalty function is broadly similar to (6.8). However, it may be seen from Figure 6.4 that the valley floor apparent in Figure 6.2 when the turn separation distance is 2.65 mm has changed somewhat. There is now a non-zero local minimum of 0.0677376 when the number of turns is 10, another local minimum of 25.0 at 13

Revised penalty function values below 50 given a turn separation distance of 2.65mm

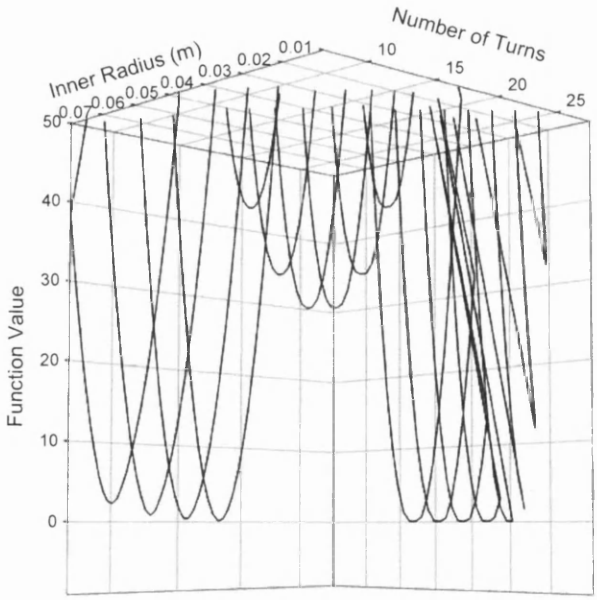

Figure 6.4 - The amended demonstration problem penalty function when the turn separation distance is 2.65 mm and the graphing program is restricted to only show function values below 50

turns, and a zero valued global minimum which spreads over the region from 17 to 21 turns. The parabolic nature of the function against inner radius value and turn separation distance is maintained.

Thus, the objective of the demonstration optimisation problem will be to show that the combination of SA, penalty function and thin wire modelling can find a point on the global minimum of the penalty function; this will be zero valued and corresponds to design variable values that would result in a coil that meets the peak electric field constraints given earlier – i.e. a valid solution to the problem. The results of applying the combination to this problem are presented in the next section.

It should be noted that this sample problem is a little different to the bulk of the optimisation that will be undertaken in this work. There, as stated in Section 6.3, the task will be to find a set of design variable values that minimises focality, i.e. seeks a coil having the best focality, subject to, in the Main Module, a constraint on the normalised nerve membrane potential value. The functions used in the New Shape and Main Modules that involve optimising towards a coil having the best focality are given in Sections 7.5 and 7.13 respectively. Here though, a satisfactory solution to the problem would be any set of design variable values meeting the field value constraints given above. Thus this problem will consist of only a penalty function and no objective function as such. Nevertheless, this sample problem is perfectly suited to demonstrating that, after the construction of an adequate penalty function, the combination of SA, penalty function and thin wire modelling works as required since the optimisation in the Main and New Shape Modules may also include situations where the composite function has several broad global minima – i.e. where the objective function takes on the same minimum value because the focality is the same and is a minimum, and the penalty function is zero because the nerve membrane constraint is met. However, it should also be noted that the algorithm can only identify one point on one global minimum, even if there is more than one equal global minimum and a minimum extends over a region of the variable space.

Additionally, because of the random factor inherent to SA's operation, re-running the algorithm when more than one such valid solution exists could result in a different valid solution being identified. If the solutions are truly equally valid then this should

not be a problem – any of the coils resulting from the solution's design variables would work just as well as each other. However, if it were later felt that one of these solutions had more desirable properties than another, the penalty function would need to be altered in a way so as to take on its least value only for the more desirable solution. This possibility of different equally valid solutions being reported at each algorithm run is inherent to the chosen SA optimisation technique and will feature in both this sample problem and the optimisation in the remainder of this work.

6.6 Results from the Demonstration Problem

In order to solve the demonstration problem described in the previous section, the combined C++ and FORTRAN program used to plot the problem's penalty function was extended so that its core routine was the Simulated Annealing algorithm of Corona et al given in Section 6.4. Each time the algorithm required a penalty function evaluation, the routines previously used to evaluate the function for plotting in terms of the design variables were called. Thus the algorithm was able to systematically alter the design variables and establish whether the penalty function value reduced or not in an attempt to find the function's global minimum. When the minimum was found, the program would then determine whether the function was zero valued, indicating that the constraints had been met and a valid solution coil found.

In this problem, the inner radius and turn separation distance variables are real valued, but the number of turns variable is an integer. The chosen optimisation algorithm of Section 6.4 is intended for real variables, although slightly different SA algorithms have been devised specifically for integer problems, e.g. [202]. In this work, it was decided, for programmatic simplicity, to accommodate integer variables within the chosen SA algorithm. This is achieved by, each time a new value of an integer variable is calculated by the algorithm at an exploratory step, rounding the variable value to the nearest integer before using the value to construct a coil model and evaluate the function. For the sample problem, this has the effect that the penalty function, against the number of turns variable, resembles a staircase with any step edges occurring at half way points between integer values. It was also decided that, if this method of accommodating integers was found to cause the algorithm to not

converge quickly enough or fail to find solutions correctly, then a different method would be used.

To solve the demonstration problem to obtain the results given below, the following values used in the SA algorithm, whose meanings are given in Section 6.4, were found to give an efficient performance: $N_I = 5$, $N_C = 20$, $r_T = 0.5$ and $r_s = 0.9$. An initial annealing temperature of 1000 K was used. The algorithm was set to terminate if convergence on a minimum did not occur in 20 temperature steps, or the penalty function minimum at the end of a temperature step was not less than the minimum at the end of the previous step by more than a margin of 10^{-6} plus 10^{-10} times the penalty function minimum.

The combined C++ and FORTRAN program was repeatedly run 200 times on a Pentium 4 1.8 GHz personal computer and each set of suggested coil design variable values recorded. Figure 6.5 shows these design variable values as points in a three dimensional space.

It should be noted that the program did not fail to converge and report a valid solution at any of the 200 runs undertaken. This is very encouraging given that it is known from the analysis of the penalty function undertaken in the previous section that a region of valid solutions exists in the variable space. It may also be seen that each run required 11 temperature steps and took between 13 and 21 seconds to execute. This is certainly not an excessively long time given that a thin-wire coil model would have been solved at each exploratory step during the SA algorithm, and suggests that one run of the Main or New Shape Finding Modules should not take many tens of minutes or longer to run.

Examination of Figure 6.5 reveals that the program has only reported solutions having between 17 and 21 turns. This means that the SA algorithm has avoided becoming trapped in the penalty function's local minima at 10 and 13 turns and has not been sidetracked into failing to converge on a valid solution at the global minimum due to the presence of the local minima. Furthermore, it is apparent that the program has not been induced to fail to converge because of the fact that the global minimum extends

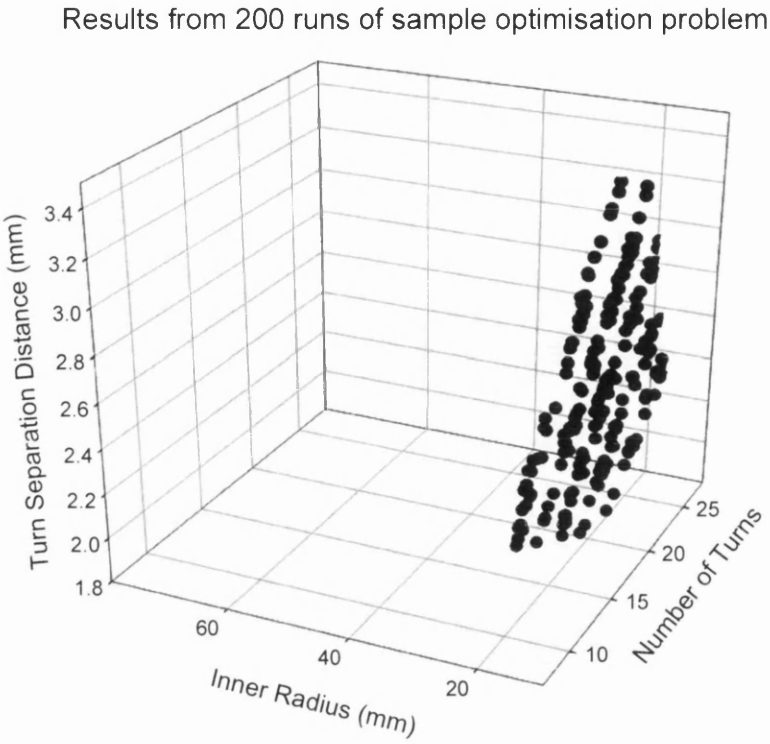

Figure 6.5 – The design variable values obtained from 200 runs of the demonstration optimisation problem

over a region of several sets of design variable values rather than existing at only one set.

From knowledge of the penalty function's behaviour across the whole of the variable space, it is also apparent from the results that the program has not erroneously suggested solutions at which the function is non-zero and the constraints not met. The lack of spurious solutions has been verified by separately solving thin wire coil models at a random group of variable space points not suggested as solutions by the program and verifying that the peak electric field constraints are indeed not met at those points.

In Figure 6.5 it can be clearly seen that the program's suggested solutions all occupy a distinct region in the variable space, and, from knowledge of the penalty function, it can be confirmed that this region corresponds to the function's global minimum region at which it is zero valued and the field constraints met. Additionally, a random sample of suggested solutions were used to construct models of spiral coils using the

discretised thin-wire coil modeller of Section 3.7 in which a spiral coil is represented as a spiral rather than concentric loops of thin-wire. These models confirmed that coils having the dimensions of the suggested solutions do meet the field constraints. An example of this is given in Figure 6.6 for a suggested solution that has: number of turns = 18, inner radius = 15.2904 mm and turn separation distance = 2.97853 mm. In the figure, the field constraint points are marked as brown and green points, and the blue line represents the peak electric field that would result along a line parallel to the coil's plane at a distance of 70 mm below it with the graph's radius axis referring to the distance away from the coil's axis along that line. A hypothetical stimulator that always generates a peak rate of change of current of 1 A/s was used to 'feed' the coil model so as to match the stimulator used in the optimisation program. It may be seen in Figure 6.6 that the coil does indeed have a peak electric field that exceeds the field constraint of 5.9 x 10^{-7} V/m at the F_m point at 70mm radius at 70mm below the coil, and does not exceed the field constraints of 3.10 x 10^{-7} V/m and 4.66 x 10^{-7} V/m at the F_s points at radii of 20 mm and 120 mm respectively at 70mm below the coil. This is as required in the demonstration problem's specification.

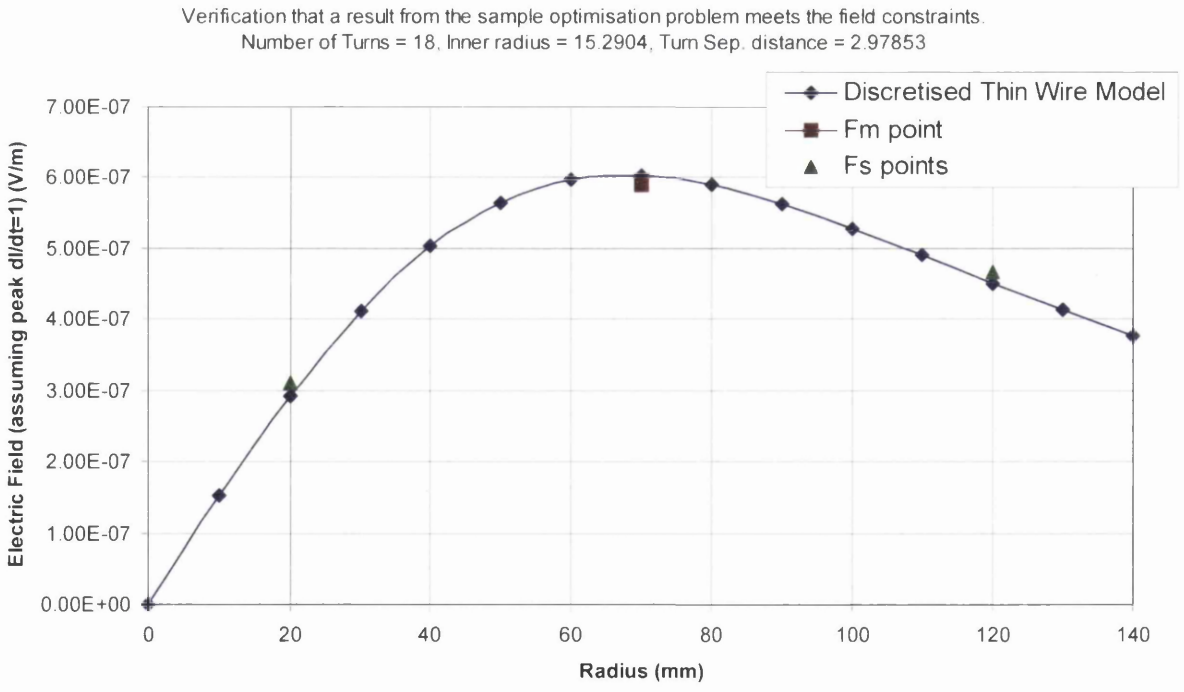

Figure 6.6 - Graphical confirmation that one of the sets of design variable values obtained from running the demonstration optimisation problem does meet the peak electric field constraints

From the results presented in this section, it has been seen that the combined C++ and FORTRAN coil optimisation program is capable of consistently producing accurate results without failing to converge, becoming algorithmically trapped or producing spurious wrong solutions. Furthermore, the program has generated results without lengthy execution times. Because of this, the program will form the basis of the Main and New Shape Finding Modules of this work. In those modules, most of the program will remain the same; however, the choice of design variables, the exact form of the penalty and hence composite objective function, and the way the design variables are translated into a thin-wire model for evaluation of the function will be slightly different. Both modules are reported upon in the next chapter. Finally, the results of this section have shown for the first time that the combination of a penalty function based on chosen constraints and coil geometry variables, a simulated annealing algorithm, the representation of a stimulating coil as concentric loops of thin wire in a field model, and a means of translating the design variables via the model into a penalty function value can be used to successfully solve an optimisation problem involving an axi-symmetric magnetic stimulation coil.

7 Optimisation and the New Shape and Main Modules

7.1 Background

In the previous chapter, the simulated annealing optimisation algorithm to be used in this work was introduced and was shown to be able to solve sample problems by making use of suitable constraints, a penalty function, a composite objective function and design variables based on coil geometry. In this chapter it will be seen how these things, and the optimisation computer program written to make use of them, can be expanded to form this work's New Shape and Main Modules which are part of the tri-modular approach to finding more focal coils that meet a certain normalised nerve membrane potential value introduced in Section 2.5.3.

Here, it will first be seen how the desire to find a coil with good focality can be translated into an objective function for use with the simulated annealing optimisation procedure. It will be seen that, for the computer program to work effectively, it will be desirable to place a constraint on the electric field value being aimed for when performing focality optimisation and a suitable constraint function will be introduced. Later, it will become apparent that this constraint function can be very easily converted into one designed to ensure that a coil meets a normalised nerve membrane potential value. In order to calculate the peak electric field value during optimisation a method to calculate coil inductance will be seen to be required; this will be presented in this chapter.

Before the New Shape Module will be complete, it will be required to decide upon what are the design variables to be used in the optimisation process. This issue will be discussed in this chapter and two different sets of design variables will be considered at length with coil constructability in mind. The New Shape Module will then be used to find new shapes using these design variables and the designs will be presented.

An important consideration is whether the electric field modelling computer code at the heart of the New Shape and Main Modules is producing valid results. In order to prove this, the chief new coil shape suggested by the New Shape Module will be built

and field value measurements will be taken around it and compared to those being observed at the same positions around the coil by the computer code. These results will be presented together with the results of a similar comparison performed using a Magstim HP90 coil.

The Main Module will then be discussed and the three stages required in allowing the module to make use of this work's chief new basic coil shape in a problem will be described. The problem is that of finding a size of basic shape that meets a required normalised nerve membrane potential value whilst keeping focality as restricted as possible. So, firstly consideration will be given to what is a suitable set of size only governing variables needed to add the shape to the Main Module's database of basic shapes. Secondly, use will be made of this work's Finite Element Module to find expressions for how this shape's resonant frequency, resistance and inductance change with coil size, and these expressions will be added to the Main Module database. Thirdly, to illustrate that the Main Module is working as intended, it will be used to find a particular size of coil that meets a required normalised nerve membrane potential value at a particular distance below the coil whilst keeping focality as restricted as possible. Repetitive use will be made of (2.6) from Section 2.3 when calculating the normalised nerve membrane potential during the module's optimisation procedure. It should be noted that the first two stages above would need to be repeated for each basic shape that it is desired to add to the Main Module's database of basic shapes.

7.2 Focality and the Objective Function

In Section 6.5 it was seen that it was possible to define a penalty function for the demonstration optimisation problem of Chapter 6 in terms of a chosen set of design variables which always took a single scalar value given a particular set of variable values. The first key stage in the evaluation of the penalty function was the conversion of the design variable values into spatial location values for each of the thin-wire circular loops that made up the model of the axi-symmetric coil described by the design variables. This was followed by solving the thin-wire circular loop coil model to obtain the peak electric field at three locations below the coil. Then, these

field values were used in (6.9) to obtain the actual penalty function values. In this section, a similar method will be developed to obtain the objective function of this work's New Shape and Main Modules from a set of design variables.

As was stated at the beginning of Section 2.5.3.1, in the New Shape Module, the focality of a coil that arises during the module's optimisation algorithm will be defined in terms of the peak electric field generated by the coil when used with a particular stimulator, and the focality will be measured along a straight line at a distance below the coil specified by the module user's input. This is also true of the Main Module which, as was explained in Section 6.3, will have an objective function defined in terms of peak electric field focality although it will have different design variables from the New Shape Module. In both modules, the definition used for focality will derive from those used in [26], [27] and [28] which, as was explained in Section 1.5, are essentially equivalent to one another. Thus focality will be defined as the distance over which the peak electric field magnitude falls to 70.7% of its largest value along a straight line at a specified distance below the coil's base.

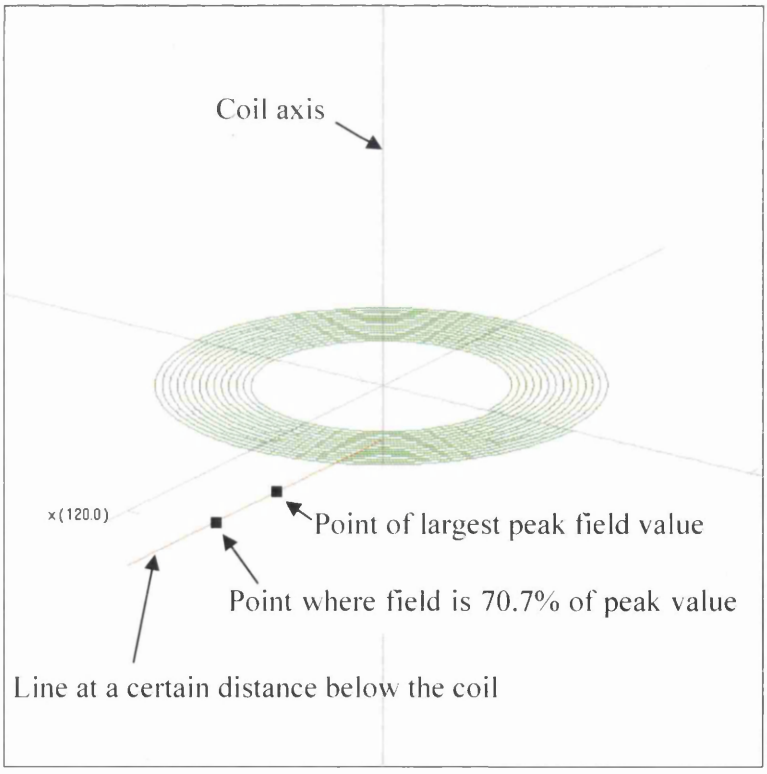

Figure 7.1 - Field points along a line below a Magstim HP90 coil

The above definition of focality can be understood as follows in the context of an axi-symmetric coil. Consider such a coil, e.g. the Magstim HP90 flat spiral coil. Let a straight line be defined at some specified distance below the coil's base which extends in a radial direction away from the coil's axis and which is perpendicular to that axis. This is similar to the brown line seen below the model of the HP90 in Figure 7.1. If one begins at the axis and travels along this line, the point of the largest peak electric field magnitude along the line will be reached at a certain distance from the axis which varies according to the geometry of the coil under consideration. Travelling further along the line, the point where the peak electric field is 70.7% of the largest value will also be reached, and is the point of interest in calculating the focality. With an axi-symmetric coil, it can reasonably be expected that the peak electric field magnitude profile along the radial line which extends in the diametrically opposite direction from the coil's axis to the one being considered is identical to the magnitude profile along the line already considered. Therefore, the focality will be defined as that obtained by taking the radial distance of the 70.7% field magnitude point and multiplying this distance by two. Thus the focality is then indeed a measure of the distance along a line (that is parallel to the base of the coil, some distance below it and which runs through the coil's axis) over which the peak electric field magnitude falls to 70.7% of its largest value, matching the accepted definition.

Both the New Shape and Main Module computer programs of this work were designed by making additions to the combined C++ and FORTRAN program used to solve the demonstration coil optimisation problem in Section 6.6. The code added for the evaluation of focality executes after the design variables have been converted into spatial locations for the circular thin-wire loops which form the model of a coil that has arisen during the optimisation algorithm. (The subject of design variables will be returned to later in this chapter.) The focality of a coil that had arisen at a particular iteration of the optimisation algorithm would then be obtained as follows. First, by solving the thin-wire model, the peak electric field magnitude would be obtained at points 2.5 mm apart at radii from 0 mm to 140 mm from the coil's axis along a straight line located at the user's specified distance below the coil's base. Then, starting at the point corresponding to the largest field magnitude and working radially outwards, the first point at which the field magnitude was 70.7% or less of the largest

magnitude would be identified. The radial distance of this point on the line would then be multiplied by two to obtain the coil's focality.

From the discussion in the last paragraph, it is clear that, as coded in this work, the New Shape and Main Modules cannot deal with coil's having focalities greater than 2 x 140 = 280 mm. This is perfectly adequate since the focalities of coils in current use, e.g. the HP90, are already significantly less than that value, and the objective of this work is to find coils with better focalities than at present. It is also adequate since the coils that are likely to arise during optimisation, given the limits that will be placed on the design variables, should result in focalities that are below this value. Nevertheless, should a coil arise during optimisation where 70.7% field magnitude or lower does not occur at a line point within the 140 mm limit, it will be deemed to have a focality of 280 mm. It is also clear from the previous paragraph that the program's reported focality values can only occur at 2 x 2.5 = 5 mm intervals. This should mean that a reasonable trade-off between the number of line points at which the field must be evaluated at every iteration of the optimisation algorithm and focality resolution has been achieved – if a new coil geometry were more focal than a presently existing one by only less than 5 mm, the improvement would not be regarded as very significant.

Given that program code had been added to the New Shape and Main Modules to calculate coil focality from a set of design variables, it was then possible to define the objective function to be used in both modules' optimisation algorithms. This is as follows:

$$O(\mathbf{x}) = c_o U^2(\mathbf{x}) \tag{7.1}$$

where $\mathbf{x}$ refers to the design variable vector, and U is the focality obtained using the method described above. The factor c_o governs how steeply the objective function's value increases as the focality increases and its value may be chosen so as to result in an adequately performing optimisation algorithm. This is similar to the way c_p was chosen in the penalty function (6.9) of the last chapter's demonstration optimisation problem. Thus, the objective in both modules will be to find a set of design variable

values that minimise $O(\mathbf{x})$, although the Main Module will also have a penalty function to ensure that the constraint on meeting a required normalised nerve membrane potential value is met; this penalty function is discussed further in Section 7.13.

From the above discussion, it is apparent that establishing coil focality involves calculating the ratios of the peak electric field magnitudes at various line points to the value at the point having the largest peak electric field magnitude in order to establish which one is the 70.7% point. Thus the calculations are always ratios of peak electric field magnitudes. In Section 2.5.2 it was explained that the peak electric field at any point around a stimulation coil is directly proportional to the maximum rate of change of current within the coil and that the maximum rate of change of current occurs at the beginning of the current pulse through the coil. Therefore, it is also apparent that, when calculating the ratio of the peak electric field magnitudes at two points, both terms in the ratio are proportional to the maximum rate of change of current within the coil, and this proportionality cancels out in the division process of calculating the ratio. It therefore appears to be unnecessary to calculate the true maximum rate of change of current in the coil just in order to ascertain focality, and using a dummy maximum rate of change of current of 1 A/s would suffice.

The New Shape Module program was originally coded so as to calculate $O(\mathbf{x})$ by using the thin-wire loop field modelling code as if coupled to a stimulator that always produces a maximum rate of change of current of 1 A/s in a coil, as was the case with the demonstration optimisation problem of Chapter 6. However, whatever design variables were used, this led to problems in that, although coil geometries with very good focalities were suggested by the program, the coils would often only be capable of inducing a small peak electric field when used with a realistic stimulator such as the Magstim Rapid^2. This in turn would suggest that, in use, the coil / stimulator combinations would not be capable of generating a sufficiently large normalised nerve membrane potential since the E_0 term in (2.6) would be too small. Therefore it was decided that the New Shape Module's optimisation scheme should have a constraint function added to it. This would be that the peak electric field magnitude at

the line point having the largest magnitude be at least as large as some user specified value.

The above constraint on field magnitude was formed into a penalty function, of a similar type to that used with the demonstration optimisation problem of Chapter 6, which is zero valued when the constraint is met and becomes sharply more positive as the constraint is broken. This is:

$$P(\mathbf{x}) = c_p \left[\max\left(0, F_m - f_m(\mathbf{x})\right)^2 \right] \tag{7.2}$$

where **x** refers to the design variable vector, m to the line point having the largest peak electric field magnitude, F to the field constraint limit, and $f(\mathbf{x})$ to the peak electric field magnitude at the point given a particular set of design variables and obtained via the thin wire loop coil modelling technique of Section 3.8. Once evaluated at an iteration of the optimisation scheme, this penalty function would then be added to the objective function to form a compound function:

$$C(\mathbf{x}) = O(\mathbf{x}) + P(\mathbf{x}) \tag{7.3}$$

$$C(\mathbf{x}) = c_o U^2(\mathbf{x}) + c_p \left[\max\left(0, F_m - f_m(\mathbf{x})\right)^2 \right] \tag{7.4}$$

and it is the global minimum of this compound function which will be sought in the New Shape Module's optimisation scheme. It will be the case that $C(\mathbf{x})$ will always be non-zero since the design variable limits will always result in a coil having a non-zero focality.

It will be apparent that, since evaluation of the penalty function requires knowledge of the actual peak electric field magnitude at a point below the coil, it will not be sufficient just to use a dummy maximum rate of change of current value in the New Shape Module's thin-wire coil models. Instead, it will be necessary to establish, for each iteration's coil model, what would be the maximum rate of change of current if

that coil were used with the stimulator being considered. In the next section, a method to establish this value for a coil used with a biphasic stimulator is presented.

7.3 Calculation of the Maximum Rate of Change of Current

As was explained in Section 2.5.2, the maximum rate of change of current in a stimulation coil occurs at the beginning of the current pulse which is discharged through the coil. In order to calculate the maximum rate of change of current through a coil connected to a biphasic stimulator, consider again the simplified circuit of the stimulator / coil combination shown in Figure 5.6 of Section 5.10. As was explained in that section, at the instant at which the stimulator trigger switch is pressed (time t=0) there is no current in the circuit, but the current immediately begins to increase in size. Since there is no current at t=0, there is no voltage drop across the resistances. Therefore, if the initial voltage across the capacitor is V_0, Kirchhoff's voltage law gives:

$$L\left.\frac{di(t)}{dt}\right|_{t=0} - V_0 = 0 \tag{7.5}$$

By transposing (7.5), the maximum rate of change of current is therefore:

$$\left.\frac{di(t)}{dt}\right|_{t=0} = \frac{V_0}{L} \tag{7.6}$$

where L is the total inductance in the circuit and is the sum of the stimulator and connecting leads' combined inductance, L_S, and the coil's inductance, L_C, at t=0. As was stated in Section 3.7, a value for L_S, in relation to a Magstim Rapid^2 stimulator and connecting leads, of 1 μH was obtained by measurement using a Wayne Kerr 6425 impedance bridge. A method is therefore required to obtain a reasonable estimate of L_C for the new coil geometries that will arise during this work's

optimisation algorithm. Such a method, suited to the axi-symmetric shapes that are to be generated in the optimisation scheme, is presented below.

7.4 A Method to Estimate Initial Axi-Symmetric Coil Inductance

As was seen in the previous section, in order to calculate the peak rate of change of current in a coil coupled to a biphasic stimulator using (7.6), a good estimate of the coil inductance at the instant that the current begins to flow (L_C at t=0) in the coil is required. At that initial instant in time it will be noted that the skin and proximity effect will not have begun to influence the distribution of the current within the coil. As a result of this, and the fact that the coils in the thin-wire electric field models used in this work's New Shape and Main Modules will be represented as coaxial loops of wire, use may be made of the work of Rosa and Grover [204] to estimate the inductance.

In the inductance calculations that follow, each coaxial loop in a particular thin-wire loop coil model for which the initial inductance is trying to be calculated, will be thought of as a loop of wire that has an actual cross-section. As was stated in Section 3.7, the cross-section of a Magstim HP90 coil is 6mm x 1.75mm, and it is this wire cross-section which will be assumed in all the initial inductance calculations undertaken in this work's New Shape and Main Modules.

Starting with the coil's self inductance S_C, this may be obtained by adding together the self inductances of each of the coaxial loops of wire making up the coil's model:

$$S_C = \sum_{n=1}^{N} S_n \tag{7.7}$$

where N refers to the number of loops in the coil. Rosa and Grover provide a formula ((88) in their work) after Weinstein for the self inductance of a circular loop of wire having a rectangular cross-section. This self inductance of loop n is given by:

$$S_n = \mu_0 r_n (\lambda_{1n} + \lambda_{2n}) \tag{7.8}$$

where μ_0 is the permeability of free space, and r is the radial distance of the loop's cross sectional centre from the coil's axis. The factor of 4π present in Rosa and Grover's (88) is omitted in (7.8) due to the use of SI units in this work. λ_1 and λ_2 are as follows:

$$\lambda_{1n} = \log\frac{8r_n}{w} + \frac{1}{12} - \frac{\pi x}{3} - \frac{1}{2}\log\left(1+x^2\right) + \frac{1}{12x^2}\log\left(1+x^2\right) + \frac{1}{12}x^2\log\left(1+\frac{1}{x^2}\right) + \frac{2}{3}\left(x-\frac{1}{x}\right)\tan^{-1}x \tag{7.9}$$

$$\lambda_{2n} = \frac{w^2}{96r_n}\left[\left(\log\frac{8r_n}{w} - \frac{1}{2}\log\left(1+x^2\right)\right)\left(1+3x^2\right) + 3.45x^2 + \frac{221}{60} - 1.6\pi x^3 + 3.2x^3\tan^{-1}x - \frac{1}{10}\frac{1}{x^2}\log\left(1+x^2\right) + \frac{1}{2}x^4\log\left(1+\frac{1}{x^2}\right)\right] \tag{7.10}$$

where w is the coil cross sectional width and $x = h/w$ where h is the coil cross sectional height. As explained earlier h = 6mm and w = 1.75mm in this work.

Moving on to the mutual inductance of the coil M_C, this may be obtained by adding together the mutual inductances of each of the concentric loops of wire making up the coil's model:

$$M_C = \sum_{n=1}^{N}\sum_{p=1}^{N} M_{np} \quad \text{where } n \neq p \tag{7.11}$$

where N refers to the number of loops in the coil. Rosa and Grover provide a method to calculate the mutual inductance of two coaxial loops of wire of rectangular cross

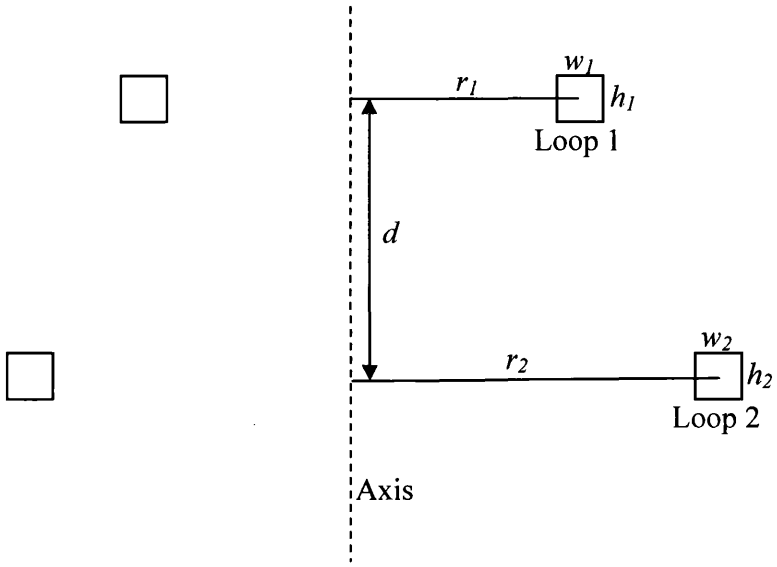

Figure 7.2 - Two coaxial loops of wire have cross section

section in the equation that precedes (20) in their work. To understand the method, consider first two coaxial coil loops having rectangular cross sections where once again w is the coil cross sectional width and h is the coil cross sectional height:

Note that in this work $h_1 = h_2$ and $w_1 = w_2$.

Extending to two general loops n and p, the mutual inductance between them is given by:

$$M_{np} = M_{0_{np}} + \frac{1}{24}\left\{h_n^2 \frac{d^2 M_{0_{np}}}{dx_n^2} + h_p^2 \frac{d^2 M_{0_{np}}}{dx_p^2} + w_n^2 \frac{d^2 M_{0_{np}}}{dr_n^2} + w_p^2 \frac{d^2 M_{0_{np}}}{dr_p^2}\right\} \quad (7.12)$$

In (7.12), $x_n = {}^{h_n}\!/_{w_n}$ and likewise for p. $M_{0_{np}}$ is given by the expression:

$$M_{0_{np}} = \mu_0 \sqrt{r_n r_p}\,\frac{2}{k}\left[\left(1 - \frac{k^2}{2}\right)K(k) - E(k)\right] \quad (7.13)$$

where the factor of 4π present in Rosa and Grover's (1) is replaced by μ_0 in (7.13) due to the use of SI units in this work. K and E are elliptic integrals of the first and second kind respectively and k is given by:

$$k = \frac{2\sqrt{r_n r_p}}{\sqrt{\left(r_n + r_p\right)^2 + d^2}} \tag{7.14}$$

The derivative terms in (7.12) are given by the following expressions:

$$\frac{d^2 M_{0_{np}}}{dx_n^2} = \frac{\mu_0}{4}\frac{k^3}{r_n}\left\{K(k) - \frac{1-2k^2}{1-k^2}E(k)\right\} \tag{7.15}$$

$$\frac{d^2 M_{0_{np}}}{dx_p^2} = \frac{\mu_0}{4}\frac{k^3}{r_p}\left\{K(k) - \frac{1-2k^2}{1-k^2}E(k)\right\} \tag{7.16}$$

$$\frac{d^2 M_{0_{np}}}{dr_n^2} = \frac{\mu_0}{4}\frac{k}{r_n}\left\{\left(2-k^2\right)K(k) - \left(2-k^2\frac{1-2k^2}{1-k^2}\right)E(k)\right\} \tag{7.17}$$

$$\frac{d^2 M_{0_{np}}}{dr_p^2} = \frac{\mu_0}{4}\frac{k}{r_p}\left\{\left(2-k^2\right)K(k) - \left(2-k^2\frac{1-2k^2}{1-k^2}\right)E(k)\right\} \tag{7.18}$$

where the factor of $\mu_0/4$ replaces π present in Rosa and Grover's (22) in (7.15) to (7.18) due to the use of SI units in this work.

In this work it was found desirable to slightly improve the estimation of mutual inductance provided by the above method. This was done by splitting the representation of the coil cross section in the calculation into four separate coaxial coil loops as shown:

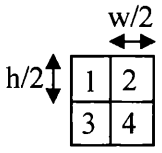

Figure 7.3 - The cross section of a circular loop of wire split into four equal coaxial loops

Here, each of the resulting loops was regarded as a separate loop for mutual inductance calculation purposes.

Thus, by using the above formulae, an estimate of the coil inductance L_C at the instant that the current begins to flow (time t=0) may then be obtained by summing:

$$L_C = S_C + M_C \tag{7.19}$$

This value may then be used in (7.6) to calculate the maximum rate of change of current through a coil connected to a biphasic stimulator as in this work's New Shape and Main modules. L at t=0 in that equation may be obtained by adding the stimulator and connecting leads' combined inductance, L_S, to the coil's inductance L_C from (7.19).

It will be seen that an initial capacitor voltage V_0 is also required in (7.6). In this work's New Shape and Main module work initially to be presented, this value was taken as 90% charge on a Magstim Rapid[2] which was found by measurement to be 1530V. Thus by using this value of V_0, L_C from (7.19) and L_S together in (7.6), the value of maximum rate of change of current to be used in this work's New Shape and Main module electric field calculations is obtained.

7.5 The Choice of a Set of Coil Design Variables

In Section 7.2 it was seen that the optimisation problem to be solved in this work's New Shape and Main Modules requires that the coil shape be described by a set or vector of design variables. In the Main Module, these variables would be restricted to those that would alter the size of a particular basic coil shape under consideration. However, in the New Shape Module, the variables would allow the coil shape to be altered more freely and both the coil basic shape and size could be altered. In this section, the question what would be a suitable set of variables to be used in the New Shape Module is considered.

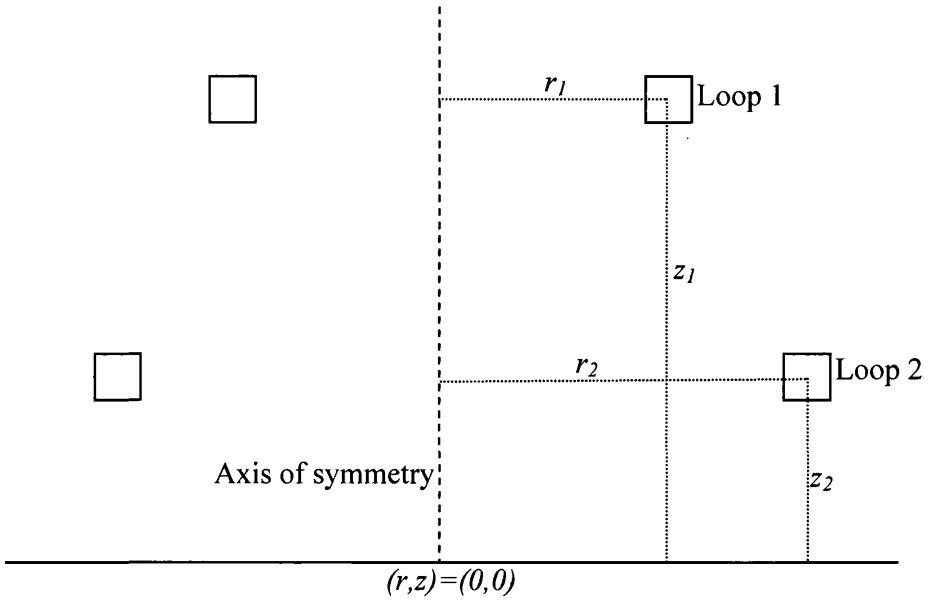

Figure 7.4 - The r and z coordinates of the loop cross section centres of an axisymmetric coaxial circular loop coil

A little thought will reveal that an axisymmetric coil represented as a group of coaxial circular wire loops may have its shape described in many ways. Perhaps the simplest set of variables describing such a coil would be one that allows the rand z coordinates of each loop wire cross section centre (as in Figure 7.4) to be freely varied. This would allow very original coil shapes to be investigated and will be the set of design variables used in the first report of results from the New Shape Module described below.

Thus, in the first instance, the New Shape Module will be set to find coil shapes that minimise $C(\mathbf{x})$ in (7.4). The number of loops in the coil will be set at 14, the same number of turns as a Magstim HP90 coil. The design variables will be the axial radius of each coil loop, e.g. r_1 or r_2 in Figure 7.4, and the height above the stimulation plane (the line $z = 0$ in Figure 7.4) of each loop, e.g. z_1 or z_2 in Figure 7.4. It may be seen that there will be 14 x 2 = 28 independently alterable variables. The limits placed on the radius variables will be 3mm to 100mm and for the height variables 3mm to 50mm. Given a wire cross sectional height of 6mm, the lower height limit will allow for the loop cross section centre to be able to be at a height of 6mm ÷ 2 = 3mm. The

lower radius limit of 3mm was chosen since anything smaller would result in a loop that could not be practicably formed.

The user's inputs to the New Shape Module are the peak electric field constraint value to be used as F_m in (7.4) and the distance below the coil's base at which the line containing the electric field evaluation points is located. Using Figure 7.4 for illustration, this line of points would be parallel to the line $z = 0$ and have a z coordinate having a minus value equal in magnitude to the distance entered as input by the user. Thus the line $z = 0$ is used as a datum line considered as the 'base' of the coil.

It may be seen from examination of (7.4) that the values of the two constants c_o and c_p must be decided upon. After some considerable experimentation, taking about 2 – 3 hours, in running the New Shape Module, it was found that a value of 10^6 was found to work well in both cases. This time compares with the solution time of one circuit coupled two dimensional axisymmetric FEM model of the gull-wing shaped coil seen in Section 7.12 of some 23 minutes using the FEM code developed in this work on a Pentium 4 1.8 GHz personal computer. However, it must be borne in mind that the values of c_o and c_p, once set, may be used for many executions of the module using different input values and do not need to be changed for each execution. The value is of 10^6 is large enough to ensure that the function $C(\mathbf{x})$ becomes rapidly more positive as either the focality or the electric field size constraint becomes worse. Nevertheless it was found that using constant values higher than 10^6 caused $C(\mathbf{x})$ to become so much higher when the focality or the field constraint became worse that $C(\mathbf{x})$ developed a number of very sharp local minima within the variable space. This meant that the optimisation algorithm found it difficult to close in on the minima as solution values. Thus 10^6 was found to be a good trade off value that allowed the algorithm to close in on $C(\mathbf{x})$ minima quite quickly but without becoming confused by sharp minima and constantly jumping about the variable space.

In addition, after discussion with the potential users of the New Shape Module, it was decided that the field constraint value in the program need not be as strict as was originally coded. It was decided that the field constraint should be altered so that the

desired peak electric field value at the point of evaluation have an error tolerance of 10% either way. This was thought to make the program of greater practical use because that tolerance would be acceptable. This alteration in the New Shape Module meant that (7.4) became:

$$C(\mathbf{x}) = c_o U^2(\mathbf{x}) + c_p \left\{ \max\left[0, \left(\left|F_m - f_m(\mathbf{x})\right| - 0.1F_m\right)\right]^2 \right\} \qquad (7.20)$$

7.6 Results from the New Shape Module

The New Shape Module, by finding the minima of (7.20), was used to obtained new coil shapes as solutions. It should be noted that the Magstim HP90 coil, when used with a Magstim Rapid^2 at 90% charge as reported in Section 3.7, is able to produce a peak electric field magnitude of 210 V/m with a focality of 110 mm at a distance of 12.5 mm below the base of the coil. Therefore, to facilitate a direct comparison of the focalities and peak fields of the coil shapes suggested by the New Shape Module and those of the HP90, the inputs used to the New Shape Module in this instance were a peak electric field magnitude of 210 V/m and a distance below the coil of 12.5 mm.

The New Shape Module was run many times for these inputs and many different solutions were obtained indicating that the compound function $C(\mathbf{x})$ in (7.20) has numerous different design variable values that correspond to function minima given the inputs used. These solutions were all valid solutions – i.e. coil shapes that when used with a Magstim Rapid^2 at 90% charge produced an electric field of within 10% of 210 V/m at a distance of 12.5mm below the coil base. As discussed in the final paragraph of Section 6.5, because of the inherent random nature of the Simulated Annealing procedure used to find the minimum of $C(\mathbf{x})$ and the fact that many function minima existed, running the New Shape Module produced a different answer each time it was run.

The results from a sample of running the New Shape Module three times are presented below. In the graphs of Figure 7.5, Figure 7.6 and Figure 7.7, plots of the r and z coordinates of the solution coils' loop cross section centres relative to the origin

$r = 0$, $z = 0$, as in Figure 7.4,are given. Because of Figure 7.4's z axis symmetry, only the positive r half of the graphs are shown. The exact values of the axial radius and height above the coil base for each loop from each run are shown in Appendix D. The other relevant results from each run are shown in the table below:

	Run 1	Run 2	Run 3
Peak E field (V/m)	194.134	206.556	194.288
Focality (mm)	60	60	65
Final penalty function value	2500	2500	3025

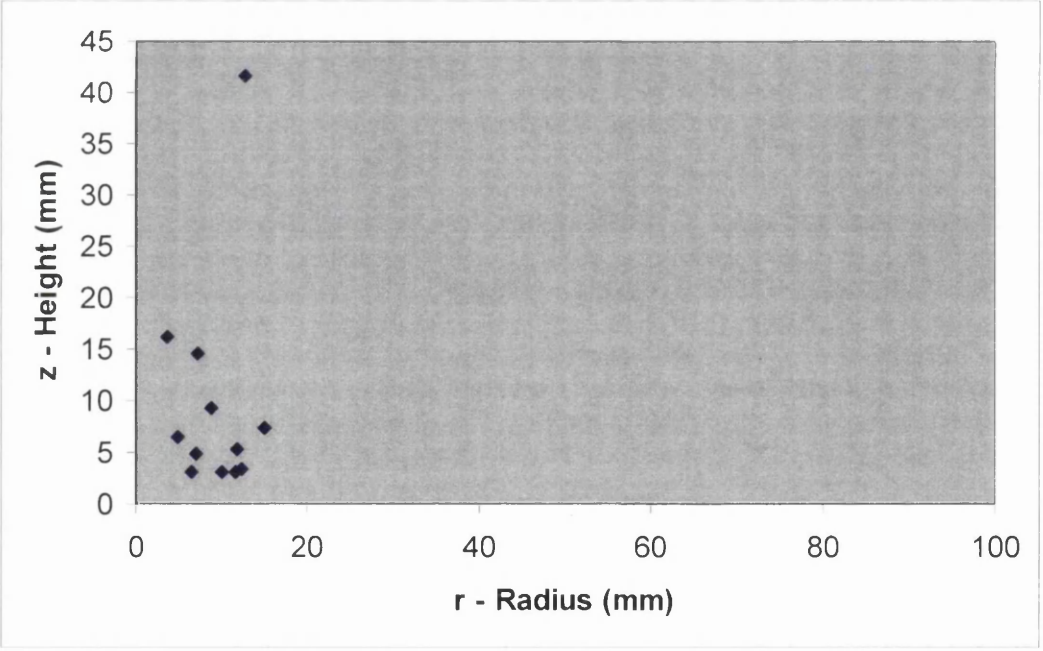

Figure 7.5 - 14 loop cross section centre locations from New Shape Module run 1

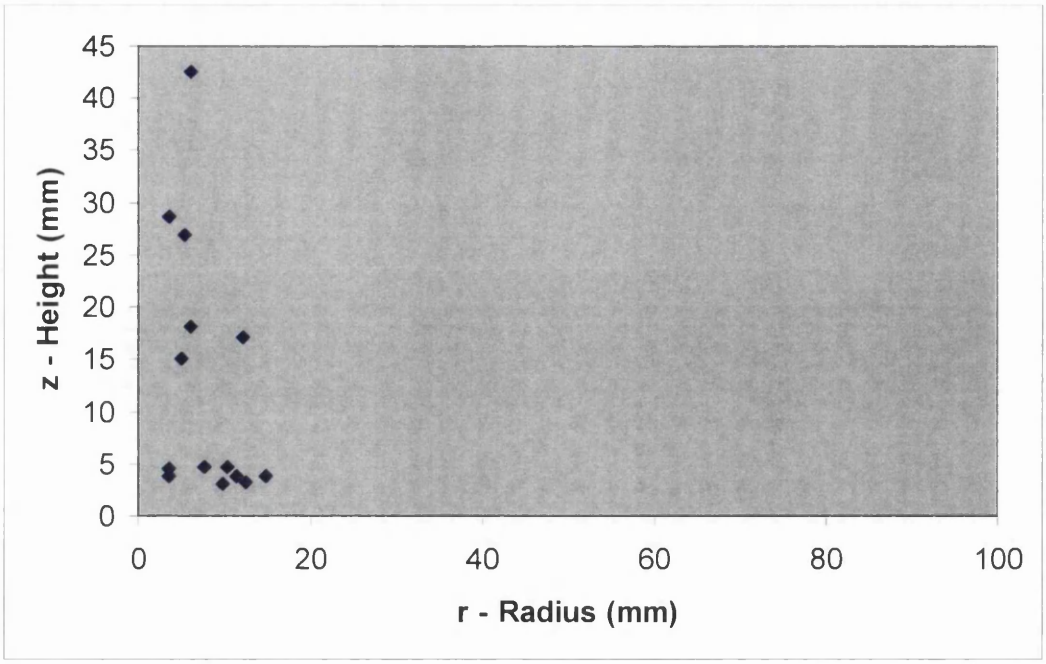

Figure 7.6 - 14 loop cross section centre locations from New Shape Module run 2

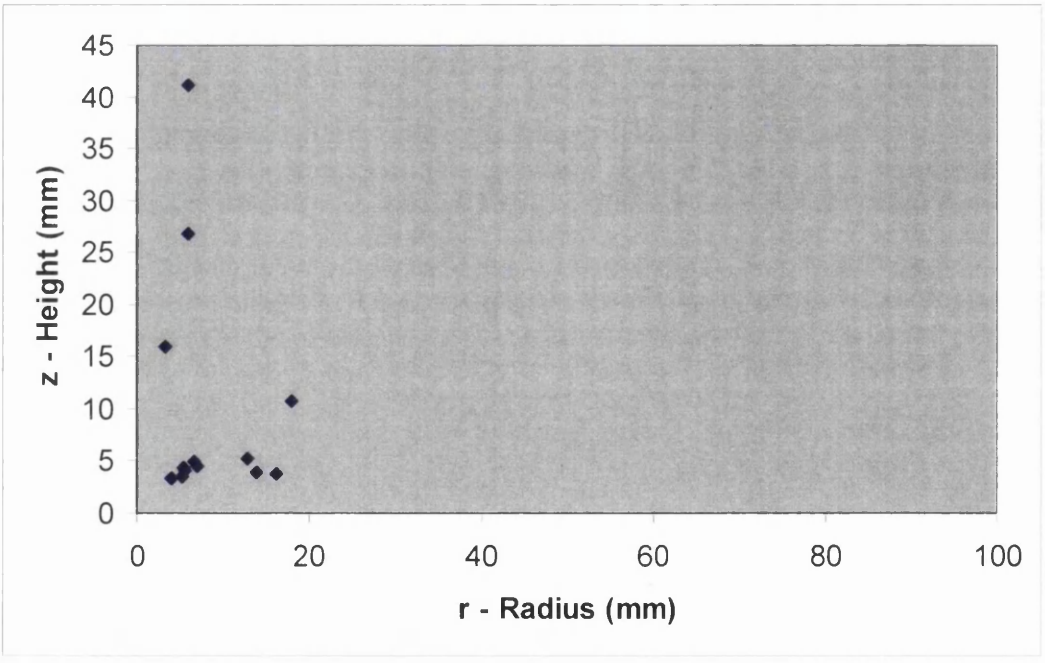

Figure 7.7 - 14 loop cross section centre locations from New Shape Module run 3

It may be seen from the sample run results above that three different coil shapes have been suggested as solutions by the New Shape Module. Although all three shapes are distinct from one another they share the property that a number of loops are present towards the bottom left hand corners of the graphs. In addition, on each graph, some loops centres are located towards the left hand graph side, roughly forming a line parallel to the *z* axis. Running the New Shape Module many times for the inputs of a peak field of 210 V/m and a distance of 12.5 mm below the coil base almost always results in solutions that share these shape properties.

From the above table it may be seen that the peak electric field values in the solution runs are within 10% of the input value of 210 V/m showing that the solutions are valid solutions as discussed above. The focalities of two of the coils are 60 mm, a value also obtained in other repeat program runs, and which appears to be the minimum focality coil obtainable in this problem. One of the coils in the table has a focality of 65 mm, and this run is an example of an occasion when the New Shape Module's optimisation algorithm has got stuck on a local minimum of the compound function $C(\mathbf{x})$. Although this does not happen frequently, it is reported here for the sake of completeness. If one of the optimisation algorithms discussed in Section 6.2 that does not share Simulated Annealing's ability to find a global minimum from amongst a number of local minima was chosen as this work's algorithm then it could be expected that the New Shape Module would become stuck far more often on local minima and miss the most focal coil shapes.

Finally, it should be noted that the focality of each coil above is significantly better than the focality of 110 mm obtained form the Magstim HP90 coil at 12.5mm. This is very encouraging and shows that the New Shape Module, given an user's chosen peak field requirement and field assessment distance below a coil, is capable of finding superior coil shapes than exist at present.

7.7 Choosing a Set of Basic Shape Variables

In the previous section it was seen that three shapes were suggested by the New Shape Module as shapes having good focality at a distance of 12.5 mm below the coil base.

In this section it will be seen how these shapes can be used to define a new basic shape that may be added to the Main Module's database of basic shapes for use in its optimisation work.

In the last section, all three shapes, although different, were seen to share some properties. These are firstly that some loops are arranged with their cross section centres roughly in a line parallel to the common axis shared by the coaxial loops – i.e. roughly parallel to the *z* axis in Figure 7.5, Figure 7.6 and Figure 7.7. Secondly, there are some loops whose cross sectional centres are towards the bottom left hand corner of the Figures and whose centres are roughly in a line parallel to the *r* axis. This is summarised in Figure 7.8, where the loops in the illustrative coil are arranged with their cross sectional centres along one of the two lines drawn, i.e. the loops fall into one of two groups.

These two groups form the basis for the description of the new basic coil shape in that the variables describing the new shape are related to the groups. The variables suggested in this work are:

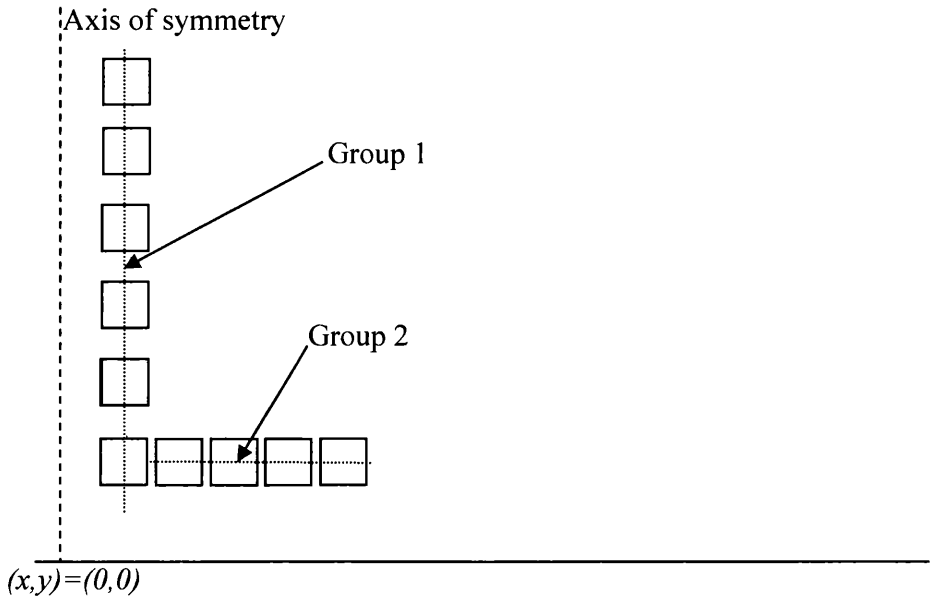

Figure 7.8 - New coil basic shape showing the two loop groups

1) The number of loops in group 1. If the total number of loops were known then the number of loops in group 2 could be calculated by subtraction.

2) The common radius of all the loops in group 1. This variable would have a lower limit of, say, 3 mm to ensure coil buildability. The upper limit could be 10mm. If the radius of every loop in group 2 were some fixed radial distance larger than this value, then this variable would also control the radius of each loop in group 2.

3) The height of the lowest loop in group 1. If the height of every other loop in group 1 above the loop below it was fixed, then this variable would control the height of each loop in group 1. In addition, this variable could be used to represent the height of all the loops in group 2. A lower limit of 3mm could be used since this would equal half the height of the coil cross section to be used in this work. An upper limit of 15mm could be used.

It may be seen by consideration of the variables, that they contain within them the complete description of a coil geometry whose basic shape is similar to that seen in Figure 7.8 but whose size, in the form of the radius, height and number of loops variables, is changeable. Clearly other variables could be chosen to approximate the shapes seen in Section 7.6. However the important factor in choosing any set of variables is that it is possible to obtain from them a complete representation of a coil geometry which may then be used to model the field around a particular coil geometry in the Main Module program.

7.8 A Coil Shape More Easily Constructible Using Current Methods

Whilst it has the advantage of being considerably more focal than the Magstim HP90 coil, the new basic coil shape presented in the last section has the disadvantage that it would be time consuming to build using current methods owing to the vertical stack of loops in group one. Current methods are partially automated based on the assumption of a gradually increasing turn radius. In these methods, a coil is built via a 'spinning' process starting at the innermost turn and gradually moving to the

outermost turn. It should be noted that the distance between turns need not remain uniform and various angles may exist between turns, as illustrated in Figure 7.9.

Thus it would be advantageous to alter the New Shape Module so that it was restricted in some way to only consider coil shapes that were buildable using current methods while still looking for coil shapes that are more focal than the Magstim HP90. This was achieved by changing the set of design variables used in the New Shape Module from the simple loop r and z locations used in Section 7.6 to a set that implicitly contained within them assumptions about the solution coil shape to be produced while also containing information about where and how the program could alter the coil shape. This could be done in a number of ways, but, with reference to Figure 7.9, for a coil having a particular number of turns, the set of variables chosen in this work are as in the list below. The total number of turns in the coil was still kept at 14.

1) The number of loops in section 1. This has a lower limit of zero and an upper limit equal to 5. The number of turns in section 2 would be 5 minus the number of turns in section 1. The number of turns in section 3 was fixed at 9.

2) The radius of the innermost loop in section 1. This had a lower limit of 3 mm and an upper limit of 10 mm. The horizontal distance between the loop cross section centres in section 1 was fixed at 2.0 mm.

3) The amount the radius of the innermost loop in section 2 was greater than the innermost loop radius in section 1. This had a lower limit of 5.8 mm and an upper limit of 10mm. The horizontal distance between the loop cross section centres in section 2 was fixed at 2.0 mm

4) The amount the radius of the innermost loop in section 3 was greater than the innermost loop radius in section 2. This had a lower limit of 5.8 mm and an upper limit of 15 mm. The horizontal distance between the loop cross section centres in section 3 was fixed at 5.8 mm

5) The height above the coil base line of the first loop in section 1. This had a lower limit of 3mm (half the coil cross section's height) and an upper limit of 15mm.

6) The angle of dip between turns in section 1. This had a lower limit of 0° and an upper limit of 70°.

7) The angle of dip between turns in section 2. This had a lower limit of 0° and an upper limit of 50°.

8) The angle of dip between turns in section 3. This had a lower limit of 0° and an upper limit of 30°.

Thus the set of variables above restrict the nature of the coil shape that can be suggested as a solution by the New Shape Module but still allow some freedom in its ability to vary the coil shape.

Some thought applied to the results of Section 7.6, where the initial voltage across the stimulator capacitor was fixed at 90% charge i.e. 1530 V, reveals that different coil shapes to those suggested by the New Shape Module could be suggested by the program as meeting the target field value of 210 V/m if the initial voltage were allowed to vary as part of the optimisation process. This facility was added to the New Shape Module as used in Section 7.6 (i.e. with the simple r and z set of geometry variables), and the program re-run for the same inputs as used in that section. Very similar results to those presented in Section 7.6 were obtained, and the initial voltage value obtained from the optimisation process tended to be close to 90% charge in each run.

However, even though similar results were obtained when including the capacitor charge as a variable with the r and z variables, it does not follow that the same similarity would occur with the set of variables listed above in this section. Therefore the final design variable to be added to the New Shape Module as described in this section was:

9) The initial stimulator capacitor voltage. This had a lower limit of 10%, i.e. 170V, and an upper limit of 100%, i.e. 1700V.

Once the new set of design variables were chosen, the New Shape Module program was altered to include code that allowed it to model the electric field around a set of coaxial circular loops whose positions were calculated from the set of variables. A problem was then set for the New Shape Module to solve using the new variables. This was to solve the optimisation problem of (7.20), and suggest the most focal coil it could given two inputs. These were that the line along which focality was judged would be 10 mm below the coil's base line, and that the electric field at the point of the greatest field should be within 10% of 210 V/m.

The results of running the New Shape Module with this problem are given below. A set of optimal design variable values found by the program were:

1) 3 loops in section 1. This meant that there should be 2 loops in section 2 and 9 loops in section 3.

2) 4.8754 mm.

3) 6.1375 mm.

4) 4.1155 mm.

5) 6.4876 mm.

6) 65.5°.

7) 36.2°.

8) 7.4°.

9) 53.246% charge i.e. 905.19 V.

The focality of the coil was evaluated as 70mm.

A labelled drawing of the solution coil is given in Figure 7.9. It may be seen that, in the plot of the loops making up the coil, the loop arrangement resembles the wing shape of a gull. Therefore it is proposed to call this coil shape a 'gull-wing' coil.

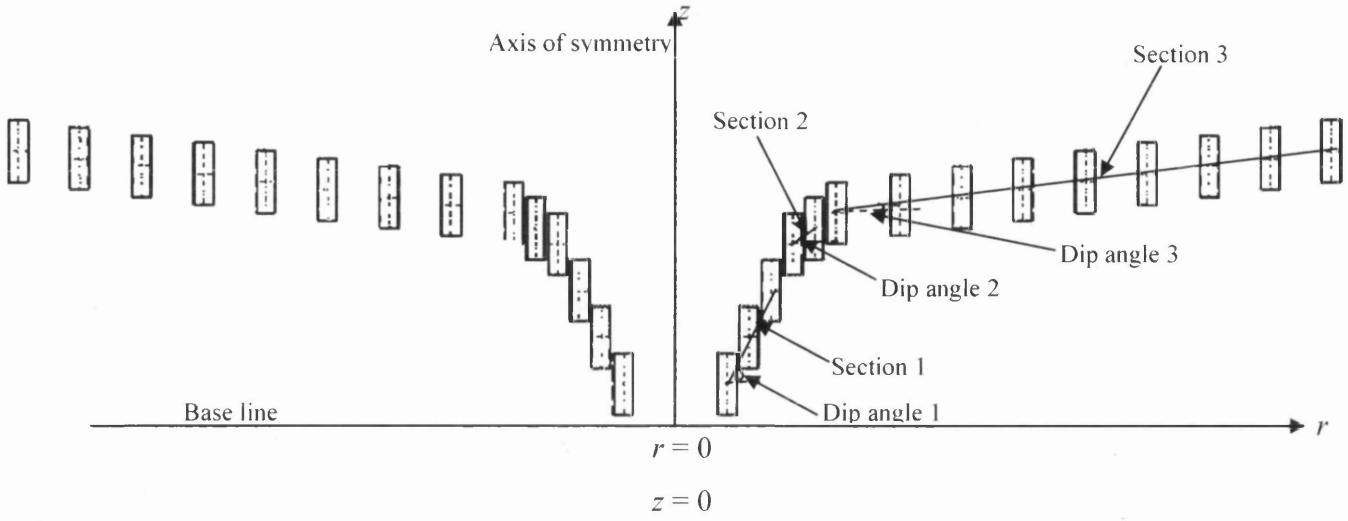

Figure 7.9 - The gull-wing coil

As will be seen in the next section, the focality of a Magstim HP90 coil at a distance of 10mm below the coil base is 100 mm. The focality of the gull-wing coil at that depth is therefore superior to the Magstim HP90's by 30 mm, a value which is very creditable considering that the variables involved in coming up with the gull-wing design were restrictive compared to the r and z variables responsible for the designs seen in Section 7.6 and the gull-wing coil should be buildable by the present process.

In addition, it may be seen from variable 9 that the gull-wing coil should only require the stimulator capacitor be charged to 53% in order to achieve the field target value of 210 V/m at 10 mm below the coil base line. This is superior to the value of 77% required when using the HP90 coil, as measured in the next section.

The gull-wing coil was therefore seen to have desirable properties in terms of its focality and the stimulator charge required to achieve a certain electric field value. As a result of this, it was decided that the gull-wing be adopted in this work as a new basic shape. In the remainder of this work, starting at Section 7.11, it will be demonstrated how this basic shape can be used with this work's Main Module to solve a normalised nerve membrane potential optimisation problem. This means that it will first be necessary to decide on a set of variables that can alter the shape's size without changing its essential topology. Next the Finite Element Module will be used to obtain expressions for how the resistance and inductance of the coil change as the

size governing variables are altered when the coil is used with a Magstim Rapid^2 stimulator. Then these expressions will be used to add the gull-wing as a new basic shape in the Main Module's database. Finally, the Main Module will be used to solve the membrane potential problem.

7.9 The Measurement of the Electric Field Due to an Axi-Symmetric Coil

In the previous section it was seen that the gull-wing coil was proposed by this work's New Shape Module as a more focal coil in response to a set of input values. It would be useful at this stage to verify that the focalities of coil shapes proposed by the New Shape Module are the same as the focalities of these shapes if they were actually built as practical coils. Additionally, it would be useful to verify that the electric field values seen by the New Shape Module during its calculations of field values at various points below the coil shapes it is considering during the optimisation process are close to the values that would be measured around these shapes if the coil shapes were built.

It is therefore proposed to, in this section, take measurements of the electric field around a Magstim HP90 coil at various points below the coil. Then, it is proposed to take the New Shape Module computer code and bypass the optimisation section of the code so that only a model of a HP90 coil coupled to a Magstim Rapid^2 stimulator is solved and the modelled electric field at the same points below the coil obtained as output from the program. The validity of the program's field modelling could then be investigated by comparison of the measured and modelled field values at the points. To further validate the New Shape Module's field modelling, the results of a similar comparison based upon the gull-wing coil will be presented in the next section.

In order to take measurements of the electric field around the HP90 coil, some equipment capable of taking reliable measurements was required. Such equipment was kindly supplied by the Magstim Company, and this equipment was the same as that used in [205] and designed by the University of Sheffield. The equipment is reported in [205] to be accurate to within ±2%. The equipment is shown in Figure

7.10 and consists of a printed circuit board (PCB) of concentric circular copper tracks, each of which has a 1 mm gap in the locations illustrated in Figure 7.11. (Figure 7.10 and Figure 7.11 are reproduced from [205] by kind courtesy of the Magstim Co. Ltd.) Each gap has wires connected to each end and, by applying a voltmeter across the pair of wires belonging to a particular gap, the voltage across the gap may be measured. It may be seen that the gaps are arranged so that voltage readings may be taken for each concentric track which are at radii ranging from 5 mm to 140 mm.

The height of the PCB above the HP90 coil could be altered and the height could be maintained by using adjustable plastic ties. The HP90 was located such that its centre coincided with the centre of printed guidelines which were located on the base board directly below the tracks on the PCB. Thus voltage measurements could be made from the wires connected to the PCB for the particular height above the coil that the PCB was set to and for each 5 mm radius from the coil's axis. Due to the HP90's flat

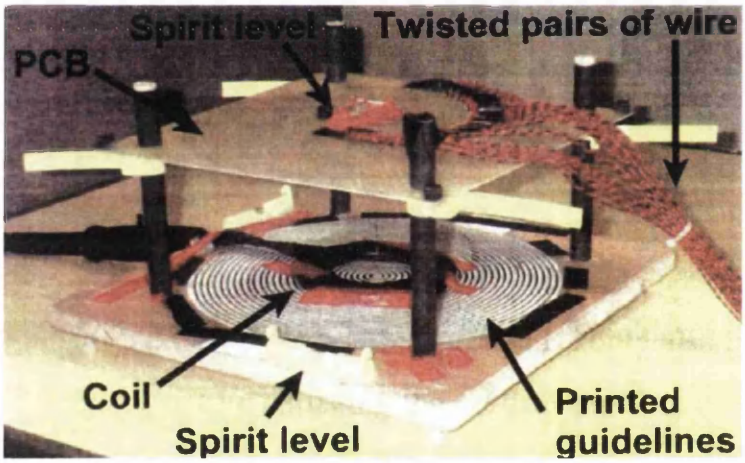

Figure 7.10 - A Magstim HP90 coil on the electric field measurement device

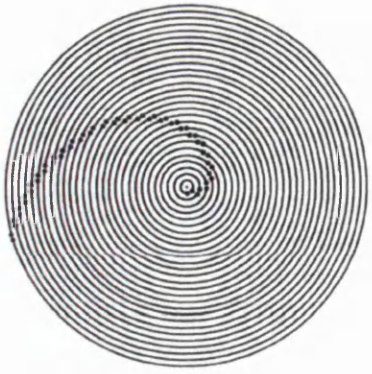

Figure 7.11 - The 1 mm gap layout on the field measurement device PCB tracks

profile and axi-symmetry, measurements taken at a certain distance above the coil are the same as measurements taken at the same distance below the coil.

Now, it is possible to convert a voltage value measured across one of the 1 mm gaps into a value representing the electric field magnitude around the coil at that particular location using the following method. This starts with the assumption that the electric field around an axi-symmetric coil, such as the HP90, exists only in the θ direction and contains no components in the r and z directions using a cylindrical coordinate system [206]. Given the design of the track pattern on this measurement equipment's PCB, the voltage measurement at each 1 mm gap is an indirect measurement of the electric field magnitude at that location. A formula to obtain the electric field magnitude from the voltage measured at a gap is given by (56) of [206] and is:

$$|\mathbf{E}| = E_\theta = \frac{V}{2\pi r - g} \tag{7.21}$$

where V is the voltage across a gap and g is the gap distance, i.e. 1 mm.

Thus this measurement equipment was used to measure the electric field around a HP90 coil at the gap locations for a coil connected to a Magstim Rapid^2 stimulator. In order to measure the peak electric field, i.e. the electric field at the beginning of a current discharge pulse, the stimulator was allowed to charge and then was discharged for each gap voltage measurement taken. The voltage at each gap was analysed by connecting that gap's wires to an oscilloscope and the voltage viewed on the oscilloscope's screen. The peak voltage value could then be read off the oscilloscope. For these measurements, the stimulator's capacitor was charged to 100%, i.e. 1700V.

The peak electric field around the HP90 coil as measured at the 1 mm gaps representing radii of 5 mm to 140 mm when the PCB was positioned at heights from 10 mm to 60 mm is plotted in Figure 7.12. Also in the figure are lines representing the peak electric field at the same points around the HP90 coupled to a Rapid^2 stimulator obtained from the field modelling code of the New Shape Module with the optimisation code bypassed as described above. It may be seen that the measured and modelled fields are in good agreement with one another. This gives one confidence

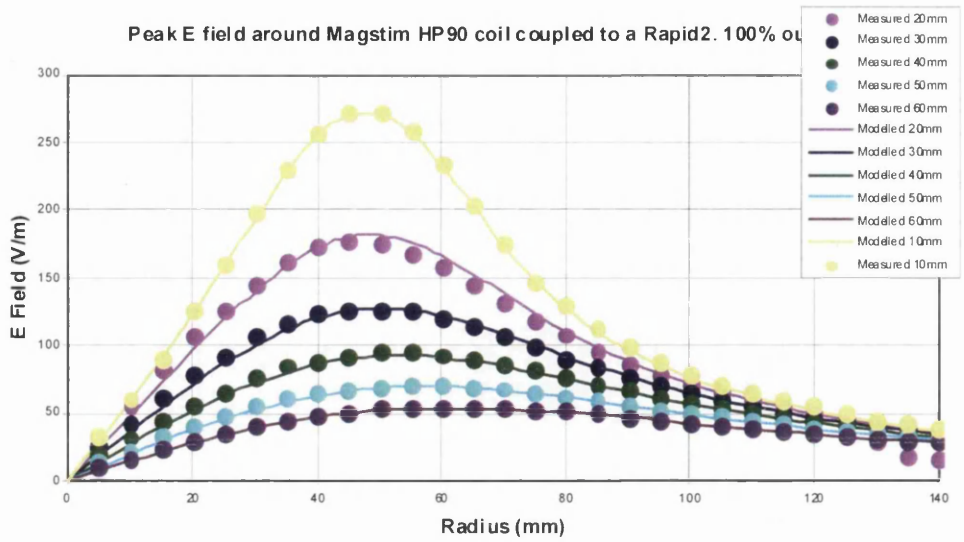

Figure 7.12 - The measured and modelled electric field values at distances from 10 mm to 60 mm above / below a HP90 coil

that the New Shape Module's field modelling code provides sufficiently accurate field values from the HP90 model. A slight radial offset is present, and this can be attributed to the fact that the HP90 is modelled as a series of concentric circular loops rather than a spiral. Each turn's radius varies gradually around the spiral, whereas, in the model, each turn's radius is fixed. So, a slight, but not significant, discrepancy exists between each turn's radius in the actual HP90 and the computer models.

Additionally, running the model of the HP90 resulted in a reported coil focality of 100 mm at a distance of 10 mm above the coil. It may be seen from the measured values in Figure 7.12 that the highest electric field value at 10 mm above the coil occurs at a radius of 50 mm. This equates to a focality of 2 x 50 = 100 mm. Therefore the field modelling code appears to be able to accurately evaluate the focality of a stimulating coil.

7.10 The Measurement of the Electric Field Due to the Gull-Wing Coil

In the previous section it was seen that the electric field modelling code of this work's optimisation programs was able to correctly model the field around a HP90 coil

coupled to a Magstim Rapid^2 stimulator as well as correctly predict the focality of the coil. In this section, a similar verification of the modelling code will be undertaken using this work's gull-wing coil design rather than a HP90 coil.

To facilitate the comparison, the gull-wing coil design described in Section 7.8 was first built at the Magstim Company's factory. Then, given that, like the HP90, the gull-wing coil is also axi-symmetrical and its electric field is also only in the θ direction, it was decided to use the same measuring equipment for the field around the gull-wing coil as was used for the HP90.

Thus, the gull-wing coil was positioned upside down on the measurement equipment's printed guidelines with its axis immediately above the guidelines' centre point. By being upside down, the printed circuit board could be moved to planes above the coil which would be the same as planes below the coil if it was the correct way around. Therefore field measurements which are as if they were below the coil could be made and, in the discussion that follows, the measured and modelled field values will be treated as if they were taken below the coil.

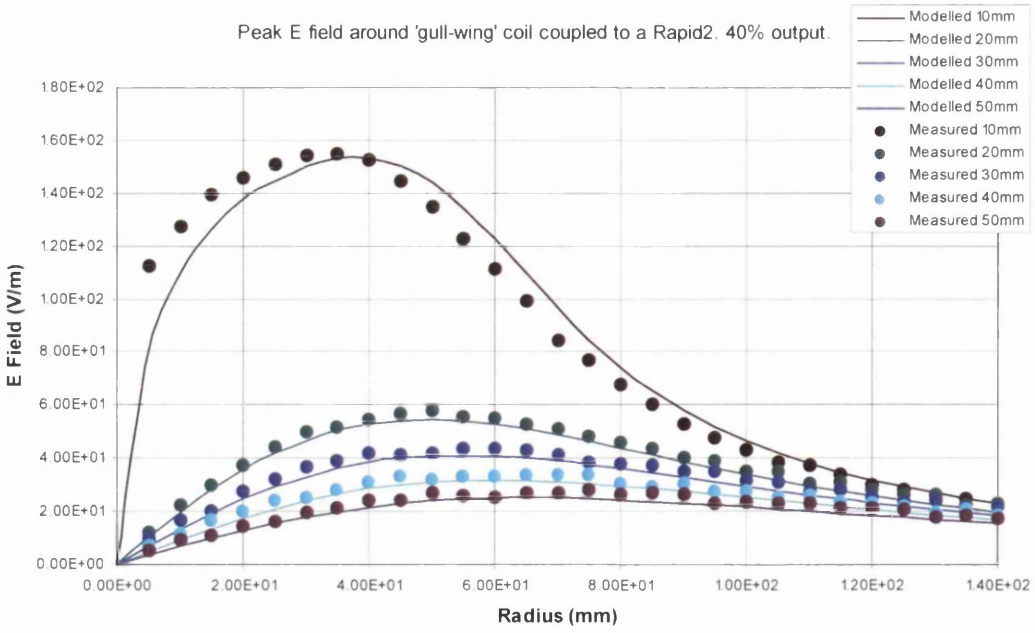

Figure 7.13 - The measured and modelled electric field values at distances from 10 mm to 50 mm below the gull-wing coil

In this section's work, field measurements and modelled field results were taken for the gull-wing coil in planes which were between 10 mm and 50 mm below the coil. A plot showing the field values obtained at radial points from 10 mm to 140 mm is given in Figure 7.13. For this case, the stimulator's capacitor was charged to 40%, i.e. 680 V.

From Figure 7.13 it can be seen that both the magnitudes and trends of the measured and modelled fields are in general agreement with one another. However, slight radial and value offsets are present. As was the case for the HP90 coil, these can again be attributed to the fact that the coil is modelled as a series of horizontal rings rather than as a helical spiral; the constructed coil's turns gradually taper in both radius and height around the coil, whereas the modelled coil has turns of constant height and radius. It may be seen that the radial offset is greater at 10 mm below the coil than for the other distances: thus the model is more accurate at distances further away from the coil. Nevertheless, the measured and modelled field values are close enough for the model to be deemed sufficiently accurate.

In Figure 7.13 it may be seen that the highest modelled field value at a distance of 10 mm below the coil occurs at a radius of 35 mm. This equates to a coil focality of 2 x 35 = 70 mm. However, the highest measured field value at the same distance below the coil occurs at a radius of 30 mm equating to a focality of 60 mm. Given that the two focality values are reasonably close and the computer code is not over estimating the coil focality, and therefore not suggesting coils as being more focal than they actually are, this is considered to be acceptable.

7.11 The Choice of a Size Governing Variable for the Gull-Wing Coil

In Section 7.8 it was seen that the Gull-Wing Coil possesses desirable properties in terms of good focality and ease of buildability using already existing processes. Given these properties, it would be useful if it were possible to add the gull-wing as a basic shape to the Main Module's database of basic shapes. In order to do this, it would be necessary to define a variable which alters the size of the gull-wing coil whilst its basic topology remains the same during the Main Module's optimisation process

which is centred around finding the most focal coil that allows a certain nerve membrane potential value to be achieved at a certain distance below the coil. This section considers a suitable size governing variable for the gull-wing basic shape.

From Figure 7.9, it may be seen that the key feature of the gull-wing coil's topology is that it contains three sections. Other aspects of the topology come from the variable values which were obtained from the revised New Shape Module output in Section 7.8. These aspects are that the number of turns in the coil equals 14, the number of turns in sections 1, 2 and 3 are 3, 2 and 9 respectively, and the angles of dip between the turns in sections 1, 2 and 3 are 65.5°, 36.2° and 7.4° respectively. These aspects, if taken together, should always ensure that a coil geometry retains the gull-wing basic shape.

However, retaining just these aspects allows some flexibility in the coil size whilst the basic gull-wing topology is retained. It may be seen that the variable values presented in Section 7.8 may be translated into r and z values for the loop cross-section centre locations for each of the coaxial loops making up the gull-wing coil geometry presented. These r and z values are given in Appendix E. Thus, taking these values as a base, it becomes apparent that, if the r and z values are all multiplied by a common factor, the separation of all the turns making up the coil becomes greater or less with the factor (as does the radius of the innermost loop) while the topologically fixed aspects listed in the previous paragraph remain the same. Thus this factor becomes a variable by which the gull-wing coil size may be altered whilst the coil's overall topology remains the same. It is this factor which is the size governing variable with which the gull-wing will be added as a new basic shape to this work's Main Module's database of basic shapes.

7.12 Obtaining Resonant Frequency Resistance and Inductance Expressions for the Gull-Wing Basic Shape

In Section 2.5.3.2.1 it was explained that, when a new basic shape is added to this work's Main Module's database of basic shapes, expressions for how the coil's

resistance and inductance when used with a stimulator and the resonant frequency of such a system change with the shape's size governing variables are required. For the coil and biphasic stimulator combination considered in this work, this means that the expressions must yield the resistance and inductance for a particular size of a certain basic shape which are the resistance and inductance at the resonant frequency which would exist when that coil is used with the particular biphasic stimulator under consideration together with the resonant frequency itself. These resistance, inductance and frequency values could then be used in (2.6) to obtain normalised nerve membrane potential values at locations around the coil. In this section it will be considered how resistance, inductance and frequency expressions can be obtained for the gull-wing new basic shape.

In the previous section, one size governing variable for the gull-wing shape was used and this variable is a size multiplication factor which causes the r and z values of the loop cross-section centres to increase or decrease with the factor. The first step in obtaining resistance, inductance and resonant frequency expressions is to decide what the limits are over which the size factor may be varied. In the lower limit, this is bound by the proximity that adjacent turn centres can be to one another. Each cross-section is 1.75 mm wide and, if there is to be a gap of at least 0.1 mm between each turn, then there needs to be a gap of at least 1.85 mm between each turn cross-section centre. In the gull-wing coil of Section 7.8, the smallest cross-section centre gap is 2.0 mm. This means that the size factor variable when adding the gull-wing to the Main Module can have a lower limit of 1.85 / 2.0 = 0.925. The upper limit is bound by the limit where the coil size has increased by enough to become difficult to handle. This would equate to a size factor of about 5. Therefore the size factor variable for the gull-wing basic shape in the Main Module would have lower and upper limits of 0.925 and 5 respectively.

The next step in obtaining the expressions is to decide upon at which values of the size factor variable should Finite Element Method (FEM) Module models of the gull-wing shape coupled to a Magstim Rapid^2 stimulator be solved. The FEM Module would calculate the resistance, inductance and resonant frequency of coils of those sizes and the resistance, inductance and resonant frequency at intermediate size values would then be obtained by interpolation. For the expressions to be reasonably

accurate, FEM models would need to be solved at sufficient points over the size factor variable's range to maintain the accuracy of the interpolation. In this work, it was decided that FEM Module models would be used to obtain resistance, inductance and resonant frequency values for a size factor variable value of 0.925 then at 0.5 intervals over the range 1.0 to 5.0.

Thus FEM meshes were constructed using the gmsh computer program of gull-wing coils of the relevant sizes. These meshes were then used as input to the circuit coupled time domain FEM program used in Section 5.12 to obtain the resonant frequencies of those gull-wing coil sizes when used with a Magstim Rapid^2 stimulator. Then, as in Section 5.12, a frequency domain FEM model at the resonant frequency was solved for each mesh to give the resonant frequency resistance and inductance of each size of gull-wing coil as required. These resistance, inductance and resonant frequency values are tabulated in Appendix F and are plotted as points in Figure 7.14 and Figure 7.15.

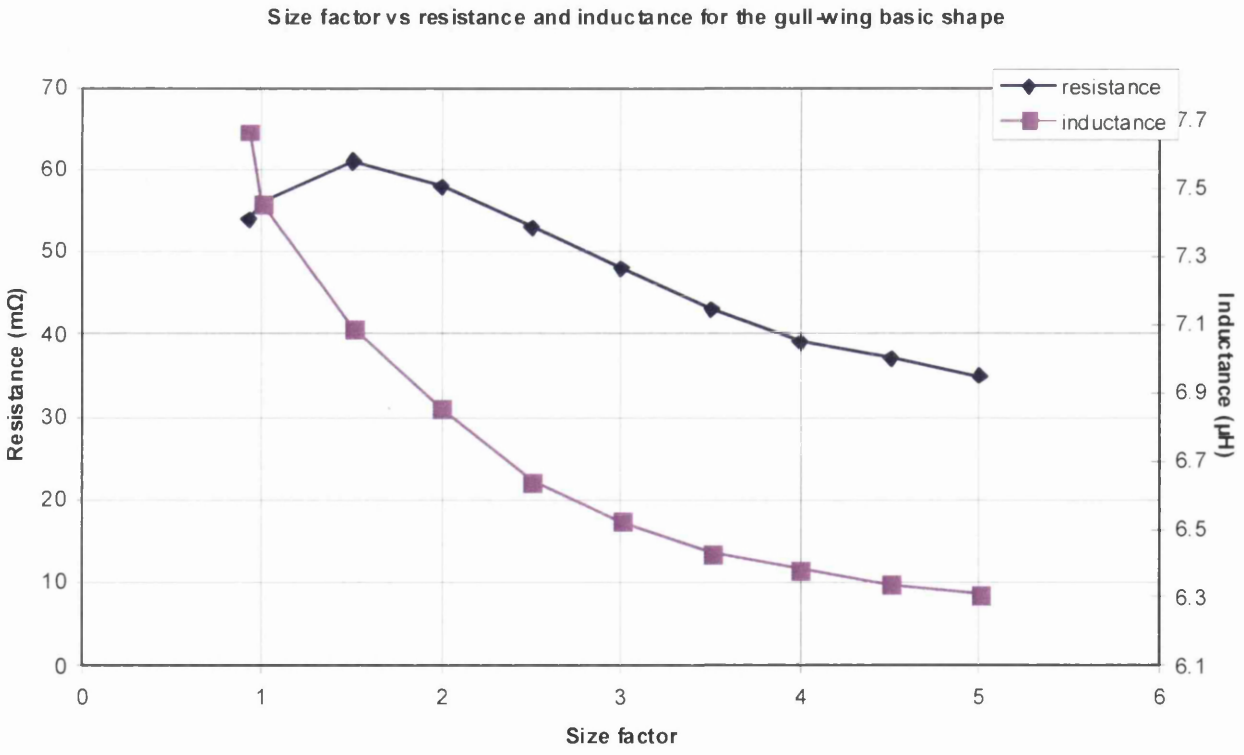

Figure 7.14 - Gull-wing shape resistance and inductance for different size factor variable values

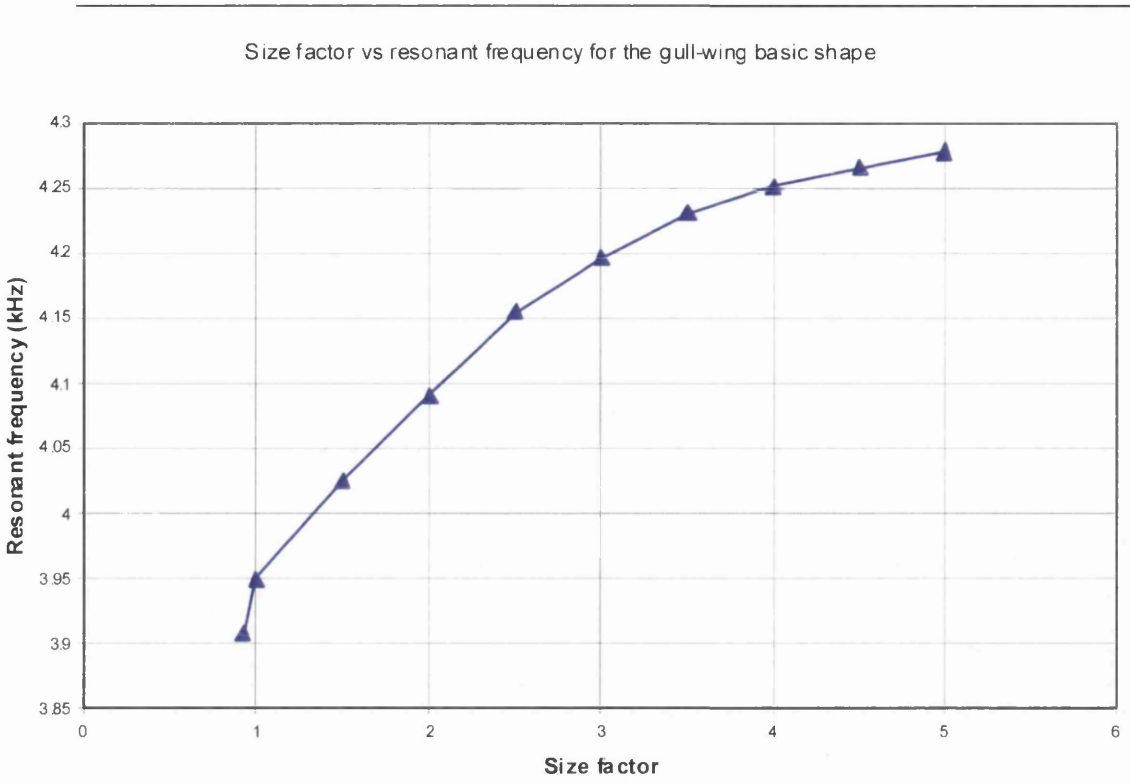

Figure 7.15 - Gull-wing shape resonant frequency for different size factor variable values

The question then remains of what interpolation scheme will be used to obtain resistance, inductance and resonant frequency values at size factor variable values between those at which FEM models have been solved. In this work, it was decided that linear interpolation would be used. Here, in the expression for linear interpolation that follows, x values represent the size factor, y values represent either resistance, inductance or resonant frequency values depending upon which one is desired to be obtained, subscript 0 values represent values at the next lowest size factor value at which resistance, inductance or resonant frequency values are known, subscript 1 values represent values at the next highest size factor value at which resistance, inductance or resonant frequency values are known, the subscriptless x value is the size factor value at which the resistance, inductance or resonant frequency is desired to be known and the subscriptless y value is the actual resistance, inductance or resonant frequency value which is desired to be known. Thus linear interpolation [207] as used in this work may be expressed as:

$$y = y_0 + (x - x_0)\frac{y_1 - y_0}{x_1 - x_0} \tag{7.22}$$

Therefore the resistance, inductance and resonant frequency expressions to be used when adding the gull-wing basic shape to the Main Module database in this work are actually (7.22) used together with the resistance, inductance and resonant frequency values plotted as points in Figure 7.14 and Figure 7.15 and tabulated in Appendix F. The graphs of Figure 7.14 and Figure 7.15 show the linear interpolation of (7.22) between the point values that have been obtained using this work's FEM Module.

7.13 The Use of the Main Module to Solve a Nerve Membrane Potential Problem Using the Gull-Wing Basic Shape

Once expressions for the resistance, inductance and resonant frequency of the gull-wing basic shape in terms of the size factor variable had been added to this work's Main Module, it was decided to attempt to use the Main Module to solve an optimisation problem. This involved using the Main Module to find a size of gull-wing coil that would, when used coupled to a Magstim Rapid^2 stimulator, produce a normalised nerve membrane potential value within 10% of a specified value at a certain distance below the coil. In addition, the coil should be as focal as possible.

Thus the Main Module would use the same simulated annealing optimisation code as the New Shape Module except that the expression whose minimum was being sought was:

$$C(\mathbf{x}) = c_o U^2(\mathbf{x}) + c_p \left\{ \max\left[0, \left(\left|V_{nm} - v_{nm}(\mathbf{x})\right| - 0.1V_{nm}\right)\right]^2 \right\} \qquad (7.23)$$

where the notation and constant values are as was used in (7.20) in Section 7.5 except that the penalty function field values are replaced by a target normalised nerve membrane potential V_{nm} and an actual running normalised nerve membrane potential value v_{nm} which depends on the design variable value (the size factor) at a particular iteration of the optimisation process. Thus the first term on the right hand side of (7.23) refers to the coil focality and is evaluated as in the New Shape Module from

the electric field modelling computer code. The second term on the right hand side refers to getting as close as possible to within 10% of a V_{nm} value and the running v_{nm} value is evaluated using (2.6). In this evaluation of (2.6) the peak electric field value E_0 is obtained from the electric field modelling code as in the New Shape Module and the values R_{tot}, L_{tot} and ω are obtained using the expressions for coil resistance, inductance and resonant frequency referred to at the beginning of the last paragraph based upon the size factor value at the optimisation iteration in question. It will be remembered that R_{tot} and L_{tot} are obtained by adding the values obtained from the resistance and inductance expressions to the stimulator and lead resistance and inductances as appropriate.

From (2.6), it may be seen that that expression contains a time term *t*. The question then arises of at what *t* value should (2.6) be evaluated in order to obtain the v_{nm} value at a particular optimisation iteration. In [49], [63] and [208] it may be seen that the largest nerve membrane potential during transcranial magnetic stimulation (where the nerve membrane time constant, $R_m C_m = \tau_m \approx 150\mu s$ in (2.6) as evaluated by Barker et al.) occurs three quarters of the way into the stimulator current pulse. Given that a τ_m value of $150\mu s$ will be used in the Main Module, the v_{nm} value will be evaluated at a *t* value equal to three quarters of the current pulse period as calculated from the resonant frequency obtained from the resonant frequency interpolated expression relevant to the size factor value in question. It will be noted that, in the Main Module, the magnitude of v_{nm} will be used as the value in the optimisation process as it does not matter for stimulation to occur whether the nerve membrane potential exceeds an action potential value in the positive or negative direction from zero, and in the studies above, the stimulation at three quarter current pulse period occurs when the nerve membrane potential is negative.

For the sample Main Module gull-wing shape optimisation problem it was decided to ask the program to find the most focal gull-wing coil that would produce a normalised nerve membrane potential of within 10% of 2.8mV at a distance below the coil plane of 10 mm. The solution coil from the program was a gull-wing shaped coil with a size factor variable of 1.36. This coil resulted in a resonant frequency (obtained by

interpolation using the expression outlined in the last section) of 4.01 kHz when used with a Magstim Rapid^2 stimulator and the resonant frequency resistance and inductance of the coil was found by interpolation as 61mΩ and 7.09 μH respectively. The normalised nerve membrane potential resulting from using the coil at 10 mm below the coil was -2.68 mV which is within 10% by magnitude of the target of 2.8 mV. It should be noted that the stimulator charge level was fixed at 40% charge, i.e. 680V, for this demonstration of the Main Module. The coil focality was evaluated as 85 mm.

Thus it has been seen in this section that this work's Main Module is able to successfully use optimisation to find a certain size of a basic shape within its database of shapes that meets a particular normalised nerve membrane potential value at a particular distance below the coil's plane. To do this, in addition to the module's own code, successful use has been made of the New Shape module to find the gull-wing shape in the beginning and the FEM Module to obtain the resonant frequency, resistance and inductance expressions on which the Main Module depends.

7.14 Conclusions

In this chapter it has been seen how this work's Main, New Shape and Finite Element Method (FEM) Modules can be used together to find a size and shape of coil that can meet a certain normalised nerve membrane potential value at a certain distance below the coil.

It was firstly seen how the desire to find the most focal coil shape can be converted into an objective function to be used with this work's simulated annealing optimisation computer program. Then it was explained that it is necessary to set a target peak electric field value when searching for coil shapes using this work's New Shape Module. It was seen that this target can be converted into a penalty function for use with the optimisation code. A composite function was then constructed for the New Shape Module's optimisation code from the objective and penalty functions.

The necessity to calculate the peak electric fields that would arise when coil geometries were used with a stimulator during the New Shape and Main Module's optimisation process meant that a method to calculate this peak electric field was presented based upon the initial coil inductance.

The choice of design variables to be used with the New Shape Module's optimisation was then discussed. Variables based on simple r and z loop locations and those better suited to more constructible shapes were presented. The New Shape Module was used to find coil shapes which were then detailed and the gull-wing coil was given as an example of a more constructible coil shape.

The importance of ensuring that the field modelling code of the New Shape and Main Modules was functioning correctly was emphasised and field measurements around the gull-wing coil and a Magstim HP90 were taken. These were found to closely match what the computer code expected to find around such shapes and the computer code was deemed to be modelling electric field correctly.

The Main Module was then discussed. The objective function to be used with the simulated annealing optimisation code was detailed and this was found to be very close to that of the New Shape Module except that the penalty function involved normalised nerve membrane values instead of electric field values. A set of size governing only design variables was presented so as to add the gull-wing as a basic shape to the Main Module's database. This set had a single element in this example which was the size factor variable. The FEM Module was then used to establish how a gull-wing shaped coil's resonant frequency, resistance and inductance would vary with the size factor at certain regularly spaced size factor values. Linear interpolation was then used to form expressions for the gull-wing shape's resonant frequency, resistance and inductance with size factor which was used to add the gull-wing basic shape to the Main Module's database of shapes. The Main Module's optimisation process was found to involve repetitive evaluations of the normalised nerve membrane potential expression given in (2.6) from Section 2.3.

Finally, the Main Module was used to find a size of gull-wing shaped coil that could induce a certain normalised nerve membrane potential value at a certain distance

below the coil. This size of coil had a size factor of 1.36 and the optimisation process was set to ensure that the coil was as focal as possible. This resulted in a coil focality of 85 mm. Thus, by this stage, this work's tri-modular approach was deemed to be working as expected and how all three computer code modules work together had been demonstrated.

8 Conclusions

In this thesis a novel tri-modular computer program solution to finding more focal magnetic stimulation coil geometries has been presented and shown to be working effectively. The system combines a simulated annealing optimisation engine with thin wire approximation electromagnetic modelling computer code so that new coil shapes can be searched for – the New Shape Module. New shapes are reported and a new basic coil shape, the 'gull-wing' shape, that can be built using present methods, is also reported on.

Finite Element Method (FEM) modelling is used to construct expressions for the resistance, inductance and resonant frequency of certain basic coil topologies when used with a biphasic stimulator, in terms of size governing variables. These expressions allow the same optimisation and field modelling engine as the New Shape Module to be used to search for the sizes of basic shapes that are as focal as possible, whilst meeting a certain normalised nerve membrane potential value – in the Main Module. Use is made of (2.6) when calculating nerve membrane potential values. This module is shown to work using the gull-wing basic shape.

In Chapter 3, the modelling of stimulation coils as coils of infinitesimally thin wire is investigated so as to provide a method of reducing the computational demands of some of the electromagnetic modelling required to be undertaken in this work. There, two approximations to the shape of a spiral coil are investigated – namely the discretised thin-wire model and the model of a spiral as concentric loops of thin wire. The accuracy of the electric field values obtained from these models is reported upon for the first time. Given the good accuracy of these values, and the speed of execution of the computer models, it is decided that the technique of modelling coils as loops of thin-wires would be a good choice for use with the axi-symmetric shape modelling undertaken in the Main and New Shape Modules of this work.

In Chapter 4, the **T**-Φ method FEM formulation is introduced and in Section 4.3 a case is made for its use in this work's Finite Element Module. The frequency domain

version of the formulation is then explained in some detail. It is shown that the method is capable of efficiently producing accurate results using the QMRPACK solver for the singular equation system that results. This leads to results being presented that show the **T-Φ** method in use for the first time to solve a model that includes the internal structure of a magnetic stimulation coil. Results are presented to show the 2D axi-symmetric frequency domain **T-Φ** method correctly taking the skin and proximity effects into account and accurately modelling the current density within, and the magnetic field around, a Magstim HP90 coil used with a Magstim Rapid^2 stimulator.

Chapter 5 discusses the Finite Element Module and explains that the frequency content of the current pulse that arises when a new coil geometry (that may have arisen during an optimisation iteration) is used with a particular stimulator is not known *a priori*, meaning that the frequency domain FEM program of Chapter 4 cannot be directly used in this work to find the resistance, inductance and resonant frequency of a stimulation coil and biphasic stimulator pairing. A circuit coupled time domain FEM model is therefore required in order to find the resonant frequency of the current pulse that would arise when a coil is used with a particular stimulator. The chapter continues by showing that the electromagnetics that underlie magnetic stimulation are an example of a diffusion process which then helps in understanding the criteria for the time step size to be used in the time domain FEM modelling. Then, the time domain form of the 2D axi-symmetric **T-Φ** FEM formulation is presented which uses the implicit Galerkin time stepping method, and this is shown to be unconditionally numerically stable.

Chapter 5 then continues by presenting work that demonstrates how matrix conditioning affects solver convergence with the time domain FEM formulation chosen for use in this work. A minimum time step value is suggested so that convergence problems are avoided. The time domain FEM formulation is then shown to be able to adequately model a Magstim HP90 coil driven by a current pulse at the resonant frequency of 2.5 kHz. Then, a method for coupling the time domain FEM model to a circuit model of a biphasic stimulator is presented, before the chapter closes by reporting on how the coupled model can be used to accurately predict the resistance and inductance of a HP90 coil when used with a Magstim Rapid^2 biphasic

stimulator. The proposed method involves obtaining the resonant frequency of the coil / stimulator pairing from the coupled time domain model. The frequency domain model is then run at the resonant frequency to obtain the resistance and inductance of the coil at that frequency. This method constitutes this work's proposed Finite Element Module and is a novel approach to modelling stimulating coils and obtaining their resonant frequency resistance and inductance.

When taken as a whole, it is felt that the FEM modelling undertaken in this work has been a success. This is because the **T**-Φ FEM formulation, in both the frequency and time domains, has proven to be efficient and accurate. The formulation lent itself well to circuit coupling and the practise of running the coupled code followed by one run of the frequency domain code was not felt to be too cumbersome. As a result, this FEM modelling technique would be recommended for use in future work.

Chapter 6 introduces the simulated annealing (SA) optimisation algorithm and outlines why the technique has been chosen for the optimisation work in the New Shape and Main Modules. The chapter presents for the first time how the SA can be combined with a penalty function, the representation of an axi-symmetric coil as concentric loops of thin wire in an electric field model, coil geometry design variables with constraint limits and a means of translating the design variables into loop positions in order to solve a sample optimisation problem involving the geometry of a stimulating coil. Given the accuracy of the SA based method when solving the sample problem of Section 6.6, and the rapid computer execution times involved, it was decided that the method was a success and that the SA would prove to be a good choice as the optimisation technique upon which to build the New Shape and Main Modules. It would also be eminently suitable for use in future, related, optimisation work.

Chapter 7 explains how the optimisation computer program developed in Chapter 6 can be expanded into this work's New Shape and Main Modules. It is seen how objective, penalty and compound functions can be developed for the optimisation code so that coil shapes which are as focal as possible, and meet a certain specified target electric field value, can be searched for. A method to calculate the peak electric field obtainable for a coil shape, when it is used with a particular stimulating machine,

and that is based upon the initial coil inductance, is identified and presented in the chapter.

The chapter then goes on to consider the choice of design variables to be used in the New Shape Module. Variables based on simple r and z loop locations and those better suited to more constructible shapes were identified. The New Shape Module was then used to find new shapes based on r and z variables and the more buildable variables. The gull-wing new coil shape is given as an example of a more constructible coil shape. Then, evidence from electric field measurements taken around a gull-wing coil and a Magstim HP90 coil is presented to show that the field modelling code of the New Shape and Main Modules is functioning correctly.

The Main Module is then discussed. The compound function to be used with the simulated annealing optimisation code is detailed and this is found to be similar to that of the New Shape Module except that the penalty function involves normalised nerve membrane values instead of electric field values. The gull-wing is then added as a new basic shape to the Main Module database of shapes. The size governing variable in this instance is identified as the coil size factor whose nature is explained in Section 7.11.

The FEM Module is then used to establish how a gull-wing shaped coil's resonant frequency, resistance and inductance would vary with the size factor at certain regularly spaced size factor values. These values together with linear interpolation are used to form expressions for the gull-wing shape's resonant frequency, resistance and inductance with size factor which are used to add the gull-wing basic shape to the Main Module's database of shapes. Then the Main Module is used to find a size of gull-wing shaped coil that can induce a certain normalised nerve membrane potential value at a certain distance below the coil and is deemed to be working as desired.

Thus, this work in its totality demonstrates a novel tri-modular method of using SA optimisation, FEM field modelling and thin-wire field modelling to find new stimulating coil shapes. The method is demonstrated for axi-symmetric coils and in addition to finding more focal coil shapes ensures that the shapes suggested as solutions meet either a required electric field value or a certain normalised nerve

membrane potential value. Given the tri-modular approach's ability to successfully find novel more focal shapes that meet a certain normalised nerve membrane potential value and to do this accurately and without the need to run repetitive FEM models as part of the optimisation algorithm, the approach was deemed to be a success. The approach has the additional advantage that the Main and New Shape Modules may be used by people who are not familiar with the FEM and its requirement for correctly defined meshes.

As it stands, this work may be usefully developed in a number of ways. For example, the New Shape Module optimisation program could be extended beyond simply considering axi-symmetric coil shapes. Shapes similar to the double spiral coil, or shapes with more than two wings, could be considered and optimisation used to find the required angle between the coil's wings to achieve a target electric field value using the most focal coil geometry possible. The same circular loop thin-wire code could be used to model the field around approximations to the coil shapes. However, if it was desired to use non-axisymmetric coil shapes as basic shapes in the Main Module it should be noted that the present axi-symmetric FEM Module would need to be extended to a full three dimensional modelling tool in order to be able to construct expressions for the resistance, inductance and resonant frequency of the shapes in terms of their size governing variables. This would be because the skin and proximity effects would be different in different parts of the coil structures and would not take simpler axi-symmetric configurations as with axi-symmetric coil shapes. The **T**-Φ FEM formulation presented in this work would extend easily to modelling stimulation coils in three dimensions.

A further development could be to move beyond shapes that can be approximated using circular loops of thin wire and consider shapes that have sharp angles in their topologies such as the four leaf shape discussed in Section 1.5. This would mean changing the electric field modelling code of the New Shape and Main Modules away from that using circular loops of wire and instead adopting modelling code using the segmented thin-wire technique presented in Sections 3.3 and 3.4. Such code would take longer to run but would offer greater flexibility. It could be noted that, at present, coils having sharp angles would take longer to fabricate than coils based on circular loops, which may be built using a spinning process. However, in the future, if coils

with sharp angles were found to have particularly desirable properties, altering the repetitive manufacturing process to accommodate such coils could be investigated and considered.

In this work, the Main Module is based upon achieving a focal coil geometry that meets a required normalised nerve membrane potential. In reality, eventually, it may be more desirable to be able to find a coil geometry that meets an actual nerve membrane potential value in order to ensure that an action potential is triggered. In order to achieve this, the Main Module could be extended to include an FEM model of a human head which has currents induced in it by a nearby coil which would be modelled using a thin-wire technique. With this combined FEM / thin-wire model a user could enter a desired nerve membrane potential value for a location within the head and sizes of different basic coil shapes could be searched for using optimisation that result in that value being achieved with the best possible focality. The **T-Φ** formulation could easily be used for such a model of the structure of the human head.

During the period when the work described in this thesis was being undertaken, some interesting work by Roth et al was published [209]. In the work, the authors introduce a new coil shape called a Hesed coil. This coil has a number of turns which incorporate some sharp 90° turns so that part of the coil juts up perpendicularly to the plane occupied by most of the coil. The objective of this shape is to be able to achieve stimulation at depth without the very high electric field values seen in tissue closer to the coil that occurs with spiral or double spiral type coils. It is reported that the Hesed coil achieves at least improved results in this respect. The paper then goes on to discuss the possibility of exploiting the temporal characteristics of nerves in order to achieve much better results in stimulating deep tissue without stimulating more shallow tissue. A type of Hesed coil is presented where the current pulse in different turns of the coil may be independently controlled. Then, by adjusting when current is sent through the different turns, and by exploiting how long it takes the tissue primarily affected by the current in particular turns to be most susceptible to excitation by the current in subsequently activated turns, it becomes possible to stimulate tissue at depth preferentially. Such a system is termed Time Summation Multichannel Transcranial Magnetic Stimulation (tmTMS). Promising results are presented for this system.

Therefore it seems, at the moment, that tmTMS offers the most promising system for stimulating tissue at depth without unintentionally stimulating more shallow tissue. It would be interesting to investigate in the future whether the simulated annealing optimisation engine developed in this thesis could be used to establish the optimal way of sending current through the turns of a tmTMS coil in order to stimulate a particular location. Segmented thin-wire modelling could be used to model the electric field due to such a coil and a **T**-Φ formulation FEM model of a head could be used together with equations for how tissue reacts to field in the time immediately after first being excited.

Finally, it should be added that a preliminary investigation was undertaken in this work into how coil heating affects the electric field around magnetic stimulation coils. To do this, a Magstim HP90 coil was connected to a Magstim Rapid^2 stimulator and a continuous train of pulses discharged into the coil until its temperature rose, as measured using a spot temperature measurement gun, and became constant. The electric field around the coil was measured using the same probe as that used to measure the field in Sections 7.9 and 7.10. No change in electric field was visible when the coil was hot compared to that measured at the first biphasic pulse. Given that this initial experiment implied that heating does not affect the electric field around a stimulation coil, no further investigations were undertaken into this topic.

References

[1] C. Hovey, P. Houseman, and R. Jalinous, *The New Guide to Magnetic Stimulation*, The Magstim Co. Ltd, Whitland, United Kingdom, 2003.

[2] D. K. Cheng, *Field and Wave Electromagnetics*, 2nd ed., Addison-Wesley, Reading, Massachusetts, 1989, p. 323.

[3] C. A. Coulson, *Electricity*, Oliver and Boyd, Edinburgh, 1958, p. 226.

[4] W. J. Duffin, *Electricity and Magnetism*, McGraw-Hill, New York, 1990, p.349.

[5] G. Cerri, R. De Leo, F. Moglie, and A. Schiavoni. "An Accurate 3-D Model for Magnetic Stimulation of the Brain Cortex", *Journal of Medical Engineering and Technology*, vol. 19, no. 1, 1995, pp. 7 – 16.

[6] A. L. Hodgkin, *The Conduction of the Nervous Impulse*, Liverpool University Press, Liverpool, 1971.

[7] A. T. Barker. I. L. Freeston, R. Jalinous, and J A. Jarratt, "Magnetic Stimulation of the Human Brain and Peripheral Nervous System: An Introduction and the Results of an Initial Clinical Evaluation", *Neurosurgery*, vol. 20, no. 1, 1987, pp. 100-109.

[8] R. G. Bickford, and B. D. Fremming, "Neuronal Stimulation by Pulsed Magnetic Fields in Animals and Man", *Digest of the 6th International Conference of Medical Electronics in Biology and Engineering*, 1965, p. 112.

[9] M. J. R. Polson, A. T. Barker and I. L. Freeston, "Stimulation of Nerve Trunks with Time-Varying Magnetic Fields", *Medical & Biological Engineering & Computing*, vol. 20, 1982, pp. 243- 244.

[10] R. Jalinous, "The Use of Time-Varying Magnetic Fields to Stimulate the Human Nervous System: Theory and Practice", *Thesis*, University of Sheffield, 1988.

[11] A. T. Barker R. Jalinous, and I. L. Freeston, "Non-Invasive Magnetic Stimulation of the Human Motor Cortex", *Lancet*, no. 1, 1985, pp. 1106 – 1107.

[12] *Magnetic Stimulators and Coils*, The Magstim Co. Ltd., Whitland, United Kingdom, 2007.

[13] A. Pascual-Leone, J. R. Gates, and A. Dhua, "Induction of Speech Arrest and Counting Errors with Rapid-Rate Transcranial Magnetic Stimulation", *Neurology*, vol. 41, no. 5, 1991, pp. 697 – 702.

[14] V. Walsh, and M. Rushworth, "A Primer of Magnetic Stimulation as a Tool For Neuropsychology", *Neuropsychologia*, vol. 37, no. 2, 1999, pp. 125 – 135.

[15] T. Yamanishi, K. Yasudam S. Suda, N. Ishikawa, R. Sakakibara, and T. Hattori, "Effect of Functional Continuous Magnetic Stimulation for Urinary Incontinence", *Journal of Urology*, vol. 163, no. 2, 2000, pp. 456 - 459.

[16] O. G. Morales, H. A. Sackeim, R. M. Berman, and S. H. Lisanby, "Magnetic Seizure therapy: Development of a Novel Intervention For Treatment Resistant Depression", *Clinical Neuroscience Research*, vol. 4, no. 1, 2004, pp. 59 – 70.

[17] H. M. Haraldsson, F. Ferrarelli, N. H. Kalin, and G. Tononi, "Transcranial Magnetic Stimulation in the Investigation and Treatment of Schizophrenia: a Review", *Schizophrenia Research*, vol. 71, no. 1, 2004, pp. 1 - 16.

[18] E. M. Wasserman, "Risk and Safety of repetitive Transcranial Magnetic Stimulation: Report and Suggested Guidelines from the International Workshop on the Safety of Repetitive Transcranial Magnetic Stimulation", *Electroencephalography and Clinical Neurophysiology*, vol. 108, no. 1, 1998, pp. 1-16.

[19] A. Peterchev, R. Jalinous, and S. H. Lisanby, "A Novel Transcranial Magnetic Stimulator Inducing Near Rectangular Pulses with Controllable Pulse Width", *IEEE Transactions in Biomedical Engineering*, preprint.

[20] G. Cerri, R. De Leo, F. Moglie and A. Schiavoni, "An Accurate 3-D Model for Magnetic Stimulation of the Brain Cortex", *Journal of Medical Engineering & Technology*, vol. 19, no. 1, pp. 7 - 16.

[21] P. Ravazzani, J. Ruohonen, G. Tognola, F. Anfosso, M. Ollikainen, R. J. Ilmoniemi, and F. Grandori, "Frequency-related effects in the Optimization of Coils for the Magnetic Stimulation of the Nervous System", *IEEE Transactions on Biomedical Engineering*, vol. 49, no. 5, pp. 463 – 471, May 2002.

[22] A. Myers, *Improving the Efficiency of Magnetic Stimulation of Nerves*, PhD Thesis, University of Sheffield, Sheffield, 2005, p. 56.

[23] A. Myers, *Improving the Efficiency of Magnetic Stimulation of Nerves*, PhD Thesis, University of Sheffield, Sheffield, 2005, p. 50.

[24] D. Cohen, and B. N. Cuffin, "Developing a More Focal Magnetic Stimulator", *Journal of Clinical Neurophysiology*, vol. 8, no. 1, pp. 102 – 111, 1991.

[25] A. Myers, *Improving the Efficiency of Magnetic Stimulation of Nerves*, PhD Thesis, University of Sheffield, Sheffield, 2005, pp. 84 – 91.

[26] G. A. Mouchawar, J. A. Nyenhuis, J. D. Bourland and L. A. Geddes, "Influence of Coil Geometry on Localization of the Induced Electric field in Magnetic (Eddy-Current) Stimulation of Excitable Tissue", *IEEE Transactions on Magnetics*, vol. 26, no. 5, pp. 1545 – 1547, 1990.

[27] R. Carabunaru, and D. M. Durand, "Toroidal Coil Models for Transcutaneous Magnetic Stimulation of Nerves", *IEEE Transactions on Biomedical Engineering*, vol. 48, no. 4, pp. 434 – 441, 2001.

[28] K-H Hsu, and D. M. Durand, "A 3-D Differential Coil Design for Localized Magnetic Stimulation", *IEEE Transactions on Biomedical Engineering*, vol. 48, no. 10, pp. 1162 – 1168, 2001.

[29] R. Jalinous, "Technical and Practical Aspects of Magnetic Nerve Stimulation", *Journal of Clinical Neurophysiology*, vol. 8, no. 1, pp. 10 – 25, 1991.

[30] J. Cadwell, "Optimizing Magnetic Stimulator Design", *Electroencephalography and Clinical Neurophysiology*, supp. 43, pp. 238 – 248, 1991.

[31] I. N. Hsiao, and V. W. Lin, "Improved Coil Design for Functional Magnetic Stimulation of Expiratory Muscles", *IEEE Transactions on Biomedical Engineering*, vol. 48, no. 6, pp. 684 – 694, 2001.

[32] B. J. Roth, L.G. Cohen, and M. Hallett, "The Electric Field Induced During Magnetic Stimulation", *Electroencephalography and Clinical Neurophysiology*, supp. 43, pp. 268 – 278, 1991.

[33] S. Ueno, T Tashiro, and K. Harada, "Localized Stimulation of Neural Tissues in the Brain by Means of a Paired Configuration of Time Varying Magnetic Fields", *Journal of Applied Physics*, vol. 64, no. 10, pp. 5862 – 5864, 1988.

[34] L. G. Cohen, B. J. Roth, J. Nilsson, N. Dang, M. Panizza, S. Bandinelli, W. Friauf, and M. Hallett, "Effects of Coil Design on Delivery of Focal Magnetic Stimulation. Technical Considerations", *Electroencephalography and Clinical Neurophysiology*, vol. 75, no. 4, pp. 350 – 257, 1990.

[35] K. P. Esselle, and M. A. Stuchly, "Cylindrical Tissue Model of Magnetic Field Stimulation of Neurons: Effects of Coil Geometry", *IEEE Transactions on Biomedical Engineering*, vol. 42, no. 9. pp. 934 – 941, 1995.

[36] B. J. Roth, P. J. Maccabee, L. P. Eberle, V. E. Amassian, M. Hallett, J. Cadwell, G. D. Anslemi, and G. T. Tatarian, "In Vitro Evaluation of a 4-Leaf Coil Design for Magnetic Stimulation of Peripheral Nerves", *Electroencephalography and Clinical Neurophysiology*, vol. 93, no. 1, pp. 68 – 74, 1994.

[37] C. Ren, P. P. Tarjan, and D. B. Popovi, "A Novel Electric Design for Electromagnetic Stimulation – the Slinky Coil", *IEEE Transactions on Biomedical Engineering*, vol. 42, no. 9, pp. 918 – 925, 1995.

[38] E. R. Lontis, M. Voigt, and J. J. Struijk, "Focality Assessment in Transcranial Magnetic Stimulation with Double and Cone Coils", *Journal of Clinical Neurophysiology*, vol. 23, no. 5, pp. 462 – 471, 2006.

[39] N. Al-Mutawaly, H. de Bruin, and R. D. Findlay, "Magnetic Nerve Stimulation: Field Focality and Depth of Penetration", *Proceedings of the 23rd Annual EMBS International Conference*, pp. 877 – 880, 2001.

[40] D-H. Kim, G. E. Georghiou, and C. Won, "Improved Field Localization in Transcranial magnetic Stimulation of the Brain with the Utilization of a Conductive Shield Plate in the Stimulator", *IEEE Transactions in Biomedical Engineering*, vol. 53, no. 4, pp. 720 – 725, 2006.

[41] L. Heller, and D. B. van Hulsteyn, "Brain Stimulation Using Electromagnetic Sources: Theoretical Aspects", *Biophysical Journal*, vol. 62, pp. 129 – 138, 1992.

[42] A. D. Belegundu, and T. R. Chandrupatla, *Optimization Concepts and Applications in Engineering*, Prentice-Hall, New Jersey, 1999.

[43] J. Ruohonen, P. Ravazzani, and F. Grandori, "Functional Magnetic Stimulation: Theory and Coil Optimization", *Bioelectrochemistry and Bioenergetics*, vol. 47, pp. 213-219, 1998.

[44] P. Ravazzani, G. Tognola, J. Ruohonen, and F. Grandori, "Optimization of the Devices for Magnetic Stimulation of the Nervous System: Influence of Frequency-Related Effects and Geometrical Characteristics", *Proceedings of the 22nd Annual EMBS International Conference*, Chicago, Illinois, pp. 2625 – 2628, 2000.

[45] P. Ravazzani, J. Ruohonen, G. Tognola, F. Anfosso, M. Ollikainen, R. J. Ilmoniemi, and F. Grandori, "Frequency-Related Effects in the Optimization of Coils for the Magnetic Stimulation of the Nervous System", *IEEE Transactions on Biomedical Engineering*, vol. 49, no. 5, pp. 463 – 471, May 2002.

[46] M. Sekino, and S. Ueno, "FEM-Based Determination of Optimum Current Distribution in Transcranial Magnetic Stimulation as an Alternative to Electroconvulsive Therapy", *IEEE Transactions on Magnetics*, vol. 40, no. 4, pp. 2167 – 2169, 2004.

[47] T. Onuki, S. Wakao, T. Miyokawa, and Y. Nishimura, "Design Optimization of Stimulating Coil System for Nerve Stimulation", *IEEE Transactions on Magnetics*, vol. 34, no. 4, pp, 2159 – 2161, 1998.

[48] J. Ruohonen, and R. J. Ilmoniemi, "Focusing and Targeting of Magnetic Brain Stimulation Using Multiple Coils", *Medical and Biological Engineering and Computing*, vol. 36, pp. 297 – 301, 1998.

[49] K. Davey, and C. M. Epstein, "Magnetic Stimulation Coil and Circuit Design", *IEEE Transactions on Biomedical Engineering*, vol. 47, no. 11, pp. 1493-1499, November 2000.

[50] A. T. Barker, C. W. Garnham, and I. L. Freeston, "Magnetic Nerve Stimulation: the Effect of Waveform on Efficiency, Determination of Neural Membrane Time Constants and the Measurement of Stimulator Output", *Magnetic Motor Stimulation: Basic Principles and Clinical Experience (EEG Supplement 43)*, pp. 227-237, 1991.

[51] D. K. Cheng, *Field and Wave Electromagnetics*, 2nd ed., Addison-Wesley, Reading, Massachusetts, 1989, pp. 321-326.

[52] D. K. Cheng, *Field and Wave Electromagnetics*, 2nd ed., Addison-Wesley, Reading, Massachusetts, 1989, p. 308.

[53] G. D. Smith, *Numerical Solution of Partial Differential Equations: Finite Difference Methods*, 3rd ed., Oxford University Press, Oxford, 1986.

[54] E. Kreyszig, *Advanced Engineering Mathematics*, 9th ed., John Wiley, New York, 2006, p. 826.

[55] J. M. Jin, *The Finite Element Method in Electromagnetics*, 2nd ed., John Wiley, New York, 2002.

[56] A. F. Peterson, S. L. Ray, and R. Mittra, *Computational Electromagnetics*, IEEE Press, New York, 1997.

[57] P. P. Silvester, and R. L. Ferrari, *Finite Elements for Electrical Engineers*, 3rd ed., Cambridge University Press, Cambridge, 1996.

[58] A. Bossavit, *Computational Electromagnetism*, Academic Press, Boston, Massachusetts, 1998.

[59] P. B. Monk, *Finite Element Methods for Maxwell's Equations*, Clarendon Press, Oxford, 2003.

[60] C. A. Balanis, *Advanced Engineering Electromagnetics*, John Wiley, New York, 1989, p. 890.

[61] J. J. Wang, *Generalized Moment Methods in Electromagnetics*, John Wiley, New York, 1991.

[62] W. C. Chew, J. M. Jin, E. Michielssen, and J. Song, *Fast and Efficient Algorithms in Computational Electromagnetics*, Artech House, Norwood, Massachusetts, 2001.

[63] E. Corthout, A. T. Barker, and A. Cowey, *Transcranial Magnetic Stimulation: Which Part of the Current Waveform Causes the Stimulation?*, Experimental Brain Research, no. 141, pp. 128-132, 2001.

[64] V. Cerny, *A Thermodynamical Approach to the Travelling Salesman Problem: An Efficient Simulation Algorithm*, Journal of Optimization Theory and Applications, no. 45, pp. 41-51, 1985.

[65] C. Hovey, P. Houseman, and R. Jalinous, *The New Guide to Magnetic Stimulation*, Magstim Company Ltd., Whitland, UK, 2003.

[66] B. J. Roth, L. G. Cohen, M. Hallett, W. Friauf, and P. J. Basser, "A Theoretical Calculation Of The Electric Field Induced By Magnetic Stimulation Of A Peripheral Nerve", *Muscle & Nerve*, vol. 13, pp. 734-741, August 1990.

[67] L. G. Cohen, B. J. Roth, J. Nilsson, N. Dang, M. Panizza, S. Bandinelli, W. Friauf, and M. Hallett, "Effects Of Coil Design On Delivery Of Focal Magnetic Stimulation. Technical Considerations", *Electroencephalography And Clinical Neurophysiology*, vol. 75, no. 4, pp. 350-357, 1990.

[68] B. J. Roth and P. J. Basser, "A Model of the Stimulation of a Nerve Fibre by Electromagnetic Induction", *IEEE Transactions on Biomedical Engineering*, vol. 37, no. 6, pp. 588-597, June 1990.

[69] G. A. Mouchawar, J. D. Bourland, J. A. Nyenhuis, L. A. Geddes, K. S. Foster, J. T. Jones, and G. P. Graber, "Closed-Chest Cardiac Stimulation with a Pulsed Magnetic Field", *Medical & Biological Engineering & Computing*, vol. 30, pp. 162-168, March 1992.

[70] C. W. Garnham, A. T. Barker, and I. L. Freeston, "Measurement of the Activating Function of Magnetic Stimulation Using Combined Electrical and Magnetic Stimulation", *Journal of Medical Engineering & Technology*, vol. 19, no. 2-3, pp. 57-61, March/June 1995.

[71] R. De Leo, G. Cerri, D. Balducci, F. Moglie, O. Scarpino, and M. Guidi, "Computer Modelling of Brain Cortex Excitation by Magnetic Field Pulses", *Journal of Medical Engineering & Technology*, vol. 16, no. 4, pp. 149-156, July/August 1992.

[72] G. Cerri, R. De Leo, F. Moglie, and A. Schiavoni, "An Accurate 3-D Model for Magnetic Stimulation of the Brain Cortex", *Journal of Medical Engineering & Technology*, vol. 19, no. 1, pp. 7-16, January/February 1995.

[73] D. K. Cheng, *Field and Wave Electromagnetics*, 2nd ed., Addison-Wesley, Reading, Massachusetts, 1989, p. 232.

[74] D. K. Cheng, *Field and Wave Electromagnetics*, 2nd ed., Addison-Wesley, Reading, Massachusetts, 1989, p. 61.

[75] D. K. Cheng, *Field and Wave Electromagnetics*, 2nd ed., Addison-Wesley, Reading, Massachusetts, 1989, p. 92.

[76] G. A. Mouchawar, J. A. Nyenhuis, J. D. Bourland, and L.A. Geddes, "Influence Of Coil Geometry On Localization Of The Induced Electric Field In Magnetic (Eddy-Current) Stimulation Of Excitable Tissue", *IEEE Transactions on Magnetics*, vol. 26, no. 5, pp. 1545-1547, September 1990.

[77] G. A. Mouchawar, J. A. Nyenhuis, J. D. Bourland, and L.A. Geddes, "Guidelines for Energy-Efficient Coils: Coils Designed for Magnetic Stimulation of the Heart", *Electroencephalography And Clinical Neurophysiology*, supp. 43, pp. 255-267, 1991.

[78] T. A. Wagner, M. Zahn, A. J. Grodzinsky, and A. Pascual-Leone, "Three-Dimensional Head Model Simulation of Transcranial Magnetic Stimulation", *IEEE Transactions on Biomedical Engineering*, vol. 51, no. 9, pp. 1586-1598, September 2004.

[79] D. K. Cheng, *Field and Wave Electromagnetics*, 2nd ed., Addison-Wesley, Reading, Massachusetts, 1989, p. 239.

[80] A. Shadowitz, *The Electromagnetic Field*, McGraw-Hill, New York, 1975, p. 300.

[81] D. K. Cheng, *Field and Wave Electromagnetics*, 2nd ed., Addison-Wesley, Reading, Massachusetts, 1989, pp. 31-36.

[82] K. A. Stroud, *Further Engineering Mathematics*, 3rd ed., Macmillan, London, 1996, pp. 155-165.

[83] B. C. Carlson, "Computing Elliptic Integrals by Duplication", *Numerische Mathematik*, no. 33, 1979, pp. 1-16.

[84] P. P. Silvester, and R. L. Ferrari, *Finite Elements for Electrical Engineers*, 3rd ed., Cambridge University Press, Cambridge, 1996, p. 347.

[85] K. Hsu, and D. M. Durand, "A 3D Differential Coil Design for Localized Magnetic Stimulation", *IEEE Transactions on Biomedical Engineering*, vol. 48, no. 10, pp. 1162-1168, October 2001.

[86] O. C. Zienkiewicz and R. L. Taylor, *The Finite Element Method Volume 1*, 4th ed., McGraw-Hill, New York, 1989, p. 230.

[87] P. P. Silvester, and R. L. Ferrari, *Finite Elements for Electrical Engineers*, 3rd ed., Cambridge University Press, Cambridge, 1996, pp. 68-73.

[88] D. J. Griffiths, *Introduction to Electrodynamics*, 3rd ed., Pearson Benjamin Cummins, San Francisco, 2008, p. 326.

[89] D. K. Cheng, *Field and Wave Electromagnetics*, 2nd ed., Addison-Wesley, Reading, Massachusetts, 1989, p. 63.

[90] P. P. Silvester, and R. L. Ferrari, *Finite Elements for Electrical Engineers*, 3rd ed., Cambridge University Press, Cambridge, 1996, p. 72.

[91] P. P. Silvester, and R. L. Ferrari, *Finite Elements for Electrical Engineers*, 3rd ed., Cambridge University Press, Cambridge, 1996, p. 73.

[92] P. P. Silvester, and R. L. Ferrari, *Finite Elements for Electrical Engineers*, 3rd ed., Cambridge University Press, Cambridge, 1996, pp. 73-75.

[93] P. P. Silvester, and R. L. Ferrari, *Finite Elements for Electrical Engineers*, 3rd ed., Cambridge University Press, Cambridge, 1996, pp. 75-83.

[94] P. Dular, C. Geuzaine, and W. Legros, "A Natural Method for Coupling Magnetodynamic H-Formulations and Circuit Equations", *IEEE Transactions on Magnetics*, vol. 35, no. 3, pp. 1626-1629, May 1999.

[95] O. Biro, "Edge element formulations of eddy current problems", *Computer Methods in Applied Mechanics and Engineering*, vol. 169, pp. 391-405, 1999.

[96] C. J. Carpenter and E. A. Wyatt, "Efficiency of Numerical Techniques for Computing Eddy Currents in Two and Three Dimensions", *COMPUMAG Oxford 1976*, pp. 242-250.

[97] C. J. Carpenter, "Comparison of Alternative Formulations of 3-Dimensional Magnetic-Field and Eddy-Current Problems at Power Frequencies", *Proceedings of the IEE*, vol. 124, no. 11, pp. 1026-1034, 1977.

[98] T. W. Preston and A. B. J. Reece, "Finite Element Solution of 3-Dimensional Eddy Current problems in Electrical Machines", *COMPUMAG Grenoble 1978*, paper 7.4.

[99] T. W. Preston and A. B. J. Reece, "Solution of 3-Dimensional Eddy-Current Problems : The T-Ω Method", *IEEE Transactions on Magnetics*, vol. 18, no. 2, pp.486-491, 1982.

[100] D. Rodger and N. Atkinson, "3-D Eddy Currents in Multiply Connected Thin Sheet Conductors", *IEEE Transactions on Magnetics*, vol. 23, no. 5, pp. 3047-3049, 1987.

[101] C. J. Carpenter and D. H. Locke, "Numerical Models of Three-Dimensional End Winding Arrays", *COMPUMAG Oxford 1976*, p. 48.

[102] D. K. Cheng, *Field and Wave Electromagnetics*, 2nd ed., Addison-Wesley, Reading, Massachusetts, 1989, p. 263.

[103] T. Nakata, N. Takahashi, K. Fujiwara, K. Muramatsu and Z. G. Cheng, "Comparison of Various Methods for 3-D eddy Current Analysis", *IEEE Transactions on Magnetics*, vol. 24, no. 6, pp.3159-3161, 1988.

[104] O. Biro, K. Preis, W. Renhart, G. Vrisk, and K. R. Richter, "Computation of 3-D Current Driven Skin Effect Problems Using a Current Vector Potential", *IEEE Transactions on Magnetics*, vol. 29, no. 2, pp.1325-1328, 1993.

[105] O. Biro, and K. R. Richter, "CAD in Electromagnetism", *Advances in Electronics and Electron Physics*, vol. 82, pp. 1-96, 1990.

[106] J. Simkin and C. W. Trowbridge, "On the Use of the Total Scalar Potential in the Numerical Solution of Field Problems in Electromagnetics", *International Journal of Numerical Methods in Engineering*, vol. 14, p. 423, 1979.

[107] T. Nakata, N. Takahashi, K. Fujiwara, and Y. Okada, "Improvements of the T-Ω Method for 3-D Eddy Current Analysis", *IEEE Transactions on Magnetics*, vol. 24, no. 1, pp.94-97, 1998.

[108] O. Biro and K. Preis, "Coupling Electric and Magnetic Vector Potentials in 3D Eddy Current Analysis", *Compel*, vol. 9, supp. A, pp. 45-48, 1990.

[109] P. P. Silvester, and R. L. Ferrari, *Finite Elements for Electrical Engineers*, 3rd ed., Cambridge University Press, Cambridge, 1996, p. 29.

[110] O. Biro, and K. Preis, "Finite Element Analysis of 3-D Eddy Currents", *IEEE Transactions on Magnetics*, vol. 26, no. 2, pp.418-423, 1990.

[111] P. P. Silvester, and R. L. Ferrari, *Finite Elements for Electrical Engineers*, 3rd ed., Cambridge University Press, Cambridge, 1996, p. 79-83.

[112] T. R. Chandrupatla and A. D. Belegundu, *Finite Elements in Engineering*, 3rd ed. Prentice-Hall, New Jersey, 2002, p. 135.

[113] H. Whitney, *Geometric Integration Theory*, Princeton University Press, Princeton, 1957.

[114] J. C. Nedelec, "Mixed Finite Elements in R^3", *Numerische Mathematik*, vol. 35, no.3, pp. 315-341, 1980.

[115] A. Bondeson, T. Rylander, and P. Ingelstrom, *Computational Electromagnetics"*, Springer, New York, 2005, p.111.

[116] A. Bondeson, T. Rylander, and P. Ingelstrom, *Computational Electromagnetics"*, Springer, New York, 2005, p.122.

[117] P. P. Silvester, and R. L. Ferrari, *Finite Elements for Electrical Engineers*, 3rd ed., Cambridge University Press, Cambridge, 1996, p. 312-313.

[118] D. K. Cheng, *Field and Wave Electromagnetics*, 2nd ed., Addison-Wesley, Reading, Massachusetts, 1989, p. 50.

[119] P. P. Silvester, and R. L. Ferrari, *Finite Elements for Electrical Engineers*, 3rd ed., Cambridge University Press, Cambridge, 1996, p. 45.

[120] P. P. Silvester, and R. L. Ferrari, *Finite Elements for Electrical Engineers*, 3rd ed., Cambridge University Press, Cambridge, 1996, p. 36.

[121] O. C. Zienkiewicz and R. L. Taylor, *The Finite Element Method Volume 1*, 4th ed., McGraw-Hill, New York, 1989, p. 144.

[122] O. Biro, P. Bohm, K. Preis, and G. Wachutka "Edge Element Analysis of Transient Skin Effect Problems", *IEEE Transactions on Magnetics*, vol. 36, no. 4, pp.835-839, 2000.

[123] D. K. Cheng, *Field and Wave Electromagnetics*, 2nd ed., Addison-Wesley, Reading, Massachusetts, 1989, p. 236.

[124] O. C. Zienkiewicz and R. L. Taylor, *The Finite Element Method Volume 1*, 4th ed., McGraw-Hill, New York, 1989, p. 144.

[125] O. C. Zienkiewicz and R. L. Taylor, *The Finite Element Method Volume 1*, 4th ed., McGraw-Hill, New York, 1989, pp. 121-122.

[126] R. Hiptmair and P. D. Ledger, "Computation of Resonant Modes for Axisymmetric Maxwell Cavities Using hp-version Edge Finite Elements", *International Journal for Numerical Methods in Engineering*, vol. 62, pp. 1652-1676, 2005.

[127] P. Ravazzani, J. Ruohonen, G. Tognola, F. Anfosso, M. Ollikainen, R. J. Ilmoniemi, and F. Grandori, "Frequency Related Effects in the Optimization of Coils for the Magnetic Stimulation of the Nervous System", *IEEE Transactions on Biomedical Engineering*, vol. 49, no. 5, pp. 463-471, May 2002.

[128] L. Bostock, and S. Chandler, *Applied Mathematics*, Stanley Thornes, Cheltenham, UK, 1975, p. 449.

[129] A. Bondeson, T. Rylander, and P. Ingelstrom, *Computational Electromagnetics"*, Springer, New York, 2005, pp. 210-212.

[130] A. Bondeson, T. Rylander, and P. Ingelstrom, *Computational Electromagnetics"*, Springer, New York, 2005, pp. 138.

[131] A. Myers, *Improving the Efficiency of Magnetic Stimulation of Nerves*, PhD Thesis, University of Sheffield, Sheffield, 2005, p. 71.

[132] A. Myers, *Improving the Efficiency of Magnetic Stimulation of Nerves*, PhD Thesis, University of Sheffield, Sheffield, 2005, p. 69.

[133] C. Geuzaine, and J. Remacle, "Gmsh: A Three-Dimensional Finite Element Mesh Generator with Built-In Pre and Post-Processing Facilities", *International Journal for Numerical Methods in Engineering*, published online 7 May 2009 in advance of print.

[134] G. D. Smith, *Numerical Solution of Partial Differential Equations: Finite Difference Methods*, 3rd ed., Oxford University Press, Oxford, 1985, p.7.

[135] A. Bondeson, T. Rylander, and P. Ingelstrom, *Computational Electromagnetics"*, Springer, New York, 2005, pp. 43-45.

[136] A. Bondeson, T. Rylander, and P. Ingelstrom, *Computational Electromagnetics"*, Springer, New York, 2005, p. 131.

[137] P. P. Silvester, and R. L. Ferrari, *Finite Elements for Electrical Engineers*, 3rd ed., Cambridge University Press, Cambridge, 1996, p. 367-369.

[138] O. C. Zienkiewicz and R. L. Taylor, *The Finite Element Method Volume 2*, 4th ed., McGraw-Hill, New York, 1989, pp. 348-351.

[139] O. C. Zienkiewicz and R. L. Taylor, *The Finite Element Method Volume 2*, 4th ed., McGraw-Hill, New York, 1989, pp. 354-357.

[140] O. C. Zienkiewicz and R. L. Taylor, *The Finite Element Method Volume 2*, 4th ed., McGraw-Hill, New York, 1989, p. 354.

[141] O. C. Zienkiewicz and R. L. Taylor, *The Finite Element Method Volume 2*, 4th ed., McGraw-Hill, New York, 1989, p. 358.

[142] E. L. Cussler, *Diffusion: Mass Transfer in Fluid Systems*, 2nd ed., Cambridge University Press, Cambridge, 1997, pp. 2-3.

[143] E. Kreyszig, *Advanced Engineering Mathematics*, 9th ed., John Wiley, New York, 2006, p. 465.

[144] R. Courant, K. Friedrichs, and H. Levy, "On the Partial Difference Equations of Mathematical Physics", *IBM Journal*, vol. 11, pp. 215-234, 1967.

[145] O. C. Zienkiewicz and R. L. Taylor, *The Finite Element Method Volume 2*, 4th ed., McGraw-Hill, New York, 1989, pp. 438-505.

[146] R. W. Freund, and N. M. Nachtigal, "QMRPACK: A Package of QMR Algorithms", *ACM Transactions on Mathematical Software*, vol. 22, no. 1, pp. 46-47, March 1996.

[147] C. F. Gerald, and P. O. Wheatley, *Applied Numerical Analysis*, 7th ed., Addison-Wesley, Boston, Massachusetts, 2004, p. 14.

[148] E. Kreyszig, *Advanced Engineering Mathematics*, 9th ed., John Wiley, New York, 2006, p. 865.

[149] K. Chen, *Matrix Preconditioning Techniques and Applications*, Cambridge University Press, Cambridge, 2005.

[150] Y. Saad, Iterative *Methods for Sparse Linear Systems*, 2nd ed., Society for Industrial and Applied Mathematics, Philadelphia, Pennsylvania, 2003, p. 307.

[151] D. A. Mitsoudis, N. A. Kampanis, and V. A. Dougalis, "A Finite Element Method For the Helmholtz Equation in Axially Symmetric Problems of Underwater Acoustics: Error Estimates and Numerical Experiments",

HERCMA 2001, Proceedings of the 5th Hellenic–European Conference on Computer Mathematics and its Applications, Athens, 2002, vol. 2, pp. 530-533.

[152] C. F. Gerald, and P. O. Wheatley, *Applied Numerical Analysis*, 7th ed., Addison-Wesley, Boston, Massachusetts, 2004, pp. 117-118.

[153] I. Tsukerman, A. Konrad, G. Meunier and I. C. Sabonnadiere, "Coupled Field-Circuit Problems: Trends and Accomplishments", *IEEE Transactions on Magnetics*, vol. 29, no. 2, pp.1701-1704, 1993.

[154] G. Bedrosian, "A New Method for Coupling Finite Element Field Solutions with External Circuits and Kinematics", *IEEE Transactions on Magnetics*, vol. 29, no. 2, pp.1664-1668, 1993.

[155] P. Dular, C. Geuzaine, and W. Legros, "A Natural Method for Coupling Magnetodynamic H-Formulations and Circuit Equations", *IEEE Transactions on Magnetics*, vol. 35, no. 3, pp.1626-1629, 1999.

[156] P. Zhou, W. N. Fu, D. Lin, S. Stanton, and Z. J. Cendes, "Numerical Modelling of Magnetic Devices", *IEEE Transactions on Magnetics*, vol. 40, no. 4, pp.1803-1809, 2004.

[157] P. Zhou, D. Lin, W. N. Fu, B. Ionescu, and Z. J. Cendes, "A General Cosimulation Approach for Coupled Field–Circuit Problems", *IEEE Transactions on Magnetics*, vol. 42, no. 4, pp.1051-1054, 2006.

[158] O. C. Zienkiewicz and R. L. Taylor, *The Finite Element Method Volume 2*, 4th ed., McGraw-Hill, New York, 1989, pp. 425-433.

[159] O. C. Zienkiewicz and R. L. Taylor, *The Finite Element Method Volume 2*, 4th ed., McGraw-Hill, New York, 1989, p. 428.

[160] A. Myers, *Improving the Efficiency of Magnetic Stimulation of Nerves*, PhD Thesis, University of Sheffield, Sheffield, 2005, pp. 139-140.

[161] A. Myers, *Improving the Efficiency of Magnetic Stimulation of Nerves*, PhD Thesis, University of Sheffield, Sheffield, 2005, pp. 33 & 38.

[162] O. Biro, K. Preis, G. Buchgraber, and I. Ticar "Voltage-Driven Coils in Finite Element Formulations Using a Current Vector and a Magnetic Scalar Potential", *IEEE Transactions on Magnetics*, vol. 40, no. 2, pp.1286-1289, 2004.

[163] S. C. Chapra, and R. P. Canale, *Numerical Methods for Engineers*, 4th ed., McGraw-Hill, New York, 2002, p. 337.

[164] S. S. Rao, *Engineering Optimization: Theory and Practice*, 3rd ed., New Age International, New Delhi, 1996, p. 283.

[165] A. D. Belegundu, and T .R. Chandrupatla, *Optimization Concepts and Applications in Engineering*, Prentice-Hall, New Jersey, 1999, pp. 30-35.

[166] S. C. Chapra, and R. P. Canale, *Numerical Methods for Engineers*, 4th ed., McGraw-Hill, New York, 2002, pp. 342-349.

[167] A. D. Belegundu, and T .R. Chandrupatla, *Optimization Concepts and Applications in Engineering*, Prentice-Hall, New Jersey, 1999, pp. 39-43.

[168] W. H. Press, S. A. Teukolsky, W. T. Vetterling, and B. P. Flannery, *Numerical Recipes in C++*, 2nd ed., Cambridge University Press, Cambridge, 2002, p. 406-410.

[169] S. C. Chapra, and R. P. Canale, *Numerical Methods for Engineers*, 4th ed., McGraw-Hill, New York, 2002, pp. 351-353.

[170] L. Bostock, and S. Chandler, *Pure Mathematics 2*, Stanley Thornes, Cheltenham, 1979, pp. 488-490.

[171] A. D. Belegundu, and T .R. Chandrupatla, *Optimization Concepts and Applications in Engineering*, Prentice-Hall, New Jersey, 1999, pp. 21-30.

[172] W. H. Press, S. A. Teukolsky, W. T. Vetterling, and B. P. Flannery, *Numerical Recipes in C++*, 2nd ed., Cambridge University Press, Cambridge, 2002, p. 398.

[173] S. C. Chapra, and R. P. Canale, *Numerical Methods for Engineers*, 4th ed., McGraw-Hill, New York, 2002, p. 356.

[174] A. D. Belegundu, and T .R. Chandrupatla, *Optimization Concepts and Applications in Engineering*, Prentice-Hall, New Jersey, 1999, pp. 259-262.

[175] A. D. Belegundu, and T .R. Chandrupatla, *Optimization Concepts and Applications in Engineering*, Prentice-Hall, New Jersey, 1999, pp. 265-267.

[176] S. C. Chapra, and R. P. Canale, *Numerical Methods for Engineers*, 4th ed., McGraw-Hill, New York, 2002, p. 359.

[177] A. D. Belegundu, and T .R. Chandrupatla, *Optimization Concepts and Applications in Engineering*, Prentice-Hall, New Jersey, 1999, pp. 262-263.

[178] A. D. Belegundu, and T .R. Chandrupatla, *Optimization Concepts and Applications in Engineering*, Prentice-Hall, New Jersey, 1999, pp. 263-265.

[179] A. D. Belegundu, and T .R. Chandrupatla, *Optimization Concepts and Applications in Engineering*, Prentice-Hall, New Jersey, 1999, pp. 267-272.

[180] W. H. Press, S. A. Teukolsky, W. T. Vetterling, and B. P. Flannery, *Numerical Recipes in C++*, 2nd ed., Cambridge University Press, Cambridge, 2002, pp. 448-460.

[181] A. D. Belegundu, and T .R. Chandrupatla, *Optimization Concepts and Applications in Engineering*, Prentice-Hall, New Jersey, 1999, pp. 272-276.

[182] W. H. Press, S. A. Teukolsky, W. T. Vetterling, and B. P. Flannery, *Numerical Recipes in C++*, 2nd ed., Cambridge University Press, Cambridge, 2002, p. 448.

[183] A. D. Belegundu, and T .R. Chandrupatla, *Optimization Concepts and Applications in Engineering*, Prentice-Hall, New Jersey, 1999, pp. 276-279.

[184] C. Xudong, Q. Jingen, N. Guangzheng, Y. Shiyou, and Z. Mingliu, "An Improved Genetic Algorithm for Global Optimization of Electromagnetic Problems", *IEEE Transactions on Magnetics*, vol. 37, no. 5, pp.3579-3583, 2001.

[185] R. Schaefer, and H. Telega, *Foundations of Global Genetic Optimization*, Springer-Verlag, Berlin, 2007, pp. 153-173.

[186] S. W. Mahfoud, *Niching Methods for Genetic Algorithms*, PhD Thesis, University of Illinois, Urbana-Champaign, 1995, p. 1.

[187] A. D. Belegundu, and T .R. Chandrupatla, *Optimization Concepts and Applications in Engineering*, Prentice-Hall, New Jersey, 1999, p. 11.

[188] S. C. Chapra, and R. P. Canale, *Numerical Methods for Engineers*, 4th ed., McGraw-Hill, New York, 2002, pp. 366-371.

[189] A. D. Belegundu, and T .R. Chandrupatla, *Optimization Concepts and Applications in Engineering*, Prentice-Hall, New Jersey, 1999, pp. 70-74.

[190] A. D. Belegundu, and T .R. Chandrupatla, *Optimization Concepts and Applications in Engineering*, Prentice-Hall, New Jersey, 1999, pp. 74-78.

[191] A. D. Belegundu, and T .R. Chandrupatla, *Optimization Concepts and Applications in Engineering*, Prentice-Hall, New Jersey, 1999, pp. 78-79.

[192] S. C. Chapra, and R. P. Canale, *Numerical Methods for Engineers*, 4th ed., McGraw-Hill, New York, 2002, pp. 375-386.

[193] A. D. Belegundu, and T .R. Chandrupatla, *Optimization Concepts and Applications in Engineering*, Prentice-Hall, New Jersey, 1999, pp. 141-221.

[194] A. D. Belegundu, and T .R. Chandrupatla, *Optimization Concepts and Applications in Engineering*, Prentice-Hall, New Jersey, 1999, pp. 222-228.

[195] S. Kirkpatrick, C. D. Gelatt, and M. P. Vecchi, "Optimization by Simulated Annealing", *Science*, vol. 220, no. 4598, pp. 671-680, 1983.

[196] S. Kirkpatrick, "Optimization by simulated annealing: Quantitative studies", *Journal of Statistical Physics*, vol. 34, no. 5/6, pp. 975-986, 1984.

[197] N. Metropolis, A. W. Rosenbluth, M. N. Rosenbluth, A. H. Teller, and E. Teller, "Equations of State Calculations by Fast Computing Machines", *Journal of Chemical Physics*, vol. 21, no. 6, pp. 1087-1092, 1953.

[198] A. Corona, M. Marchesi, C. Martini, and S. Ridella, "Minimizing Multimodal Functions of Continuous Variables with the 'Simulated Annealing' Algorithm", *ACM Transactions on Mathematical Software*, vol. 13, pp. 262-280, 1987.

[199] R. Muncaster, *A-Level Physics*, 4th ed., Stanley Thornes, Cheltenham, 1993, p. 256.

[200] W. H. Press, S. A. Teukolsky, W. T. Vetterling, and B. P. Flannery, *Numerical Recipes in C++*, 2nd ed., Cambridge University Press, Cambridge, 2002, p. 449.

[201] A. D. Belegundu, and T .R. Chandrupatla, *Optimization Concepts and Applications in Engineering*, Prentice-Hall, New Jersey, 1999, p. 274.

[202] W. H. Press, S. A. Teukolsky, W. T. Vetterling, and B. P. Flannery, *Numerical Recipes in C++*, 2nd ed., Cambridge University Press, Cambridge, 2002, pp. 449-455.

[203] J. W. Nilsson, and S. A. Riedel, *Electric Circuits*, 6th ed., Prentice-Hall, New Jersey, 2000, p. 39.

[204] E. B. Rosa and F. W. Grover, *Formulas and Tables for the Calculation of Mutual and Self-Inductance*, Revised Edition, United States Government Printing Office, 1948.

[205] A. Myers, *Improving the Efficiency of Magnetic Stimulation of Nerves*, PhD Thesis, University of Sheffield, Sheffield, 2005, p. 64.

[206] A. Myers, *Improving the Efficiency of Magnetic Stimulation of Nerves*, PhD Thesis, University of Sheffield, Sheffield, 2005, p. 65.

[207] E. Kreyszig, *Advanced Engineering Mathematics*, 9th ed., John Wiley, New York, 2006, p. 798.

[208] A. Myers, *Improving the Efficiency of Magnetic Stimulation of Nerves*, PhD Thesis, University of Sheffield, Sheffield, 2005, p. 56.

[209] Y. Roth, F. Padberg, and A. Zangen, "Transcranial Brain Stimulation for Treatment of Psychiatric Disorders", *Advanced Biological Psychiatry*, vol. 23, pp. 204 – 224, 2007.

[210] R. Albanese and G. Rubinacci, "Magnetostatic Field Computations in Terms of Two-Component Vector Potentials", *International Journal in Numerical Methods*, vol. 29, pp. 515-532, 1990.

[211] O. C. Zienkiewicz and R. L. Taylor, *The Finite Element Method Volume 1*, 4th ed., McGraw-Hill, New York, 1989.

[212] J. Smajic, Z. Andjelic, and M. Bebendorf, "Fast BEM for Eddy-Current Problems Using H-Matrices and Adaptive Cross Approximation", *IEEE Transactions on Magnetics*, vol. 43, no. 4, pp.1269-1272, 2007.

[213] A. Myers, *Improving the Efficiency of Magnetic Stimulation of Nerves*, PhD Thesis, University of Sheffield, Sheffield, 2005.

Appendix A

The human nerve [6], shown in Figure A.1, consists of a nucleus surrounded by a cell body out of which extends a long axon surrounded by a sheath of myelin. It is this axon which can be thought of as the nerve fibre. A nerve is exercised, that is a 'signal' is generated along its length, when an 'action potential' occurs at a point somewhere along the axon.

Consider the membrane that forms the outer surface of an axon. At rest, the region just within the membrane of such an axon is usually negatively charged owing to there being a lower concentration of positive sodium ions and a higher concentration of positive potassium ions. Thus the transmembrane potential can be thought of as normally being negative (in fact this is about -70 mV). When an action potential occurs, the potential inside the nerve fibre at that point is increased above a certain threshold value because the membrane there becomes more permeable to sodium ions which enter the axon. This in turn causes the membrane to become even more permeable to the ions and a rapid increase in transmembrane potential occurs,

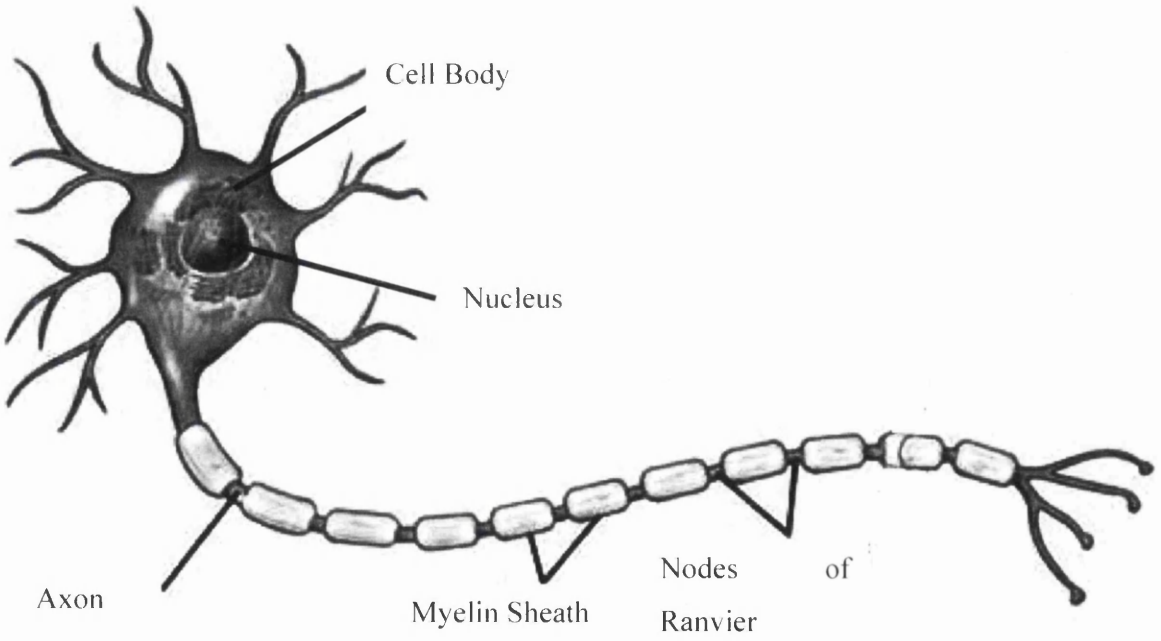

Figure A.1 - Labelled diagram of a myelinated human nerve cell (part courtesy of topfloormusic.com image gallery)

reversing the polarity of the potential. If the stimulus was removed before the potential increased above the threshold value then the potential would simply return to its resting negative value and no action potential would have been generated. It could be noted that a stronger sensation does not equate to a higher positive transmembrane potential, but rather is signalled by an increase in the repetition of action potentials.

Once an action potential has occurred at a certain point along a nerve fibre, then this signal is transmitted along the axon. This occurs owing to the localised increase of the permeability of the nerve membrane in the region adjacent to that where the original action potential has occurred. This causes positive sodium ions to enter at the new location and an action potential to occur there. The process continues along the nerve until the action potential has been 'transmitted' along its length. This occurs in both directions along the nerve but, in nature, action potentials are normally only initiated at the end of axons.

It may be seen from Figure A.1 that a myelin sheath punctuated by nodes of Ranvier normally surrounds a nerve fibre. This is an insulating layer and has the effect that, in between the nodes, the nerve membrane is impermeable to sodium ions. As a result, when an action potential occurs, the depolarisation around the nerve membrane at the action potential location causes the excess positive sodium ions to effectively travel along the nerve fibre to the location of the next node of Ranvier (owing to the attraction of the overall negative polarity at that location). The action potential therefore propagates along the nerve fibre by jumping from node to node. As a result of this phenomenon an action potential can travel along a nerve covered by a myelin sheath some ten times more quickly than a nerve not covered by a sheath. Most nerves in the human body are myelinated [6].

It may be clear from the above that, in magnetic stimulation, the objective is to pass current pulses through a stimulation coil and, by holding the coil above the body, to induce currents in the tissue that cause nerve action potentials to occur in the desired nerves. The problem with magnetic stimulation as it currently stands is that, without trial and error, it is difficult to work out beforehand whether the nerves that are desired to be stimulated actually will have action potentials generated in them. A further difficulty is that the broad nature of the electric field around the coil means

that action potentials get generated in nerves that it was not desired to stimulate. As stated in Section 1.1, the purpose of this work is to try and find improved coil geometries with more focal field profiles so that stimulating the intended nerves becomes easier and stimulating unintended nerves is avoided.

Appendix B

This appendix contains the parameters used in the thin-wire models of a helix, whose results are plotted in Section 3.9. A rate of change of current of 1A/s was assumed in the models.

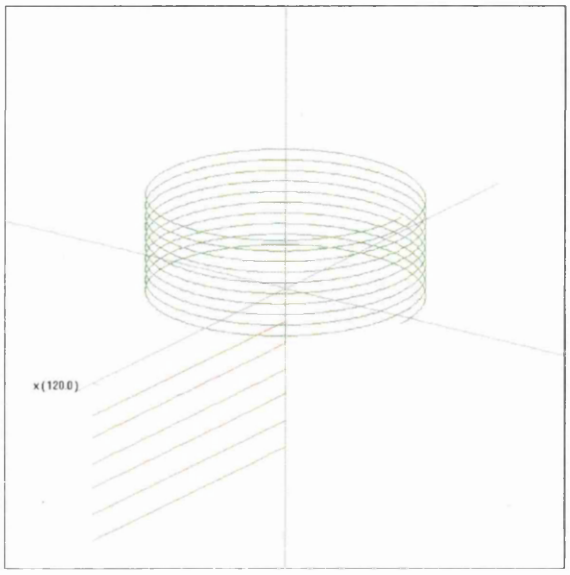

Figure B.1 - The helix as represented in the discretised thin-wire modeller with lines of field points below it

Parameters of the helix when represented as a helix in the discretised thin-wire modeller (coordinates and distances in mm):

Number of straight segments:	3000
Helix type:	Right handed
Helix axis:	z axis
Helix start point coordinates:	(0, 50, -3)
Helix end point coordinates:	(0, 50, 37)
Vertical turn spacing:	4
Number of turns:	10
Helix radius:	50
Helix x axis crossing point:	(50, 0, 0)

Parameters of the helix when represented as vertically stacked circular thin-wire loops (dimensions in mm):

Loop radii:	50
Loop axes:	z axis
Loop centre point coordinates:	(0,0,0), (0,0,4), (0,0,8), (0,0,12), (0,0,16), (0,0,20), (0,0,24), (0,0,28), (0,0,32), (0,0,36)

Appendix C

The graph presented below gives the values of the coil drive current and instantaneous resistance calculated at different time step values during the solution of the circuit coupled model of a Magstim HP90 coil coupled to a Magstim Rapid2 stimulator discussed in Section 5.12.

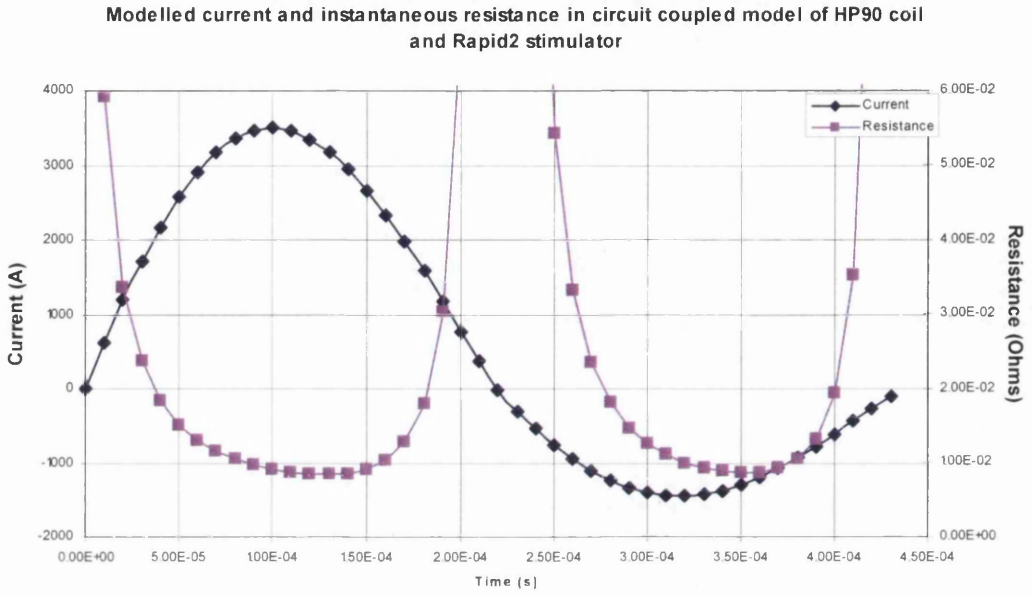

Figure C.1 - The modelled current and instantaneous resistance in a circuit coupled model of a Magstim HP90 coil with a Rapid^2 stimulator

Appendix D

The values given below are the loop cross sectional centre axial radius and height above coil base arising from the three runs of the New Shape Module discussed in Section 7.6 on page 202.

Results from run 1:

Loop	Radius (mm)	Height (mm)
1	6.45392	3.16072
2	12.6496	41.6262
3	4.58759	45.8556
4	4.98954	6.4364
5	12.3104	3.31704
6	3.70011	16.212
7	7.18206	14.5242
8	11.7575	5.22385
9	8.81781	9.28658
10	11.7004	3.08493
11	14.9445	7.35788
12	10.0098	3.07675
13	7.00023	4.88301
14	4.00872	47.3521

Results form run 2:

Loop	Radius (mm)	Height (mm)
1	5.95201	18.178
2	7.68053	4.61485
3	6.10491	42.5586
4	3.533	3.77886
5	3.6153	4.52144
6	3.53004	28.6753
7	12.345	3.25618
8	10.3163	4.73372
9	4.89622	15.0542
10	9.70368	3.01198
11	12.0305	17.0765
12	14.754	3.77291
13	5.386	26.8287
14	11.2564	3.8059

Results from run 3:

Loop	Radius (mm)	Height (mm)
1	17.8311	10.6399
2	5.30548	3.40428
3	6.5935	4.96939
4	16.0422	3.71754
5	13.1934	46.8553
6	12.6992	5.20384
7	6.00337	26.7031
8	5.49405	4.33066
9	5.59174	4.00858
10	3.25843	15.8551
11	4.06684	3.25948
12	5.93469	41.0541
13	13.8779	3.85811
14	6.9517	4.43552

Appendix E

The table below gives the r and z values of the loop cross-section centres of each coaxial loop making up the gull-wing coil presented in Section 7.8.

Loop	r location value (mm)	z location value (mm)
1	4.9	6.5
2	6.9	11
3	9.0	15.5
4	11.0	20.0
5	13.0	21.5
6	15.1	23.0
7	21.1	23.8
8	26.9	24.5
9	32.7	25.3
10	38.5	26.0
11	44.25	26.8
12	50.1	27.5
13	55.9	28.3
14	61.5	29.0

Appendix F

The table below shows the resonant frequency and resonant frequency resistance and inductance values of each size of gull-wing shaped coil size explained in Section 7.12 as calculated by the FEM Module of this work.

Size Factor Variable	Resonant Frequency Resistance (mΩ)	Resonant Frequency Inductance (μH)	Resonant Frequency (kHz)
0.925	54	7.67	3.91
1.0	56	7.46	3.95
1.5	61	7.09	4.03
2.0	58	6.85	4.09
2.5	53	6.64	4.15
3.0	48	6.52	4.20
3.5	43	6.43	4.23
4.0	39	6.38	4.25
4.5	37	6.34	4.27
5.0	35	6.31	4.28